UNIVERSITA' POLITECNICA DELLE MARCHE

FACULTY OF ENGINEERING

Master of Science Course in ENVIRONMENTAL ENGINEERING

The Earth observed from the Sky:

The Amazon Forest

Supervisor

Prof. Ing. Giorgio Passerini

Co-Supervisors

Dott. Umberto Rizza

Ing. Alessandra Chiappini

Candidate

Martina Tommasi

A.Y. 2021/2022

Summary

1. Introduction 6
   1.1 The Amazon Forest 7
2. Material and methods 11
   2.1 Remote Sensing 11
   2.2 Sensors 11
   2.3 Data Processing Level 13
   2.4 The EOS Nasa system 14
   2.5 The FIRMS system 16
      2.5.1 Aqua 18
      2.5.2 Terra 20
      2.5.3 MODIS 22
      2.5.4 SUOMI NPP 24
      2.5.5 NOAA -20 26
      2.5.6 VIIRS 27
   2.6 NASA FIRMS web Platform 28
      2.6.1 MODIS Active Fire Data 28
      2.6.2 VIIRS 375 m Active Fire Product 31
      2.6.3 Analysed data: Bright_T31 34
      2.6.4 Analysed data: FRP 34
      2.6.5 Period and location of data analysed 38
      2.6.6 How to download 39
   2.12 QGIS system 42
3. Results and discussion 44
   3.1 Qualitative analysis of firepower of FAMF 44
   3.2 Quantitative analysis of firepower of FAMF 70
      3.2.1 MODIS FRP analysis: Maximum Values 71
      3.2.2 MODIS FRP analysis: Mean Value, Standard Deviation Value and Median Value 73
      3.2.3 VIIRS SUOMI NPP FRP analysis: Maximum Values 76
      3.2.4 VIIRS SUOMI NPP FRP analysis: Mean Value and Standard Deviation Value distribution 78
      3.2.5 MODIS Bright_T31 analysis: Mean Value, Standard Deviation Value and Median Value 80

3.2.6 VIIRS SUOMI NPP Bright_T31 analysis: Mean Value and Standard Deviation Value Distribution 82
3.3 Analysis of firepower with confidence 85
3.3.1 MODIS FRP analysis with confidence ≥ 80 %: Maximum Value 86
3.3.3 VIIRS SUOMI NPP FRP analysis with confidence = high: Maximum Value 89
3.3.4 VIIRS SUOMI NPP FRP analysis with confidence = high: Mean Value,Standard Deviation Value and Median Value 91
3.4 ANALYSIS OF FIRE POWER: CLASSIFICATION OF VALUES 93
3.4.1 MODIS DATA ANALYSIS: FRP classification 93
3.4.2 VIIRS SUOMI NPP FRP ANALYSIS: FRP classification 105
3.4.3 MODIS DATA ANALYSIS: FRP classification with CONFIDENCE ≥ 80 % 112
3.4.4 VIIRS SUOMI NPP FRP ANALYSIS: FRP classification with CONFIDENCE = high 125
3.5 Statistical analysis: ANOMALIES 132
3.5.3 MODIS FRP Analysis: Anomalies of FRP Mean Values with CONFIDENCE ≥ 80 % 132
3.5.4 VIIRS SUOMI NPP FRP ANALYSIS: Anomalies of FRP mean values with CONFIDENCE = high 133
3.6 Statistical analysis: TOTAL NUMBER OF EVENTS 134
3.6.3 MODIS Data Analysis: Total Number of events with CONFIDENCE ≥ 80 % 134
3.6.4 VIIRS SUOMI NPP Data Analysis: Total Number of events with CONFIDENCE = high 135
3.7 Statistical analysis: NUMBER OF EVENTS FOR FRP≥100MW 136
3.7.3 MODIS Data Analysis: Number of FRP events ≥ 100 MW (with CONFIDENCE ≥ 80%) 136
3.7.4 VIIRS S-NPP Data Analysis: Number of FRP events ≥ 100 MW (with CONFIDENCE = high) 137
3.8 Statistical analysis: NUMBER OF EVENTS FOR FRP≥300MW 138
3.8.3 MODIS Data Analysis: Number of FRP events ≥ 300 MW (with CONFIDENCE ≥ 80%) 138
3.8.4 VIIRS SUOMI NPP Data Analysis: Number of FRP events ≥ 300 MW (with CONFIDENCE = high) 139
3.9 GRAPHICAL ANALYSIS OF IMAGES: Fire and Thermal Anomalies provides from Worldview system 140
3.9.1 Fire and Thermal Anomalies provides from Worldview system 141
4. Conclusions 143
5. References 147

Abstract

The Amazon Rainforest is an important place for the carbon and water cycle in the climate system, whose function has been degraded in recent decades by land use and climate change.

Since 2010, increases in carbon emissions, increases in deforestation (79% and 74%) and increases in forest area burned (14% and 42%) have been observed within the Amazon Rainforest.

Field notifications for illegal deforestation and related offences decreased by 42%, while fines paid for sentences issued decreased by 89%.

The year 2020 showed a 12% decrease in precipitation, also indicating a climate impact due to carbon emissions.

The changes in 2019 and 2020 are mainly due to the western Amazon becoming a carbon source. It is assumed that the consequences of the collapse of enforcement has led to increased deforestation, biomass burning and degradation producing net carbon losses and enhancing drying and warming of forest regions.

In addition, extreme droughts and high temperatures have become more frequent in the last two decades, increasing fire risk in the Amazon.

This work analyses forest fire from both qualitative and quantitative perspective over the last 20 years in the Amazon Forest using satellite data from various satellites.

Sommario in lingua italiana

La Foresta Amazzonica è un luogo importante per il ciclo del carbonio e dell'acqua nel sistema climatico terrestre, la cui funzione è stata degradata negli ultimi decenni dall'uso del suolo e dai cambiamenti climatici.

Dal 2010, nella Foresta amazzonica sono stati osservati aumenti delle emissioni di carbonio, della deforestazione (79% e 74%) e della superficie forestale bruciata (14% e 42%).

Le notifiche sul campo per deforestazione illegale e reati correlati sono diminuite del 42%, mentre le multe pagate per le sentenze emesse sono diminuite dell'89%.

Il 2020 ha registrato una diminuzione del 12% delle precipitazioni, indicando anche un impatto climatico dovuto alle emissioni di carbonio.

I cambiamenti nel 2019 e nel 2020 sono dovuti principalmente al fatto che l'Amazzonia occidentale diventa una fonte di carbonio. Si presume che le conseguenze del crollo dell'applicazione abbiano portato a un aumento della deforestazione, della combustione e del degrado della biomassa, producendo perdite nette di carbonio e aumentando l'essiccazione e il riscaldamento delle regioni forestali.

Inoltre, negli ultimi due decenni sono diventate più frequenti le siccità estreme e le alte temperature, aumentando il rischio di incendi in Amazzonia.

Questo lavoro analizza gli incendi boschivi da un punto di vista sia qualitativo che quantitativo negli ultimi 20 anni nella Foresta Amazzonica, utilizzando dati satellitari provenienti da diversi satelliti.

La variabile più importante per caratterizzare gli incendi selvatici è il potere radiativo degli incendi (FRP) (cioè l'energia radiante rilasciata dagli incendi), perché è una variabile cruciale per stimare gli impatti socio-ecologici degli incendi, nonché la biomassa bruciata e le emissioni indotte dagli incendi.

Le rilevazioni di FRP sono disponibili da diversi satelliti in orbita polare e geostazionaria. Lo strumento MODIS (Moderate Resolution Imaging Spectroradiometer) a bordo dei satelliti Aqua e Terra del National Aeronautics and Space Administration (NASA) rileva operativamente gli incendi attivi a livello globale dal 2000. L'ultimo prodotto MODIS Collection 6 sugli incendi attivi fornisce rilevamenti di incendi e recuperi di FRP più affidabili dal punto di vista scientifico (Giglio, Schroeder, & Justice, 2016). Tuttavia, i sensori Aqua e Terra MODIS stanno invecchiando e si stanno avvicinando alla fine della loro vita. La continuità con Aqua MODIS è garantita dallo strumento di nuova generazione a risoluzione moderata chiamato Visible Infrared Imaging Radiometer Suite (VIIRS). Il primo sensore VIIRS si trova a bordo del satellite Suomi National Polar-orbiting Partnership (Suomi NPP), lanciato nel 2011.

I dati del MODIS, dall’anno 2001 al 2022, e del VIIRS, dall’anno 2012 al 2022, sono stati scaricati attraverso il portale web FIRMS, che è stato utilizzato anche per scaricare le immagini satellitari usare nell’analisi qualitativa degli incendi.

FIRMS offre la possibilità di scaricare informazioni sugli incendi attivi e sui punti caldi più vecchi degli ultimi 7 giorni.

Per l'analisi qualitativa sono stati scelti tre mesi, rappresentativi degli eventi, che sono Agosto, Ottobre e Dicembre e i dati mensili, rappresentati sulle immagini, sono stati confrontati per tutti gli anni.

L'analisi quantitativa invece si è svolta attraverso i seguenti step:

1. individuazioni dei valori massimi di FRP annuali;
2. individuazioni dei valori medi di FRP annuali;
3. individuazioni dei valori di deviazione standard della media di FRP annuali;
4. individuazioni della mediana di FRP annuali;
5. applicazione di un livello di filtraggio ai dati e ripetizione dei punti 1,2,3,4;
6. suddivisione dei valori di FRP in 10 classi;
7. calcolo delle anomalie dei valori medi di FRP;
8. calcolo dei valori totali di eventi.

In conclusione, tutte le analisi mostrano che la maggiore intensità e il maggior numero di eventi si verificano negli anni 2004, 2005, 2007 e dal 2019 al 2022 per i valori di FRP rilevati dal MODIS e negli anni 2012,205, 2019, 2020 per i valori di FRP rilevati dal VIIRS.

1. Introduction

The Amazon is the most extensive tropical rainforest in the world, supporting a high level of biodiversity and playing an essential role in global biosphere-atmosphere interactions. The dynamics of Amazon ecosystems exert considerable influence on biogeochemical cycles, moisture transport, and regional climate of local and remote regions.

Extreme droughts in the Amazon seem to have become more frequent since 1995, and the drought magnitude has been positively associated with the number of active fires, which release significant amounts of greenhouse gases and aerosols into the atmosphere. (Marengo and Espinoza, 2016)

The exceptional droughts of 2005 and 2010, for instance, deeply affected the Brazilian economy and caused an intensification of wild fires and associated impacts. (Lima, 2017)

Over the past years illegal deforestation and fires has strongly increased in parallel to changes in governance.

This research, which deals with the fires in the Amazon rainforest, was made possible thanks to the collaboration between:

- Institute of Atmospheric Science and Climate of the Italian National research Council (CNR/ISAC);
- Department of Industrial Engineering and Mathematical Sciences of the Polytechnic University of Marche (UNIVPM/DIISM).

This study focuses on the statistical analysis of the number of fires in Amazon Forest and some parameters representative of the rainforest provided by the NASA satellites.

Fire data and images come from the Moderate Resolution Imaging Spectroradiometer (MODIS) instrument, which is on board the Terra and Aqua satellites, and the Visible Infrared Imaging Radiometer Suite (VIIRS) instrument, which is on board the NASA/NOAA Suomi NPP and NOAA-20 spacecrafts.

Satellite-derived fire data and imagery available in https://worldview.earthdata.nasa.gov (Worldview) and fire data are available for download in the Fire Information for Resource Management System (FIRMS; https://firms.modaps.eosdis.nasa.gov) system.

MODIS data are available from November 2000 (for Terra) and from July 2002 (for Aqua) to the present. VIIRS S-NPP 375 m data is available from January 2012 to the present. VIIRS 375 m (NOAA-20) data are currently available from 01 January 2020 to the present.

Data used for this work are from:

- **MODIS** : from 01 January 2001 to 31 December 2022
- **VIIRS S-NPP**: from 01 January 2012 to 31 December 2022

Data analysed concern:

- FRP: Fire radiative power (FRP) [MW]
- Bright_T31: Infrared (10.78-11.28 μm) MODIS Band 31 brightness temperature of fire pixel [K]

Software that are utilised for the statistical analysis are:

- QGIS
- Excel

1.1 The Amazon Forest

The Amazon is a vast geographical region in South America characterised by a rainforest, known as the Amazon Rainforest.

With immense forests and rivers filled with unique natural environments that support a remarkable cultural diversity across 7 million square kilometres, the Amazon is extraordinarily important to South America and the entire planet.

The Amazon rainforest spans eight countries and one overseas territory, of which:

- about 60% is located in Brazil;
- 13% is in Peru;
- 10% in Colombia;
- smaller part in Venezuela;
- smaller part in Ecuador;
- smaller part in Bolivia;
- smaller part in Guyana;
- smaller part in Suriname;
- smaller part in French Guiana.

Figure 1 - Amazon Forest Location Map (WWF 2022)

Figure 2 - Map of the Amazon rainforest according to WWF classification (white) and the Amazon river basin (blue)(WWF 2022)

Also known as the Earth's Green Lung due to its size and importance, it constitutes more than half of the world's remaining tropical forests and is home to more biodiversity than any other tropical forest; it is one of Brazil's six main biomes, and constitutes approximately 59.4% of Brazil's territory, covering three of the country's five statistical regions (North, Northeast and Centre-West).

The Amazon is undergoing rapid changes, and these changes threaten the survival of native species, humans and animals, and threaten regional and global stabilisation of the climate.

More than in any previous era, the biome faces large-scale destruction, disconnection and degradation that manifest in various ways at the local level.

The Amazon is currently in a critical situation, facing a variety of pressures and threats both to its biodiversity and to the traditional peoples and communities that live there. The region was faced a complex political context in which there are stark barriers to the full participation of civil society in decision-making related to environmental protection and the pursuit of sustainable development; certain economic priorities conflict with conservation; and there has always been insufficient government capacity to address environmental issues.

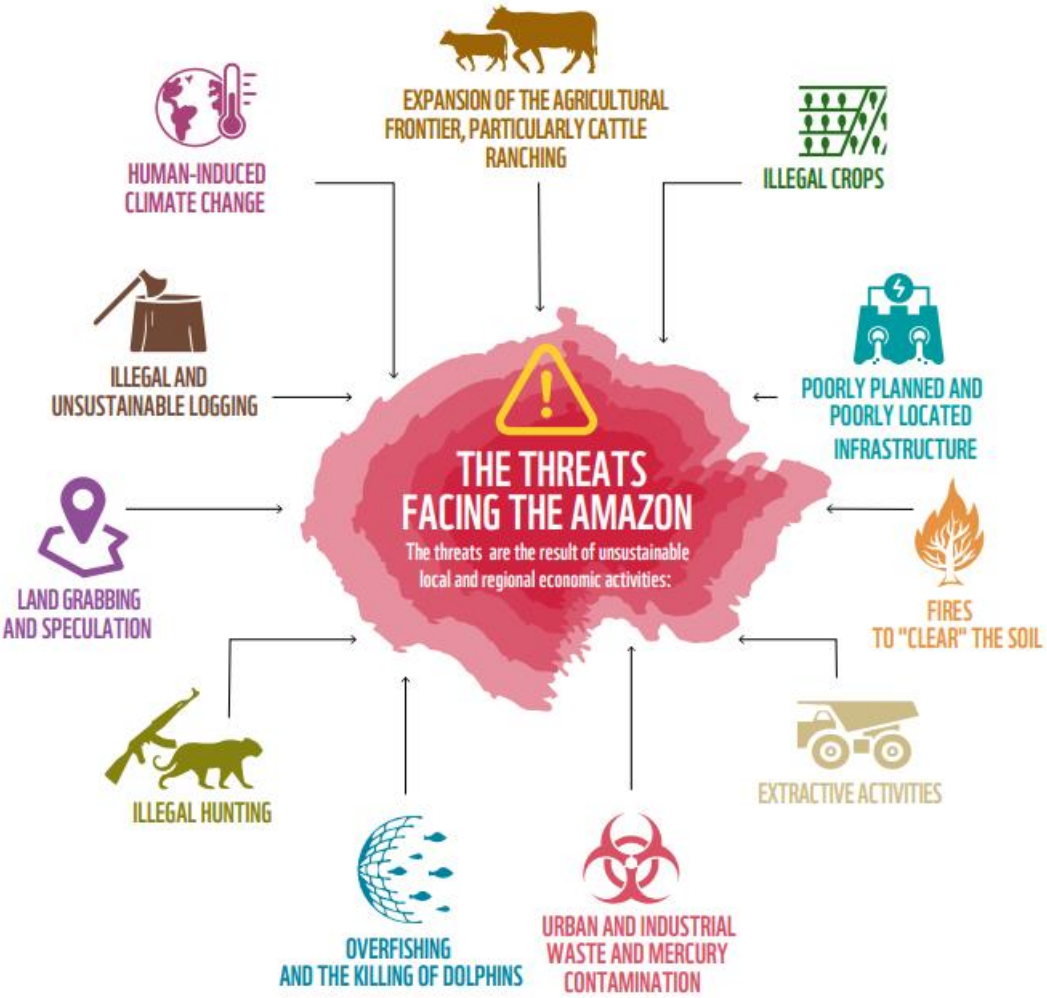

Figure 3- The threats facing the Amazon (WWF Living Amazon Report 2022)

In addition, the ongoing advance of deforestation is jeopardizing the health and long-term survival of the biome, constituting its greatest threat. The main drivers of deforestation are the expansion of agriculture and cattle ranching, as well as land grabbing and speculation. But forest loss is also associated with other phenomena that contribute to degradation and deforestation including unsustainable and illegal logging, uncontrolled forest fires, and poorly planned infrastructure.

The problems affecting the Amazon rainforest are many, but some of them lead to the outbreak of new fires, for example, through fires, parts of the Amazon rainforest are transformed into land for agriculture and pastoralism.

In this thesis, the focus is on fires occurring in the Amazon rainforest, which can be referred to as **FAMF**: Fire in the Amazon Forest.

Fire dynamics in the Amazon arise from a complex interaction of climate, vegetation, and human beings. Most fires in primary forest or disturbed vegetation cover types (logged areas, pasture, and crop fields) result from anthropogenic ignition sources, including intentionally ignited fires for forest clearing (deforestation), accidental fires, and those that escape out of control from agriculture or pasture maintenance. Deforested regions and pastures have also the potential to increase fire susceptibility in the Amazon and transform large areas of tropical forest into savanna or grass-

dominated vegetation. Ecosystem composition regulates available fuels, with fire severity, intensity, and spread rate determined by a complicated interplay between ecosystems and climate. Intact closed canopy Amazon Forest provides a natural barrier for fire ignition and spread with high moisture content in the air and low radiation near the ground. (Lima, 2017)

The Amazon region has a hot humid climate and is one of the rainiest areas in the world, with rainfall concentrated in the months between December and May.

In the dry season, from June to November, breeders and farmers burn portions of the forest to make room for new pastures or to take land from the forest for new agricultural plots.

In recent years, climate change has caused a state of drought that has favoured the development of longer lasting and more intense fires.

During severe droughts, the Amazon experiences an increase in the number of fires, which has been attributed to an increase in the forest's susceptibility to fire, due to a decrease in deep soil water storage and atmospheric moisture content in response to a persistent decrease in rainfall (Nepstad et al, 1999; Ray et al., 2005).

FAMF are becoming more intense because of climate change and yet, at the same time, contribute to it, in a vicious circle creating conditions conducive to yet further fire. Fire could surpass deforestation in the future to become the Amazon’s main source of carbon emissions 22, with climate and land use changes further expanding the areas prone to fire.

In synergy with climate and land use change, forest degradation also increases their susceptibility to fire. Degradation tends to result in less compact, and therefore drier and more flammable vegetation, so degraded forest is at greater risk from fire than the same type of well-preserved forest(WWF, Living Amazon Forest Report, 2022).

2. Material and methods

2.1 Remote Sensing

Remote sensing is the acquiring of information from a distance. NASA (National Aeronautics and Space Administration: civil government agency responsible for the United States space programme and aerospace research) observes Earth and other planetary bodies via remote sensors on satellites and aircrafts that detect, and record reflected or emitted energy.

Figure 4 - European Remote Sensing (NASA's Earth Observing System)

Remote sensors, which provide a global perspective and a wealth of data about Earth systems, enable data-informed decision making based on the current and future state of our planet. (NASA, 2022)

2.2 Sensors

Sensors, or instruments, aboard satellites and aircrafts use the Sun as a source of illumination or provide their own source of illumination, measuring energy that is reflected back. Sensors that use natural energy from the Sun are called passive sensors; those that provide their own source of energy are called active sensors.

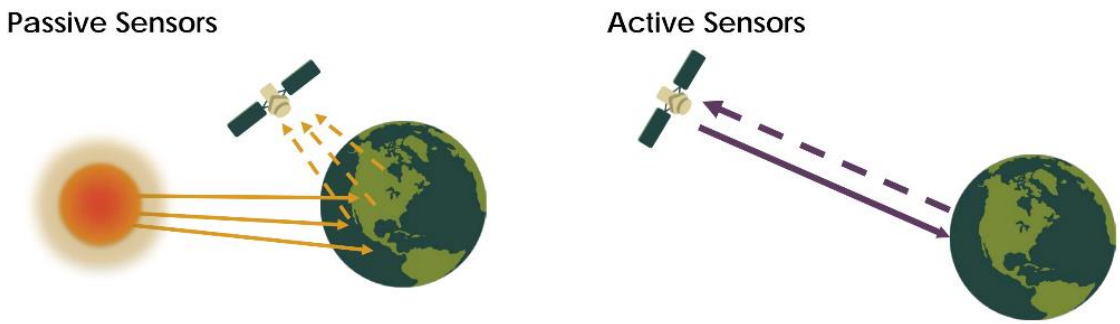

Figure 5 - Diagram of a passive sensor versus an active sensor (NASA Applied Sciences Remote Sensing Training Program.)

Passive sensors include different types of radiometers (instruments that quantitatively measure the intensity of electromagnetic radiation in select bands) and spectrometers (devices that are designed to detect, measure, and analyse the spectral content of reflected electromagnetic radiation). Most passive systems used by remote sensing applications operate in the visible, infrared, thermal infrared, and microwave portions of the electromagnetic spectrum.

Electromagnetic energy, produced by the vibration of charged particles, travels in the form of waves through the atmosphere and the vacuum of space. These waves have different wavelengths and frequencies (Fig. 6). (NASA SCIENCE)

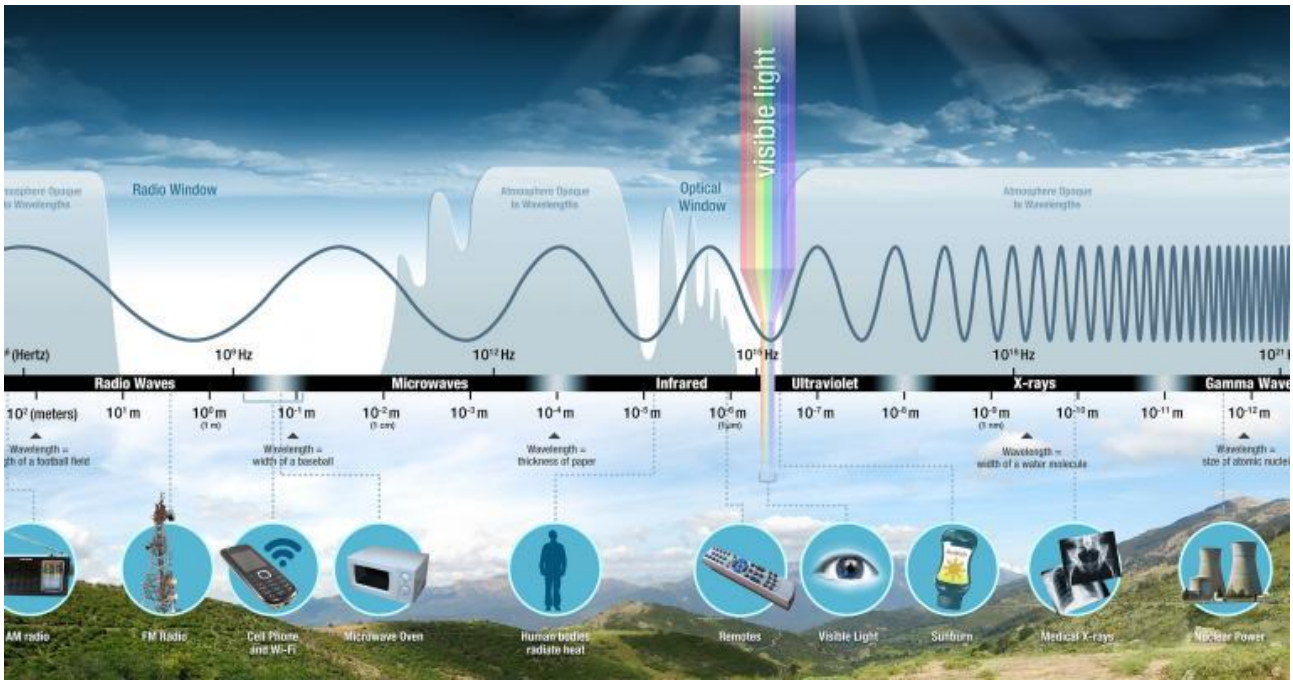

Figure 6 - Electromagnetic spectrum (NASA Science)

Radio, microwave, and infrared waves, have a higher frequency, while others, such as ultraviolet, x-rays, and gamma rays, have a much shorter frequency. Visible light sits in the middle of that range of long to shortwave radiation. This small portion of energy is all that the human eye is able to detect. Instrumentation is needed to detect all other forms of electromagnetic energy. NASA instrumentation utilizes the full range of the spectrum to explore and understand processes occurring on Earth.

These passive sensors measure land and sea surface temperature, vegetation properties, cloud and aerosol properties, and other physical attributes. Most passive sensors cannot penetrate dense cloud cover and thus may have limitations observing areas like the tropics where dense cloud cover is frequent.

Active sensors include different types of radio detection and ranging (radar) sensors, altimeters, and scatterometers. Most active sensors operate in the microwave band of the electromagnetic spectrum, which gives them the ability to penetrate the atmosphere under most conditions.

These types of sensors are useful for measuring the vertical profiles of aerosols, forest structure, precipitation and winds, sea surface topography, and ice, among others.

2.3 Data Processing Level

Remote sensing data acquired from instruments aboard satellites require processing before the data are usable by most researchers and applied science users.

NASA's Earth Observing System Data and Information System (EOSDIS; https://www.earthdata.nasa.gov/eosdis) data products are processed at various levels ranging from Level 0 to Level 4.

The EOSDIS science operations are by the Distributed Active Archive Centers (DAACs) with specific responsibilities for production, archiving, and distribution of Earth science data products. The DAACs serve a large user community by providing capabilities to search and access science data products and specialized services.

Level 0 products are raw data at full instrument resolution. At higher levels, the data are converted into more useful parameters and formats.

All EOS (NASA's Earth Observing System) instruments must have Level 1 Standard Data Products (SDPs); most have SDPs (Software Development) at Level 2 and Level 3; and many have Level 4 SDPs.

Some EOS Interdisciplinary Science Investigations also have generated Level 4 SDPs. Specifications for the set of SDPs to be generated are reviewed by the Earth Observing System Project Science Office (EOSPSO) and NASA Headquarters to ensure completeness and consistency in providing a comprehensive science data output for EOS.

Data Level	Description
Level 0	Reconstructed, unprocessed instrument and payload data at full resolution, with any and all communications artefacts (e.g., synchronization frames, communications headers, duplicate data) removed. (In most cases, NASA's EOS Data and Operations System provides these data to the DAACs (Distributed Active Archive Centers) as production data sets for processing by the Science Data Processing Segment or by one of the SIPS (Science Investigator-led Processing Systems) to produce higher-level products.)
Level 1A	Level 1A (L1A) data are reconstructed, unprocessed instrument data at full resolution, time-referenced, and annotated with ancillary information, including radiometric and geometric calibration coefficients and georeferencing parameters (e.g., platform ephemeris) computed and appended but not applied to L0 data.
Level 1B	L1B data are L1A data that have been processed to sensor units (not all instruments have L1B source data).
Level 1C	L1C data are L1B data that include new variables to describe the spectra. These variables allow the user to identify which L1C channels have been copied directly from the L1B and which have been synthesized from L1B and why.
Level 2	Derived geophysical variables at the same resolution and location as L1 source data.
Level 2A	L2A data contains information derived from the geolocated sensor data, such as ground elevation, highest and lowest surface return elevations, energy quantile heights ("relative height" metrics), and other waveform-derived metrics describing the intercepted surface.
Level 2B	L2B data are L2A data that have been processed to sensor units (not all instruments will have a L2B equivalent).
Level 3	Variables mapped on uniform space-time grid scales, usually with some completeness and consistency.
Level 3A	L3A data are generally periodic summaries (weekly, ten-day, monthly) of L2 products.
Level 4	Model output or results from analyses of lower-level data (e.g., variables derived from multiple measurements).

Table 1 - Description of data processing level (NASA's Earth Observing System)

2.4The EOS Nasa system

The Earth Observing System (EOS; https://eospso.nasa.gov/content/nasas-earth-observing-system-project-science-office)is a NASA programme for observing the Earth from space, comprising a series of artificial satellites and scientific instruments placed in orbit around the planet. (Wikipedia, 2020).

It is a coordinated series of polar-orbiting and low inclination satellites for long-term global observations of the land surface, biosphere, solid Earth, atmosphere, and oceans.

As a major component of the Earth Science Division of NASA's Science Mission Directorate, EOS enables an improved understanding of the Earth as an integrated system. The EOS Project Science Office (EOSPSO) is committed to bringing program information and resources to the Earth science research community and the general public alike. (NASA, 2022)

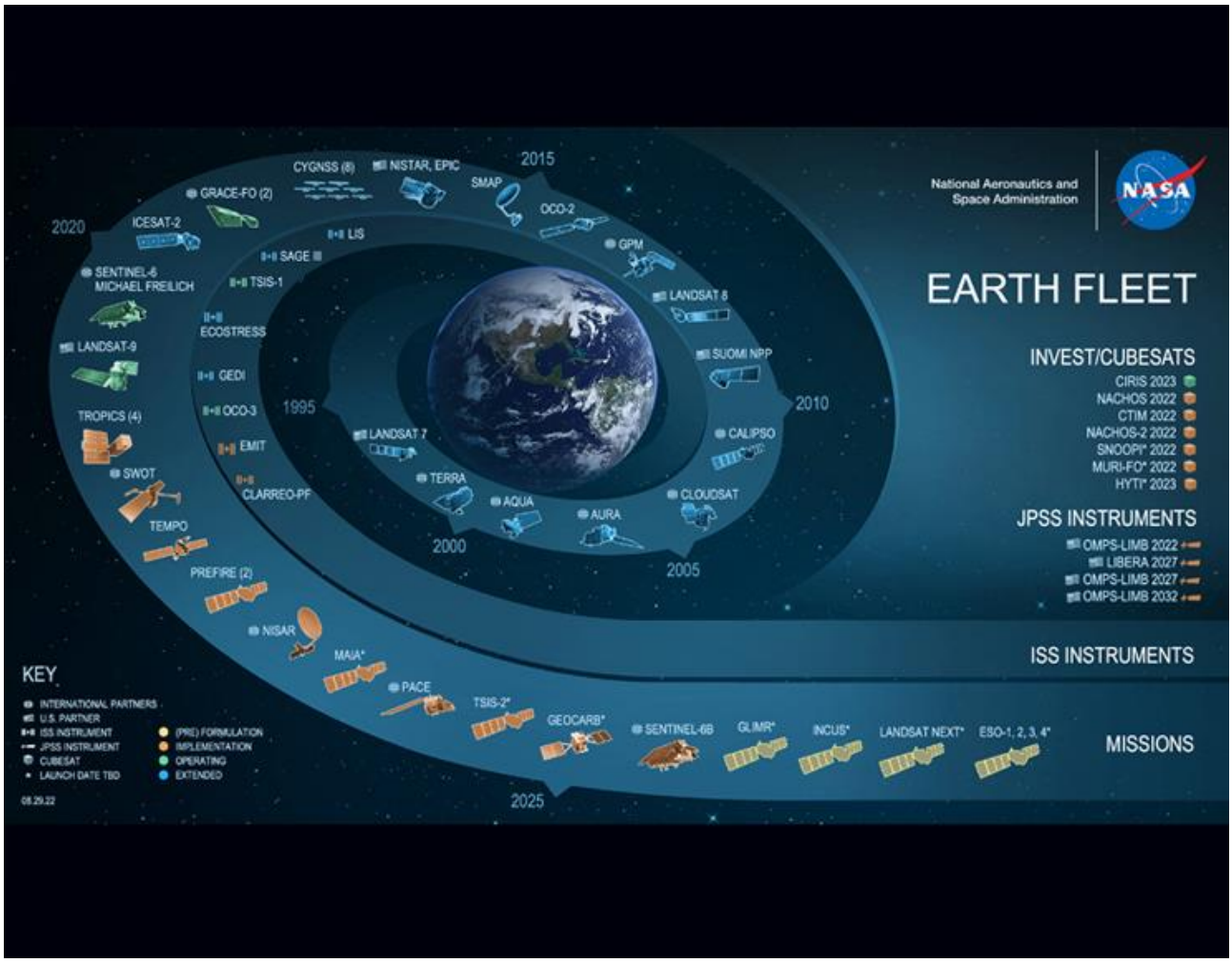

Figure 7 - NASA Earth Science Division Missions (NASA,2022)

Results from early missions shed light on critical components of the Earth system while prompting further, more advanced investigations. The NASA Earth Observing System (EOS) program was conceived in the 1980s and began to take shape in the early 1990s. EOS is comprised of a series of coordinated polar-orbiting satellites designed to monitor and understand key components of the climate system and their interactions through long-term global observations. The EOS missions focus on the following climate science areas: radiation, clouds, water vapor, and precipitation; the oceans; greenhouse gases; land-surface hydrology and ecosystem processes; glaciers, sea ice, and ice sheets; ozone and stratospheric chemistry; and natural and anthropogenic aerosols. (NASA,2022)

2.5 The FIRMS system

The NASA EOS programme therefore uses satellites to collect environmental data on our planet through two types of sensors: the Moderate Resolution Imaging Spectroradiometer (MODIS) on the Terra and Aqua satellites and the Visible Infrared Imaging Radiometer Suite (VIIRS) on Suomi-NPP and NOAA 20 – collect data critical to wildfire management.

Within three hours of a satellite observation the NASA Fire Information for Resource Management System (FIRMS) distributes active fire data to institutions responsible for wildfire management.

This data, referred to as Near Real-Time (NRT), consists of thermal anomalies, or hot-spots, identified as a satellite passes overhead.

Satellites observe the planet multiple times daily and these hot-spots can be used to identify new wildfires or track changes to existing wildfires around the globe when conditions make local monitoring difficult (NASA 2022).

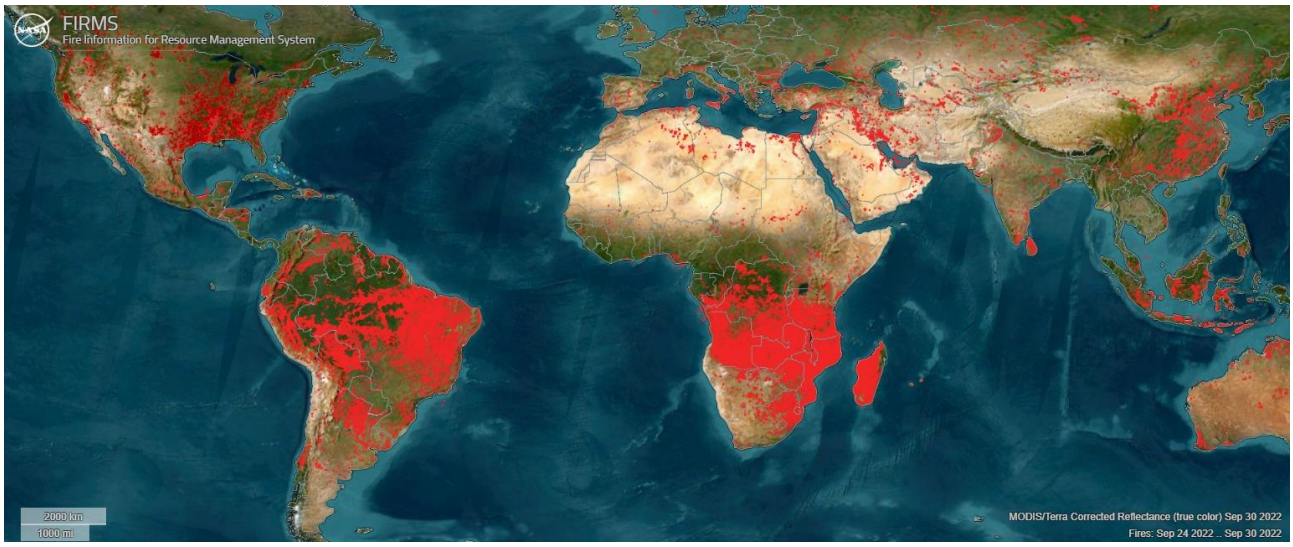

Figure 8 - FIRMS fire map showing fire activity (in orange) detected by Terra MODIS worldwide during the week 24 September 2022 to 30 September 2022 (FIRMS Global)

NASA FIRMS has two independent platforms, “FIRMS Global” and “FIRMS US/Canada”.

FIRMS Global was initially developed at the University of Maryland with funding from “NASA Applied Sciences” to provide wildfire data to firefighters and support staff worldwide.

FIRMS US/Canada is a collaboration between NASA and the USDA (United States Department of Agriculture) Forest Service and provides data to support strategic wildland fire monitoring and response by the interagency fire management community and to inform the general public.

Both FIRMS platforms are now part of NASA's Land, Atmosphere Near real-time Capability for EOS (LANCE).

FIRMS Key Features

• Global active fire/hotspots data and imagery from MODIS and VIIRS updated throughout the day.

• Geostationary active fire/hotspots data coming in Summer 2022.

• Enhanced interactive tools to visualize satellite imagery, active fire detections, and other NASA science products relevant to wildfire management.

• Customized maps for viewing and sharing.

• Active fire detection data in multiple GIS formats and WMS, WMS-T and WFS web services.

• Download historical data in GIS formats.

• Automated detection alert system for user-defined areas of interest.

2.5.1 Aqua

Aqua is a major international Earth Science satellite mission centered at NASA. Launched on May, 2002, the satellite has six different Earth-observing instruments on board and is named for the large amount of information it collects about water in the Earth system. Aqua gathers this information from its stream of approximately 89 Gigabytes of data a day. The water variables being measured include almost all elements of the water cycle and involve water in its liquid, solid, and vapor forms. Additional variables being measured include radiative energy fluxes, aerosols, vegetation cover on the land, phytoplankton and dissolved organic matter in the oceans, and air, land, and water temperatures.

The Aqua mission is a part of the NASA-centered international Earth Observing System (EOS). Aqua was formerly named EOS PM, signifying its afternoon equatorial crossing time.

Aqua was originally developed for a six-year design life but has now far exceeded that original goal. (NASA,2022)

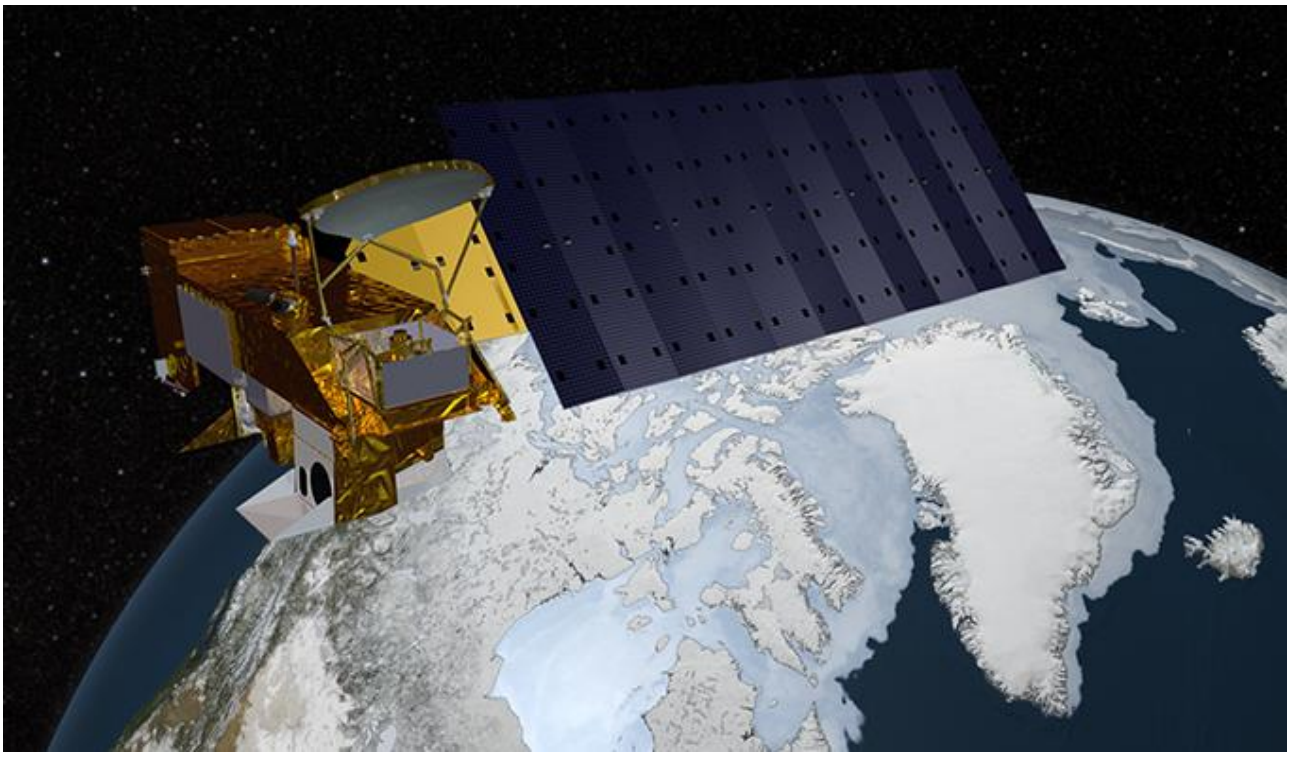

Figure 9 - Aqua Earth-observing satellite mission (NASA's Earth Observing System)

It continues collecting and transmitting high-quality data from four of its six instruments:

- Atmospheric Infrared Sounder (AIRS),
- Advanced Microwave Sounding Unit (AMSU),
- Clouds and the Earth's Radiant Energy System (CERES),
- Moderate Resolution Imaging Spectroradiometer (MODIS),
- Advanced Microwave Scanning Radiometer for EOS (AMSR-E),
- Humidity Sounder for Brazil (HSB).

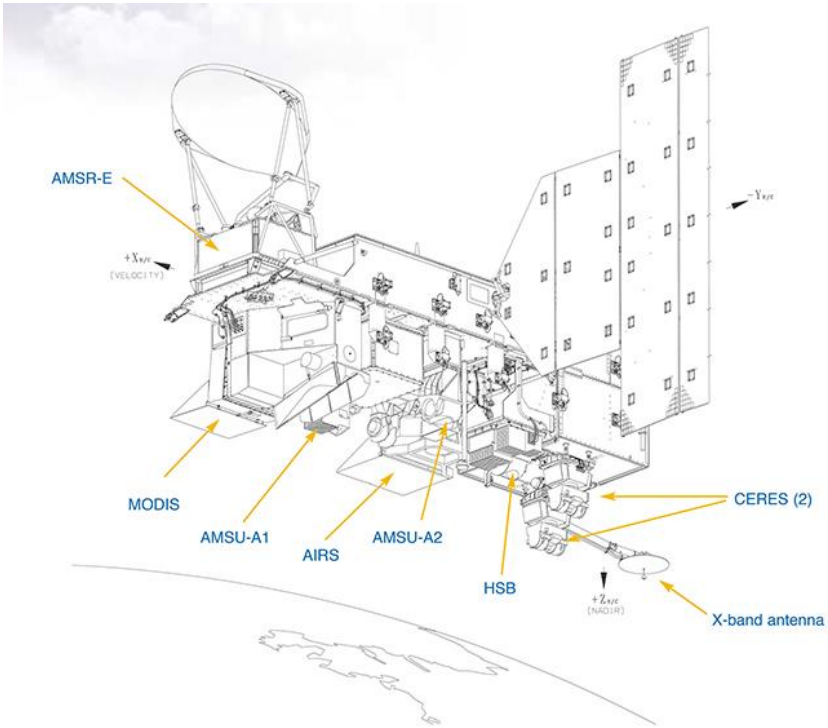

Figure 10 - Aqua instruments (NASA's Earth Observing System)

Specifications

Orbit:	Sun synchronous, near polar orbit
Equatorial crossing:	1:30 p.m. ascending node
Inclination:	98.2°
Altitude:	705 km
Period:	98.8 minutes
Semi-major axis:	7085 km
Eccentricity:	0.0015
Vehicle:	Two-stage Delta II 7920-10L with 9 strap-on solid rocket motors and 10 foot, bisector, composite fairing
Site:	SLC-2W, Western Range, Vandenberg Air Force Base, California
Launch date:	May 4, 2002 @ 2:55 a.m. PDT
Weight (at launch):	2,934 kg (6,468 pounds)
Power:	4,860 watts end of life
Size (stowed):	2.7 m (8.8 ft) x 2.5 m (8.2 ft) x 6.5 m (21.3 ft)
Size (deployed):	4.8 m (15.8 ft) x 16.7 m (54.8 ft) x 8 m (26.4 ft)
Mission design life:	6 years

2.5.2 Terra

In December 1999, NASA launched the Terra satellite as the flagship mission of the Earth Observing System.

Terra carries five instruments that observe Earth's atmosphere, ocean, land, snow and ice, and energy budget. Taken together, these observations provide unique insight into how the Earth system works and how it is changing. Terra observations reveal humanity's impact on the planet and provide crucial data about natural hazards like fire and volcanoes.

Terra is an international mission carrying instruments from the United States, Japan, and Canada.

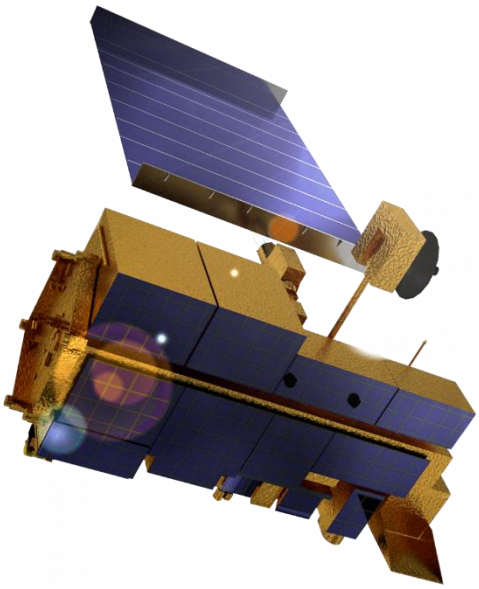

Figure 11 – Terra (NASA's Earth Observing System)

Specifications
Launch Date: December 18,1999
Size: the spacecraft bus is 6.8 m long and 3.5 m across.
Weight: 5,190 kg (11,442 lbs.) at launch.
KSC-99PP-1412_web
Altitude: 705 kilometers (438 miles) above Earth's surface
Inclination: 98.5 degrees
Period: 99 minutes (14 complete orbits per day)
Ground track repeat: 16 days
Equatorial crossing: 10:30 a.m., descending mode

Terra collects data about the Earth's bio-geochemical and energy systems using five sensors that observe the atmosphere, land surface, oceans, snow and ice, and energy budget. Each sensor has unique features that enable scientists to meet a wide range of science objectives. The five Terra onboard sensors are:

- ASTER (Advanced Spaceborne Thermal Emission and Reflection Radiometer)
- CERES (or Clouds and Earth's Radiant Energy System)
- MISR (Multi-angle Imaging SpectroRadiometer)

- MODIS (Moderate-resolution Imaging Spectroradiometer)
- MOPITT (Measurements of Pollution in the Troposphere)

For nearly 20 years, the Terra satellite maintained a consistent orbital speed and altitude, resulting in a near-constant morning equator-crossing time around 10:30 AM. However, since February 2020, the Terra satellite has been allowed to drift in time to an increasingly earlier equator crossing. In October 2020, Terra reached a 10:15 AM equator-crossing time, and was then lowered about 5km to make room for other upcoming Low-Earth Orbit (LEO) missions, while continuing to drift to an earlier and earlier morning equator crossing time. Despite these orbital changes, Terra instruments will continue to collect high quality earth observations. (NASA,2022)

2.5.3 MODIS

MODIS (or Moderate Resolution Imaging Spectroradiometer) is a key instrument aboard the Terra (originally known as EOS AM-1) and Aqua (originally known as EOS PM-1) satellites.

Terra's orbit around the Earth is timed so that it passes from north to south across the equator in the morning, while Aqua passes south to north over the equator in the afternoon.

Terra MODIS and Aqua MODIS are viewing the entire Earth's surface every 1 to 2 days, acquiring data in 36 spectral bands, or groups of wavelengths. These data will improve our understanding of global dynamics and processes occurring on the land, in the oceans, and in the lower atmosphere. MODIS is playing a vital role in the development of validated, global, interactive Earth system models able to predict global change accurately enough to assist policy makers in making sound decisions concerning the protection of our environment.

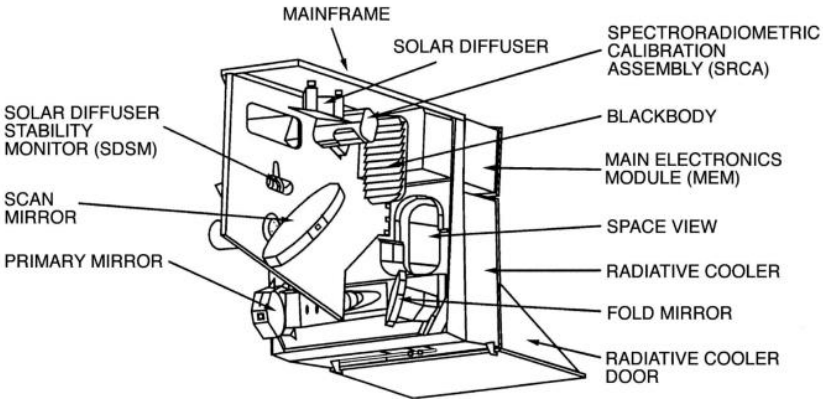

Figure 12 - MODIS components (NASA's Earth Observing System)

The MODIS instruments were designed with the following subsystems and abilities. Follow the highlighted links for more technical descriptions of each subsystem.

- Atmospheric, land, and ocean imaging in a single instrument
- 1,000-m, 500-m, and 250-m resolution spectral bands
- Custom-tailored spectral bands from 0.4 to 14.4 µm; low out-of-band response
- Opto-Mechanical System
- Mainframe
- Continuously rotating double-sided Scan Mirror Assembly for long life
- Passive Radiative Cooler
- Advanced Focal Plane Assembly (FPA) technology for unsurpassed sensitivity
- Optical Bench Assembly
- Optical System Description
- Door Assemblies
- Electronics System
- Space-Viewing Analog Module
- Forward-Viewing Analog Module

- Main Electronics Module (MEM)
- On-Board Calibration System
- IR calibration every scan for low 1/f noise and high accuracy
- Low ghosting, low scatter optics
- On-board Solar Diffuser and Solar Diffuser Stability Monitor (SDSM)
- On-board full-aperture Blackbody (BB)
- On-board Spectroradiometric Calibration Assembly (SRCA)

The fire detection strategy is based on absolute detection of a fire (when the fire strength is sufficient to detect), and on detection relative to its background (to account for variability of the surface temperature and reflection by sunlight).

The product include:

- fire occurrence (day/night),
- fire location,
- the logical criteria used for the fire selection,
- detection confidence,
- Fire Radiative Power,
- numerous other layers describing fire pixel attributes.

The product distinguishes between fire, no fire and no observation.

Level 3 Daily fire products include 8 separate days of data detailing pixels according to their level of confidence as fires. This information will be used in monitoring the spatial and temporal distribution of fires in different ecosystems, detecting changes in fire distribution and identifying new fire frontiers, wild fires, and changes in the frequency of the fires or their relative strength.

MODIS data on Terra and Aqua are acquired from each platform twice daily at mid-latitudes. These four daily MODIS fire observations that are typically acquired serve operational fire management needs while also advancing global monitoring of the fire process and its effects on ecosystems, the atmosphere, and climate.

Specifications
Orbit: 705 km, 10:30 a.m. descending node (Terra) or 1:30 p.m. ascending node (Aqua), sun-synchronous, near-polar, circular
Scan Rate: 20.3 rpm, cross track
Swath Dimensions: 2330 km (cross track) by 10 km (along track at nadir)
Telescope: 17.78 cm diam. off-axis, afocal (collimated), with intermediate field stop
Size: 1.0 x 1.6 x 1.0 m
Weight: 228.7 kg
Power: 162.5 W (single orbit average)
Data Rate: 10.6 Mbps (peak daytime); 6.1 Mbps (orbital average)
Quantization: 12 bits
Spatial Resolution: 250 m (bands 1-2), 500 m (bands 3-7), 1000 m (bands 8-36) Design Life: 6 years

2.5.4 SUOMI NPP

Since 2012, NASA has been helping to create a new generation of satellites to extend and improve the Earth system data established by EOS.

The Suomi National Polar-orbiting Partnership (https://www.nasa.gov/mission_pages/NPP/main/index.html), formerly known as the NPOESS Preparatory Project, will serve as a bridge between the EOS satellites and the next set of Joint Polar Satellite System (JPSS) satellites. The Suomi NPP represents a key first step in the construction of this next-generation satellite system.

Suomi NPP will carry five scientific instruments and test key technologies for JPSS missions. Suomi NPP is the first satellite mission to address the challenge of acquiring a wide range of land, ocean and atmospheric measurements for Earth system science while preparing to meet operational requirements for weather forecasting.

Suomi NPP's main scientific goals and capabilities include:

- Climate change -- contributing to long-term records of global environmental data critical to understanding the dynamics of climate change.
- Ozone layer health -- daily measurements of the atmospheric ozone layer that will determine whether the ozone layer is recovering as expected.
- Natural disasters -- monitoring of fires, volcanic eruptions, snowstorms, droughts, floods, hurricanes, and dust plumes.
- Weather forecasting -- a survey instrument will collect information on cloud cover, atmospheric temperatures, humidity, and other variables critical to accurate weather forecasting.
- Vegetation -- map global terrestrial vegetation and quantify changes in plant productivity to understand the global carbon cycle and monitor agricultural processes to predict and respond to food shortages and famines.
- Global ice cover -- monitor changes in the Earth's sea, land and glacier ice to track the pace of climate change.
- Air pollution -- monitor the spread of health-damaging pollutants such as soot, particulate matter, nitrogen dioxide and sulfur dioxide.
- Temperature-- maintain a global record of atmospheric and land surface temperatures.

Suomi NPP instruments:

- VIIRS – Visible Infrared Imaging Radiometer Suite
- CERES – Clouds and the Earth’s Radiant Energy System
- CrIS – Cross-track Infrared Sounder
- ATMS – Advanced Technology Microwave Sounder
- OMPS – Ozone Mapping and Profiler Suite

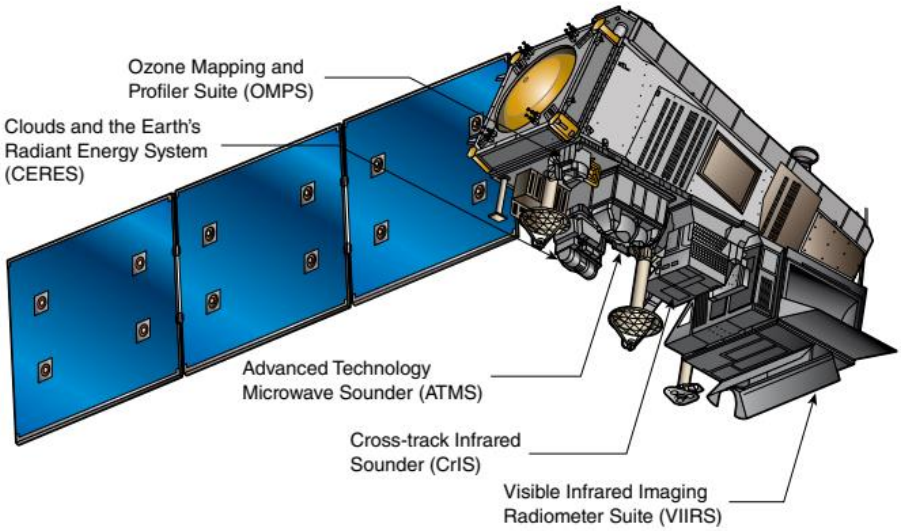

Figure 13 – Suomi NPP instrument (NASA's Earth Observing System)

Specifications

Launch date 28 October 2011, 09:48:01.828 UTC[2]
Rocket Delta II 7920-10C (Delta D357)
Launch site Vandenberg, SLC-2W
Contractor United Launch Alliance
Reference system Geocentric orbit[3]
Regime Sun-synchronous orbit
Perigee altitude 833.7 km (518.0 mi)
Apogee altitude 834.3 km (518.4 mi)
Inclination 98.79°
Period 101.44 minutes

2.5.5 NOAA -20

NOAA-20, designated JPSS-1 prior to launch, is the first of the United States National Oceanic and Atmospheric Administration's latest generation of U.S. polar-orbiting, non-geosynchronous, environmental satellites called the Joint Polar Satellite System.

NOAA-20 was launched on 18 November 2017 and joined the Suomi National Polar-orbiting Partnership satellite in the same orbit. NOAA-20 operates about 50 minutes behind Suomi NPP, allowing important overlap in observational coverage. Circling the Earth from pole-to-pole, it crosses the equator about 14 times daily, providing full global coverage twice a day. This gives meteorologists information on "atmospheric temperature and moisture, clouds, sea-surface temperature, ocean colour, sea ice cover, volcanic ash, and fire detection" so as to enhance weather forecasting including hurricane tracking, post-hurricane recovery by detailing storm damage and mapping of power outages.

Figure 14 - NOAA – 20 (NASA's Earth Observing System)

The project incorporates five instruments, and these are substantially upgraded since previous satellite equipment.

Specifications

Launch date 18 November 2017, 09:47:36 UTC
Rocket Delta II 7920-10C (Delta D378)
Launch site Vandenberg, SLC-2W
Contractor United Launch Alliance
Entered service 30 May 2018
Orbital parameters
Reference system Geocentric orbit
Regime Sun-synchronous orbit
Perigee altitude 824.3 km (512.2 mi)
Apogee altitude 833.0 km (517.6 mi)
Inclination 98.79°
Period 101.44 minutes

2.5.6 VIIRS

The first Visible Infrared Imaging Radiometer Suite (VIIRS) instrument was launched on the Suomi National Polar-orbiting Partnership (S-NPP) satellite on Oct. 28, 2011 from Vandenberg Air Force Base in California. VIIRS extends and improves upon a series of measurements initiated by its predecessors, the Advanced Very High-Resolution Radiometer (AVHRR) and the Moderate Resolution Imaging Spectroradiometer (MODIS) instruments.

The Joint Polar Satellite System (JPSS), a NOAA/NASA program, and the Defense Weather Satellite System, a U.S. Air Force program, were tasked with the next-generation requirements for environmental research, weather forecasting and measurement capabilities for climate monitoring that S-NPP represents. Today, there are three VIIRS instruments on orbit, the original S-NPP satellite, the JPSS-1, which transitioned to NOAA-20, and the third VIIRS instrument, JPSS-2, launched on November 10, 2022, and is now designated as NOAA-21.

The VIIRS instrument observes and collects global satellite observations that span the visible and infrared wavelengths across land, ocean, and atmosphere. A whiskbroom radiometer by design, it has 22 channels ranging from 0.41 µm to 12.01 µm.

Five of these channels are high-resolution image bands or I-bands, and sixteen serve as moderate-resolution bands or M-bands. VIIRS also hosts a unique panchromatic Day/Night band (DNB), which is ultra-sensitive in low-light conditions that allows us to observe night-time lights with better spatial and temporal resolutions compared to previously provided night-time lights data by the Defense Meteorological Satellite Program.

VIIRS is one of five instruments onboard the Suomi National Polar-orbiting Partnership (NPP) satellite platform that was launched on October 28, 2011.

VIIRS-derived data products are used to measure cloud and aerosol properties, ocean color, ocean and land surface temperature, ice movement and temperature, fires, and Earth's albedo. Climatologists use VIIRS data to improve our understanding of global climate change.

Specifications
Orbit: 830km, 1:30pm mean local solar time. sun-synchronous, polar
Repeat Cycle: 16 days
Swath Dimensions: 3000km, nearly global coverage every day
Weight: 275kg
Spatial Resolution: 750m
Data Rate: 5.9 Mbps
Quantization: 12 bits
Field of View: deg
Wavebands: 9 visible/NIR bands plus day/night pan band
8 mid-IR
4 LW IR
Design Life: 7 years
Duration: Operational

2.6 NASA FIRMS web Platform

NASA's Fire Information for Resource Management System (FIRMS) distributes on a dedicated web portal (https://firms.modaps.eosdis.nasa.gov) near real-time (NRT) active fire data within three hours of a satellite observation from NASA's Moderate Resolution Imaging Spectroradiometer (MODIS) and Visible Infrared Imaging Radiometer Suite (VIIRS). FIRMS is part of NASA's Land, Atmosphere Near real-time Capability for EOS (LANCE).

NASA FIRMS uses satellite observations from the MODIS and VIIRS instruments to detect active fires and thermal anomalies and deliver this information in near real-time to decision makers through email alerts, analysis ready data, online maps and web services.

NASA's FIRMS enables access to global near real-time (NRT) satellite imagery, active fire detections and other data from multiple satellites. FIRMS combines value-added data products to provide critical information to wildfire management organizations and impacted individuals.

The download of fire data from FIRMS it's possible from the following sensors:

- MODIS C6.1 is available from November 2000 (for Terra) and from July 2002 (for Aqua) to the present.
- VIIRS 375 m (S-NPP) data are currently available from 20 January 2012 to the present.
- VIIRS 375 m (NOAA-20) data are currently available from 01 January 2020 to the present.

Data provided by the NOAA-20 instrument are not enough to give statistically significant results, so calculations are based only on those from the MODISs and SUOMI NPP instruments.

2.6.1 MODIS Active Fire Data

Satellites take a 'snapshot' of events as they pass over Earth. Each hotspot/active fire detection represents the center of a pixel flagged as containing one or more fires or other thermal anomalies (such as volcanoes).

For MODIS the pixel is approximately 1 km. The "location" is the center point of the pixel (not necessarily the coordinates of the actual fire). The actual pixel size varies with the scan and track. The fire is often less than the size of the pixel. We are not able to determine the exact fire size; what we do know is that at least one fire is located within the flagged pixel. Sometimes you will see several active fires in a line. This generally represents a fire front.

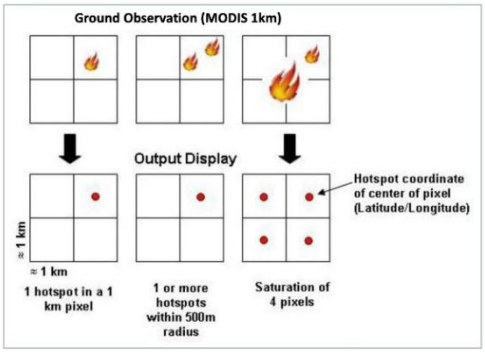

Figure 15 - MODIS active fire detection (FIRMS web portal)

The thermal anomalies / active fire represents the centre of a 1 km pixel that is flagged by the MODIS MOD14/MYD14 Fire and Thermal Anomalies algorithm (Giglio 2003) as containing one or more fires within the pixel. This is the most basic fire product in which active fires and other thermal anomalies, such as volcanoes, are identified.

The MODIS Land Data Operational Product Evaluation (LDOPE) provides interactive daily global browse imagery of many MODIS land products from the MODIS Land Global Browse Images web site in near-real time (NRT) (Figure 16). For most products (including the fire products) the browse imagery is generated using only the daytime overpasses. The site allows you to arbitrarily zoom into any region of the globe and examine features of interest in more detail.(MODIS Fire User Guide)

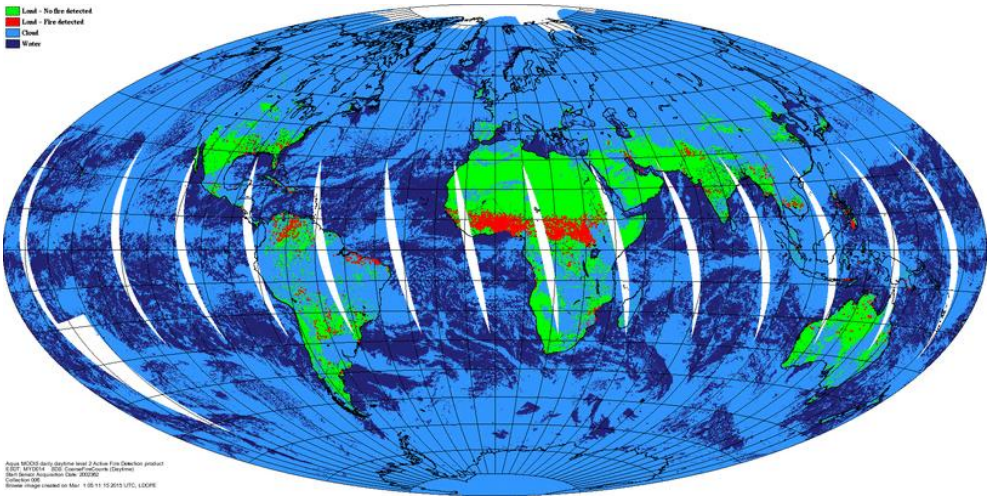

Figure 16 - Collection-6 Aqua MODIS active fire global browse image for 28 December 2002 showing all daytime overpasses. Fire pixels are shown in red, cloud pixels are shown in light blue, and areas lacking data are shown in white. Image produced by the MODIS. (https://modis-fire.umd.edu/af.html)

Each data item provided by MODIS contains several attributes with their own characteristics, described in the table below:

Attribute	**Short Description**	**Long Description**
Latitude	Latitude	Center of 1 km fire pixel, but not necessarily the actual location of the fire as one or more fires can be detected within the 1 km pixel.
Longitude	Longitude	Center of 1 km fire pixel, but not necessarily the actual location of the fire as one or more fires can be detected within the 1 km pixel.
Brightness	Brightness temperature 21 (Kelvin)	Channel 21/22 brightness temperature of the fire pixel measured in Kelvin.
Scan	Along Scan pixel size	The algorithm produces 1 km fire pixels, but MODIS pixels get bigger toward the edge of scan. Scan and track reflect actual pixel size.
Track	Along Track pixel size	The algorithm produces 1 km fire pixels, but MODIS pixels get bigger toward the edge of scan. Scan and track reflect actual pixel size.
Acq_Date	Acquisition Date	Data of MODIS acquisition.

Acq_Time	Acquisition Time	Time of acquisition/overpass of the satellite (in UTC).
Satellite	Satellite	A = Aqua and T = Terra.
Confidence	Confidence (0-100%)	This value is based on a collection of intermediate algorithm quantities used in the detection process. It is intended to help users gauge the quality of individual hotspot/fire pixels. Confidence estimates range between 0 and 100% and are assigned one of the three fire classes (low-confidence fire, nominal-confidence fire, or high-confidence fire).
Version	Version (Collection and source)	Version identifies the collection (e.g., MODIS Collection 6.1) and source of data processing (Ultra Real-Time (URT suffix added to collection), Real-Time (RT suffix), Near Real-Time (NRT suffix) or Standard Processing (collection only). For example: "6.1URT" - Collection 6.1 Ultra Real-Time processing. "6.1RT" - Collection 6.1 Real-Time processing. "6.1NRT" - Collection 61 Near Real-Time processing. "6.1" - Collection 61 Standard processing.
Bright_T31	Brightness temperature 31 (Kelvin)	Channel 31 brightness temperature of the fire pixel measured in Kelvin.
FRP	Fire Radiative Power (MW - megawatts)	Depicts the pixel-integrated fire radiative power in MW (megawatts).
Type*	Inferred hot spot type	0 = presumed vegetation fire 1 = active volcano 2 = other static land source 3 = offshore
DayNight	Day or Night	D= Daytime fire, N= Nighttime fire

Table 2 - Description of data attribute provided by MODIS (FIRMS web portal)

2.6.2 VIIRS 375 m Active Fire Product

The Visible Infrared Imaging Radiometer Suite (VIIRS) 375 m thermal anomalies / active fire product provides data from the VIIRS sensor aboard the joint NASA/NOAA Suomi National Polar-orbiting Partnership (Suomi NPP) and NOAA-20 satellites.

The 375 m data complements Moderate Resolution Imaging Spectroradiometer (MODIS) fire detection; they both show good agreement in hotspot detection, but the improved spatial resolution of the 375 m data provides a greater response over fires of relatively small areas and provides improved mapping of large fire perimeters.

Satellites take a 'snapshot' of events as they pass over Earth. Each hotspot/active fire detection represents the center of a pixel flagged as containing one or more fires or other thermal anomalies (such as volcanoes).

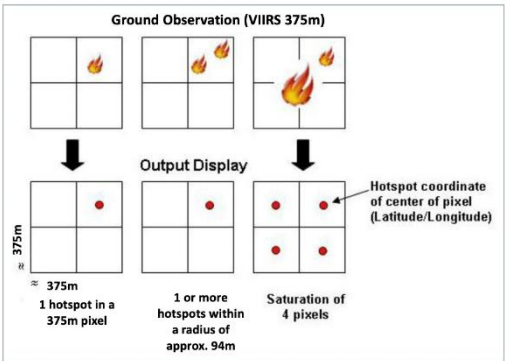

Figure 17 - VIIRS active fire detection (FIRMS web portal)

For VIIRS the pixel is approximately 375 m. The "location" is the center point of the pixel (not necessarily the coordinates of the actual fire). The actual pixel size varies with the scan and track. The fire is often less than the size of the pixel. We are not able to determine the exact fire size; what we do know is that at least one fire is located within the flagged pixel. Sometimes you will see several active fires in a line. This generally represents a fire front.

The 375 m data also has improved night-time performance. Consequently, these data are well suited for use in support of fire management (e.g., near real-time alert systems), as well as other science applications requiring improved fire mapping fidelity.

Attribute	Short Description	Long Description
Latitude	Latitude	Center of nominal 375 m fire pixel
Longitude	Longitude	Center of nominal 375 m fire pixel
Bright_ti4	Brightness temperature I-4	VIIRS I-4 channel brightness temperature of the fire pixel measured in Kelvin.
Scan	Along Scan pixel size	The algorithm produces approximately 375 m pixels at nadir. Scan and track reflect actual pixel size.
Track	Along Track pixel size	The algorithm produces approximately 375 m pixels at nadir. Scan and track reflect actual pixel size.

Acq_Date	Acquisition Date	Date of VIIRS acquisition.
Acq_Time	Acquisition Time	Time of acquisition/overpass of the satellite (in UTC).
Satellite	Satellite	N= Suomi National Polar-orbiting Partnership (Suomi NPP), 1=NOAA-20 (designated JPSS-1 prior to launch)
Confidence	Confidence	This value is based on a collection of intermediate algorithm quantities used in the detection process. It is intended to help users gauge the quality of individual hotspot/fire pixels. Confidence values are set to low, nominal and high. Low confidence daytime fire pixels are typically associated with areas of sun glint and lower relative temperature anomaly (<15K) in the mid-infrared channel I4. Nominal confidence pixels are those free of potential sun glint contamination during the day and marked by strong (>15K) temperature anomaly in either day or nighttime data. High confidence fire pixels are associated with day or nighttime saturated pixels. Please note: Low confidence nighttime pixels occur only over the geographic area extending from 11deg E to 110 deg W and 7 deg N to 55 deg S. This area describes the region of influence of the South Atlantic Magnetic Anomaly which can cause spurious brightness temperatures in the mid-infrared channel I4 leading to potential false positive alarms. **These have been removed from the NRT data distributed by FIRMS.**
Version	Version (Collection and source)	Version identifies the collection (e.g. VIIRS Collection 1) and source of data processing: Near Real-Time (NRT suffix added to collection) or Standard Processing (collection only). "1.0NRT" - Collection 1 NRT processing. "1.0" - Collection 1 Standard processing
Bright_ti5	Brightness temperature I-5	I-5 Channel brightness temperature of the fire pixel measured in Kelvin.
FRP	Fire Radiative Power	FRP depicts the pixel-integrated fire radiative power in MW (megawatts). FRP depicts the pixel-integrated fire radiative power in MW (megawatts). Given the unique spatial and spectral resolution of the data, the VIIRS 375 m fire detection algorithm was customized and tuned in order to optimize its response over small fires while balancing the occurrence of false alarms. Frequent saturation of the mid-infrared I4 channel (3.55-3.93 µm) driving the detection of active fires requires additional tests and procedures to avoid pixel classification errors. As a result, sub-pixel fire characterization (e.g., fire radiative power [FRP] retrieval) is only viable across small and/or low-intensity fires. Systematic

		FRP retrievals are based on a hybrid approach combining 375 and 750 m data. In fact, starting in 2015 the algorithm incorporated additional VIIRS channel M13 (3.973-4.128 µm) 750 m data in both aggregated and unaggregated format.
DayNight	Day or Night	D= Daytime fire, N= Nighttime fire

Table 3 - Description of data attribute provided by VIIRS (FIRMS web portal)

2.6.3 Analysed data: Bright_T31

From the data provided by FIRMS in both cases above, to analyse FAMF the data used will be:

- Bright_T31 : Band 31 brightness temperature of fire pixel [K]
- FRP: Fire radiative power (FRP) [MW]

The brightness temperature is a measurement of the radiance of the microwave radiation traveling upward from the top of the atmosphere to the satellite, expressed in units of the temperature of an equivalent black body.

The MODIS Brightness Temperature, Band 31 layer is the brightness temperature, measured in Kelvin (K), calculated from the top-of-the-atmosphere radiances. It is calculated from measured radiance (R) by the following equation:

$$T_b = \left[C_2 \nu_c / \log\left(\frac{C_1 \nu_c^{\,3}}{R} + 1 \right) - B \right] / A$$

Where v_c is the central wavenumber of the IR channel 31 (9.55 μm), R is the measured radiance mW m^{-2} $sr^{-1}(cm^{-1})^{-4}$ and A and B read only constant.

It does not provide an accurate temperature of either cloud nor the land surface, but it does show relative temperature differences which can be used to distinguish features both in clouds and over clear land. It can be used to distinguish land, sea ice, and open water over the polar regions during winter (in cloudless areas).

2.6.4 Analysed data: FRP

From the data provided by FIRMS in both cases above, to analyse FAMF the data used will be:

- Bright_T31 : Band 31 brightness temperature of fire pixel [K]
- FRP: Fire radiative power (FRP) [MW]

Quantifying fuel consumption and trace gas and aerosol emissions from biomass burning is fundamental to understanding the carbon cycle, terrestrial-atmosphere interactions, and climate change (Bowman et al., 2009). Traditionally, fuel consumption has been estimated as the product of the fire-affected area (units: m^2), the pre-burn fuel load (kg m^{-2}), and combustion completeness (unitless: 0–1) (Seiler and Crutzen, 1980).

Alternatively, Kaufman et al. (1996) proposed that the rate of emission of fire radiative energy could be used to indicate the rate of combustion. Since then, measurements of fire radiative power (FRP) from polar orbiting sensors have been used to characterize active fire (AF) properties (e.g., Wooster and Zhang, 2004; Smith and Wooster, 2005; Ichoku et al., 2008), to quantify biomass consumption and trace gas and aerosol production (e.g., Ellicott et al., 2009; Vermote et al., 2009; Kaiser et al., 2012), and to estimate smoke plume heights (Mazzoni et al., 2007; Val Martin et al., 2010).

Information on the timing, location and radiative characteristics of MODIS active fire pixels is stored in a variety of formats [Giglio, 2013].

The data currently available for download in the FIRMS web portal use the Collection 6 Level 2 Fire Products (abbreviated MOD14 for Terra and MYD14 for Aqua) as these datasets provide the geographic and image coordinates, fire pixel brightness and mean background temperatures, and FRP for each individual 1 km AF pixel detected by MODIS.

MODIS Level 2G, Level 3, and Level 4 products are defined on a global 250-m, 500-m, or 1-km sinusoidal grid (the particular spatial resolution is product-dependent). Because these grids are unmanageably large in their entirety (43200 × 21600 pixels at 1 km, and 172800 × 86400 pixels at 250 m), they are divided into fixed tiles approximately 10°× 10° in size. Each tile is assigned a horizontal (H) and vertical (V) coordinate, ranging from 0 to 35 and 0 to 17, respectively (Figure 1).

The tile in the upper left (i.e. northernmost and westernmost) corner is numbered (0,0).

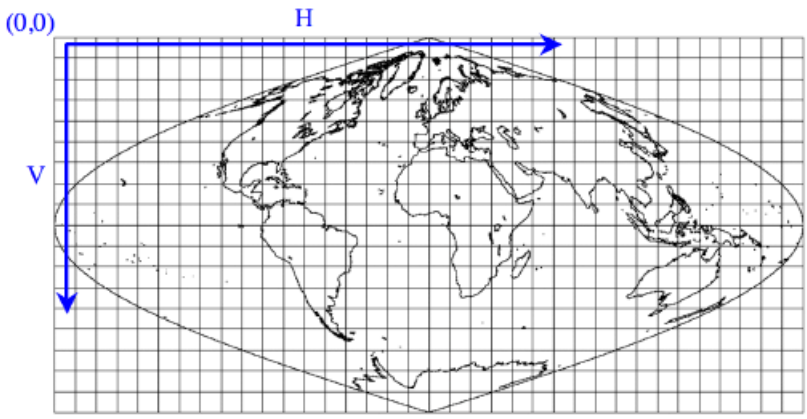

Figure 18 - MODIS tiling scheme (MODIS user guide)

Reprocessing of the entire MODIS data archive is periodically performed to incorporate better calibration, algorithm refinements, and improved upstream data into all MODIS products.

The updated MODIS data archive resulting from each reprocessing is referred to as a collection. Later collections supersede all earlier collections.

For the Terra MODIS, Collection 1 consisted of the first products generated following launch. Terra MODIS data were reprocessed for the first time in June 2001 to produce Collection 3. Collection 3 was also the first version produced for the Aqua MODIS products. Collection 4 reprocessing began in December 2002 and was terminated in December 2006. Production of the Collection 5 products, which commenced in mid-2006, will continue until the Collection 6 reprocessing is complete. Production of the "Tier-1" Collection 6 MODIS products, which includes the active fire products, commenced in February 2015.

Level 2 Fire Products is the most basic fire product in which active fires and other thermal anomalies, such as volcanoes, are identified. The Level 2 product is defined in the MODIS orbit geometry covering an area of approximately 2340 × 2030 km in the along-scan and along-track directions, respectively. It is used to generate all of the higher-level fire products, and contains the following components:

- an active fire mask that flags fires and other relevant pixels;
- a pixel-level quality assurance (QA) image that includes 19 bits of QA information about each pixel;
- a fire-pixel table which provides 27 separate pieces of radiometric and internal-algorithm information about each fire pixel detected within a granule;
- extensive mandatory and product-specific metadata;
- a grid-related data layer to simplify production of the Climate Modeling Grid (CMG) fire product.

The "FP power" in the Collection 4 Level 2 product actually contains radiative power per unit area, despite the fact that the units attribute of this is assigned a value of "megawatt" (this is an error). These values had to be multiplied by the appropriate pixel area (at the surface of the Earth) to obtain the FRP, like the following:

FRP (MW) = power values stored in the Collection 4 Level 2 product × pixel area (km^2)

Note that the area of a MODIS pixel varies with its position in the MODIS scan. Note also that starting with Collection 5 the Level 2 products have this multiplication performed during processing and therefore contain the correct FRP.(MODIS User Guide).

Therefore, the multiplication done during processing, starting with Collection 5, is essential because the area of a pixel varies with its position in the MODIS scan. The area of a MODIS pixel is nominally 1 km^2 but grows away from nadir. To find the approximate pixel area, calculate the along-scan and along-track pixel dimensions (ΔS and ΔT, respectively).

The pixel area is then the product ΔS ×ΔT. General formulas for the pixel dimensions (in km) can be found in Ichoku and Kaufman (2005) and are reproduced here:

$$\begin{aligned} \Delta S &= R_e s \left(\frac{\cos\theta}{\sqrt{(R_e/r)^2 - \sin^2\theta}} - 1 \right) \\ \Delta T &= rs \left(\cos\theta - \sqrt{(R_e/r)^2 - \sin^2\theta} \right) \end{aligned}$$

Where R_e = 6378.137 km(Earth radius), r = R_e+h, h = 705 km(satellite altitude), s = 0.0014184397, and θ is the scan angle (in radians).

Note that the errors in the above approximations are smaller than the error entailed by treating the pixel as having sharp edges.

FRP values (MW) stored in the Collection 5 MODIS fire product suite are calculated using the equation originally formulated by Kaufman et al. (1998) and amended by Giglio (2013) to account for variations in pixel size across the swath:

$$FRP = A_s \beta (T_f^8 - T_b^8)$$

where T_f is the 4 µm brightness temperature of the fire pixel, T_b is the mean 4 µm brightness temperature of the background window, A_s is the nominal MODIS pixel area evaluated at the scan angle, or sample number, s, and the coefficient β = 4.34 × 10^{-19}Wm^{-2}K^{-8} is specific to the MODIS 4 µm spectral response. Although T_b is representative of a window that expands until at least 25% of

the surrounding pixels are identified as valid cloud-free land pixels that are also not fire pixels (Giglio et al., 2003), it is still possible for T_b to be influenced by hot spots in the background window but not recognized by the MODIS active fire detection algorithm.

A detection confidence intended to help users gauge the quality of individual fire pixels is included in the Level 2 fire product. This confidence estimate, which ranges between 0%and 100%, is used to assign one of the three fire classes (low-confidence fire, nominal-confidence fire, or high-confidence fire) to all fire pixels within the fire mask.

In fact, statistical analyses of FRP values are conducted both on all data provided and on data filtered by applying a confidence filtering level.

The MODIS instrument provides an active fire product containing instantaneous fire radiative power (FRP) measurements at the native 1-km resolution ("Level 2") from both Terra and Aqua.

The VIIRS instrument also provides an active fire product at two resolutions: the "I" band (375m resolution) and the "M" band (750m resolution).

FRP represents the radiative power of the fire embedded in the pixel in MW (megawatt).

Given the exceptional spatial and spectral resolution of the data, the VIIRS 375 m fire detection algorithm was customised and fine-tuned to optimise its response on small fires, while balancing the occurrence of false alarms.

2.6.5 Period and location of data analysed

In accordance with the information above regarding data availability for various sensors, it is possible to see in Tab.1 which sensors and data time periods will be used in the qualitative and quantitative analyses in this thesis.

Spacecraft	Sensor	Launched	Data analysed
Terra	MODIS	18/12/1999	01/01/2001 – 31/12/2022
Aqua	MODIS	04/05/2002	01/01/2001 – 31/12/2022
SUOMI-NPP	VIIRS	28/10/2011	01/01/2012 – 31/12/2022

Table 4 - Period of data analised for each Sensor

Considering that the Amazon rainforest is mostly (60%) in the territory of Brazil, the data that will be used, coming from the FIRMS web portal, and all the images shown, coming from the FIRMS web portal and the WORLDVIEW web portal, were downloaded by setting the location in the geographical area of Brazil.

2.6.6 How to download

The annual fire location product contains the geographic location, date, and some additional information for each fire pixel detected by the Terra and Aqua MODIS sensors on a monthly basis.

As an example, is reported the first ten lines of MODIS data, of the December 2008 product file in ASCII (text) file with fixed-width fields delimited with spaces. The first line of each file is a header containing the abbreviated names of each column (field).

```
YYYYMMDD HHMM sat lat lon T21 T31 sample FRP conf type dn
20081201 0051 T -12.0288  143.0191 321.6 289.6  681    11.5  53  0 D
20081201 0051 T -12.0301  143.0282 317.8 287.9  682     7.8  42  0 D
20081201 0051 T -12.0391  143.0269 356.8 289.1  682    67.4   0  0 D
20081201 0051 T -12.0481  143.0255 346.6 286.7  682    46.2   0  0 D
20081201 0051 T -12.0552  141.9690 320.8 291.4  571    11.3  38  0 D
20081201 0051 T -12.9809  143.4871 330.7 301.2  752    16.8  80  0 D
20081201 0051 T -12.9999  143.4275 339.1 300.0  746    31.6  88  0 D
20081201 0051 T -13.0012  143.4368 327.6 300.5  747    14.0  76  0 D
20081201 0051 T -13.0079  143.4203 345.0 298.5  746    42.8  92  0 D
```

Table 5 - Example of ten lines of the December 2008 product file from MODIS (MODIS User Guide)

A brief description of each data column is provided in Table 3.

Column	Name	Units	Description
1	YYYYMMDD	-	UTC year (YYYY), month (MM), and day (DD).
2	HHMM	-	UTC hour (HH) and minute (MM).
3	Sat	-	Satellite: Terra (T) or Aqua (A).
4	Lan	Degrees	Latitude at center of fire pixel.
5	Lot	Degrees	Longitude at center of fire pixel.
6	T21	K	Band 21 brightness temperature of fire pixel.
7	T31	K	Band 31 brightness temperature of fire pixel.
8	Sample	-	Sample number (range 0-1353).
9	FRP	MW	Fire radiative power (FRP).
10	Conf	%	Detection confidence (range 0-100).
11	Type	-	Inferred hot spot type: 0 = presumed vegetation fire 1 = active volcano 2 = other static land source 3 = offshore
12	dn	-	Day/night algorithm flag: day (D) or night (N).

Table 6 - Description of each data column provided from FIRMS data download (MODIS User Guide)

To download data from the FIRMS web portal, a few steps need to be taken.

After locating the download archive, it is necessary to create a new request to download the relevant data. the FIRMS archive system provides all the useful information about the sensors and file types.

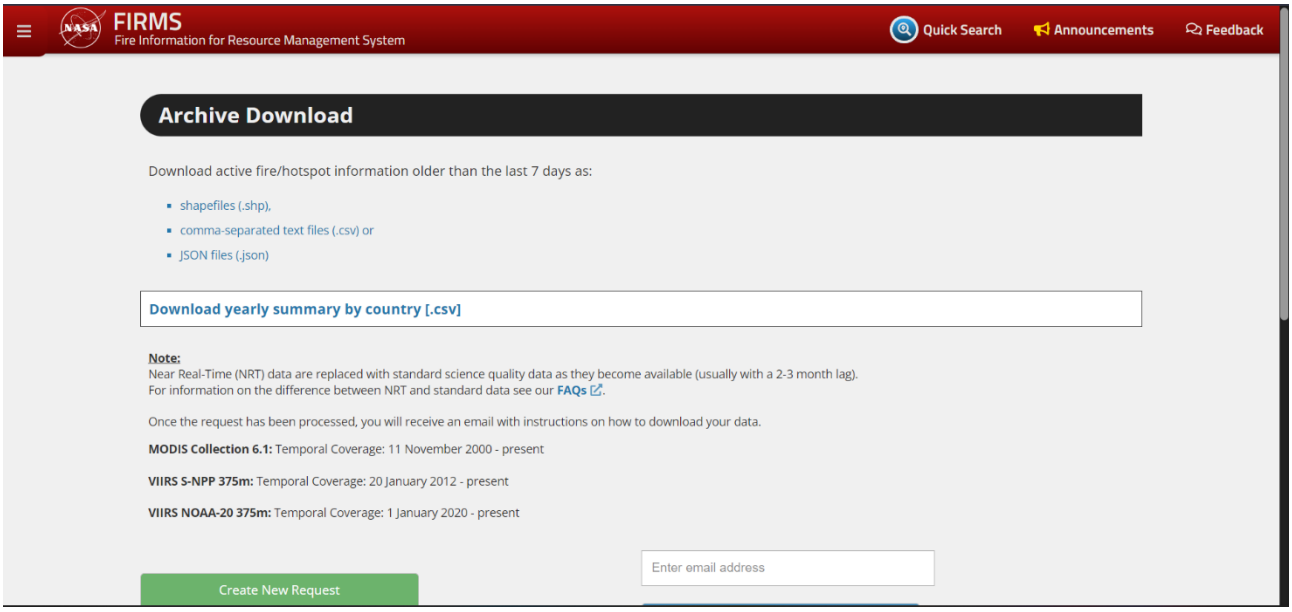

Figure 19 - FIRMS Archive download

To create a request, it is important to set the data regarding (Fig.20):

- the area of interest: Brazil
- the dates: you cannot set more than one year at a time
- the source sensor: MODIS or VIIRS S-NPP
- the format type: Shapefile (this is a popular vector format for geographic information systems (GIS), which will be used to use the files on QGIS program)

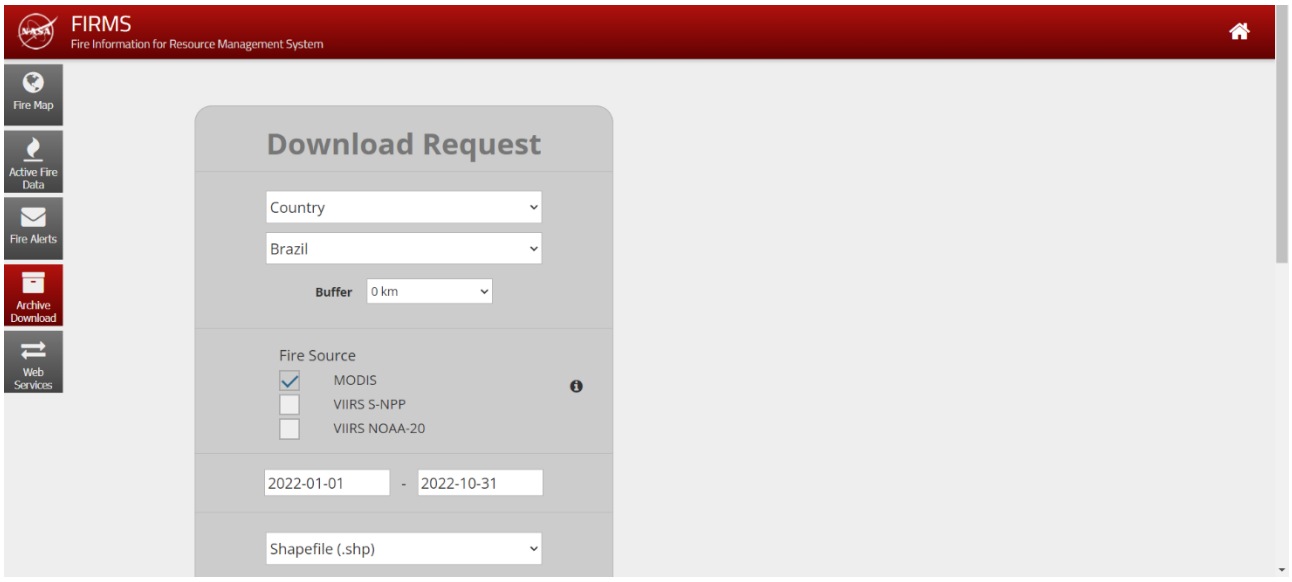

Figure 20 - Download request in FIRMS

Once you have entered all the conditions, just submit the request, and the system will send you an e-mail when the data is ready to be downloaded on the screen you see below that is provided by e-mail (Fig.21).

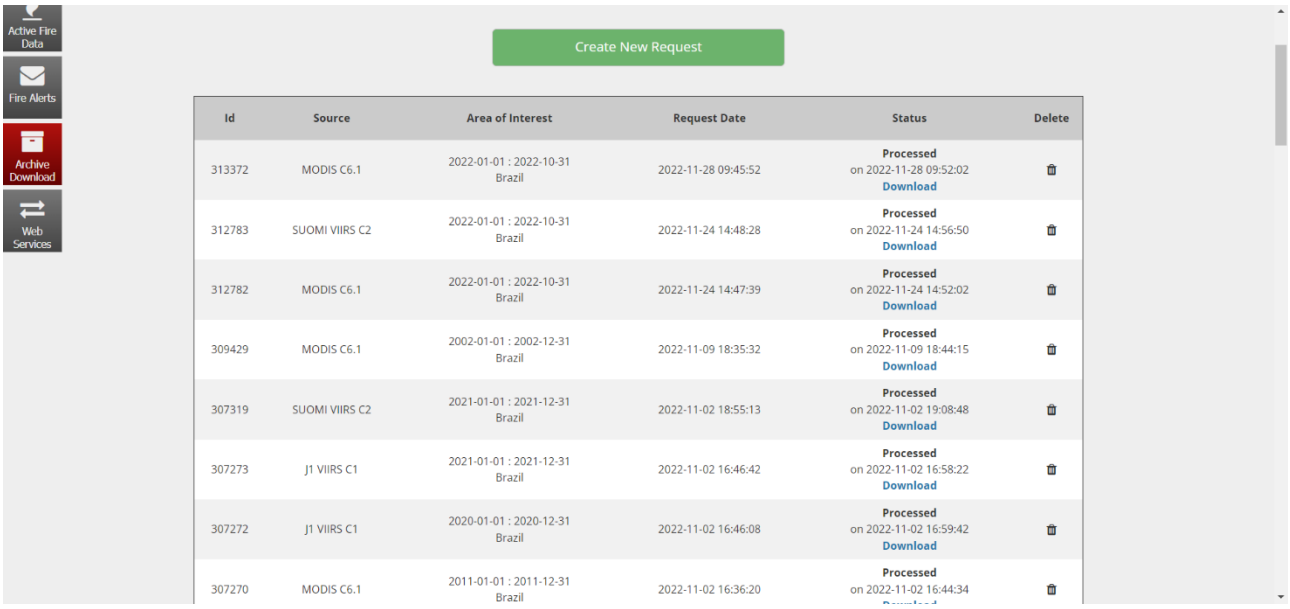

Id	Source	Area of Interest	Request Date	Status	Delete
313372	MODIS C6.1	2022-01-01 : 2022-10-31 Brazil	2022-11-28 09:45:52	Processed on 2022-11-28 09:52:02 Download	
312783	SUOMI VIIRS C2	2022-01-01 : 2022-10-31 Brazil	2022-11-24 14:48:28	Processed on 2022-11-24 14:56:50 Download	
312782	MODIS C6.1	2022-01-01 : 2022-10-31 Brazil	2022-11-24 14:47:39	Processed on 2022-11-24 14:52:02 Download	
309429	MODIS C6.1	2002-01-01 : 2002-12-31 Brazil	2022-11-09 18:35:32	Processed on 2022-11-09 18:44:15 Download	
307319	SUOMI VIIRS C2	2021-01-01 : 2021-12-31 Brazil	2022-11-02 18:55:13	Processed on 2022-11-02 19:08:48 Download	
307273	J1 VIIRS C1	2021-01-01 : 2021-12-31 Brazil	2022-11-02 16:46:42	Processed on 2022-11-02 16:58:22 Download	
307272	J1 VIIRS C1	2020-01-01 : 2020-12-31 Brazil	2022-11-02 16:46:08	Processed on 2022-11-02 16:59:42 Download	
307270	MODIS C6.1	2011-01-01 : 2011-12-31 Brazil	2022-11-02 16:36:20	Processed on 2022-11-02 16:44:34	

Figure 21 - Data download

2.12 QGIS system

QGIS is an open-source GIS desktop application that allows you to visualize, organize, analyse and represent spatial data.

Considering the importance of geolocation of data and the amount of data to be analysed, it was chosen to use this software to perform the statistical analysis of:

- Mean value (FRP and Bright_T31)
- Median Value (FRP and Bright_T31)
- Standard Deviation value (FRP and Bright_T31)
- Maximum Value (FRP and Bright_T31)

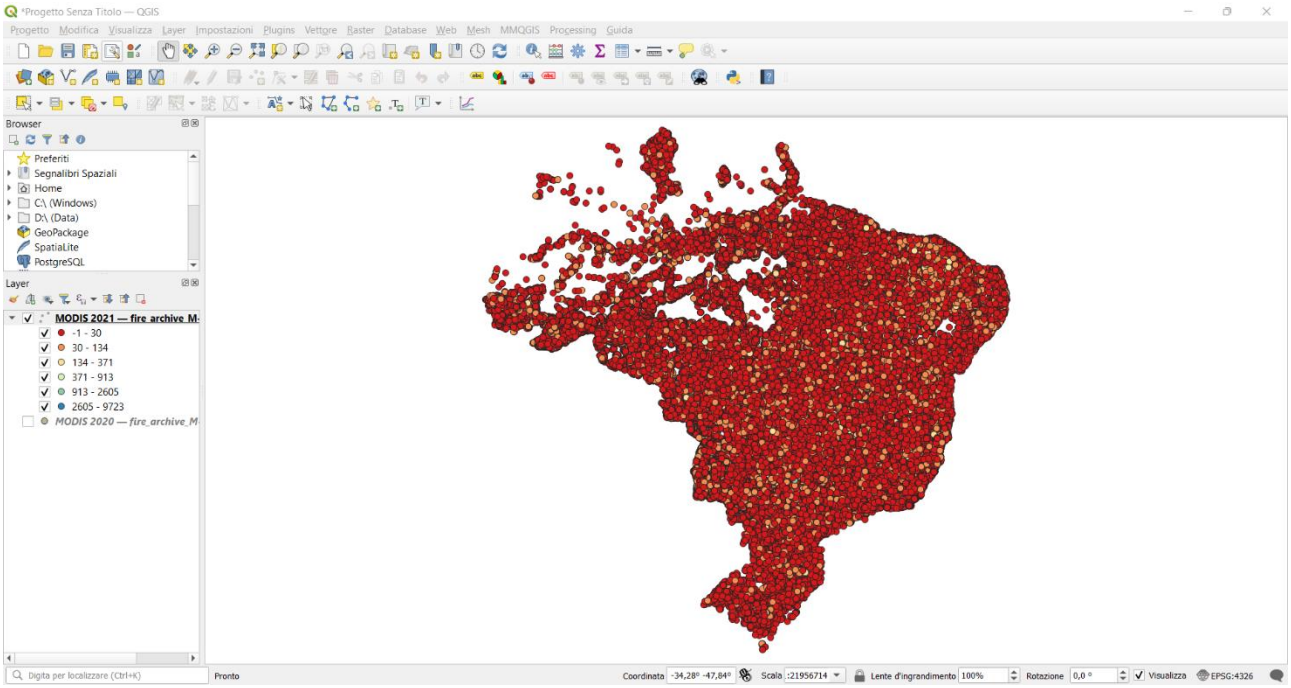

Figure 22 - Example of use of QGIS for the year 2021 of MODIS

This image shows the initial view of an annual file opened in QGIS. The shapefile provides the data that are already georeferenced.

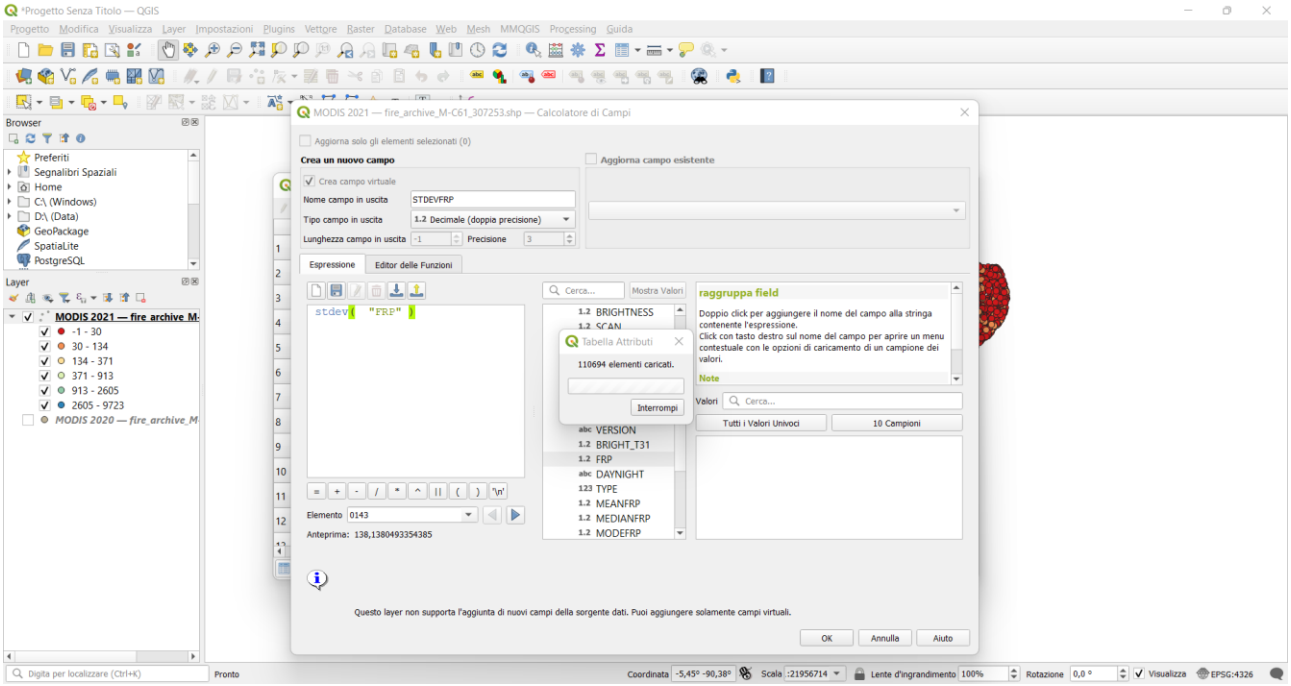

Figure 23 - Example of the use of QGIS for statistical calculation

By opening the attribute table and the field calculator, any necessary operation can be performed.

Subsequently the calculations for each year were combined into one file, the corresponding tables and graphs of which were processed through Excel and will be shown below.

3. Results and discussion

3.1 Qualitative analysis of firepower of FAMF

FIRMS give the possibility to download active fire/hotspot information older than the last 7 days as previously described, but FIRMS Fire Map, also allows to interactively browse the full archive of global active fire detections from MODIS and VIIRS. Near real-time fire data are available within approximately 3 hours of satellite overpass and imagery within 4-5 hours.

In the fire map viewer, you can create a customised view of images and geospatial data centred on a particular area of interest and share it with others as a PNG, JPG, GIF or GeoTIFF image.

To save and share a map image, click on the screenshot icon at the bottom of the viewer ("Capture") and select your preferred option.

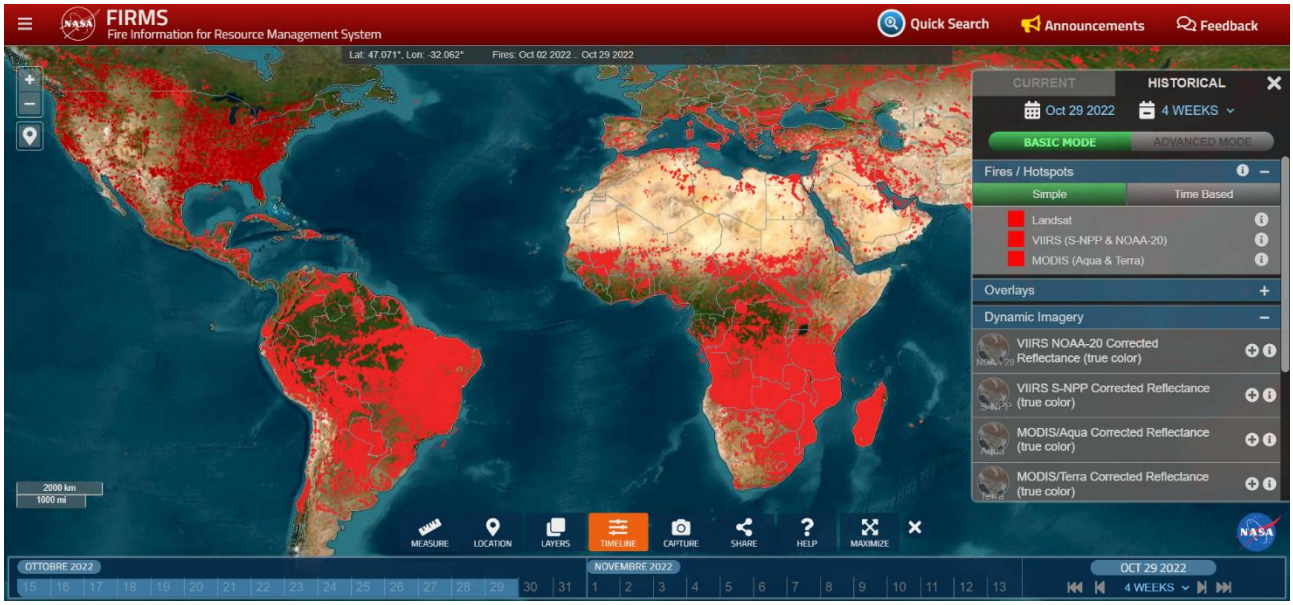

Figure 24 - Display of the principal FIRMS, it is possible to see at the bottom centre the button for downloading the complete FAMF images (FAMF about October 2022) (FIRMS)

It's possible to decide and fix a location, and in this case the location is Brazil.

Right of Fig.24, are the layers of the respective sensors present, the downloaded images, the FAMFs present will be provided by the sensors:

- MODIS
- VIIRS

After providing a "snapshot" through the "Capture" option, the FIRMS system will download the image with indications of the respective scale, and the respective date (days, month, year).

The next pages will show images representing FAMF from the year 2001 to 2022. For each year, images were acquired covering 31 days for three months of the year, which are:

- August
- October
- December

The choice of these months depended on:

- existence of the dry and wet seasons, so the months chosen do not include the wet season;
- prevalence of fires in certain months of the year, an analysis carried out in the next chapter.

The format of the downloaded images is PNG, chosen because the resolution is better than JPEG.

Regardless of the variation of FAMF events across months and years, from 2001 to 2012 only MODIS provides data, whereas, from 2012 the data available will be from both MODIS and VIIRS, this will surely lead to an increase in the number of events detected.

The first block of FIRMS images that will be shown concern the month of August for all years, from 2001 to 2022, in order to facilitate the comparison of different years for the same month.

Figure 25 - FIRMS Fire Map of Amazon Forest 1st August to 31st August 2001

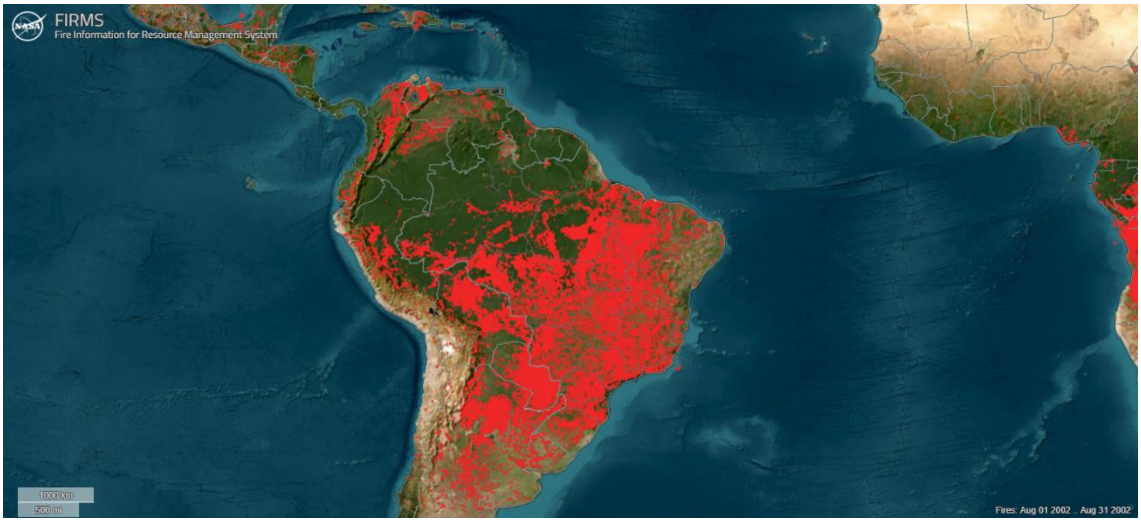

Figure 26 - FIRMS Fire Map of Amazon Forest 1st August to 31st August 2002

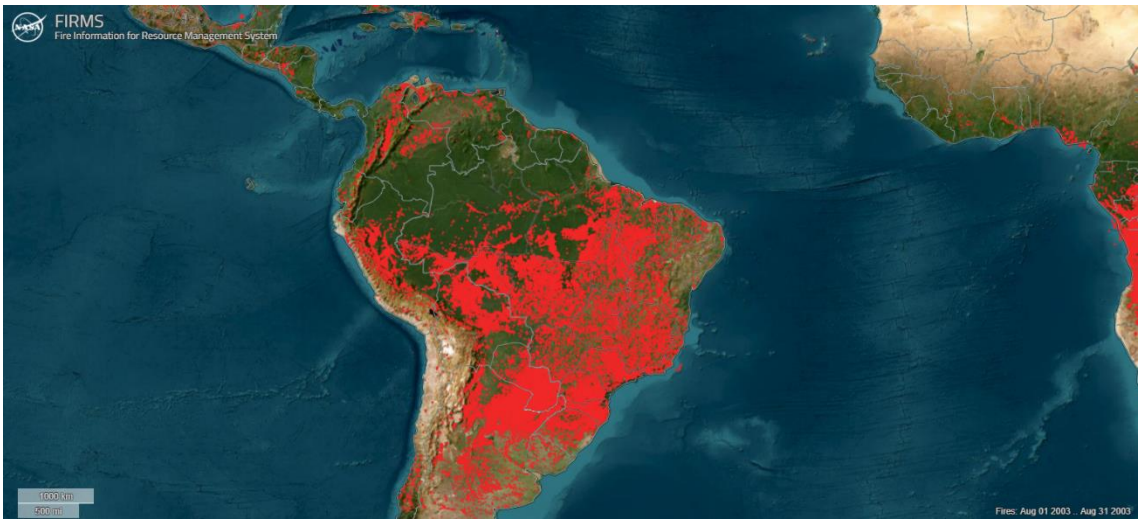

Figure 27 - FIRMS Fire Map of Amazon Forest 1st August to 31st August 2003

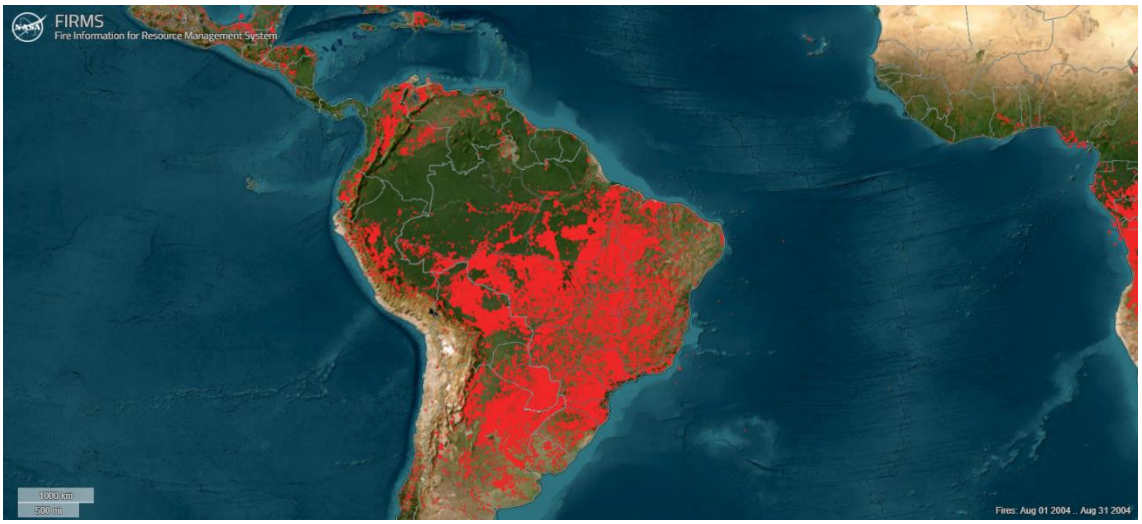

Figure 28 - FIRMS Fire Map of Amazon Forest 1st August to 31st August 2004

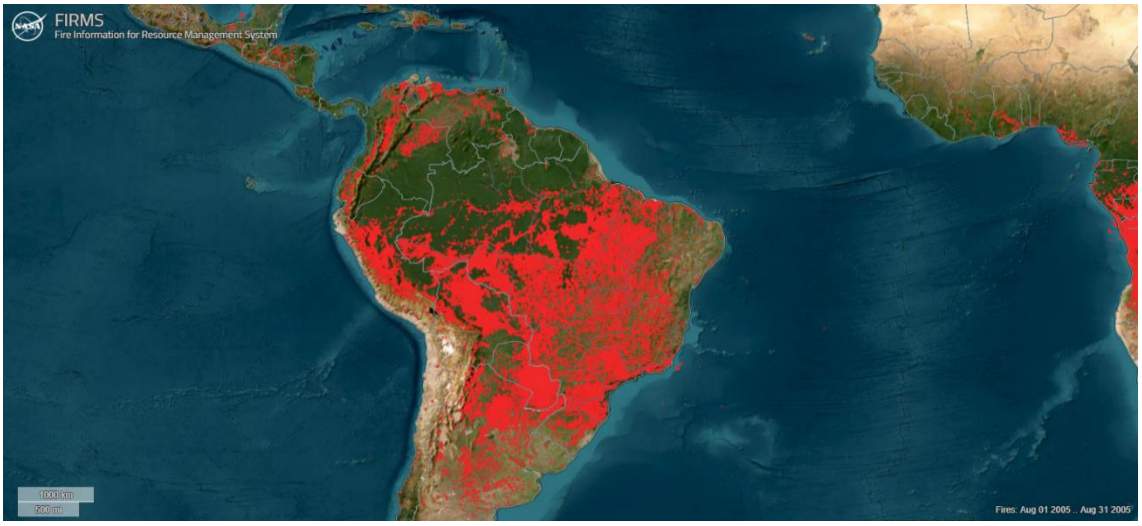

Figure 29 - FIRMS Fire Map of Amazon Forest 1st August to 31st August 2005

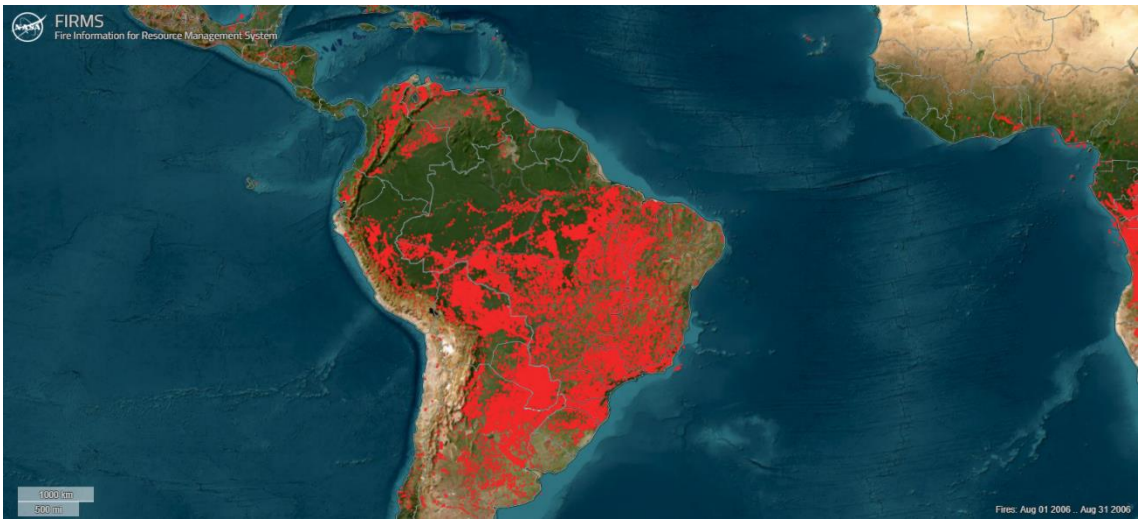

Figure 30 - FIRMS Fire Map of Amazon Forest 1st August to 31st August 2006

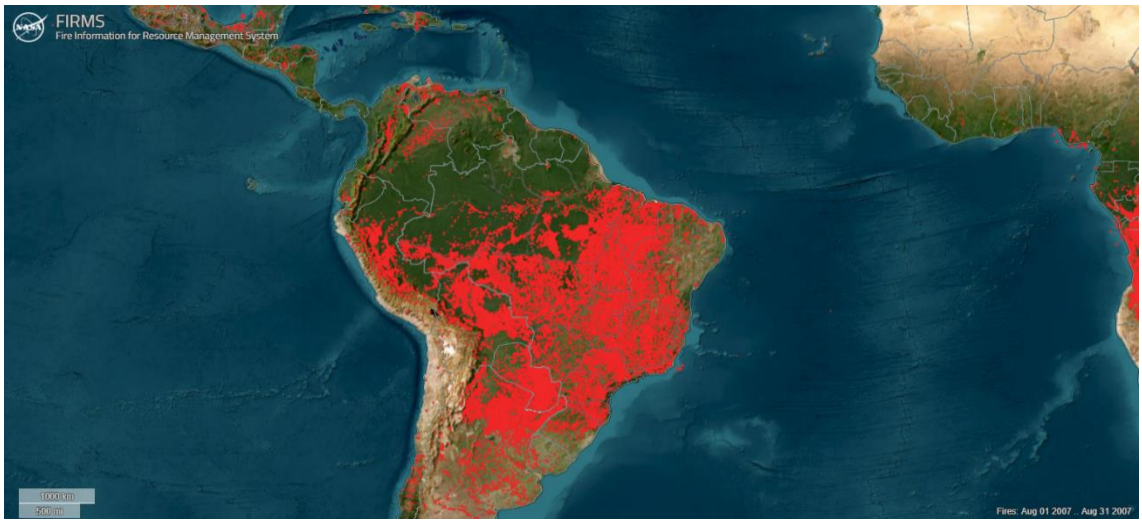

Figure 31 - FIRMS Fire Map of Amazon Forest 1st August to 31st August 2007

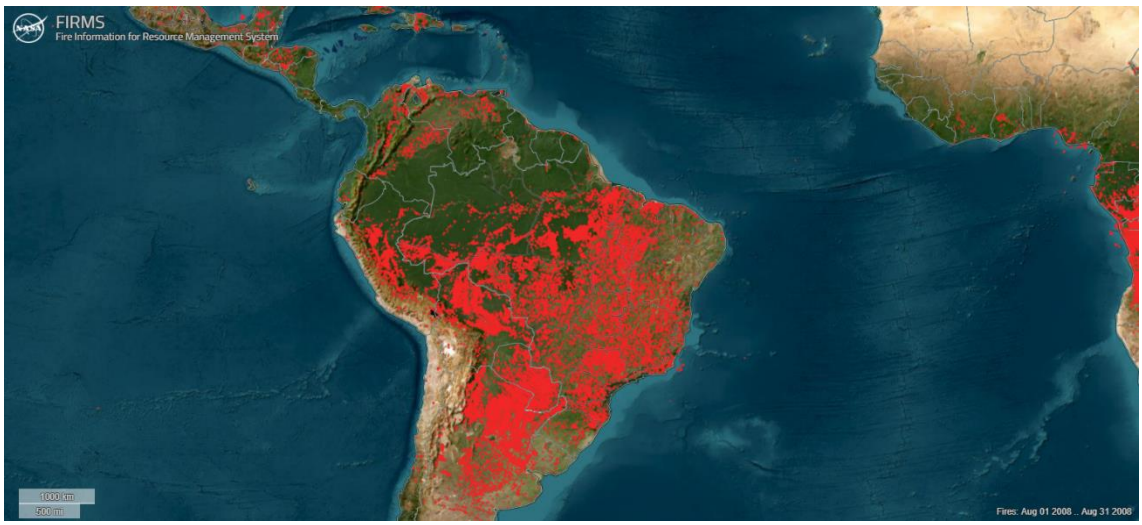

Figure 32 - FIRMS Fire Map of Amazon Forest 1st August to 31st August 2008

Figure 33 - FIRMS Fire Map of Amazon Forest 1st August to 31st August 2009

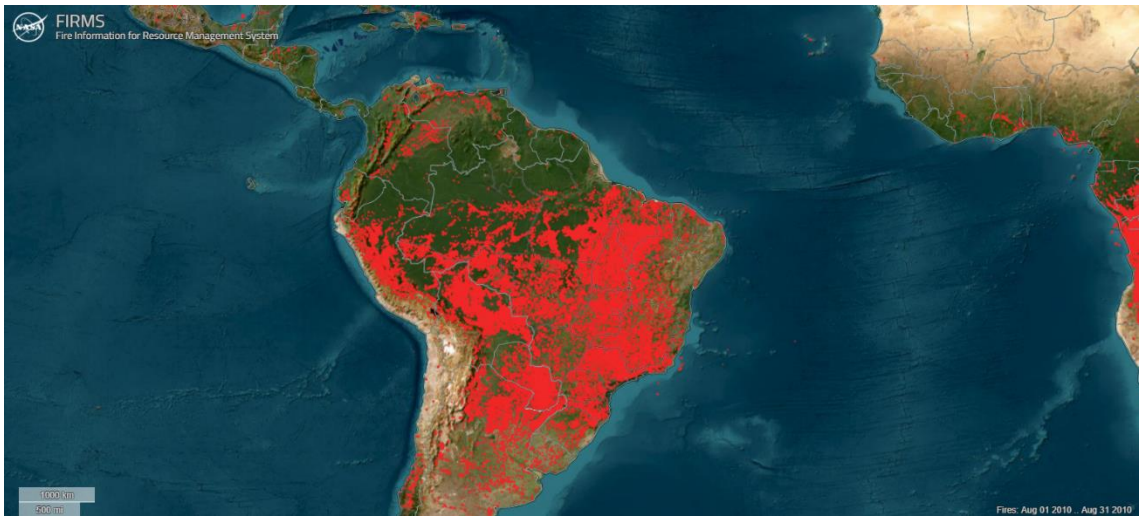

Figure 34 - FIRMS Fire Map of Amazon Forest 1st August to 31st August 2010

Figure 35 - FIRMS Fire Map of Amazon Forest 1st August to 31st August 2011

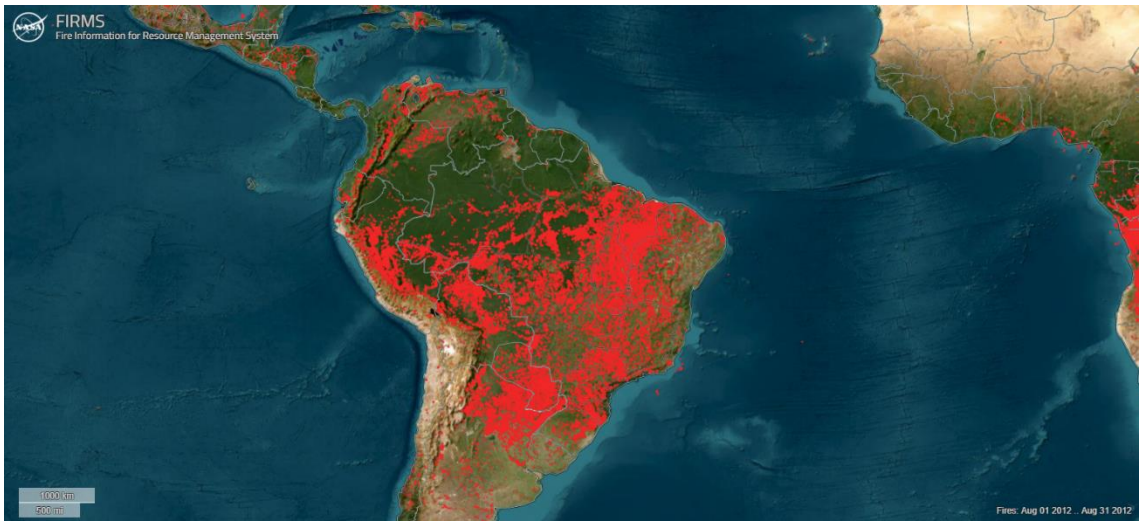

Figure 36 - - FIRMS Fire Map of Amazon Forest 1st August to 31st August 2012

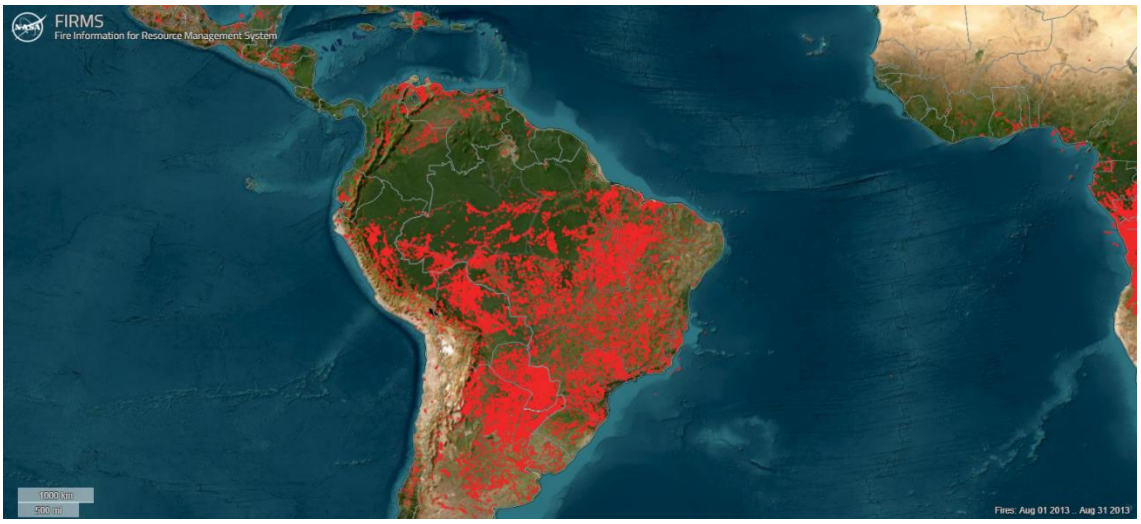

Figure 37 - FIRMS Fire Map of Amazon Forest 1st August to 31st August 2013

Figure 38 - FIRMS Fire Map of Amazon Forest 1st August to 31st August 2014

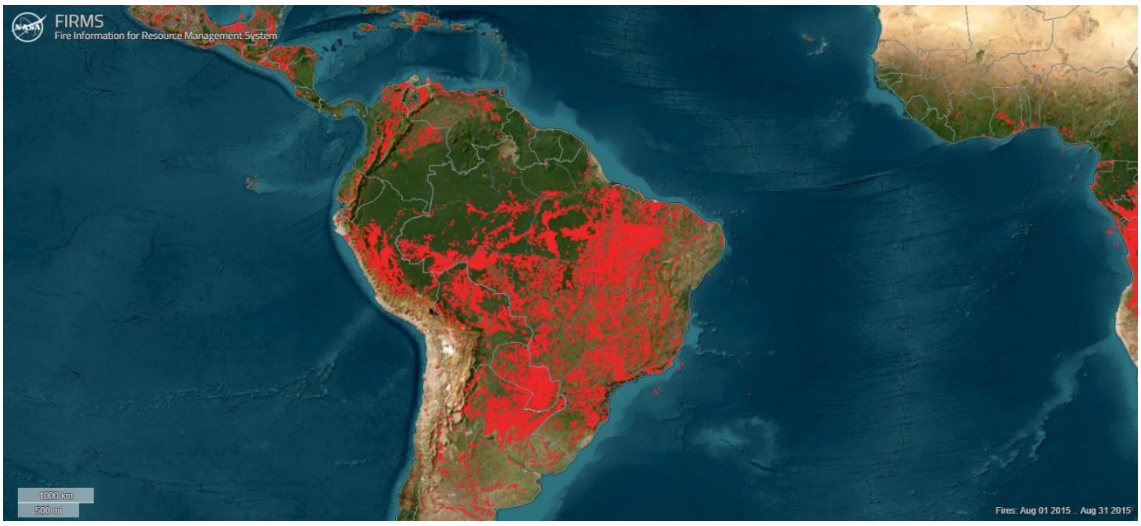

Figure 39 FIRMS - Fire Map of Amazon Forest 1st August to 31st August 2015

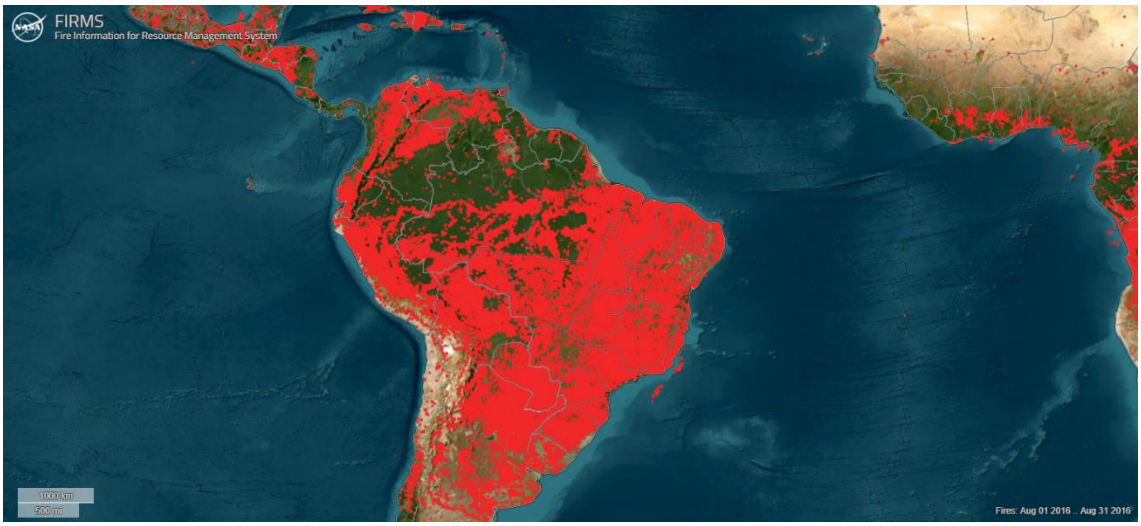

Figure 40 - FIRMS Fire Map of Amazon Forest 1st August to 31st August 2016

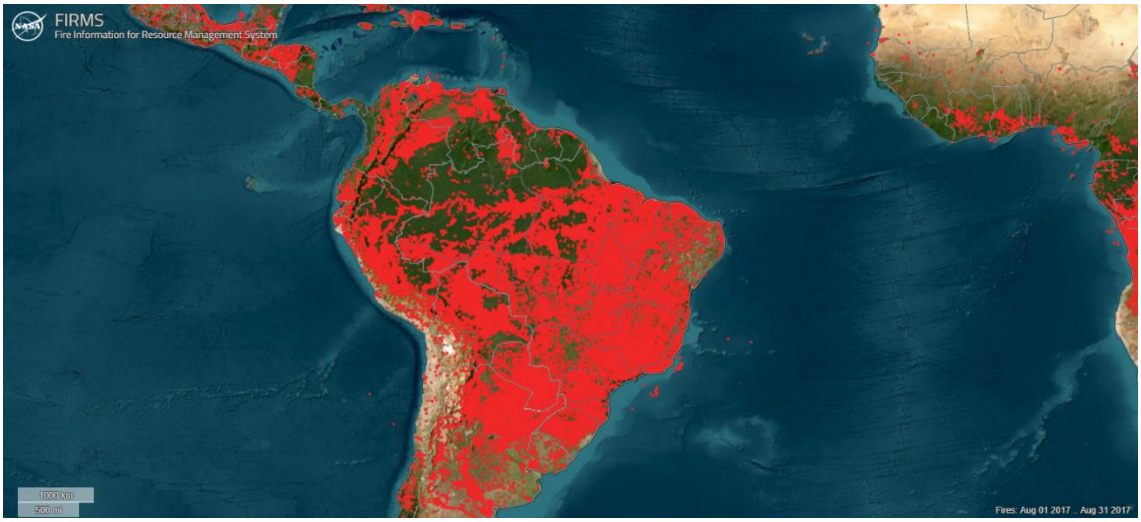

Figure 41 - FIRMS Fire Map of Amazon Forest 1st August to 31st August 2017

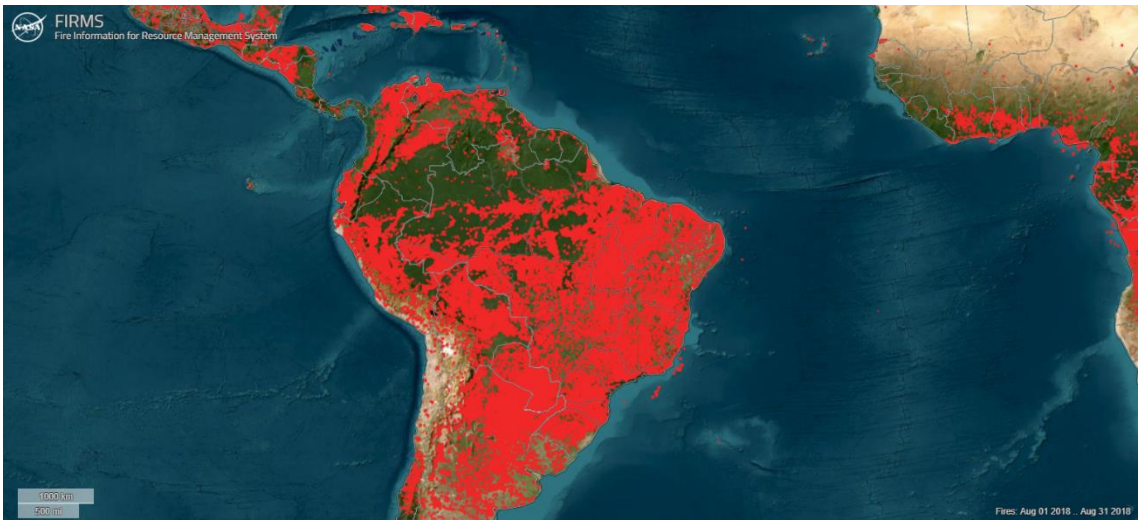

Figure 42 - FIRMS Fire Map of Amazon Forest 1st August to 31st August 2018

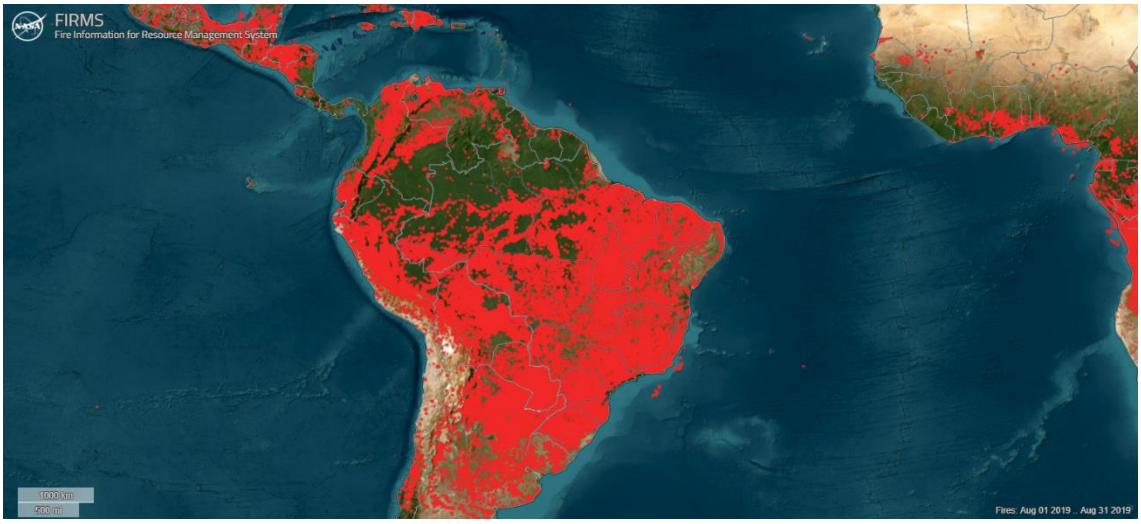

Figure 43 - FIRMS Fire Map of Amazon Forest 1st August to 31st August 2019

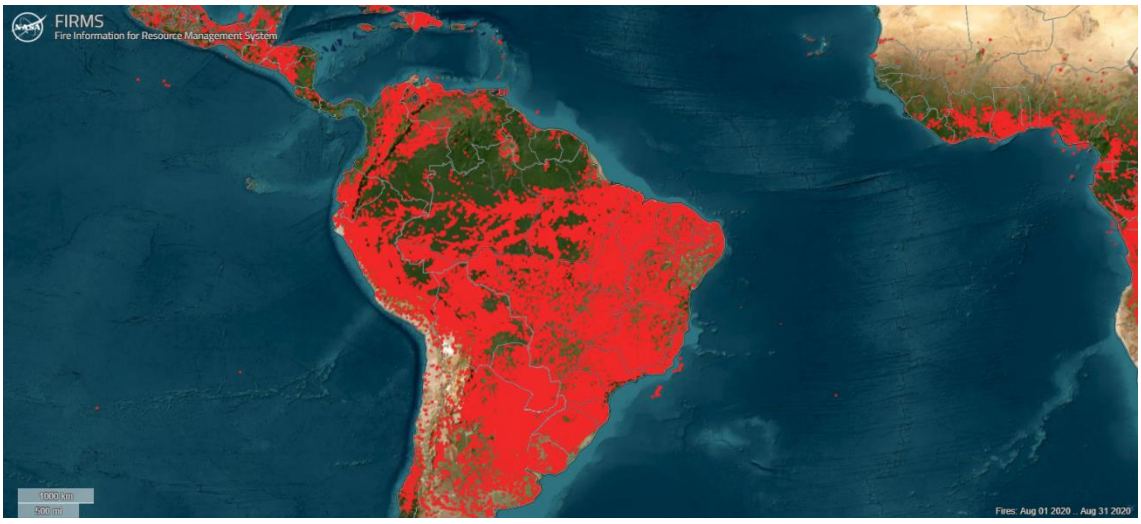

Figure 44 - FIRMS Fire Map of Amazon Forest 1st August to 31st August 2020

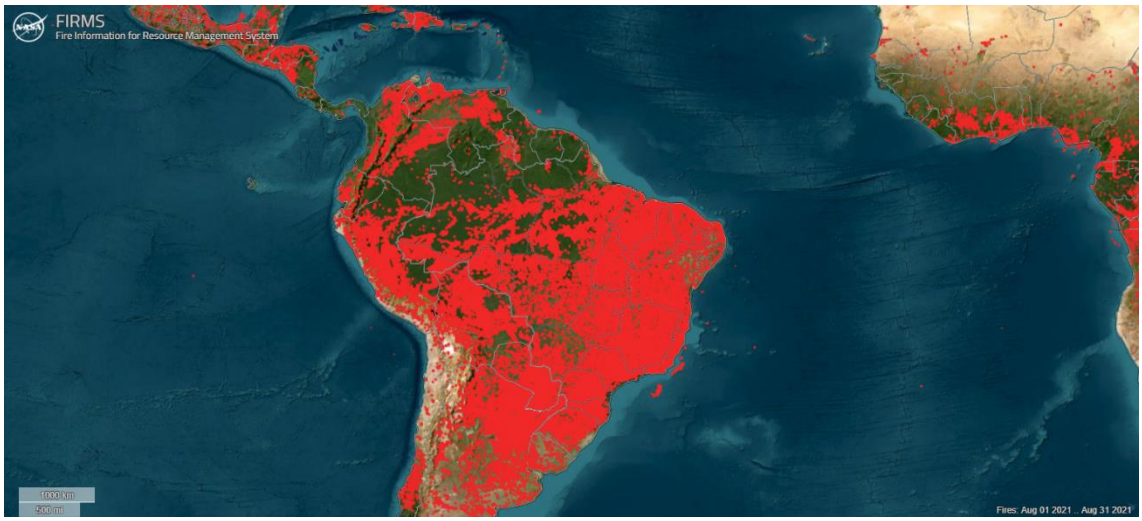

Figure 45 - FIRMS Fire Map of Amazon Forest 1st August to 31st August 2021

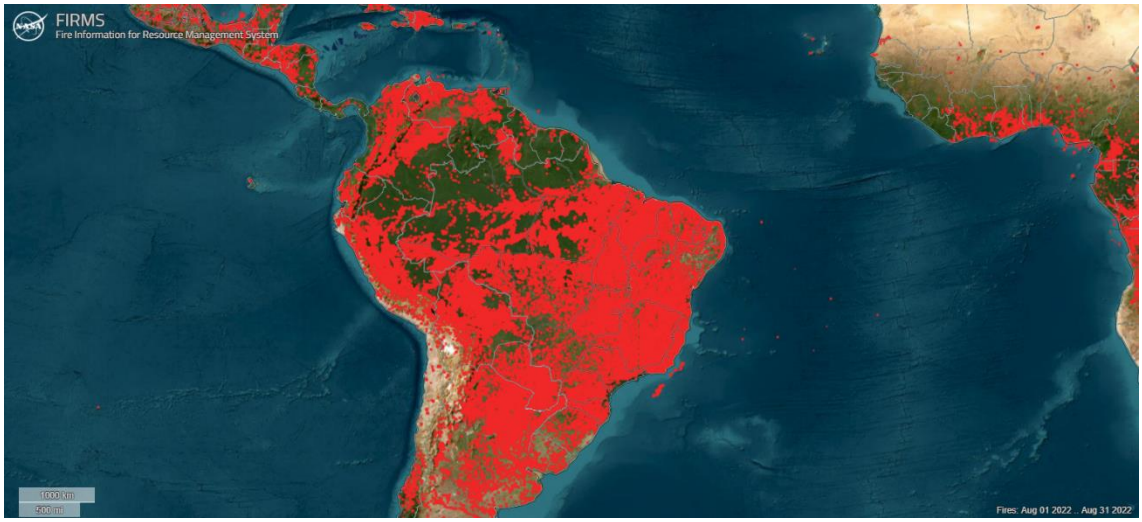

Figure 46 - FIRMS Fire Map of Amazon Forest 1st August to 31st August 2022

The images show FAMFs for month of August in each year since 2001. Comparing the various images, it can be seen that: for the month of August, the highest number of events is recorded in the years 2004, 2005, 2007 and then from 2017 to 2022.

The second block of FIRMS images that will be shown concern the month of October for all years, from 2001 to 2022, in order to facilitate the comparison of different years for the same month.

Figure 47 - FIRMS Fire Map of Amazon Forest 1st October to 31st October 2001

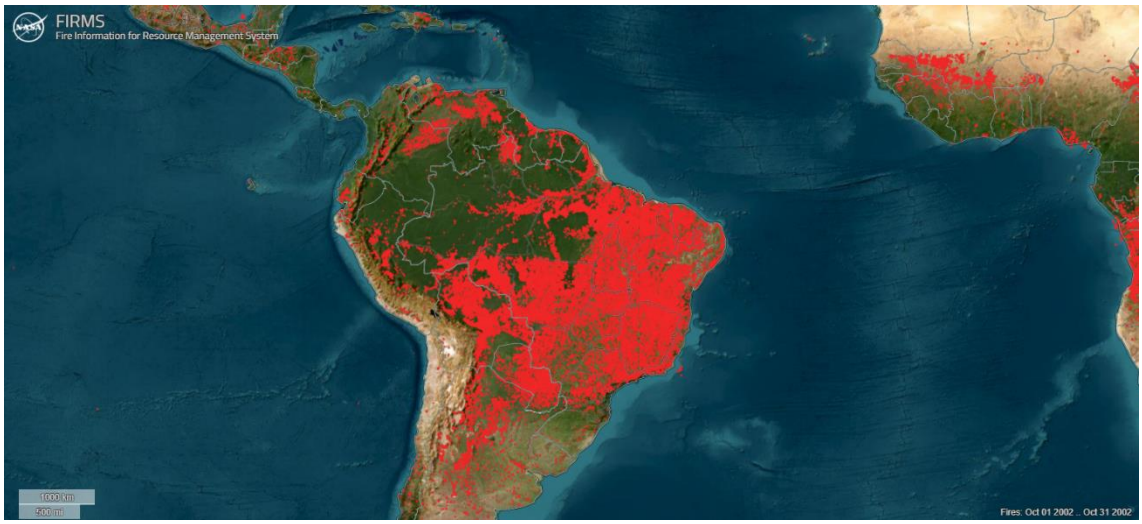

Figure 48 - FIRMS Fire Map of Amazon Forest 1st October to 31st October 2002

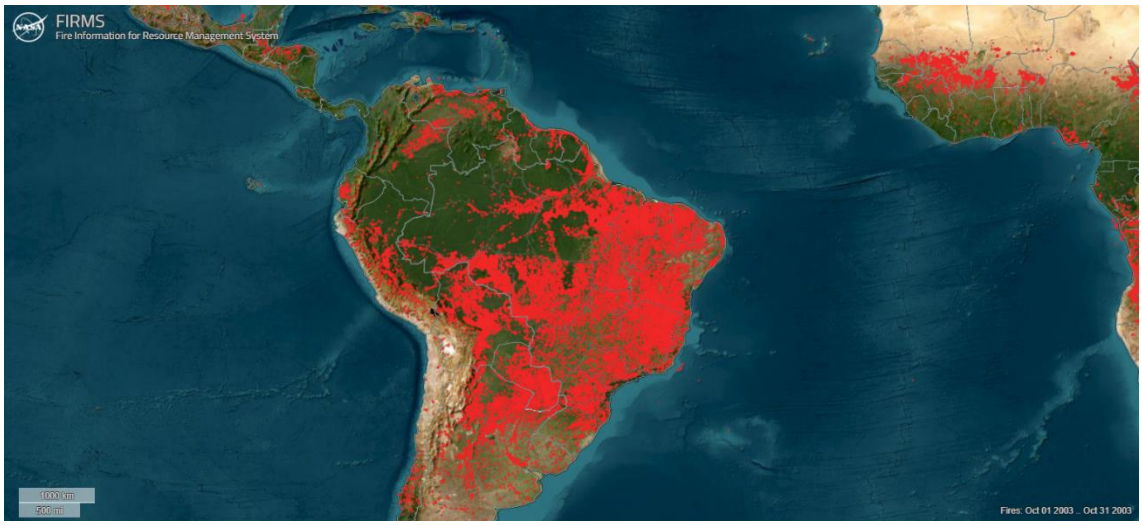

Figure 49 - FIRMS Fire Map of Amazon Forest 1st October to 31st October 2003

Figure 50 - FIRMS Fire Map of Amazon Forest 1st October to 31st October 2004

Figure 51 - FIRMS Fire Map of Amazon Forest 1st October to 31st October 2005

Figure 52 - FIRMS Fire Map of Amazon Forest 1st October to 31st October 2006

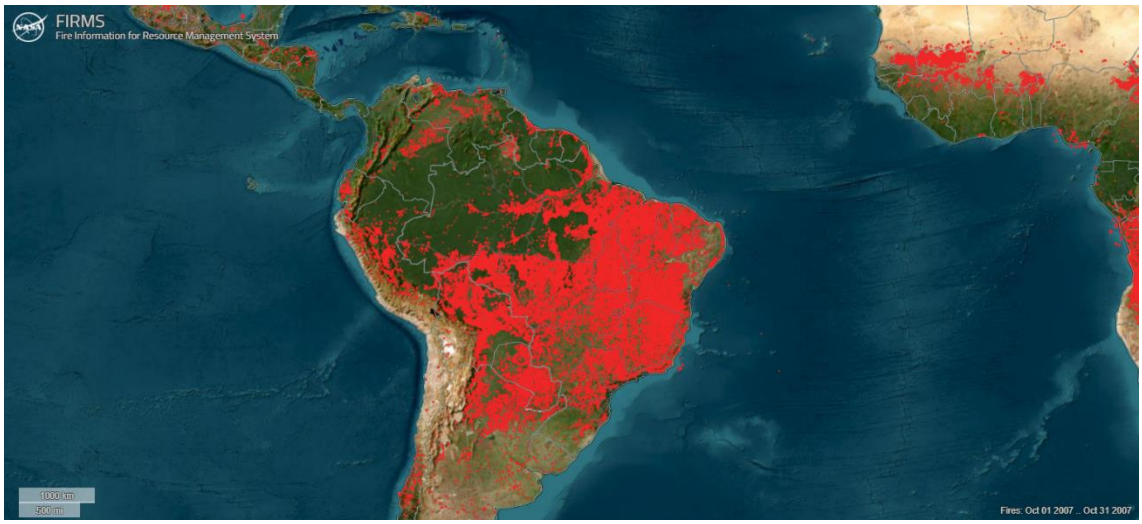

Figure 53 - FIRMS Fire Map of Amazon Forest 1st October to 31st October 2007

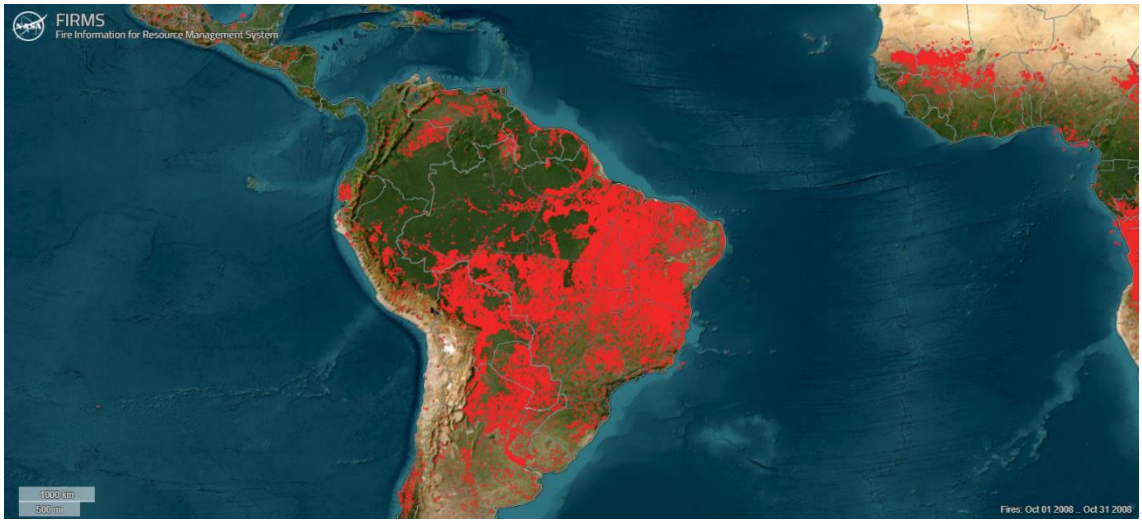

Figure 54 - FIRMS Fire Map of Amazon Forest 1st October to 31st October 2008

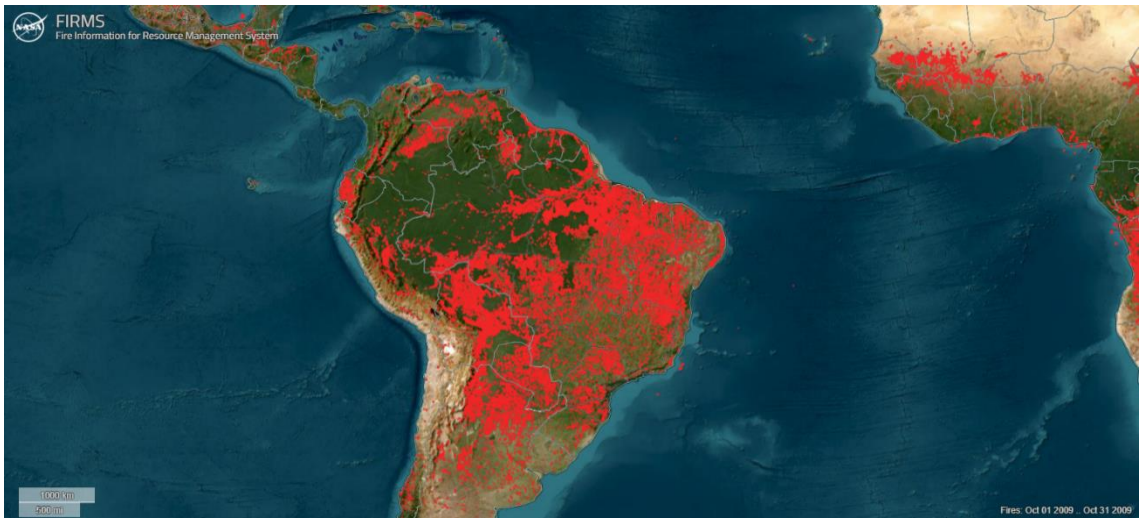

Figure 55 - FIRMS Fire Map of Amazon Forest 1st October to 31st October 2009

Figure 56 - - FIRMS Fire Map of Amazon Forest 1st October to 31st October 2010

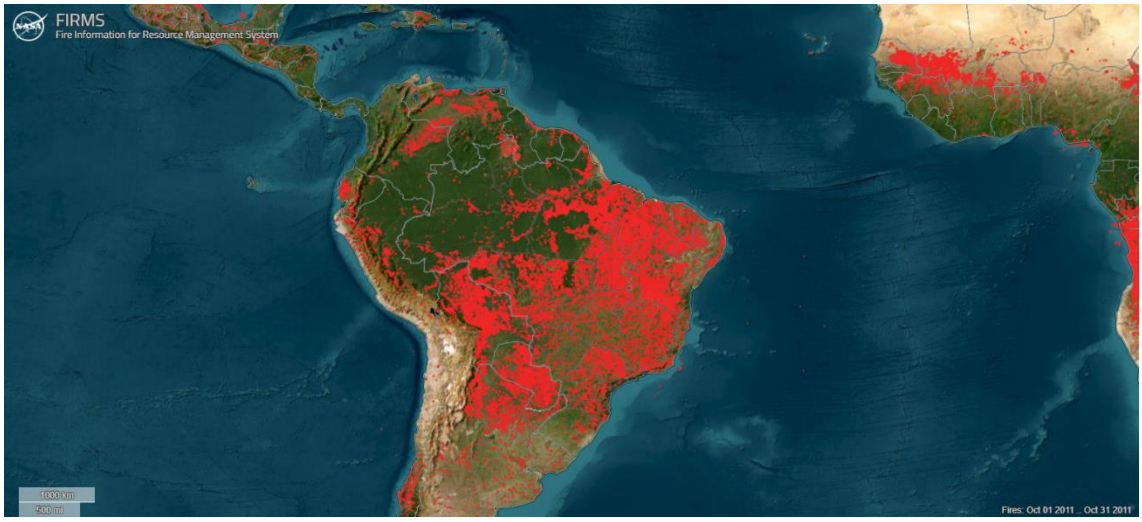

Figure 57 - FIRMS Fire Map of Amazon Forest 1st October to 31st October 2011

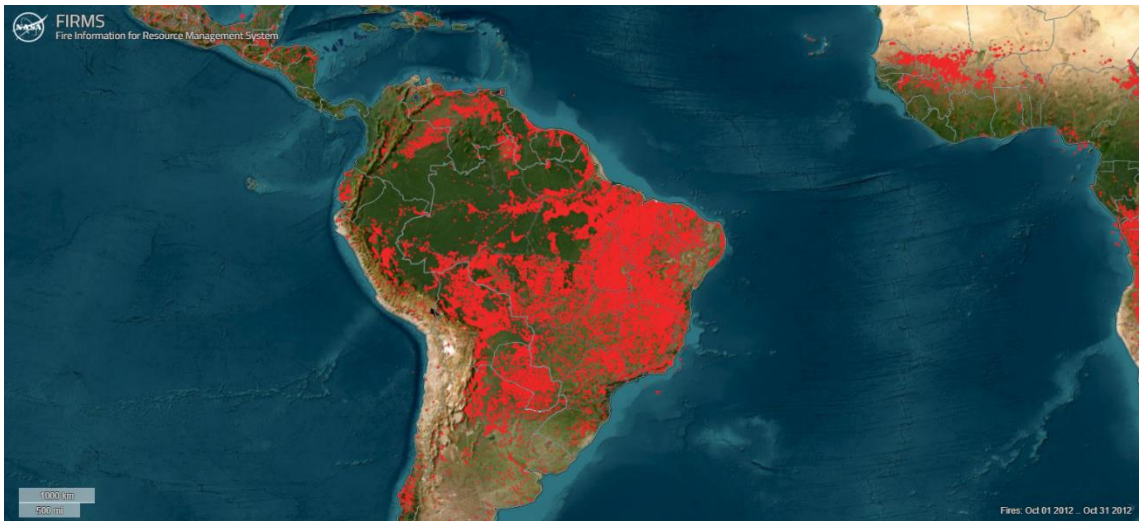

Figure 58 - FIRMS Fire Map of Amazon Forest 1st October to 31st October 2012

Figure 59 - FIRMS Fire Map of Amazon Forest 1st October to 31st October 2013

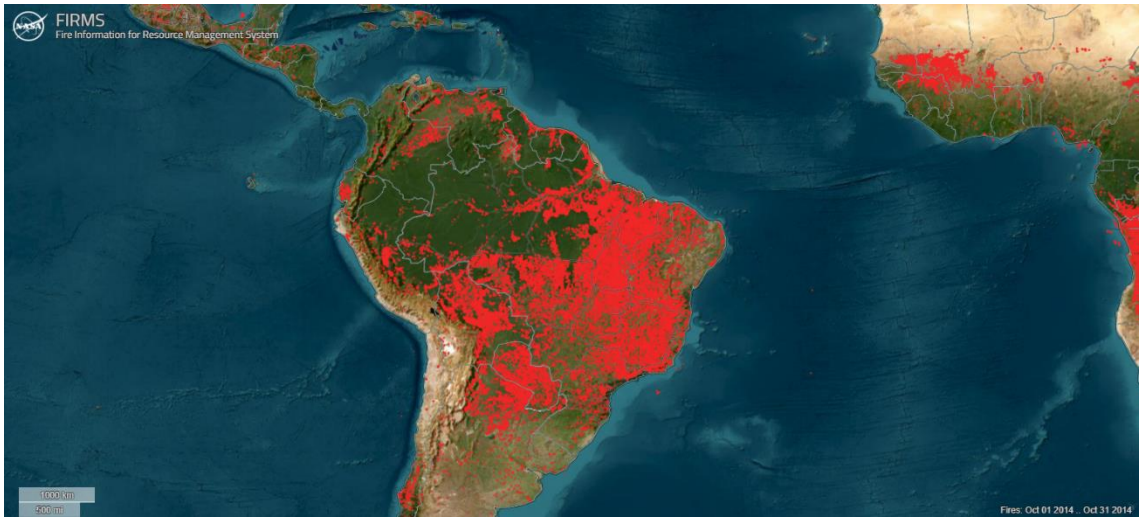

Figure 60 - FIRMS Fire Map of Amazon Forest 1st October to 31st October 2014

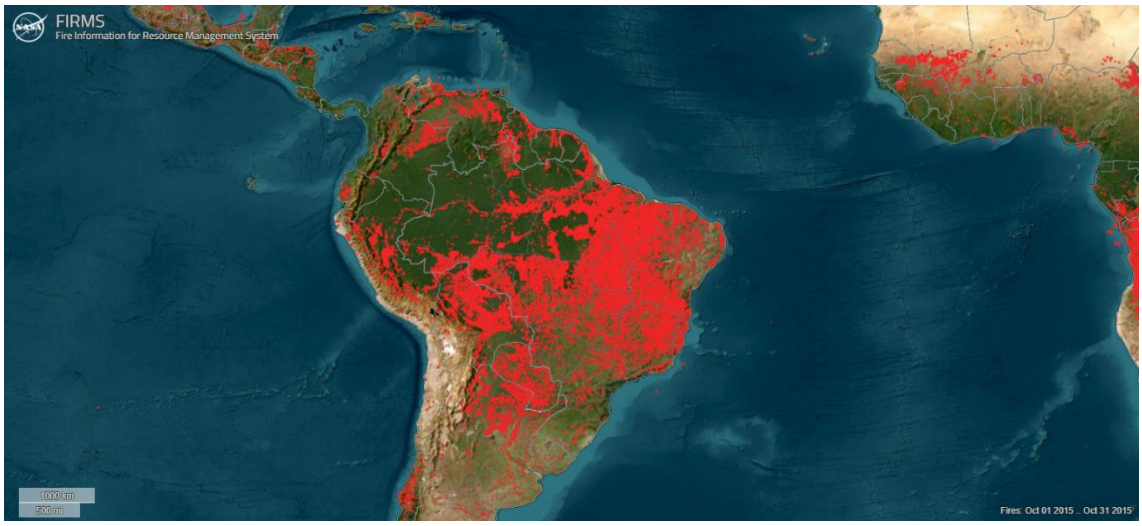

Figure 61 - FIRMS Fire Map of Amazon Forest 1st October to 31st October 2015

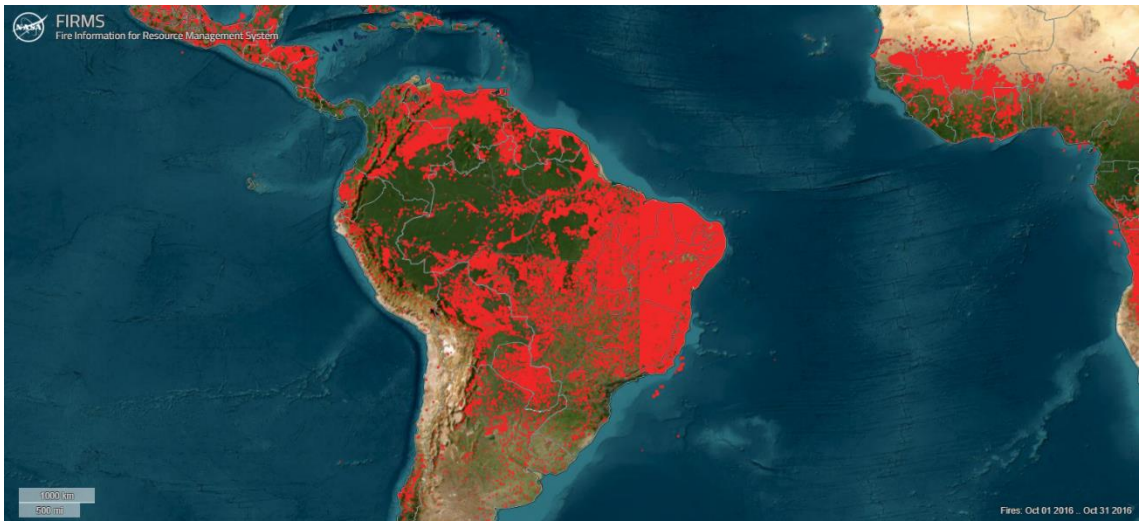

Figure 62 - FIRMS Fire Map of Amazon Forest 1st October to 31st October 2016

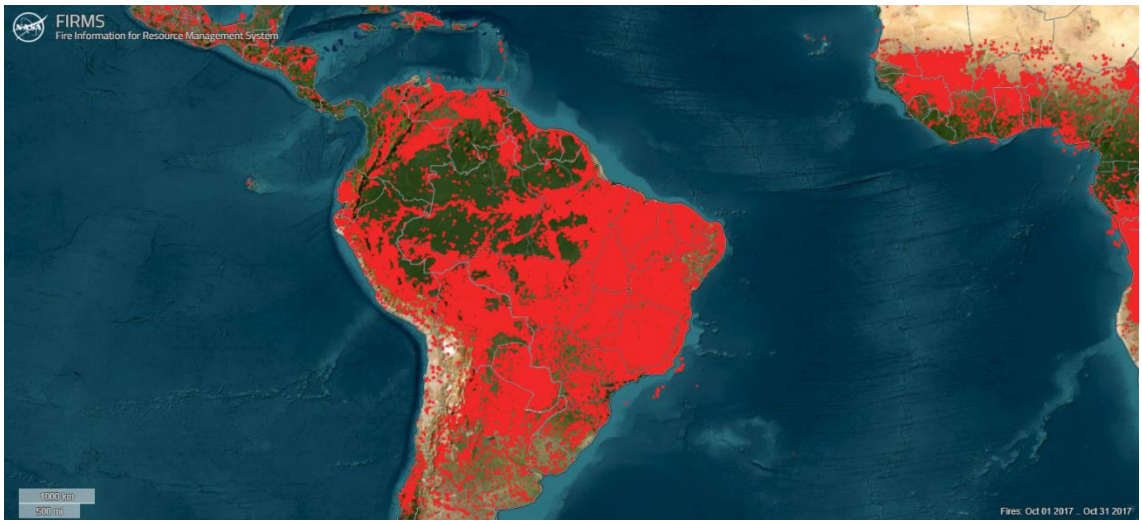

Figure 63 - FIRMS Fire Map of Amazon Forest 1st October to 31st October 2017

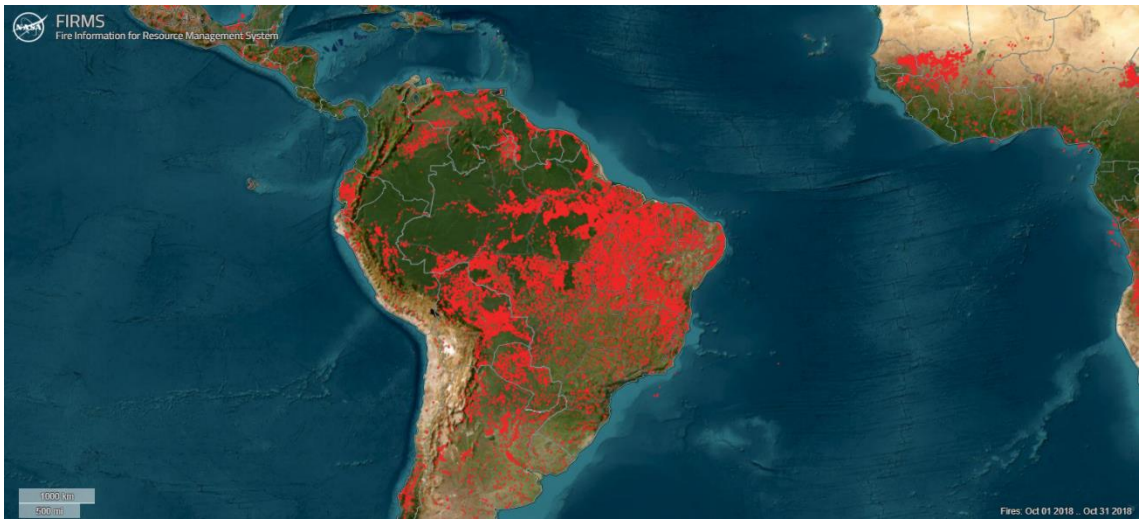

Figure 64 - FIRMS Fire Map of Amazon Forest 1st October to 31st October 2018

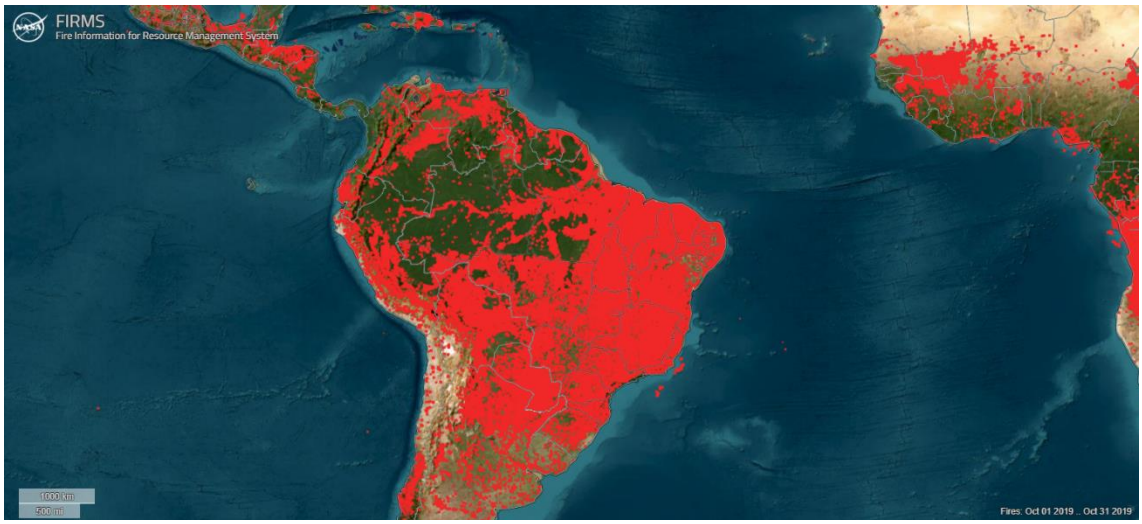

Figure 65 - FIRMS Fire Map of Amazon Forest 1st October to 31st October 2019

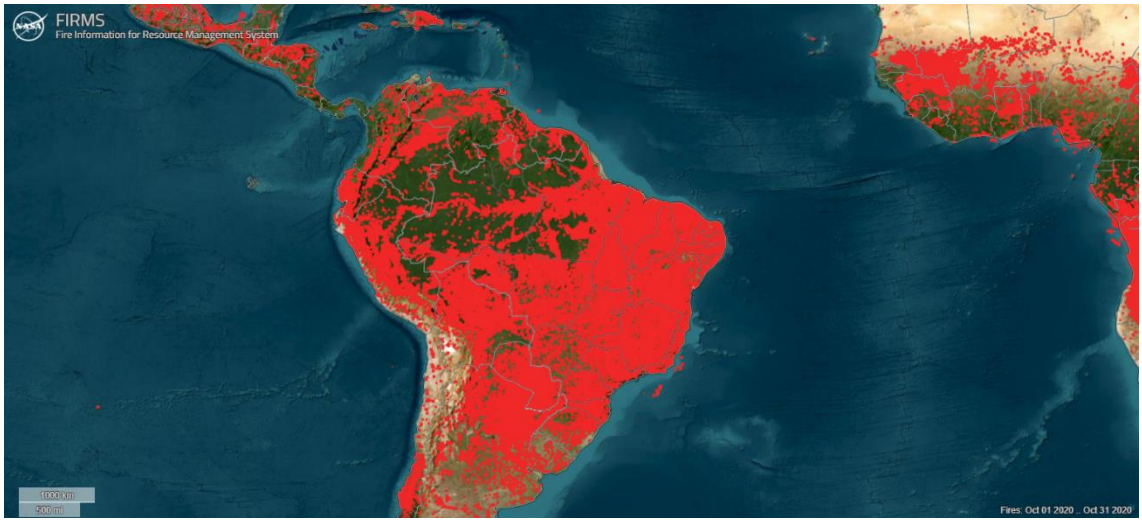

Figure 66 - FIRMS Fire Map of Amazon Forest 1st October to 31st October 2020

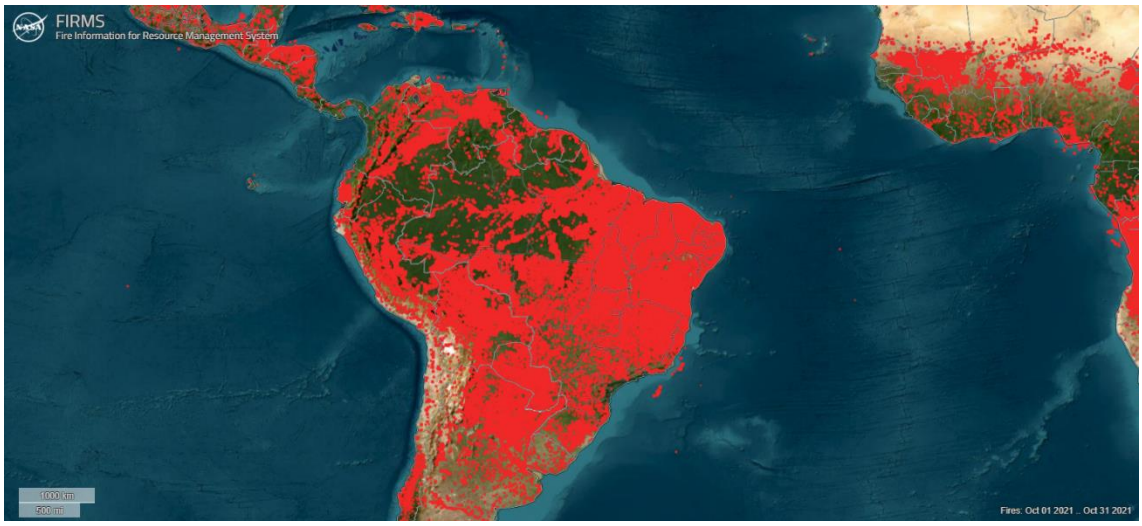

Figure 67 - FIRMS Fire Map of Amazon Forest 1st October to 31st October 2021

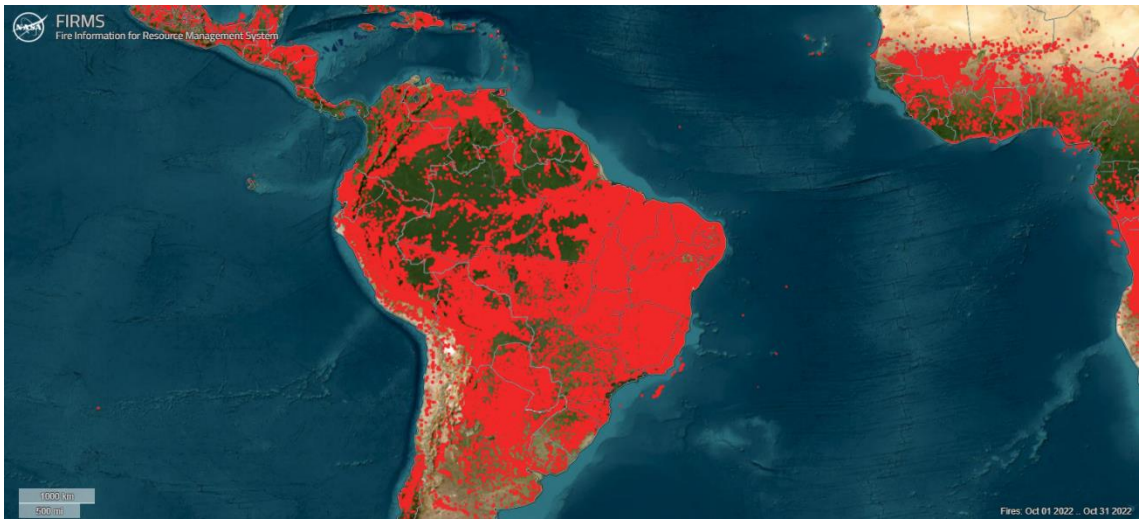

Figure 68 - FIRMS Fire Map of Amazon Forest 1st October to 31st October 2022

The images show FAMFs for month of October in each year since 2001. Comparing the various images, it can be seen that: for the month of October, the highest number of events is recorded in the year 2004 and from 2017 to 2022.

The third block of FIRMS images that will be shown concern the month of December for all years, from 2001 to 2022, in order to facilitate the comparison of different years for the same month.

Figure 69 - FIRMS Fire Map of Amazon Forest 1st December to 31st December 2001

Figure 70 - FIRMS Fire Map of Amazon Forest 1st December to 31st December 2002

Figure 71 - FIRMS Fire Map of Amazon Forest 1st December to 31st December 2003

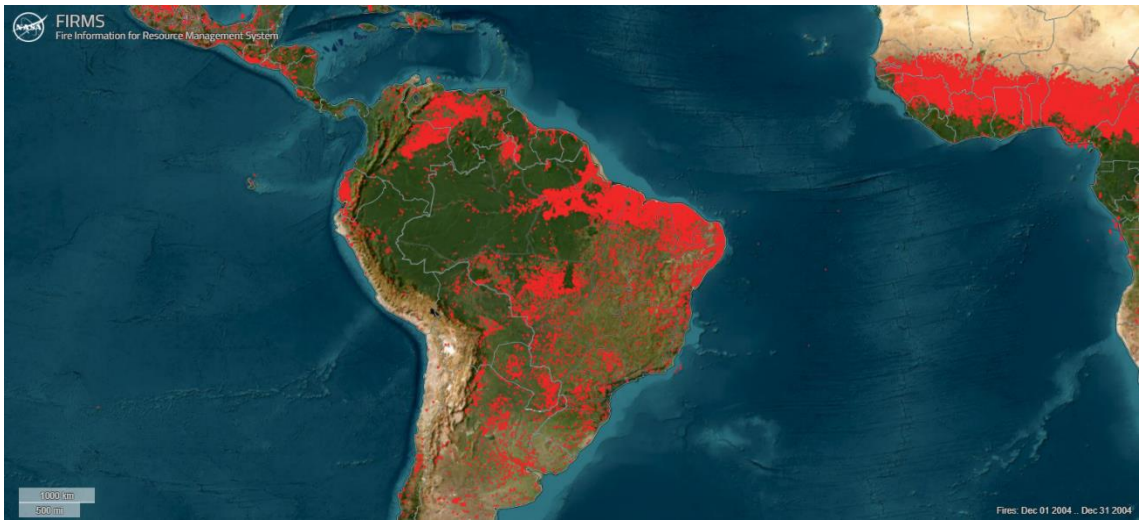

Figure 72 - FIRMS Fire Map of Amazon Forest 1st December to 31st December 2004

Figure 73 - FIRMS Fire Map of Amazon Forest 1st December to 31st December 2005

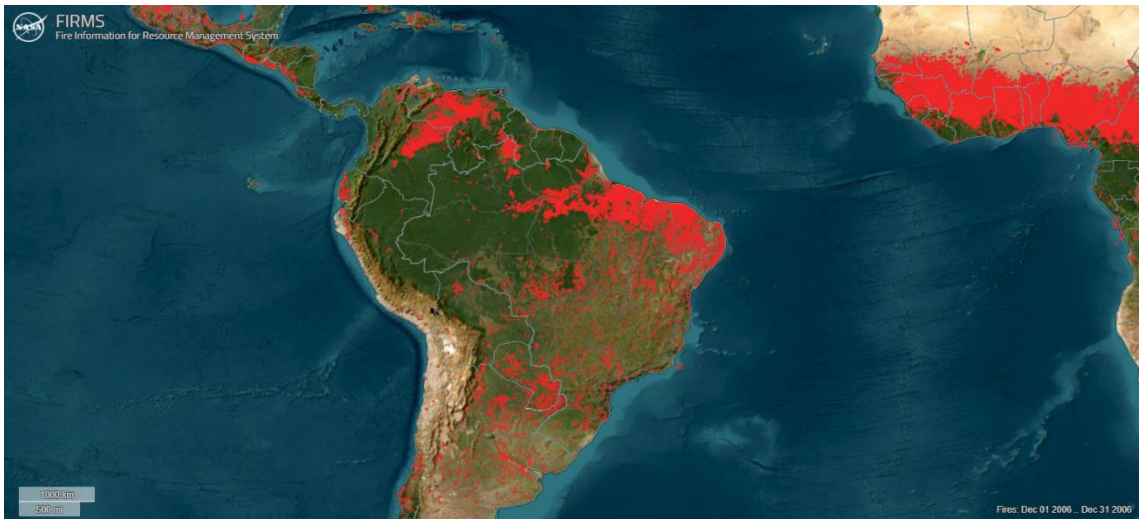

Figure 74 - FIRMS Fire Map of Amazon Forest 1st December to 31st December 2006

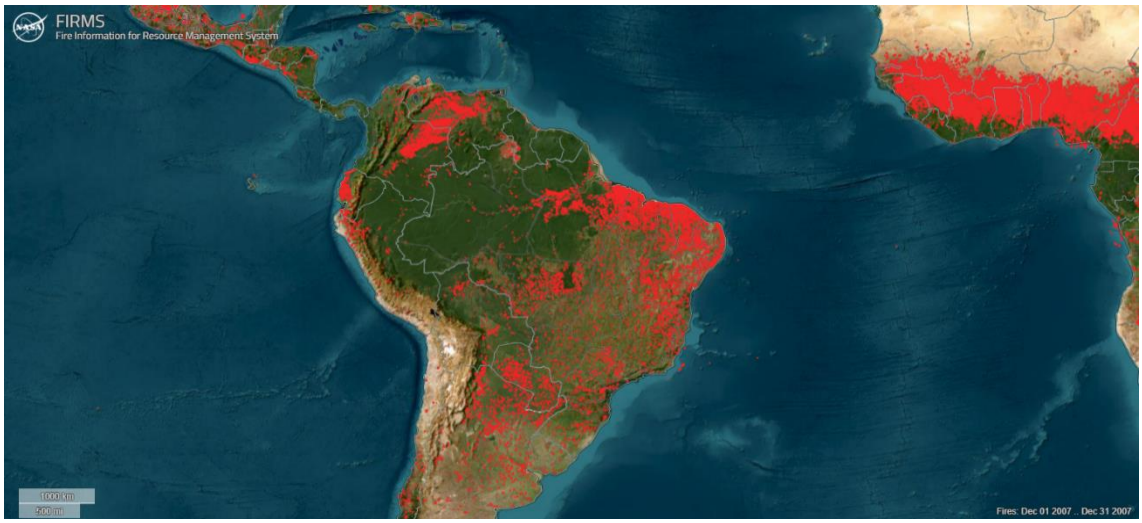

Figure 75 - FIRMS Fire Map of Amazon Forest 1st December to 31st December 2007

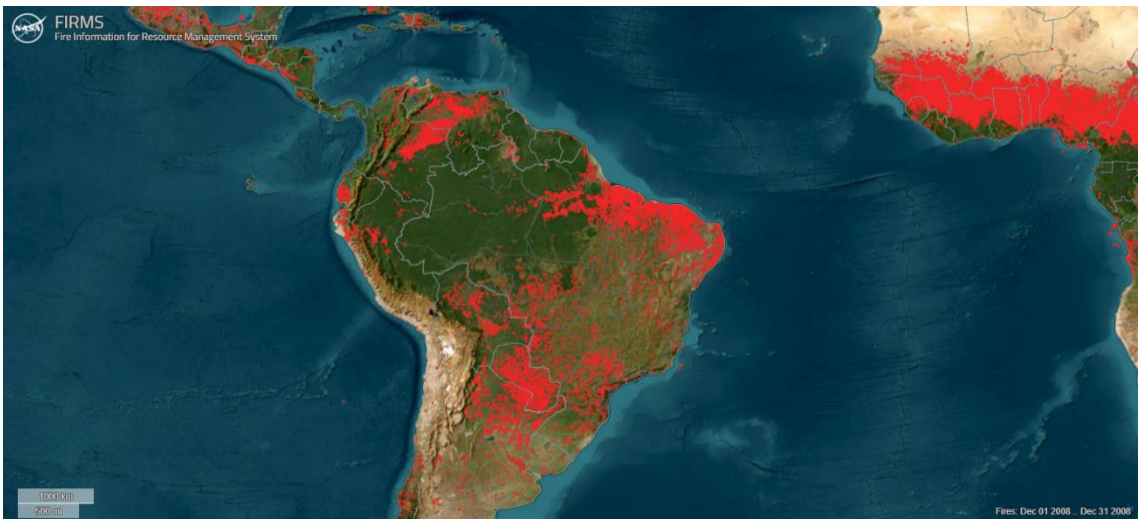

Figure 76 - FIRMS Fire Map of Amazon Forest 1st December to 31st December 2008

Figure 77 - FIRMS Fire Map of Amazon Forest 1st December to 31st December 2009

Figure 78 - FIRMS Fire Map of Amazon Forest 1st December to 31st December 2010

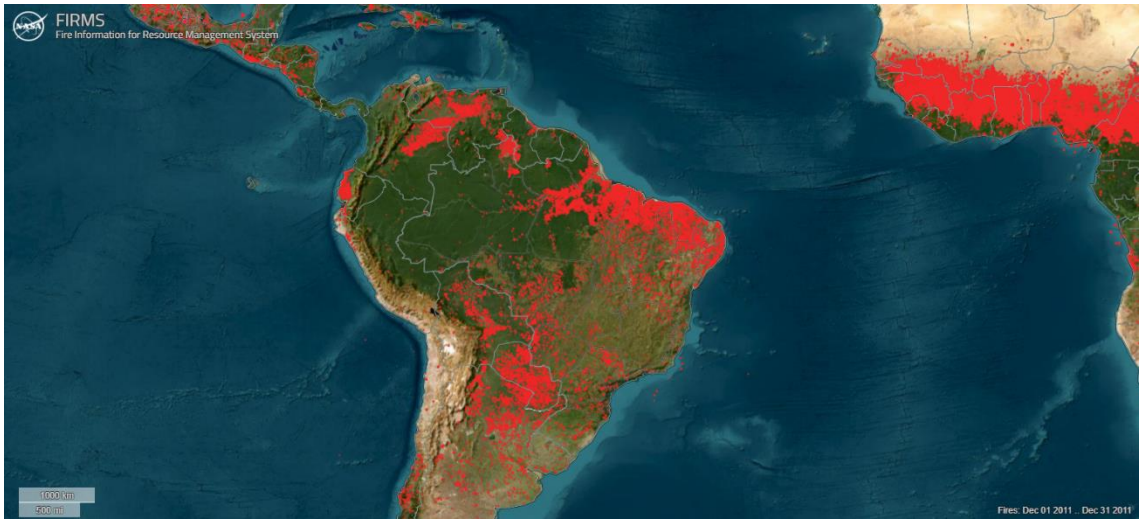

Figure 79 - FIRMS Fire Map of Amazon Forest 1st December to 31st December 2011

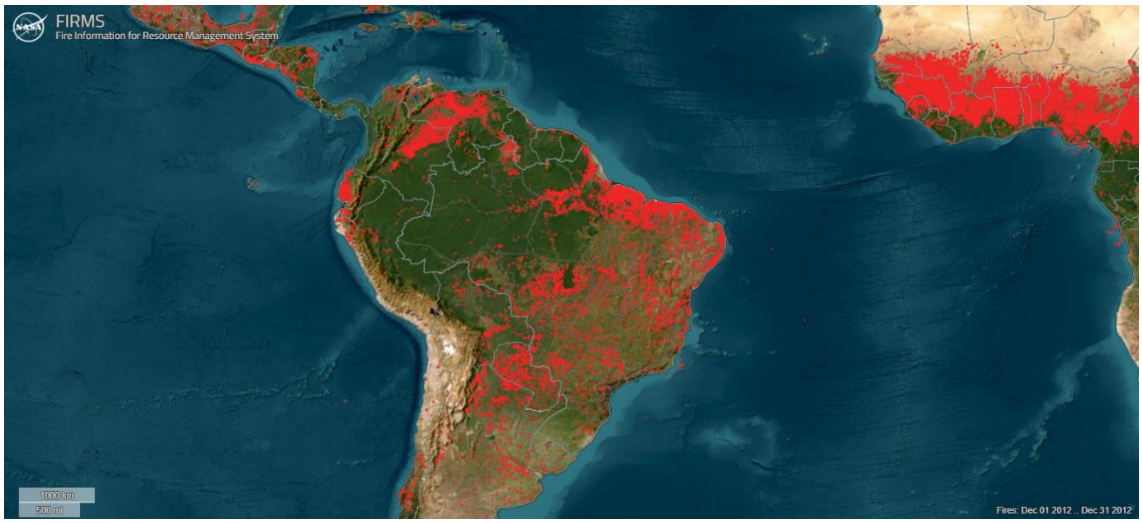

Figure 80 - FIRMS Fire Map of Amazon Forest 1st December to 31st December 2012

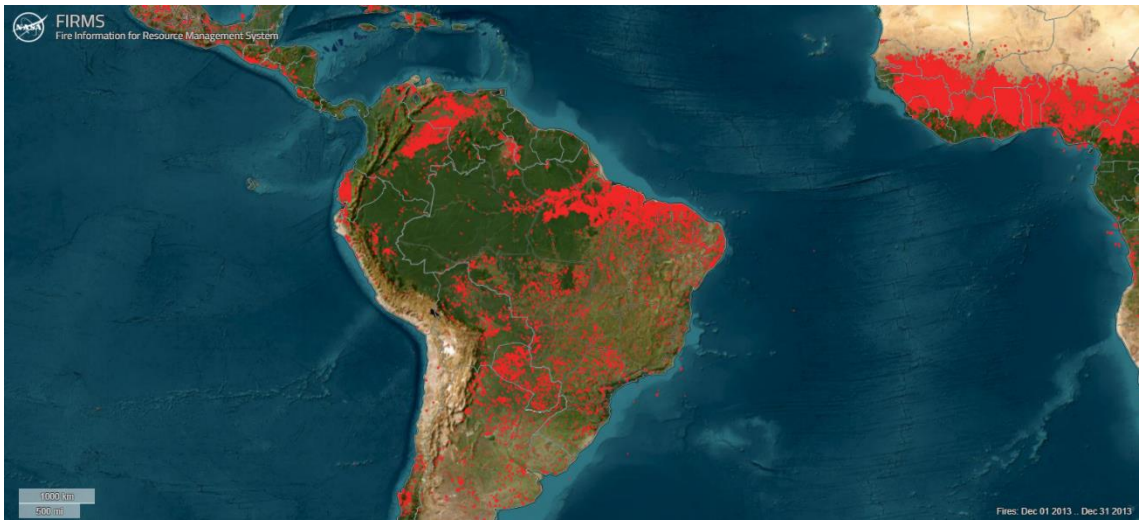

Figure 81 - FIRMS Fire Map of Amazon Forest 1st December to 31st December 2013

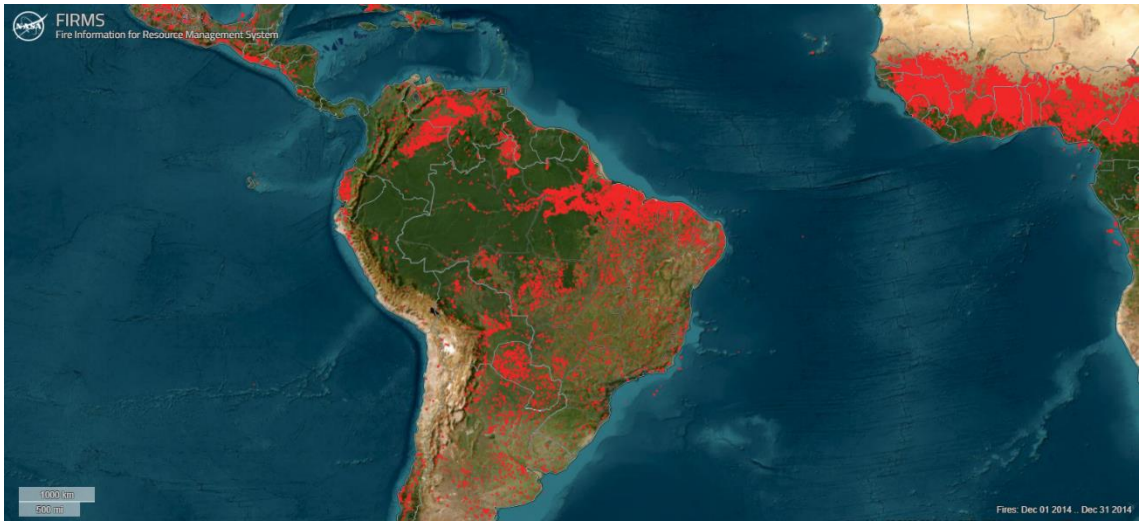

Figure 82 - FIRMS Fire Map of Amazon Forest 1st December to 31st December 2014

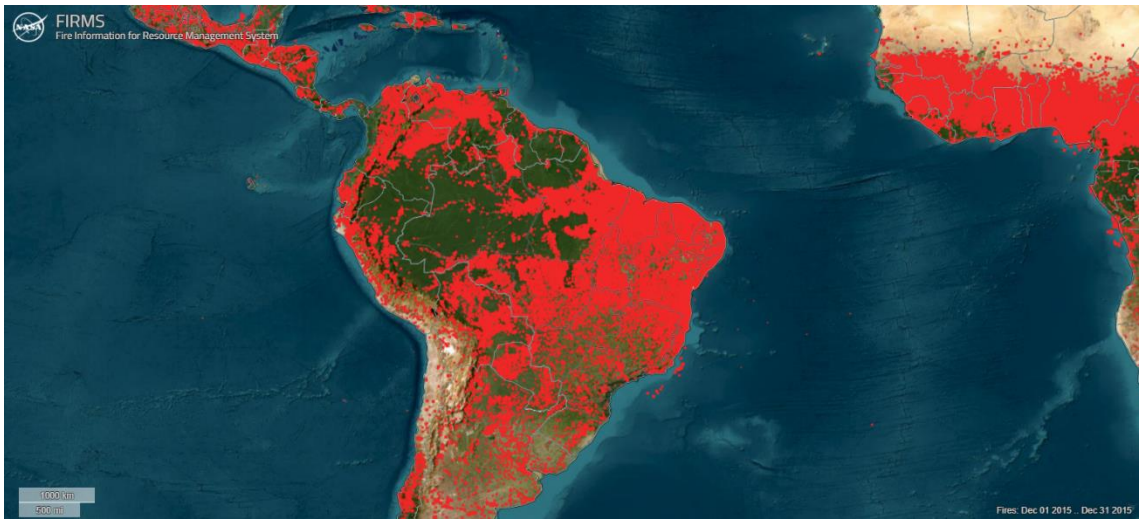

Figure 83 - FIRMS Fire Map of Amazon Forest 1st December to 31st December 2015

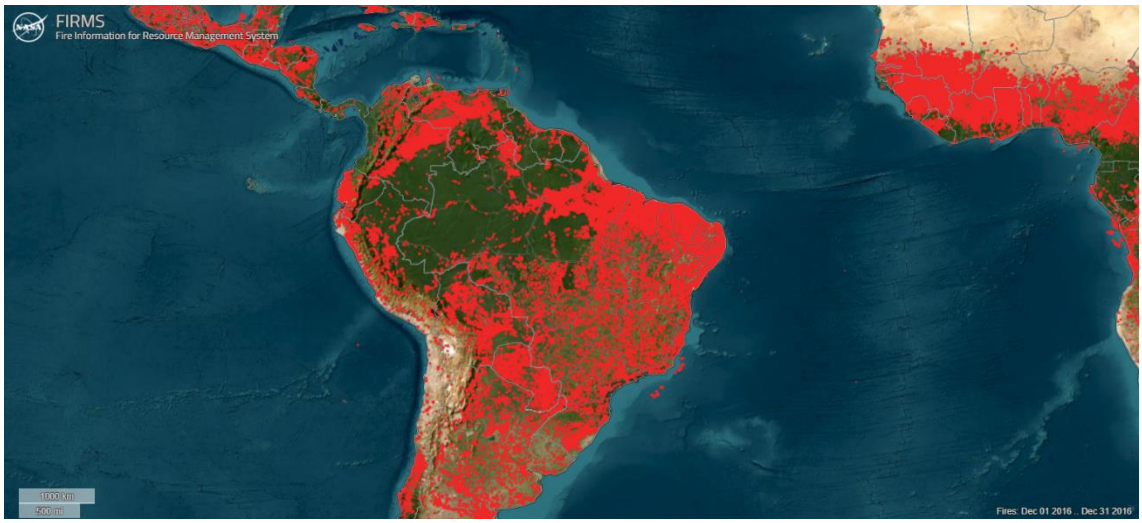

Figure 84 - FIRMS Fire Map of Amazon Forest 1st December to 31st December 2016

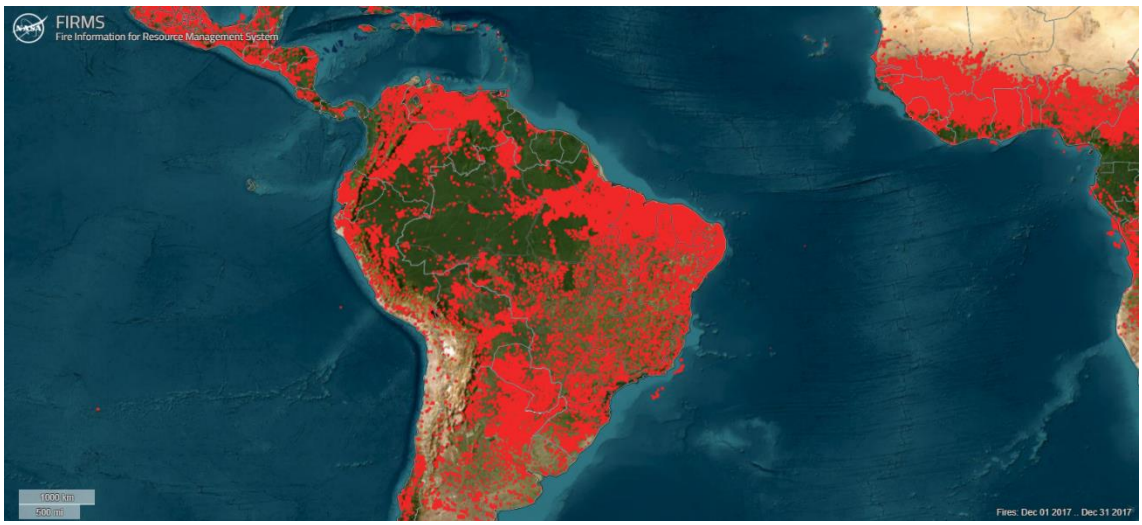

Figure 85 - - FIRMS Fire Map of Amazon Forest 1st December to 31st December 2017

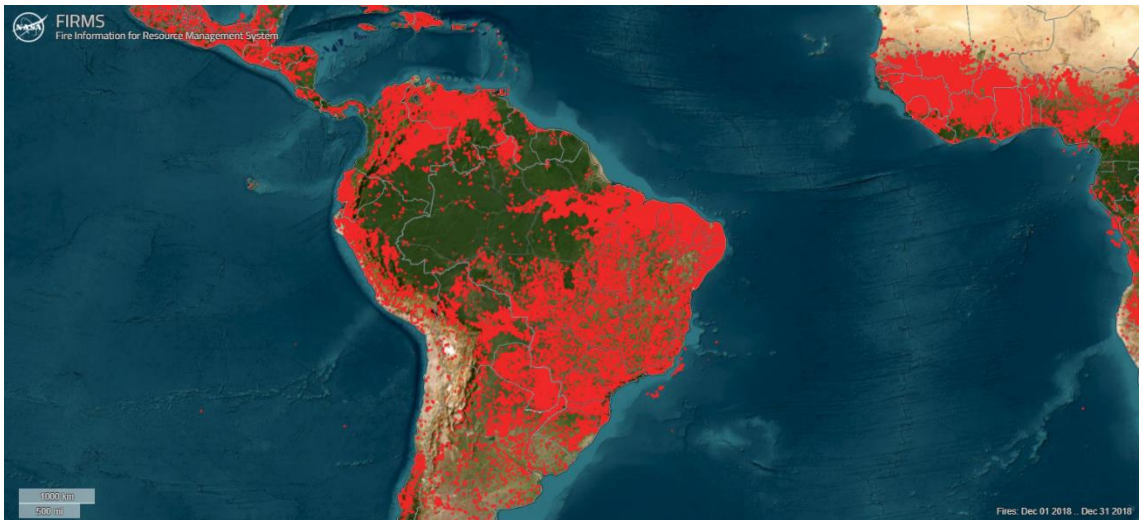

Figure 86 - FIRMS Fire Map of Amazon Forest 1st December to 31st December 2018

Figure 87 - FIRMS Fire Map of Amazon Forest 1st December to 31st December 2019

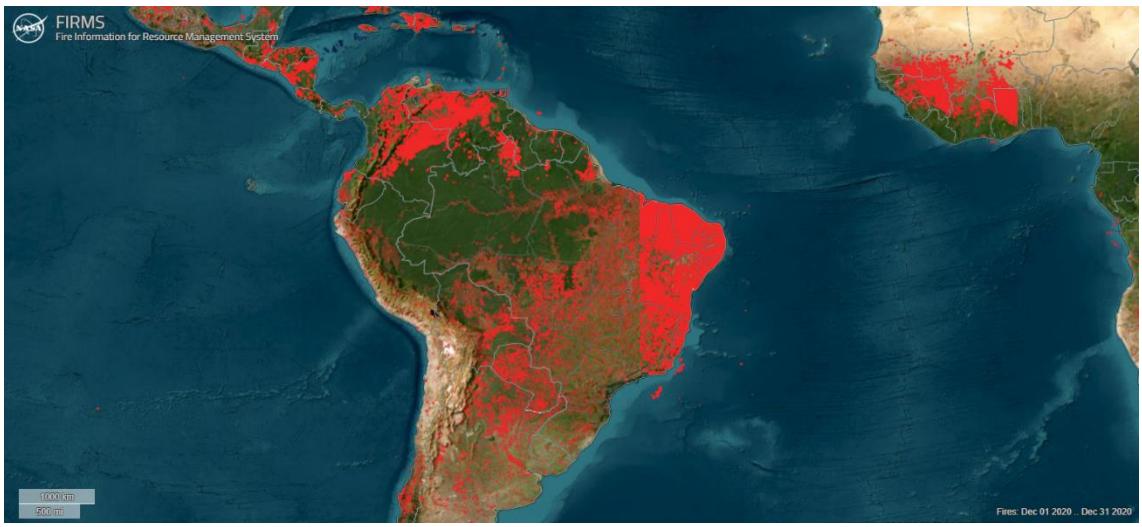

Figure 88 - FIRMS Fire Map of Amazon Forest 1st December to 31st December 2020

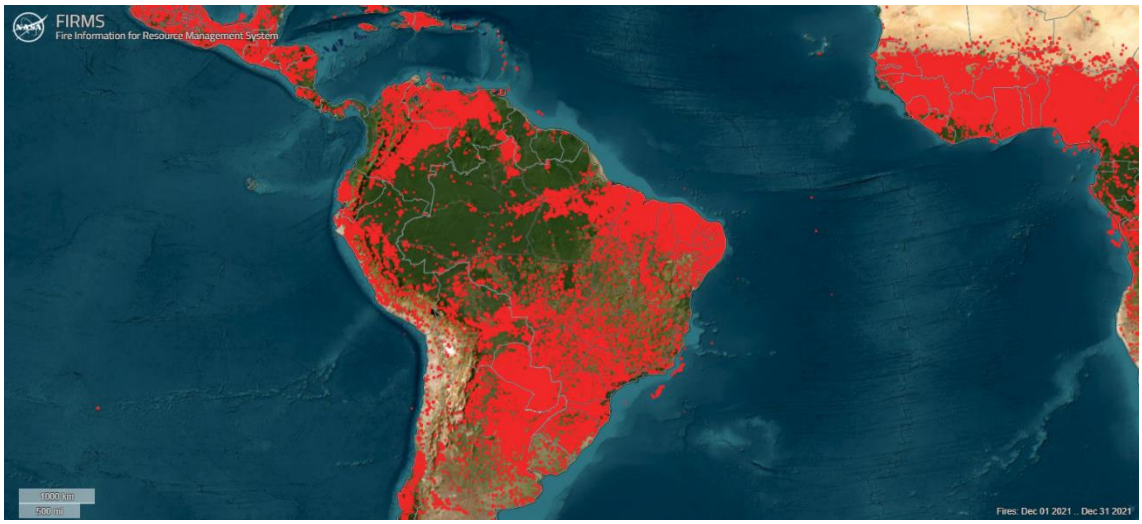

Figure 89 - FIRMS Fire Map of Amazon Forest 1st December to 31st December 2021

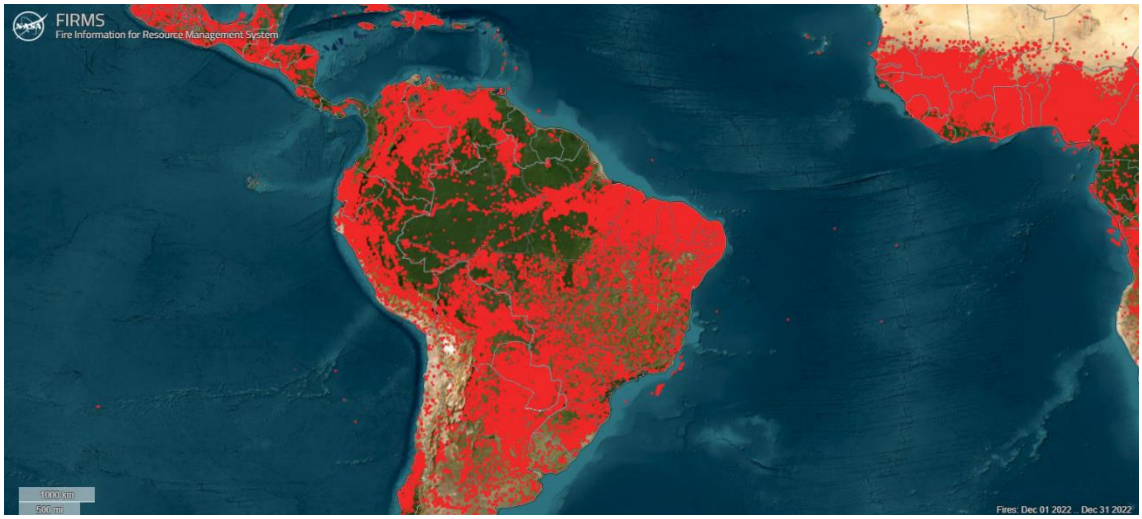

Figure 90 - FIRMS Fire Map of Amazon Forest 1st December to 31st December 2022

The images show FAMFs for month of October in each year since 2001. Comparing the various images, it can be seen that: for December, the highest number of events is recorded in the year 2017 and from 2019 to 2022.

Note that for all three months used for the comparison the years 2019 to 2022 have a significant increase in fires, this could be due to an increase in the data collected because the VIIRS satellite has been in operation since 2012, but more probably it is due to Bolsonaro taking office as President of Brazil.

3.2 Quantitative analysis of firepower of FAMF

Quantitative analysis of FRP and Bright_T31 events of FAMF events was carried out by calculating or identifying the following statistical calculations:

- Maximum Value
- Mean Value
- Standard Deviation Value
- Median value

To correctly describe a variable, it is not sufficient to use a statistical average such as the arithmetic mean or median. These indices, although very important for summarising data, in fact provide only a partial view of the variable you are analysing. You also need to use an index of variability, such as the standard deviation.

One of the combinations most frequently used to describe a quantitative variable is the mean combined with the standard deviation. The mean in fact serves to measure the centre of gravity of the distribution, but it alone is not sufficient to adequately describe the distribution of a quantitative variable. It tells you nothing, in fact, about the variability of the data.

To make up for this shortcoming, there is the standard deviation, which is used precisely to measure how far statistical units are from the mean. In practice, the standard deviation summarises the deviations (or deviations) from the mean.

These two indices are calculated by considering all observations that are part of the sample. A strong skewness or the presence of outliers can greatly increase the value of the mean square deviation and thus distort the results of the analysis. In these situations, it could also happen that the value of the standard deviation is greater than that of the mean. This is not an error, but simply an indication that the statistical units have very different values.

3.2.1 MODIS FRP analysis: Maximum Values

This chapter identifies and analyses through a histogram the maximum annual FRP values concerning the MODIS data.

As explained in Fig. 23 of Chapter 2.12, each annual data package (Shapefiles) was loaded into QGIS and, after opening the table with all attributes, the 'field calculator' command was used to choose which calculation method and data type to perform.

In this case, the command used is "maximum" and was executed for all years from 2001 to 2022. The maximum value data for a specific year, aggregated with date and location information, etc. (Tab.7), was exported individually and combined with the respective results of the following years in a single table (Tab.7).

LATITUDE	LONGITUDE	ACQ_DATE	ACQ_TIME	SATELLITE	INSTRUMENT	CONFIDENCE	BRIGHT_T31 [K]	Max value of FRP [MW]
-14.143	-43.537	01/10/2001	1330	Terra	MODIS	100	321.70	6'955.90
-10.979	-58.885	10/10/2002	1714	Aqua	MODIS	100	306.10	8'005.80
-12.893	-61.744	24/09/2003	1642	Aqua	MODIS	100	307.60	12'414.70
-12.650	-55.487	24/05/2004	1714	Aqua	MODIS	100	293.60	13'290.90
-9.837	-50.532	05/06/2005	1706	Aqua	MODIS	100	304.80	10'900.60
-13.390	-53.999	14/01/2006	1623	Aqua	MODIS	100	306.40	11'777.00
-10.855	-52.317	09/08/2007	1651	Aqua	MODIS	100	332.30	11'499.60
-13.138	-54.959	14/08/2008	1725	Aqua	MODIS	100	314.20	7'958.70
-6.547	-56.100	02/07/2009	1714	Aqua	MODIS	100	310.60	3'970.00
-18.293	-52.970	03/06/2010	1712	Aqua	MODIS	100	318.20	9'783.90
-7.989	-44.275	06/08/2011	1639	Aqua	MODIS	100	302.70	8'016.10
-12.654	-54.824	15/08/2012	1647	Aqua	MODIS	100	314.90	6'691.00
-10.022	-43.688	21/08/2013	1717	Aqua	MODIS	100	307.10	4'858.80
-11.473	-43.339	21/06/2014	1716	Aqua	MODIS	100	339.80	6'433.50
-6.439	-55.272	05/08/2015	1616	Aqua	MODIS	100	309.50	6'785.50
-5.955	-59.965	12/09/2016	1726	Aqua	MODIS	100	317.30	7'836.10
-13.865	-56.757	03/07/2017	1652	Aqua	MODIS	94	330.70	7'295.00
-6.828	-45.710	22/02/2018	1733	Aqua	MODIS	94	318.70	7'303.40
-10.840	-54.035	03/07/2019	1728	Aqua	MODIS	100	341.10	6'980.10
-12.358	-57.424	16/07/2020	1710	Aqua	MODIS	100	317.10	8'589.80
-12.098	-54.520	27/05/2021	1653	Aqua	MODIS	100	315.10	9'722.60
-13.868	-59.624	27/06/2022	1702	Aqua	MODIS	100	325.10	7'118.07

Table 7 - MODIS Maximum Value of FRP for each year, with relative location and information about the instrument

The maximum FRP values of MODIS have been shown in the histogram (Fig.92), which allows a more direct consultation of the trend over the years of this value.

To realise the histogram, the data was transferred to Excel and the histogram was created there.

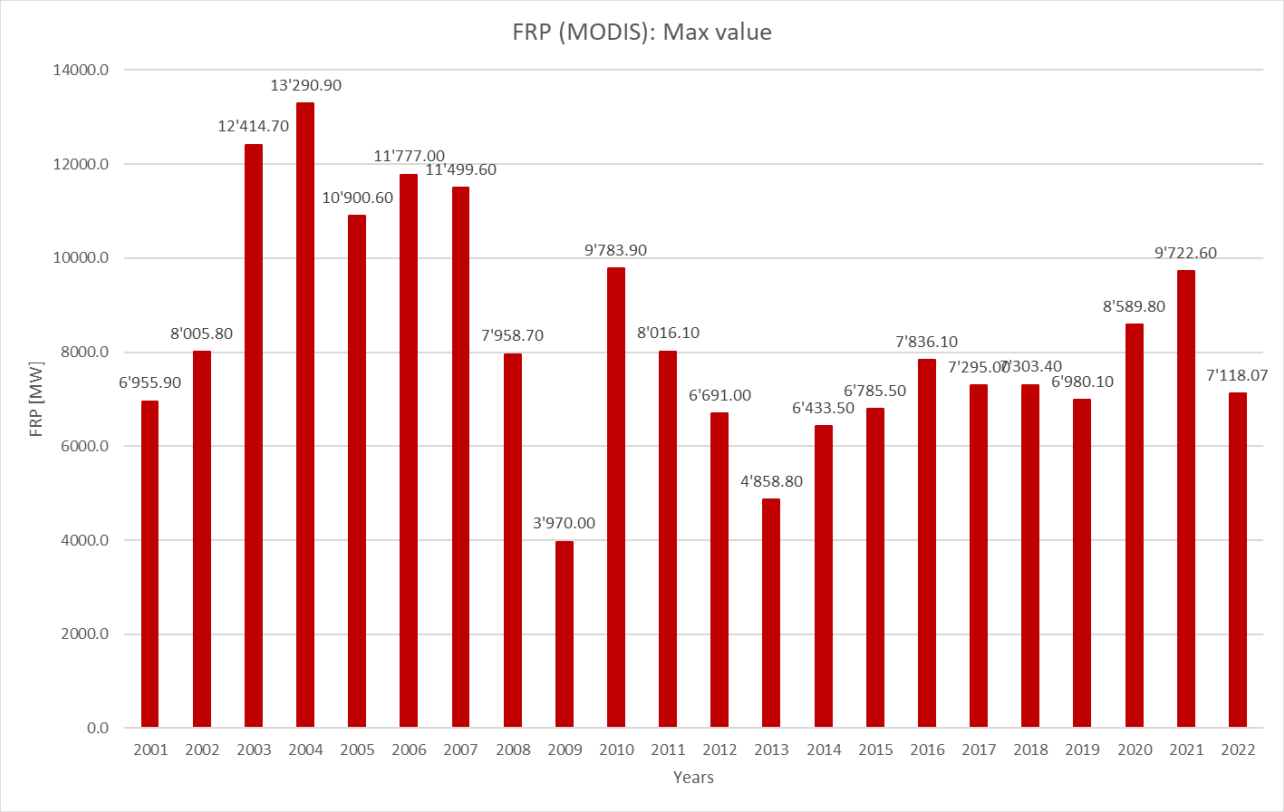

Figure 92-Trend of maximum FRP values detected by MODIS for each year

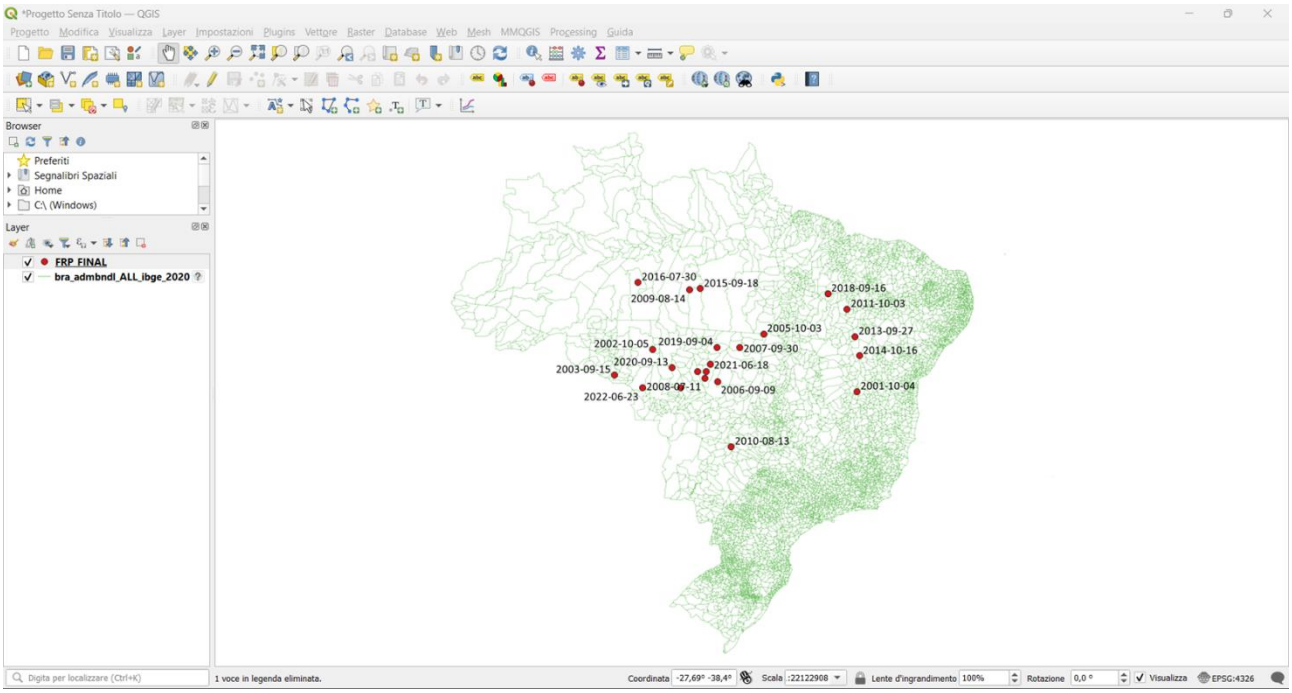

Figure 91 – Location of maximum value of FRP (MODIS)

Maximum FRP values detected from MODIS data, which can be read in the table and histogram, are placed in that imagine, realised in QGIS, with location (point on map) and date of occurrence indicated.

The trend of maximum values, observed in Fig.92 does not give a constant distribution, rather it is possible to see peaks in the years 2004, 2006, 2007, 2010, after 2010 the situation reports a decrease in maximum values of fires and then increases again from 2016, with a peak in 2021.

The years where peaks can be seen correspond to the same years with significant events observed in the qualitative analysis in Chapter 3.1.

The months of August, October, and December were chosen both because of the presence of the dry season but also because as can be seen in the quantitative analysis, in the Tab 7 that discusses the identification of the maximum FRP value, the maximum FRP values occur more or less during those months.

3.2.2 MODIS FRP analysis: Mean Value, Standard Deviation Value and Median Value

In this statistical analysis, the mean value with the corresponding standard deviation value and the median value of the FRP for the MODIS data were calculated, with which graphs were constructed to compare them directly.

As explained in Fig. 23 in Chapter 2.12, each annual data package (Shapefiles) was loaded into QGIS and, after opening the table with all the attributes, the 'field calculator' command was used to choose the FRP data column and apply the “mean” “standard deviation” and “median” operations to it. The operation was repeated for all years 2001 to 2022 of the MODIS measurements.

The mean, the standard deviation and the median data of a specific year were exported individually and combined with the respective results of the following years in a single table (Tab.8).

YEARS	Mean value of FRP [MW]	Standard deviation value of FRP [MW]	Median value of FRP [MW]
2001	36.636	82.123	18.100
2002	56.036	137.850	23.700
2003	55.712	150.367	23.400
2004	59.084	159.571	24.200
2005	57.395	149.665	24.000
2006	52.974	137.656	22.800
2007	54.743	122.506	24.600
2008	50.244	106.607	23.800
2009	41.097	77.702	20.900
2010	54.970	119.478	25.400
2011	46.165	93.131	22.300
2012	49.937	106.969	23.400
2013	41.798	84.159	21.200
2014	45.255	91.776	22.200
2015	47.441	104.660	22.000
2016	43.998	90.282	21.400
2017	47.714	97.296	22.700
2018	42.101	88.929	20.700
2019	49.282	111.446	22.600
2020	52.922	121.696	23.400
2021	54.139	138.138	23.000
2022	47.631	108.937	21.800

Table 8 - Mean value, Standard Deviation value and Median Value of FRP for each year

These data were imported into excel, where the graph in Fig.93 was produced showing the value of the mean FRP and its respective standard deviation.

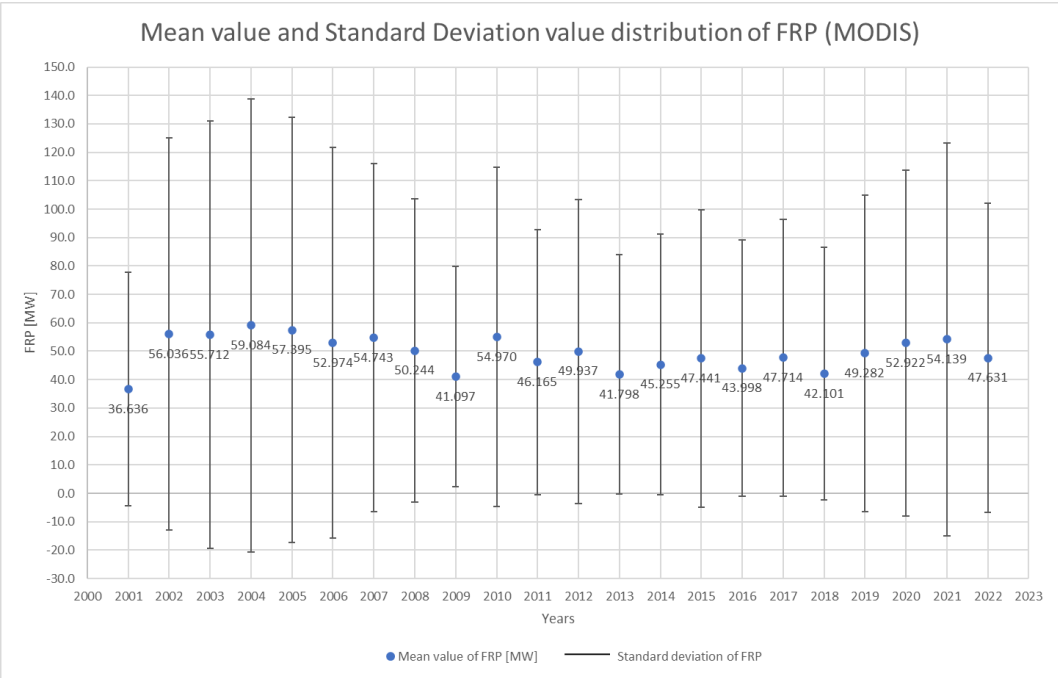

Figure 93 - Annual mean values of FRP with relative distribution of standard deviation (MODIS)

Data in Tab.8 about median value are shown in Fig 94 as histogram, produced in Excel.

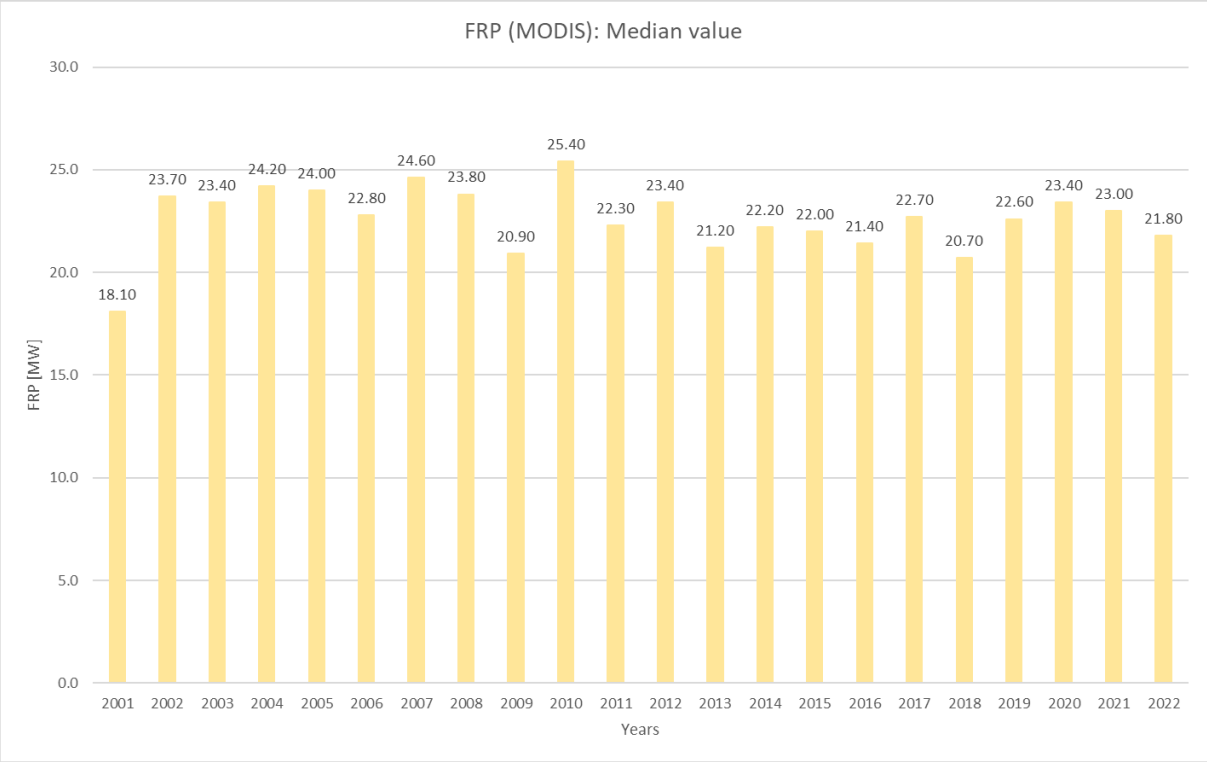

Figure 94 - Trend of median FRP values detected by MODIS for each year

The Fig.93 shows that the mean value of the MODIS FRP values, has an almost constant distribution around 40 MW. The standard distribution (Fig.93) shows a considerable deviation which stands for the presence of very different FRP values. In some cases, the median could be used, instead of the mean, but in this case the low values of the FRP median (Fig.94) confirm the previous statement.

3.2.3 VIIRS SUOMI NPP FRP analysis: Maximum Values

This chapter identifies and analyses through a histogram the maximum annual FRP values concerning the VIIRS SUOMI NPP data.

As explained in Fig. 23 of Chapter 2.12, each annual data package (Shapefiles) was loaded into QGIS and, after opening the table with all attributes, the 'field calculator' command was used to choose which calculation method and data type to perform.

In this case, the command used is "maximum" and was executed for all years from 2012 to 2022. The maximum value data for a specific year, aggregated with date and location information, etc. (Tab.9), was exported individually and combined with the respective results of the following years in a single table (Tab.9).

LATITUDE	LONGITUDE	ACQ_DATE	ACQ_TIME	SATELLITE	INSTRUMENT	CONFIDENCE	BRIGHT_T31 [K]	Max value of FRP [MW]
-11.578	-44.485	04/09/2012	1606	N	VIIRS	l	380.00	1369.96
-12.378	-57.441	21/09/2013	1648	N	VIIRS	l	380.00	1900.97
-12.948	-44.278	25/07/2014	1600	N	VIIRS	l	380.00	1804.80
-2.894	-52.791	15/11/2015	1630	N	VIIRS	l	380.00	1634.04
-12.258	-57.176	19/10/2016	1712	N	VIIRS	h	359.65	1920.15
2.093	-61.230	18/03/2017	1706	N	VIIRS	h	371.74	1725.14
-8.183	-62.886	28/09/2018	1718	N	VIIRS	h	376.12	1626.27
-19.923	-49.238	18/09/2019	1618	N	VIIRS	h	355.61	1282.11
-16.720	-57.398	18/10/2020	1736	N	VIIRS	h	372.01	1945.18
-15.628	-41.686	03/10/2021	1636	N	VIIRS	l	380.00	1319.69
-12.036	-57.461	08/11/2022	1800	N	VIIRS	l	335.39	1585.54

Table 9 - VIIRS SUOMI NPP Maximum Value of FRP for each year, with relative location and information about the instrument

The maximum FRP values of VIIRS SUOMI NPP have been shown in the histogram (Fig.95), which allows a more direct consultation of the trend over the years of this value.

To realise the histogram, the data was transferred to Excel and the histogram was created there.

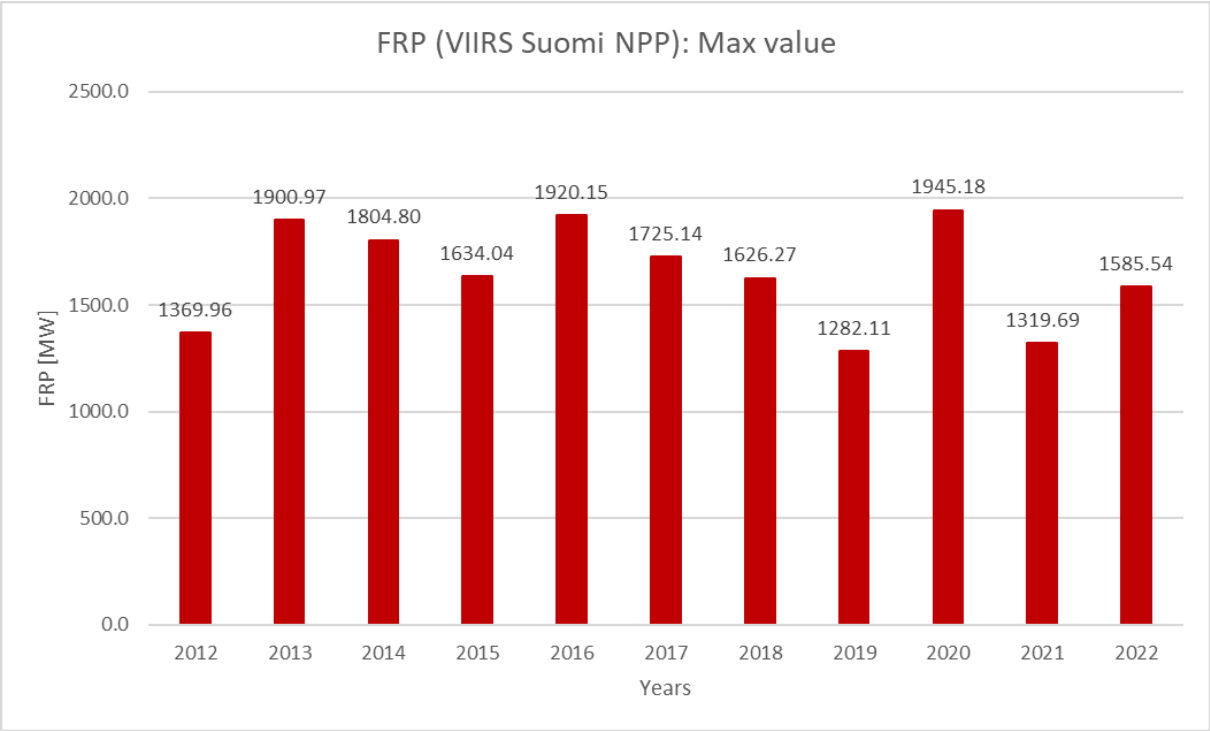

Figure 95 - Trend of maximum FRP values detected by VIIRS SUOMI NPP for each year

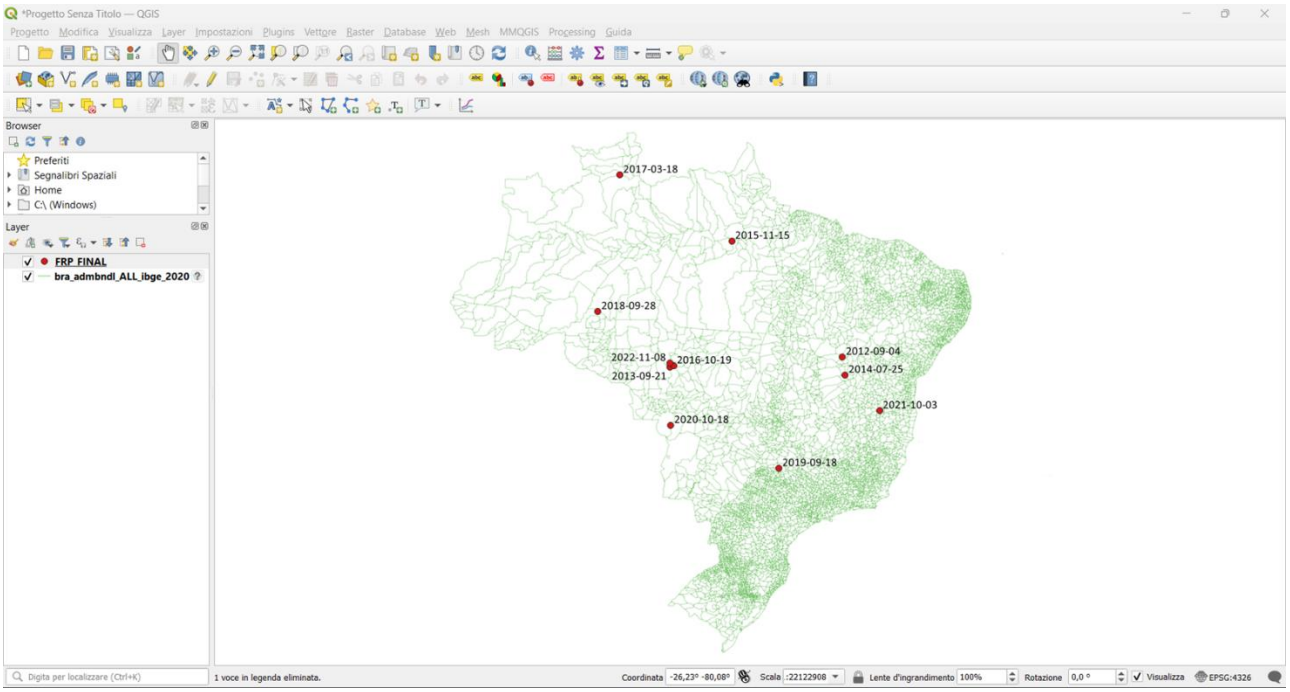

Figure 96 - Location of maximun value of FRP (VIIRS SUOMI NPP)

Maximum FRP values detected from VIIRS SUOMI NPP data, which can be read in the table and histogram, are placed in that imagine, realised in QGIS, with location (point on map) and date of occurrence indicated.

The trend of maximum values, observed in Fig.95, regarding the maximum FRP values of the VIIRS S-NPP shows an almost constant distribution, around the FRP value of 1500 MW.

It is also possible to notice a peak in the values corresponding to the year 2020.

3.2.4 VIIRS SUOMI NPP FRP analysis: Mean Value and Standard Deviation Value distribution

In this statistical analysis, the mean value with the corresponding standard deviation value and the median value of the FRP for the VIIRS S-NPP data were calculated, with which graphs were constructed to compare them directly.

As explained in Fig. 23 in Chapter 2.12, each annual data package (Shapefiles) was loaded into QGIS and, after opening the table with all the attributes, the 'field calculator' command was used to choose the FRP data column and apply the “mean”, “standard deviation” and “median” operations to it. The operation was repeated for all years 2001 to 2022 of the VIIRS S-NPP measurements.

The mean, the standard deviation and the median data of a specific year were exported individually and combined with the respective results of the following years in a single table (Tab.10).

YEARS	Mean value of FRP [MW]	Standard deviation value of FRP [MW]	Median value of FRP [MW]
2012	11.986	24.40	5.72
2013	11.516	21.91	5.94
2014	11.754	23.61	5.78
2015	11.662	24.07	5.50
2016	11.460	22.86	5.61
2017	11.976	24.66	5.68
2018	11.568	23.31	5.78
2019	12.302	25.23	5.83
2020	13.170	27.22	5.98
2021	13.577	29.60	5.90
2022	11.984	24.81	5.55

Table 10 - VIIRS SUOMI NPP: Mean value, Standard Deviation value and Median value of FRP for each year

These data were imported into excel, where the graph in Fig.97 was produced showing the value of the mean FRP and its respective standard deviation.

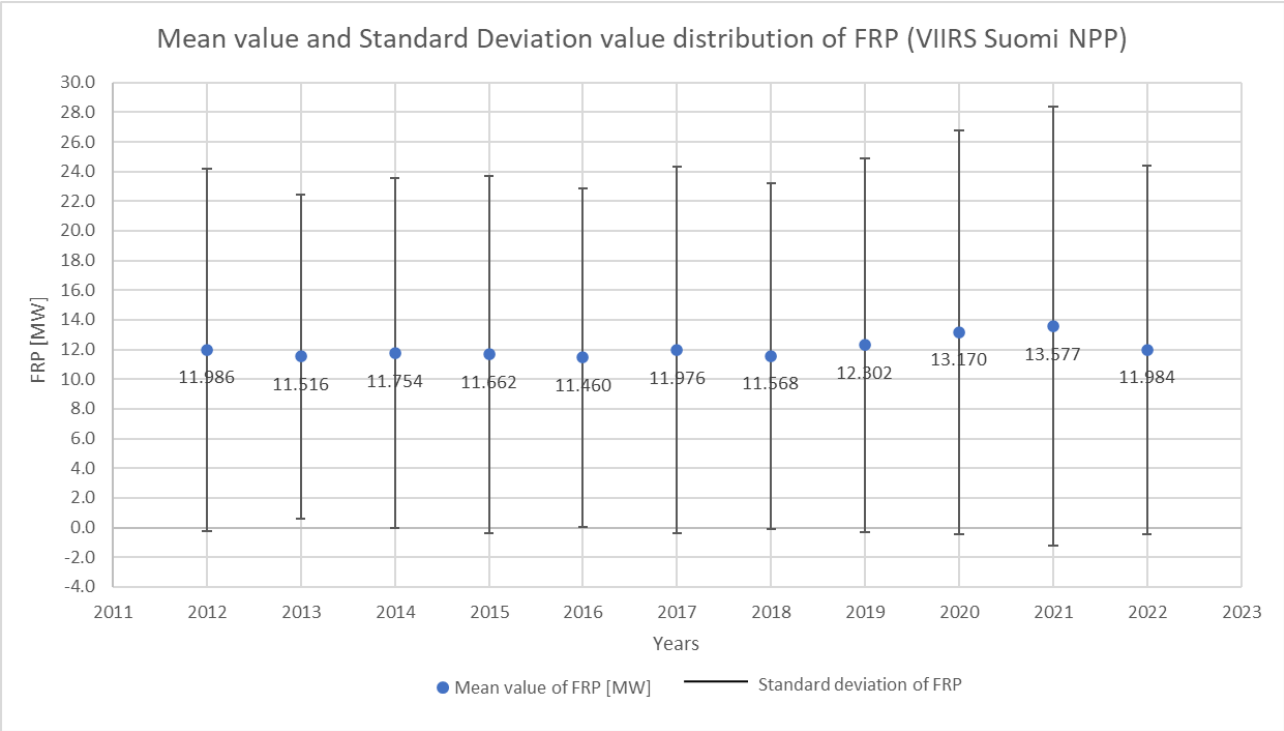

Figure 97 - Annual mean values of FRP with relative distribution of standard deviation (VIIRS SUOMI NPP)

Data in Tab.10 about median value are shown in Fig 98 as histogram, produced in Excel.

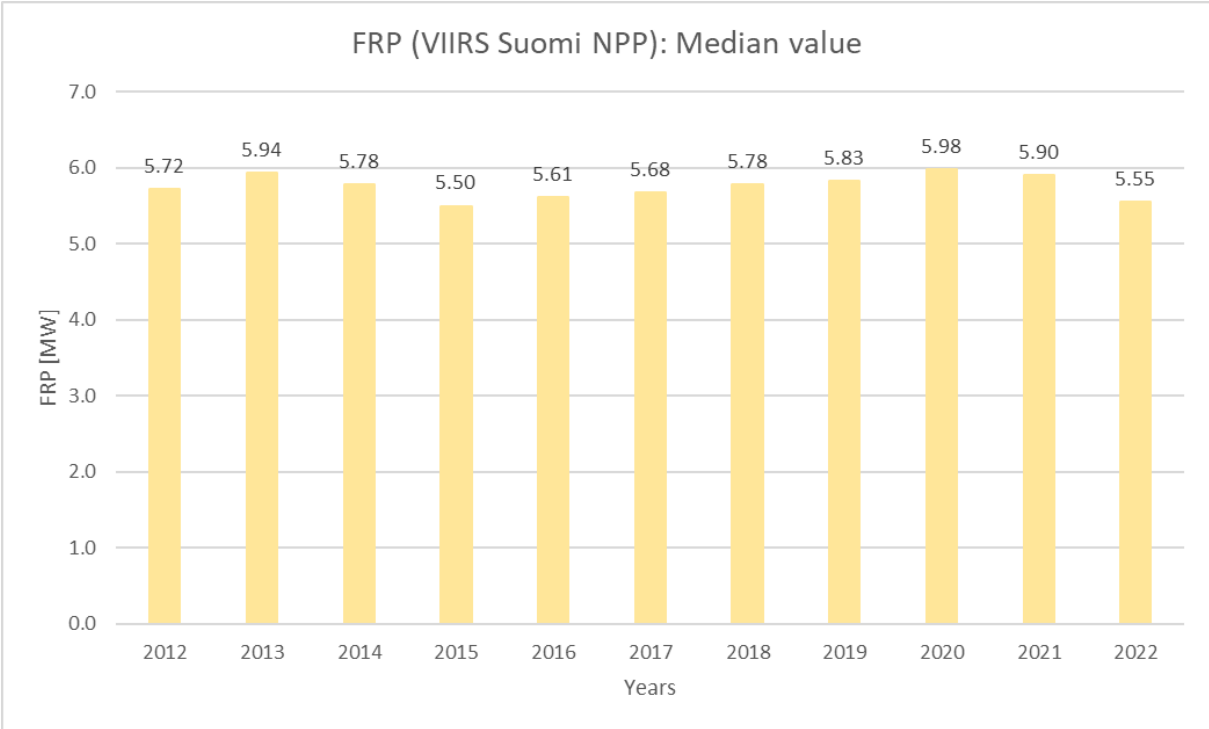

Figure 98 - Trend of median FRP values detected by VIIRS SUOMI NPP for each year

The graph in Fig. 97 shows that the mean value of FRP values of VIIRS S-NPP has an almost constant distribution around 11 MW. Thus, the standard distribution (Fig.97) also turns out to be constant, although with a considerable deviation indicating the presence of very different FRP values. In some cases, the median could be used instead of the mean, but in this case the low FRP median values (Fig. 98) confirm the previous statement.

3.2.5 MODIS Bright_T31 analysis: Mean Value, Standard Deviation Value and Median Value

In this statistical analysis, the mean value and the corresponding standard deviation value and the median value of the Bright_T31 for the MODIS data were calculated, with which graphs were constructed to compare them directly.

As explained in Fig. 23 in Chapter 2.12, each annual data package (Shapefiles) was loaded into QGIS and, after opening the table with all the attributes, the 'field calculator' command was used to choose the Bright_T31 data column and apply the mean", "standard deviation" and "median" operations to it. The operation was repeated for all years 2001 to 2022 of the MODIS measurements.

The mean and standard deviation data of a specific year were exported individually and combined with the respective results of the following years in a single table (Tab.11).

YEARS	Mean value of BRIGHT_T31 [K]	Standard deviation value of BRIGHT_T31 [K]	Median value of BRIGHT_T31 [K]
2001	297.439	7.292	297.400
2002	299.165	7.923	299.000
2003	299.044	7.973	298.900
2004	299.491	8.183	299.300
2005	299.405	7.775	299.400
2006	298.574	7.446	298.700
2007	300.841	8.323	301.100
2008	299.912	8.386	299.700
2009	298.299	7.093	298.400
2010	301.133	8.431	301.500
2011	300.030	8.522	299.900
2012	300.801	8.522	300.900
2013	299.234	7.716	299.100
2014	299.942	8.019	300.000
2015	300.822	8.428	300.100
2016	299.445	7.903	299.200
2017	300.459	8.272	300.100
2018	299.230	7.674	299.000
2019	300.072	7.968	299.700
2020	300.732	8.516	300.200
2021	299.941	8.289	299.500
2022	299.186	7.548	299.000

Table 11 - MODIS: Mean value, Standard Deviation value and Median Value of BRIGHT_T31 for each year

These data were imported into excel, where the graph in Fig.99 was produced showing the value of the mean Bright_T31 and its respective standard deviation.

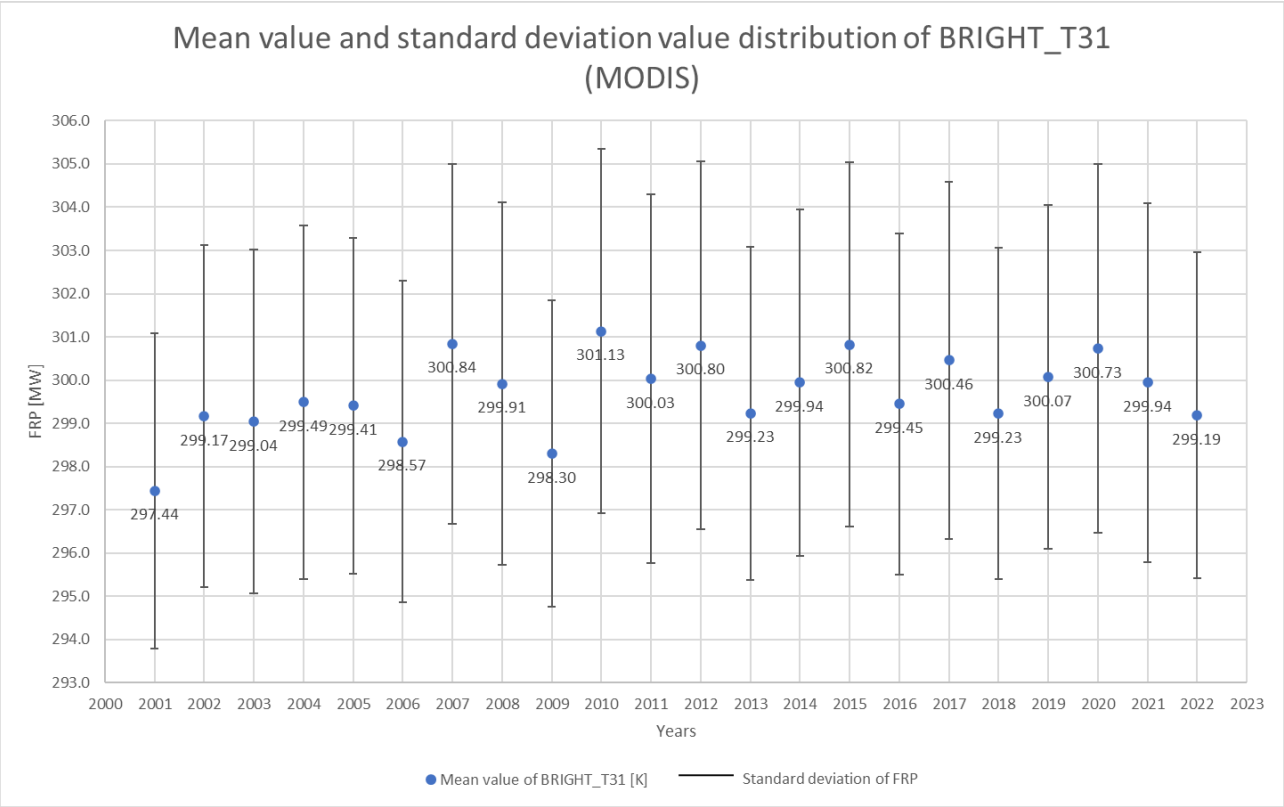

Figure 99 - Annual mean values of BRIGHT_T31 with relative distribution of standard deviation (MODIS)

Data in Tab.11 about median value are shown in Fig 100 as histogram, produced in Excel.

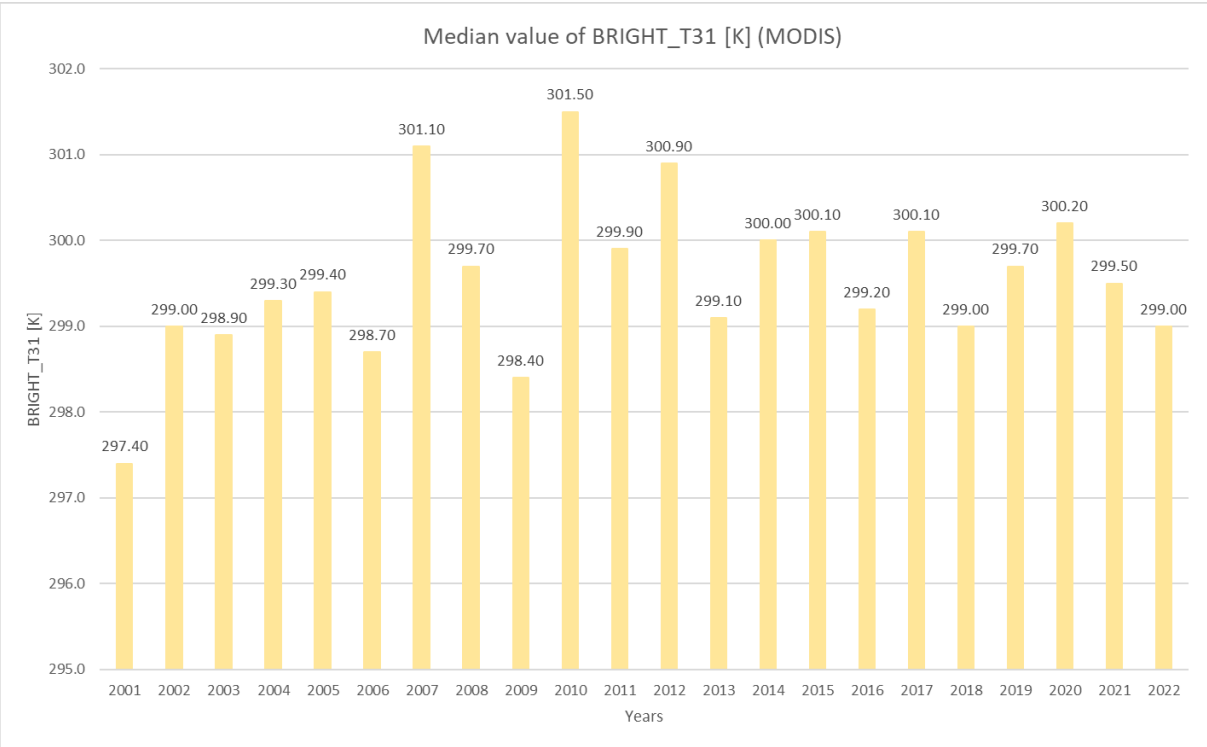

Figure 100 - Trend of median BRIGHT_T31 values detected by MODIS for each year

Statistical analyses of the brightness temperature of the focus pixels for maximum values, of MODIS, indicated channel saturation, so the data are not significant.

The mean values have a more or less constant trend around the value BR_T31=299 K and the standard deviation is also constant for all values, in which case the deviation values are not high, precisely because the Bright_T31 values do not differ greatly from each other.

As for the median, there are peaks in 2007 and 2010, and an increase from 2018 to 2022, but noting the scale of the histogram, the values are quite constant.

3.2.6 VIIRS SUOMI NPP Bright_T31 analysis: Mean Value and Standard Deviation Value Distribution

In this statistical analysis, the mean value and the corresponding standard deviation value and the median value of the Bright_T31 for the VIIRS S-NPP data were calculated, with which graphs were constructed to compare them directly.

As explained in Fig. 23 in Chapter 2.12, each annual data package (Shapefiles) was loaded into QGIS and, after opening the table with all the attributes, the 'field calculator' command was used to choose the Bright_T31 data column and apply the mean", "standard deviation" and "median" operations to it. The operation was repeated for all years 2001 to 2022 of the VIIRS S-NPP measurements.

The mean and standard deviation data of a specific year were exported individually and combined with the respective results of the following years in a single table (Tab.12).

These data were imported into excel, where the graph in Fig.101 was produced showing the value of the mean Bright_T31 and its respective standard deviation.

YEARS	Mean value of BRIGHT_T31 [K]	Standard deviation value of BRIGHT_T31 [K]	Median value of BRIGHT_T31 [K]
2012	299.361	10.201	298.810
2013	297.881	9.459	297.450
2014	298.367	9.699	297.890
2015	299.245	9.759	297.990
2016	297.889	9.838	297.110
2017	298.776	10.086	297.700
2018	297.759	9.484	297.180
2019	298.661	9.778	297.760
2020	299.381	10.517	298.370
2021	298.503	10.284	297.310
2022	297.873	9.690	296.790

Table 12 - VIIRS SUOMI NPP : Mean value and Standard Deviation value of BRIGHT_T31 for each year

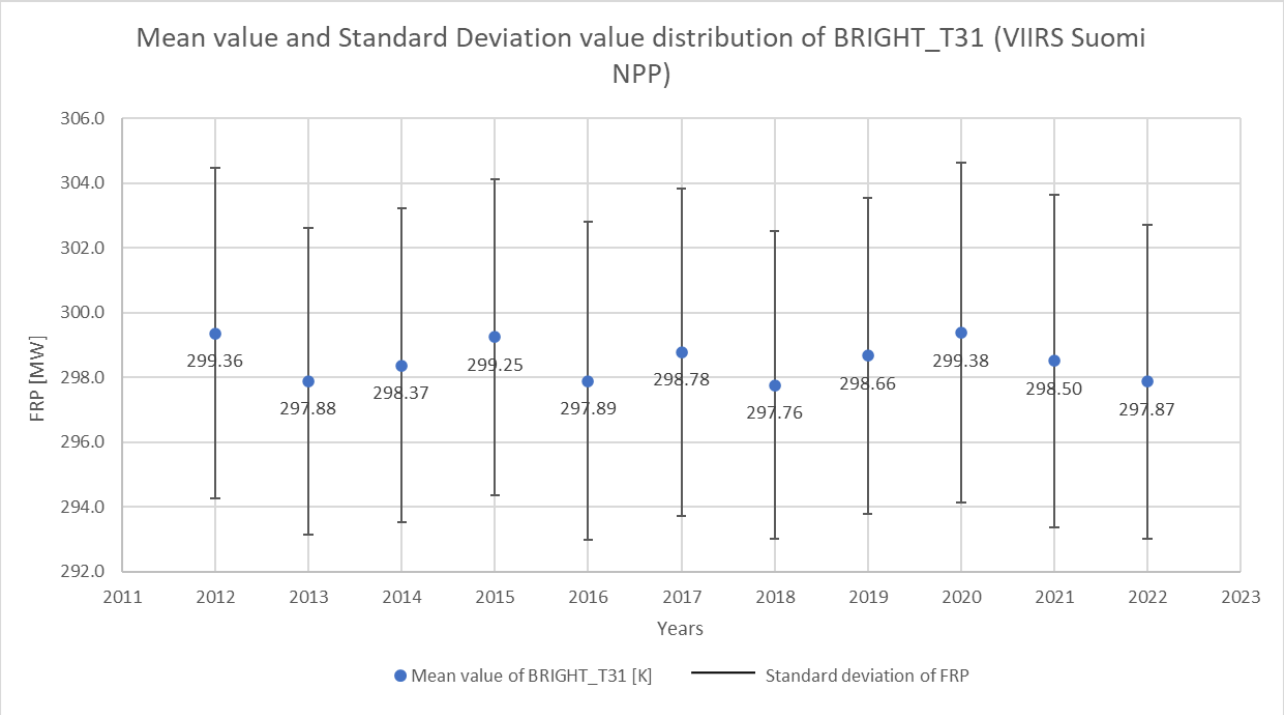

Figure 101 - Annual mean values of BRIGHT_T31 with relative distribution of standard deviation (VIIRS SUOMI NPP)

Data in Tab.12 about median value are shown in Fig 102 as histogram, produced in Excel.

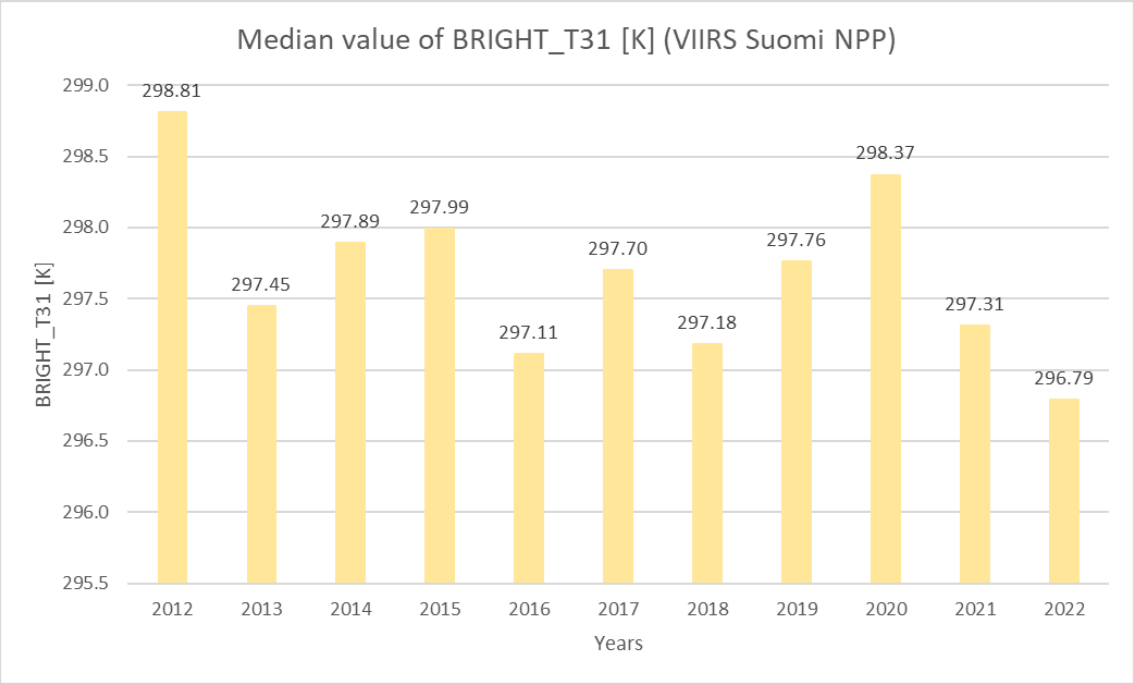

Figure 102 - Trend of median BRIGHT_T31 values detected by VIIRS SUOMI NPP for each year

Statistical analyses of the brightness temperature of the focus pixels for maximum values, of MODIS, indicated channel saturation, so the data are not significant.

The mean values have a more or less constant trend around the value BR_T31=298 K and the standard deviation is also constant for all values, in which case the deviation values are not high, precisely because the Bright_T31 values do not differ greatly from each other.

As for the median, there are peaks in 2012 and 2020, but noting the scale of the histogram, the values are quite constant.

3.3 Analysis of firepower with confidence

The confidence value was added to help users gauge the quality of individual fire pixels is included in the Level 2 fire product. They are different for MODIS and VIIRS.

For MODIS, the confidence value ranges from 0% to 100% and can be used to assign one of the three fire classes (low-confidence fire, nominal-confidence fire, or high-confidence fire) to all fire pixels within the fire mask. In some applications errors of commission (or false alarms) are particularly undesirable, and for these applications one might be willing to trade a lower detection rate to gain a lower false alarm rate. Conversely, for other applications missing any fire might be especially undesirable, and one might then be willing to tolerate a higher false alarm rate to ensure that fewer true fires are missed.

The confidence class assigned to a fire pixel (low, nominal, or high) is determined by thresholding the confidence value (C) calculated for the fire pixel. These thresholds are listed in Table 13.

Range	Confidence Class
0% ≤ C < 30%	Low
30% ≤ C <80%	Nominal
80% ≤ C ≤ 100%	High

Table 13- Fire-pixel confidence classes associated with the confidence level C computed for each fire pixel (FIRMS web portal)

For VIIRS, the confidence values are set to low, nominal, and high; they are based on a collection of intermediate algorithm quantities used in the detection process and are intended to help users gauge the quality of individual hotspot/fire pixels.

Low confidence daytime fire pixels are typically associated with areas of Sun glint and lower relative temperature anomaly (<15 K) in the mid-infrared channel I4. Nominal confidence pixels are those free of potential Sun glint contamination during the day and marked by strong (>15 K) temperature anomaly in either day or night-time data. High confidence fire pixels are associated with day or night-time saturated pixels.

In this section we are going to repeat the statistical analysis but applying a confidence level only to the FRP data, respectively:

- MODIS data ≥ 80 %
- VIIRS SUOMI NPP data = “high”

3.3.1 MODIS FRP analysis with confidence ≥ 80 %: Maximum Value

This chapter identifies and analyses through a histogram the maximum annual FRP values related to the MODIS data after applying the 80% confidence limit.

As explained in Fig. 23 of Chapter 2.12, each annual data package (Shapefiles) was loaded into QGIS, and after opening the table with all attributes, the command "select/filter elements using a form" was used to select all elements according to the necessary value.

In this case 80% (greater than or equal to) was applied to the "confidence" row; the program selects all elements with confidence value greater than or equal to 80, then it is possible to export and save them to another file.

At the new filtered data package, in the "field calculator" command “maximum” was used.

The maximum FRP values of MODIS with C ≥80% have been shown in the histogram (Fig.103), which allows a more direct consultation of the trend over the years of this value.

To realise the histogram, the data was transferred to Excel and the histogram was created there.

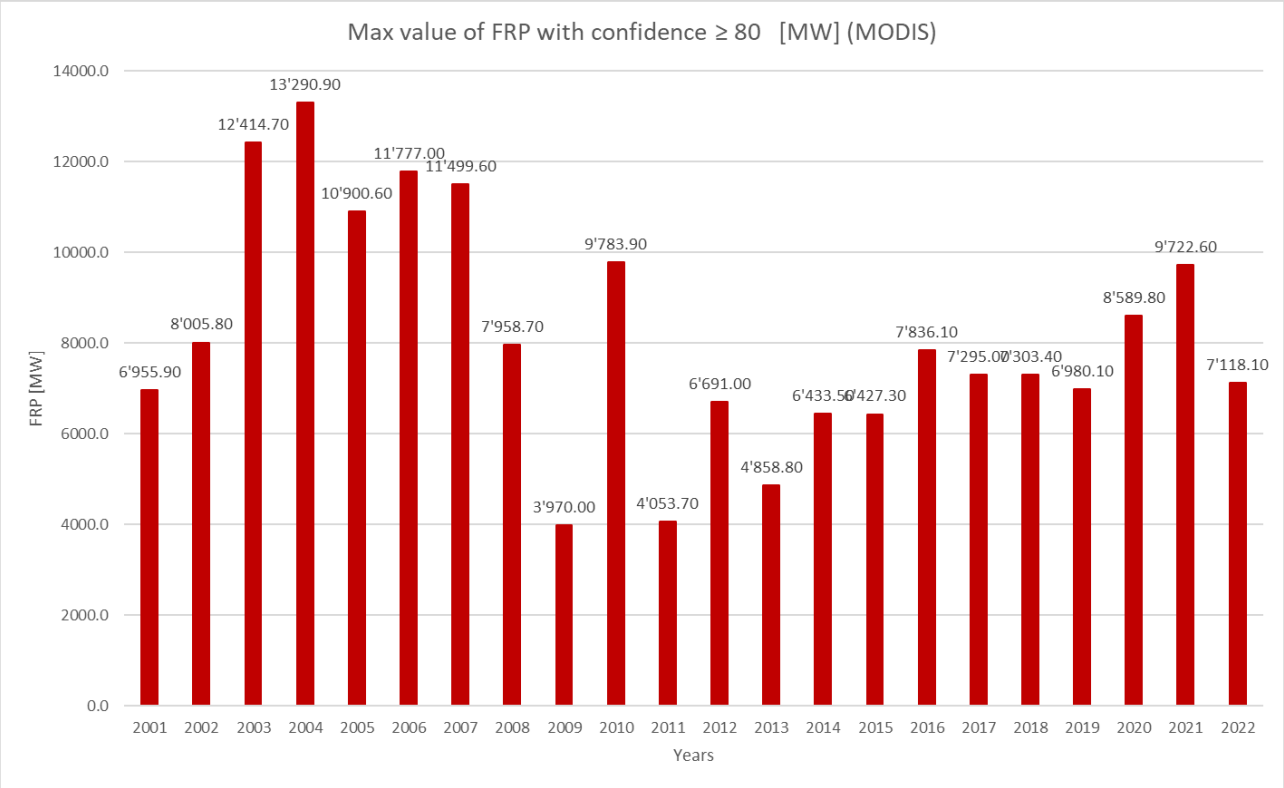

Figure 103 - Trend of maximum FRP values detected by MODIS for each year with confidence level applied

The data involving maximum FRP values are the same as the FRP data without the confidence filtering.

Again, maximum values are reported in the years 2004, 2005, 2006, and then decrease and increase again from 2016 onward, peaking in 2021.

Maximum FRP values detected from MODIS data with applied C ≥ 80 %, which can be read in the table and histogram, are placed in this imagine, realised in QGIS, with location (point on map) and date of occurrence indicated.

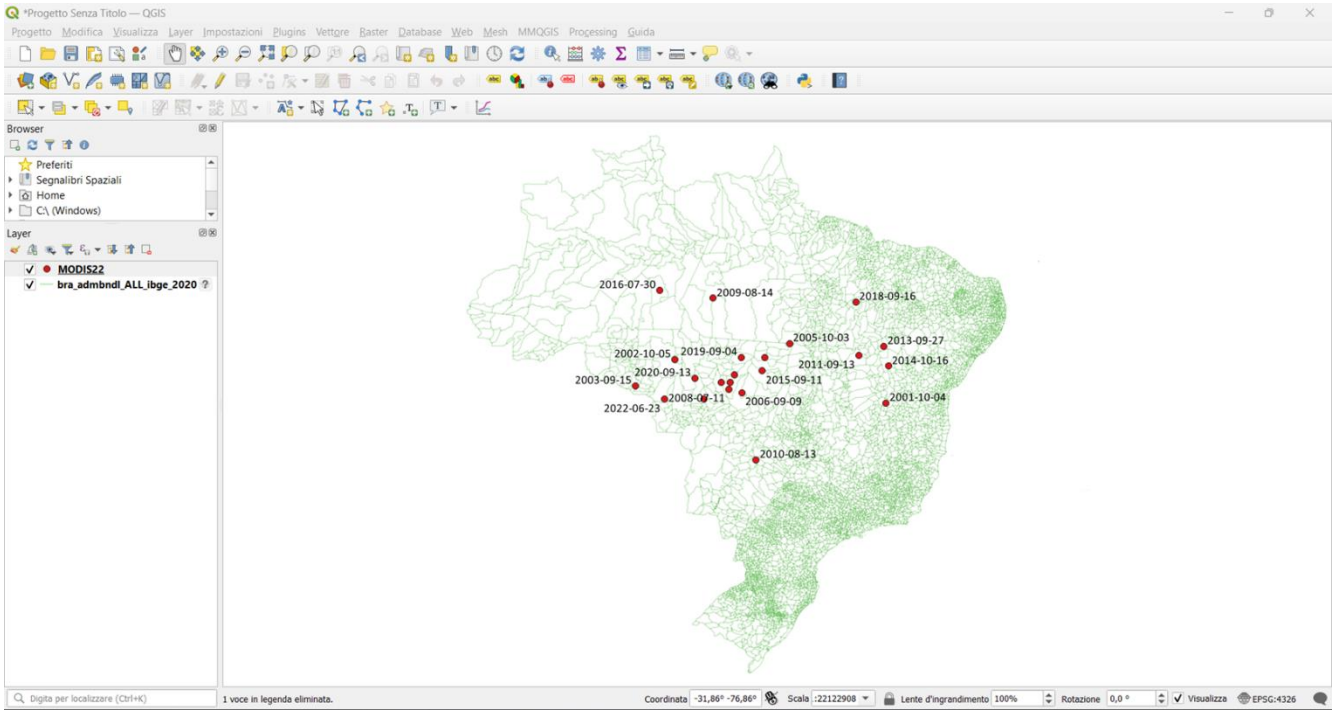

Figure 104 - Location of maximun value of FRP (MODIS) with confidence level applied

3.3.2 MODIS FRP analysis with confidence ≥ 80 %: Mean Value, Standard Deviation Value and Median Value

In this statistical analysis, the mean value and the corresponding standard deviation value and the median value of the FRP for the MODIS data, with applied C ≥ 80%, were calculated, with which a graph was constructed to compare them directly.

As explained above, each annual data package (Shapefiles) was loaded into QGIS, filtered with C ≥ 80%, and, after opening the table with all the attributes, in the 'field calculator' command applied were “mean”, “standard deviation” and “median” on the FRP data column The operation was repeated for all years 2001 to 2022 of the MODIS measurements.

These data were imported into excel, where the graph in Fig.105 was produced showing the value of the mean FRP and its respective standard deviation.

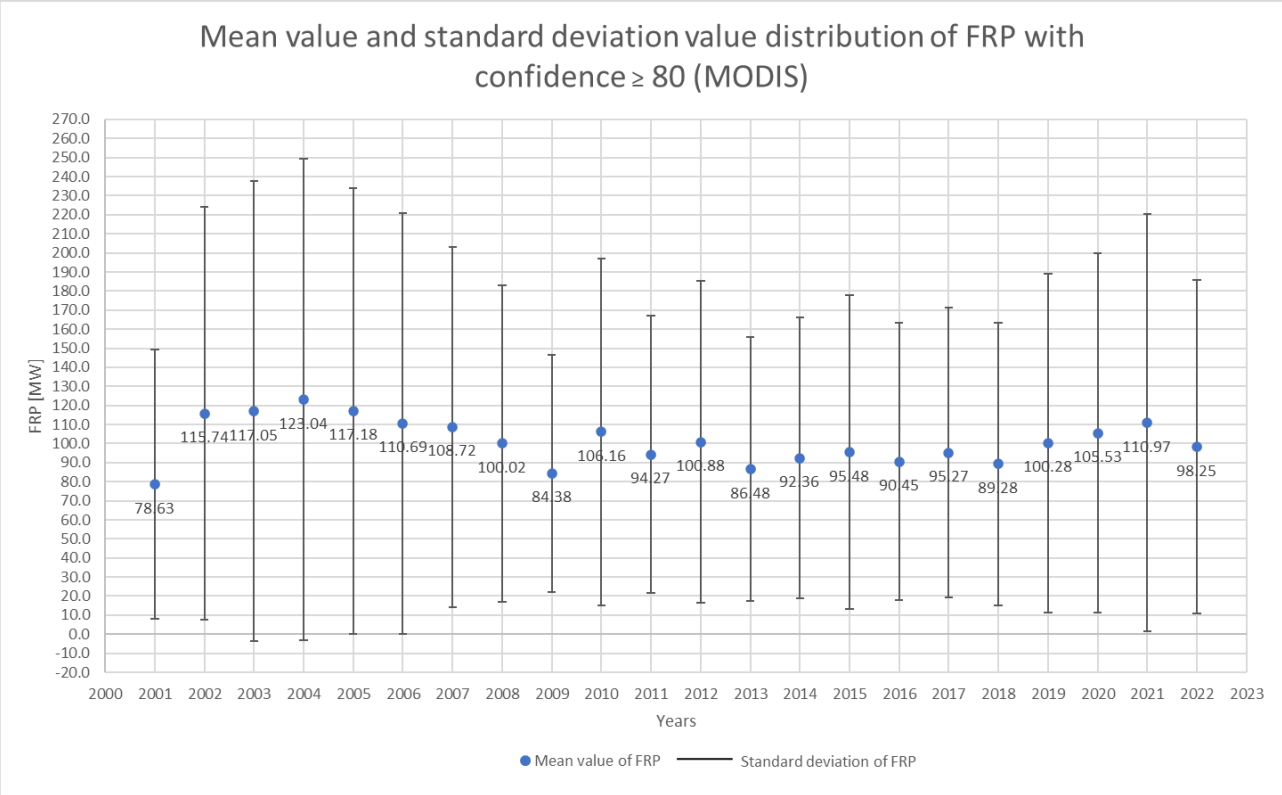

Figure 105 - Annual mean values of FRP (with confidence level applied) with relative distribution of standard deviation (MODIS)

Data about median value are shown in Fig 106 as histogram, produced in Excel.

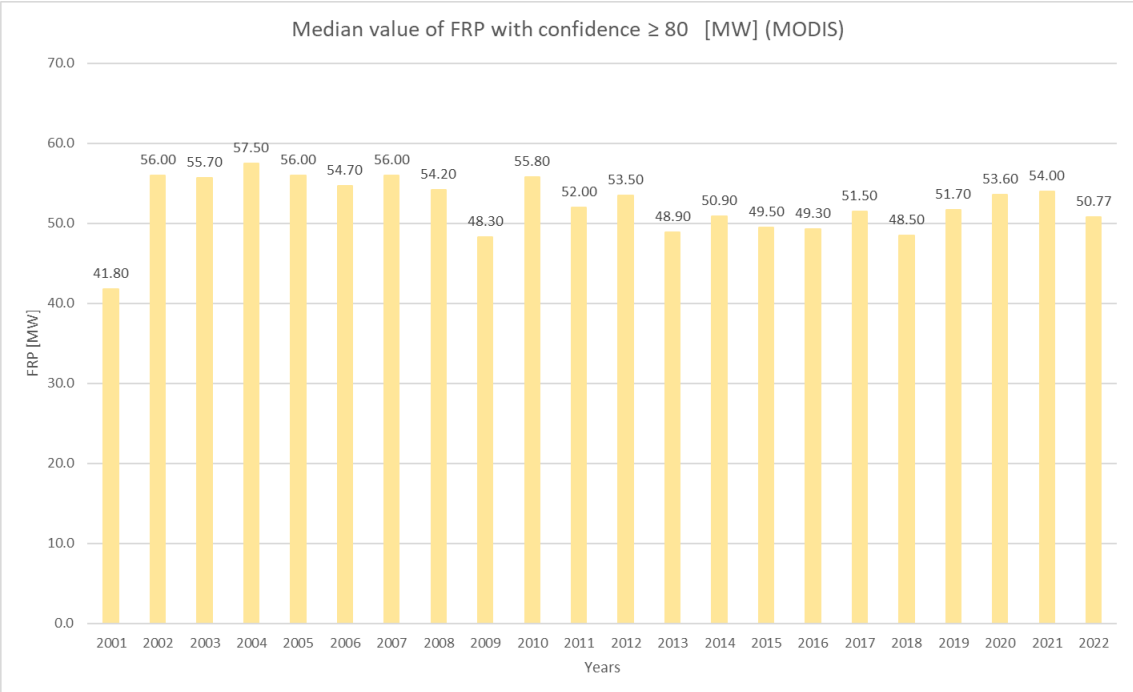

Figure 106 - Trend of median FRP values detected by MODIS for each year with confidence level applied

The confidence filtered FRP mean data follow an almost sinusoidal trend, without being particularly different; the standard deviation, as already observed for the unfiltered data, has a large deviation. The median values have a constant trend, except for 2001.

3.3.3 VIIRS SUOMI NPP FRP analysis with confidence = high: Maximum Value

This chapter identifies and analyses through a histogram the maximum annual FRP values related to the VIIRS SUOMI NPP data after applying the “h” confidence limit.

As explained in Fig. 23 of Chapter 2.12, each annual data package (Shapefiles) was loaded into QGIS, and after opening the table with all attributes, the command "select/filter elements using a form" was used to select all elements according to the necessary value.

In this case “high” (equal or not) was applied to the "confidence" row; the program selects all elements with confidence value equal to “h”, then it is possible to export and save them to another file.

At the new filtered data package, in the "field calculator" command “maximum” was used.

The maximum FRP values of VIIRS SUOMI NPP, with C = high, have been shown in the histogram (Fig.107), which allows a more direct consultation of the trend over the years of this value.

To realise the histogram, the data was transferred to Excel and the histogram was created there.

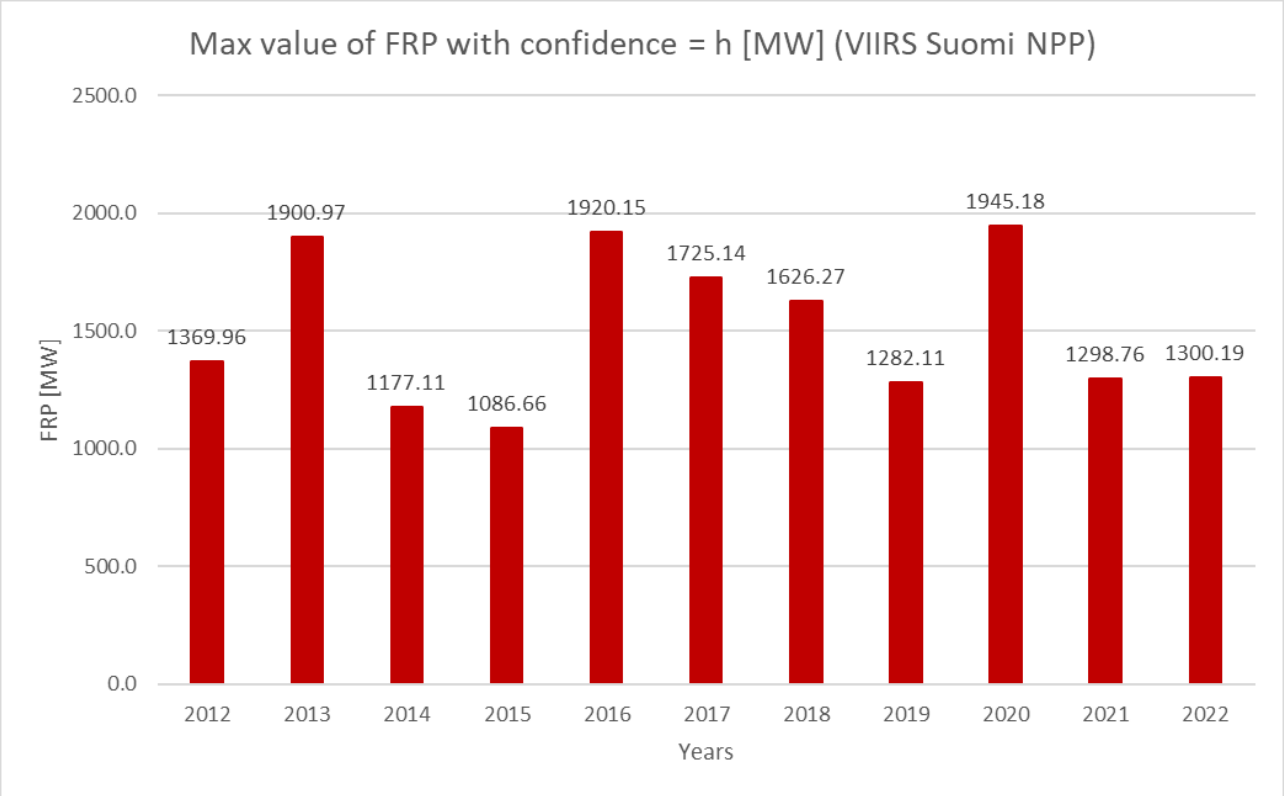

Figure 107 - Trend of maximum FRP values detected by VIIRS SUOMI NPP for each year with confidence level applied

Maximum FRP values detected from MODIS data with applied C = high, which can be read in the table and histogram, are placed in Fig.108, realised in QGIS, with location (point on map) and date of occurrence indicated.

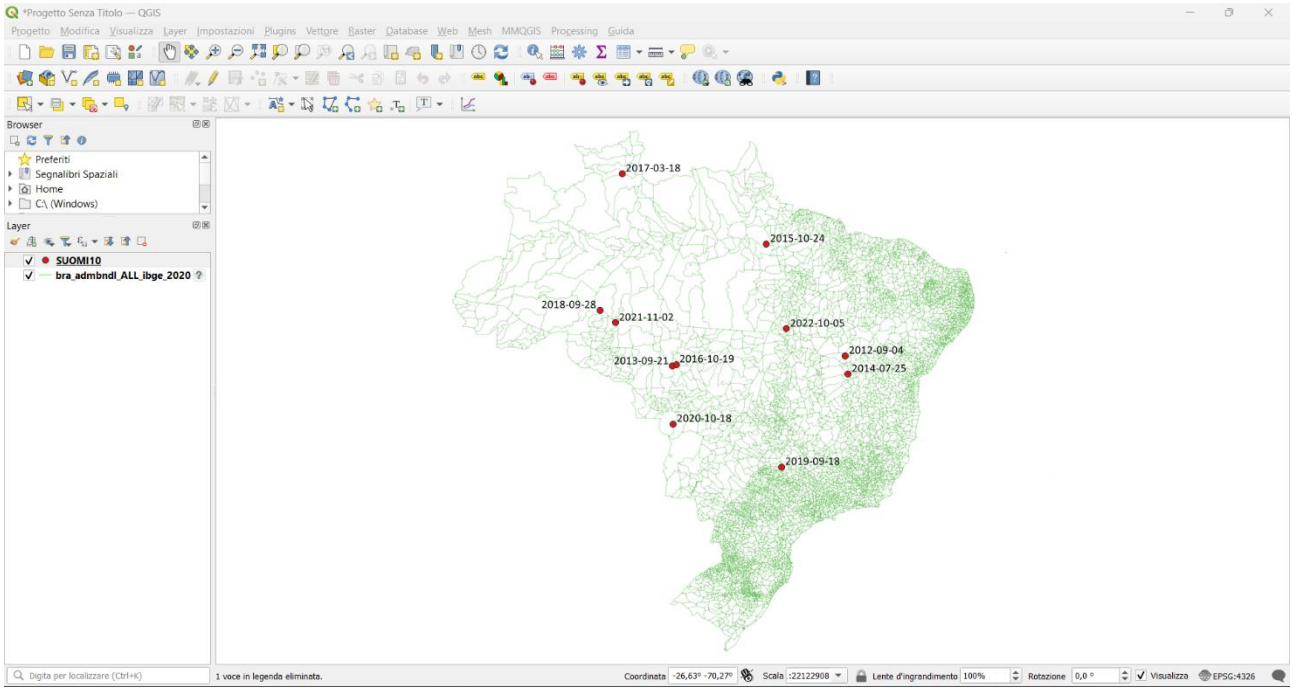

Figure 108 - Location of maximun value of FRP (VIIRS SUOMI NPP)

In Section 3.2.3, the trend of FRP VIIRS maximum values was shown to be fairly constant, the application of confidence in this case (Fig.107), unlike in MODIS, showed a change in the trend of maximum values that is not constant over the years and shows peaks in the years 2013, 2016, 2020.

3.3.4 VIIRS SUOMI NPP FRP analysis with confidence = high: Mean Value, Standard Deviation Value and Median Value

In this statistical analysis, the mean value and the corresponding standard deviation value and the median value of the FRP for the VIIRS SUOMI NPP data, with applied C = high, were calculated, with which a graph was constructed to compare them directly.

As explained above, each annual data package (Shapefiles) was loaded into QGIS, filtered with C = high, and, after opening the table with all the attributes, in the 'field calculator' command applied were “mean”, “standard deviation” and “median” on the FRP data column. The operation was repeated for all years 2012 to 2022 of the VIIRS SUOMI NPP measurements.

These data were imported into excel, where the graph in Fig.109 was produced showing the value of the mean FRP and its respective standard deviation.

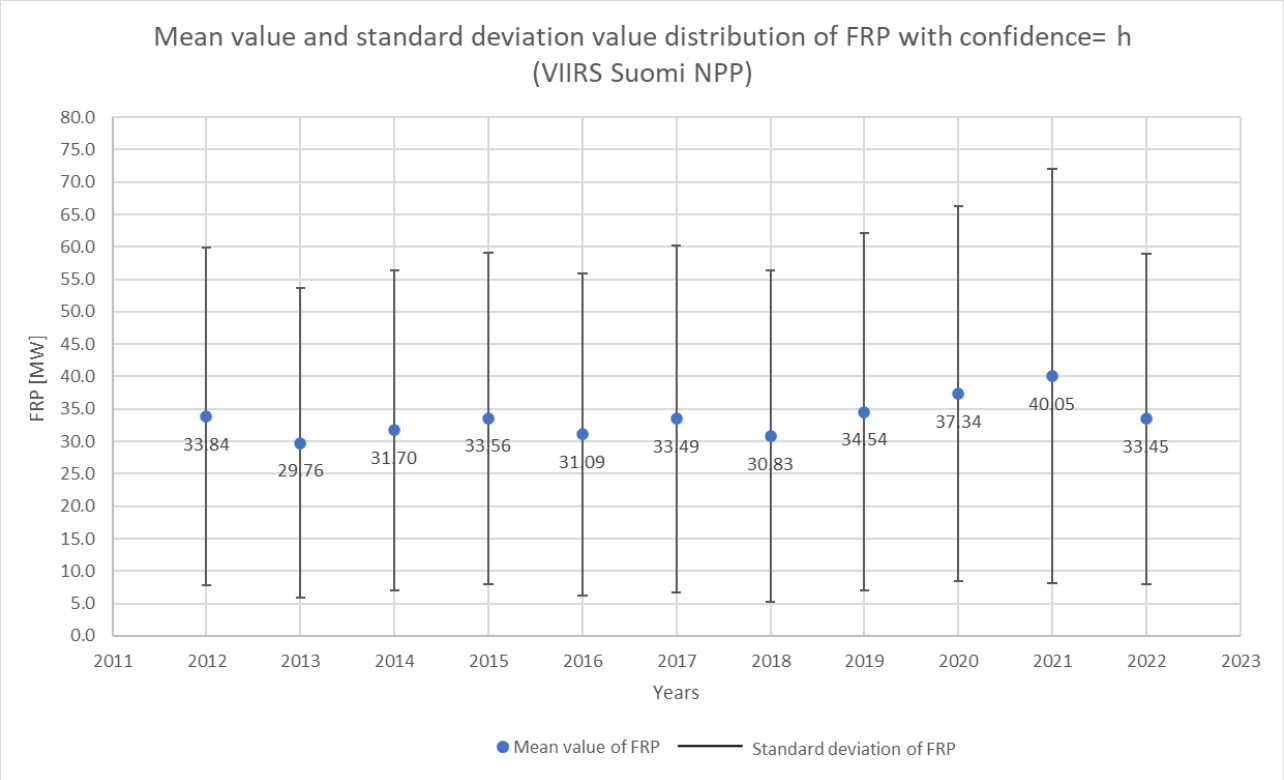

Figure 109 - Annual mean values of FRP (with confidence level applied) with relative distribution of standard deviation (VIIRS SUOMI NPP)

Data about median value are shown in Fig 110 as histogram, produced in Excel.

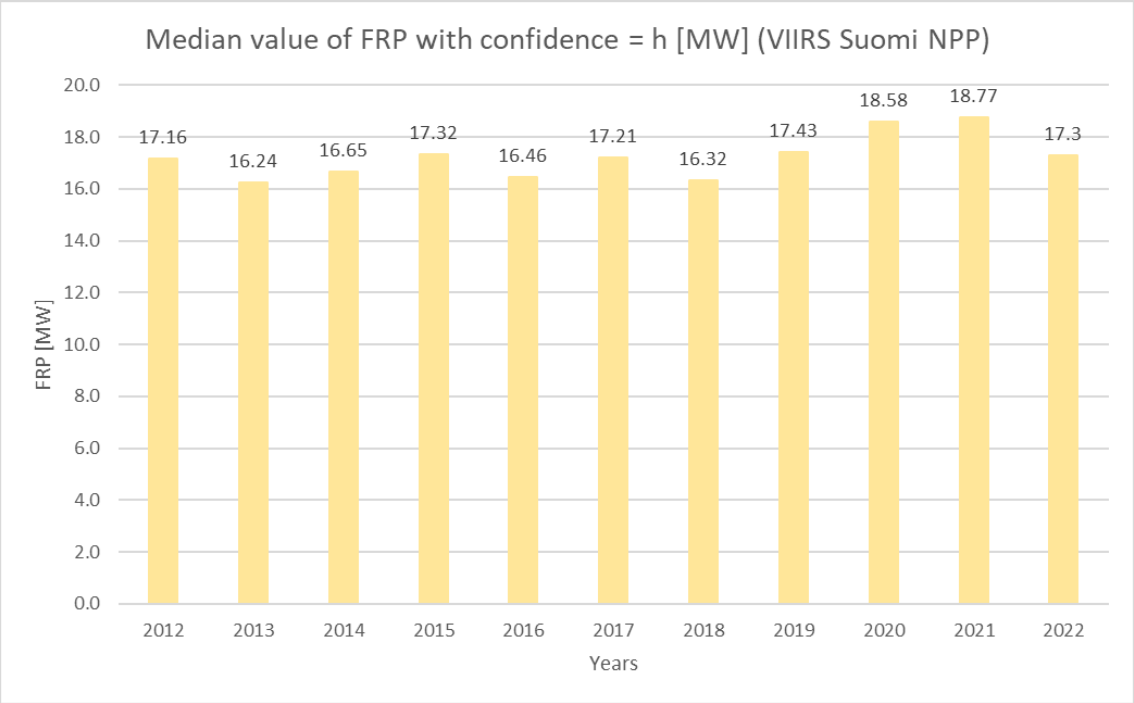

Figure 110 - Trend of median FRP values detected by VIIRS SUOMI NPP for each year with confidence level applied

In contrast to the maximum values (Fig.107), the trend of the mean values of the VIIRS FRP, standard deviation and median is constant (Fig.109 and Fig.110).

The standard deviation (Fig.109) continues to express a strong deviation despite filtering.

3.4ANALYSIS OF FIRE POWER: CLASSIFICATION OF VALUES

In order to know:

- the power of the fires,
- the quantity of all events detected based on FRP data,
- the quantity of the most powerful fires

a division into 10 classes of FRP values was carried out, both for files with and without a confidence interval.

FRP CLASSES									
0-10	10-20	20-50	50-80	80-100	100-200	200-300	300-700	700-100	1000-MaxValue

Table 14 - Classes used in the FRP value division

The number of events for each class in each year will be counted. This part was carried out in QGIS entirely.

3.4.1 MODIS DATA ANALYSIS: FRP classification

The following table shows for each year and for each class the corresponding number of events about MODIS FRP data.

Years	Number of events	FRP classes										Max Value
	[10^3]	0 - 10	10 -20	20 -50	50 -80	80 - 100	100 - 200	200 - 300	300 - 700	700 - 1000	1000 - MAX	
2001	145.72	34'600	45'164	42'569	11'673	3'523	6'198	1'541	1'241	145	126	6'955.90
2002	524.22	86'513	142'625	166'028	54'373	18'467	35'164	10'589	10'155	1'642	1'930	8'005.50
2003	548.39	93'047	149'803	172'855	56'626	19'118	35'930	10'799	10'027	1'679	2'044	12'414.70
2004	634.51	103'828	168'834	201'103	66'900	22'643	43'819	13'323	12'997	2'235	2'765	13'290.90
2005	631.83	105'244	168'377	199'298	66'243	22'438	43'824	13'365	12'549	2'058	2'359	10'900.60
2006	406.65	70'639	113'354	127'429	40'830	13'801	26'216	7'561	7'162	1'091	1'227	11'777.00
2007	700.53	111'717	185'610	223'736	76'565	26'104	49'758	14'497	13'046	1'966	1'897	11'499.60
2008	354.52	57'544	96'708	114'528	38'026	12'765	23'632	6'619	5'507	735	656	7'958.70
2009	250.52	46'922	74'856	79'723	23'848	7'379	13'130	3'265	2'533	328	217	3'970.00
2010	583.69	88'476	151'965	189'262	66'090	22'431	43'019	12'396	10'918	1'532	1'359	9'783.90
2011	271.30	47'044	77'645	86'563	27'651	8'963	16'405	4'432	3'589	469	369	8'016.10
2012	402.21	67'329	110'473	129'421	42'023	14'137	26'091	7'301	6'234	914	796	6'691.00
2013	220.41	40'620	65'146	70'796	21'248	6'732	11'673	2'885	2'191	301	232	4'858.80
2014	311.35	54'079	89'602	100'373	31'146	10'210	18'278	4'833	3'915	490	423	6'433.50
2015	419.83	77'743	117'921	131'997	41'222	13'827	25'032	7'140	6'035	875	770	6'785.50
2016	334.35	63'403	96'530	105'121	32'349	10'441	18'732	4'916	4'168	516	421	7'836.10
2017	389.24	69'266	107'890	123'178	39'855	13'131	24'592	6'781	5'757	760	548	7'295.00
2018	231.85	45'235	68'600	72'868	21'508	6'860	12'024	3'235	2'500	333	278	7'303.40
2019	374.67	65'935	104'412	118'920	38'340	12'561	23'112	6'465	5'650	851	823	6'980.10
2020	405.39	68'546	110'779	127'614	42'128	14'457	27'133	8'000	7'226	1'072	1'084	8'589.80
2021	340.58	60'630	93'200	104'873	34'537	11'813	22'479	6'810	6'445	936	1'040	9'722.60
2022	362.03	67'078	102'546	113'149	35'535	11'715	21'232	5'837	5'189	772	765	7'118.07

Table 15 - Number of events for each class in each year of the MODIS FRPs

In the second column it is possible to see the total number of events, the other columns of the tab. 15 show how many events there were for each class in each year.

The division into classes (Tab.15) draws attention to the high presence of low FRP values, i.e. the predominance of FRP values between 0 and 30 MW or otherwise the predominance of FRP values in the range 0<FRP<100 [MW].

On the following pages, it is possible to see a histogram for each year describing the trend of the quantity of FRPs events detected, according to the division into classes concerning the MODIS data, and the same events on the map given by QGIS divided by colours according to the FRPs classes.

FRP classification representation

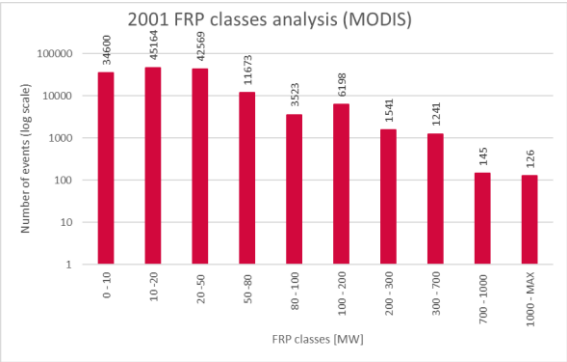

Figure 111 - Histogram describing the trend of the MODIS FRPs classes in the year 2001

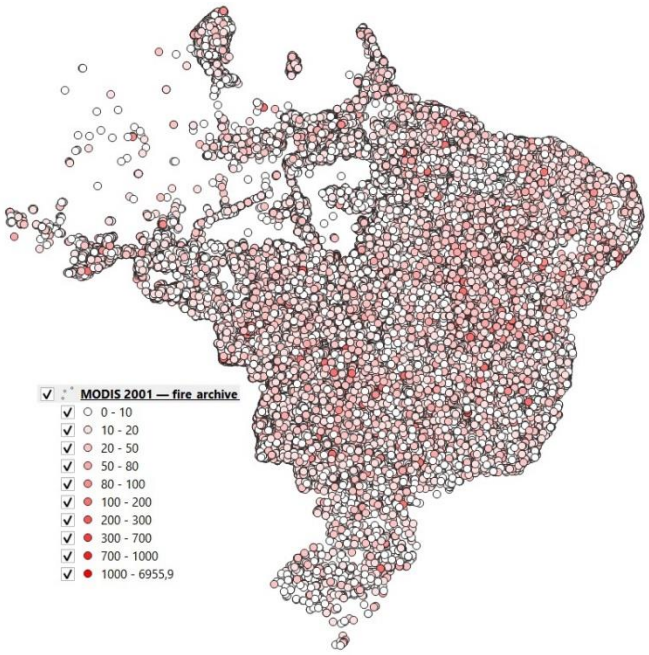

Figure 112 - Dispersion of MODIS FRPs values classified on the map for the year 2001

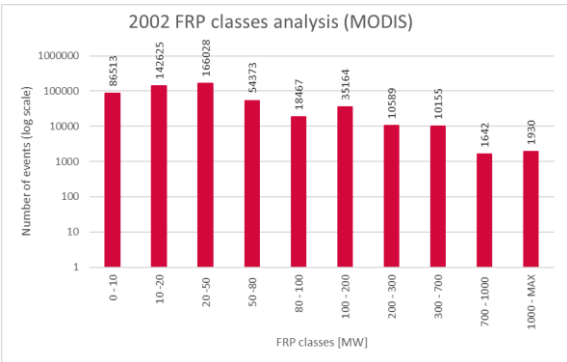

Figure 113 - Histogram describing the trend of the MODIS FRPs classes in the year 2002

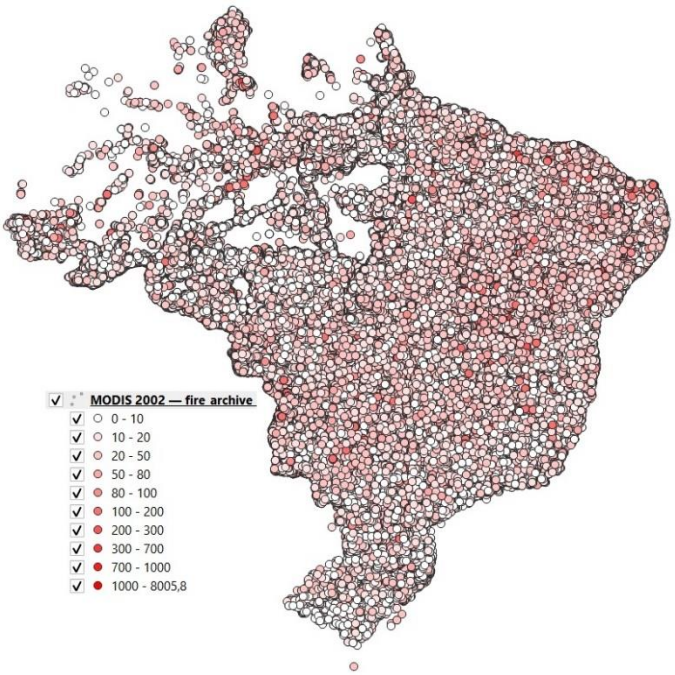

Figure 114 - Dispersion of MODIS FRPs values classified on the map for the year 2002

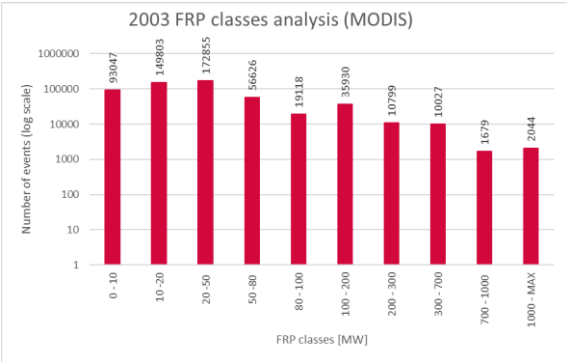

Figure 115 - Histogram describing the trend of the MODIS FRPs classes in the year 2003

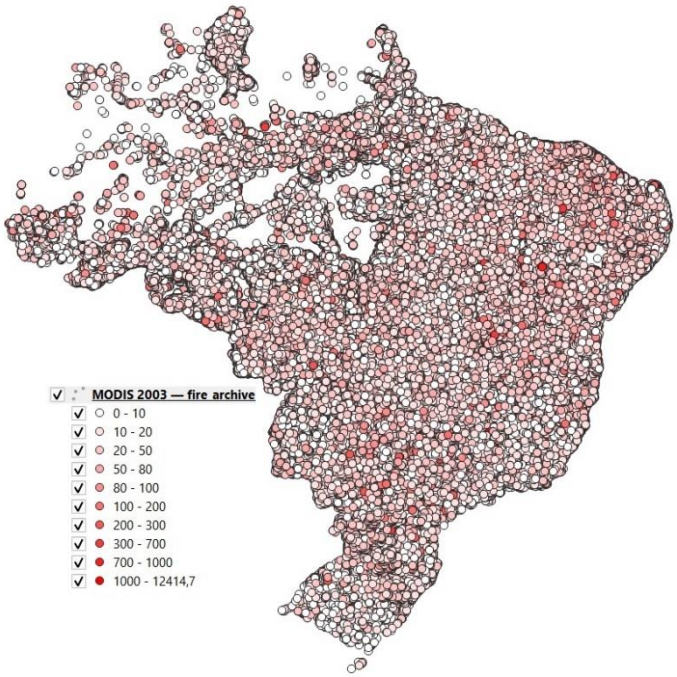

Figure 116 - Dispersion of MODIS FRPs values classified on the map for the year 2003

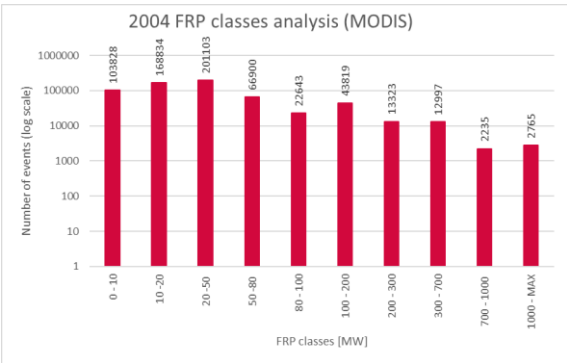

Figure 117 - Histogram describing the trend of the MODIS FRPs classes in the year 2004

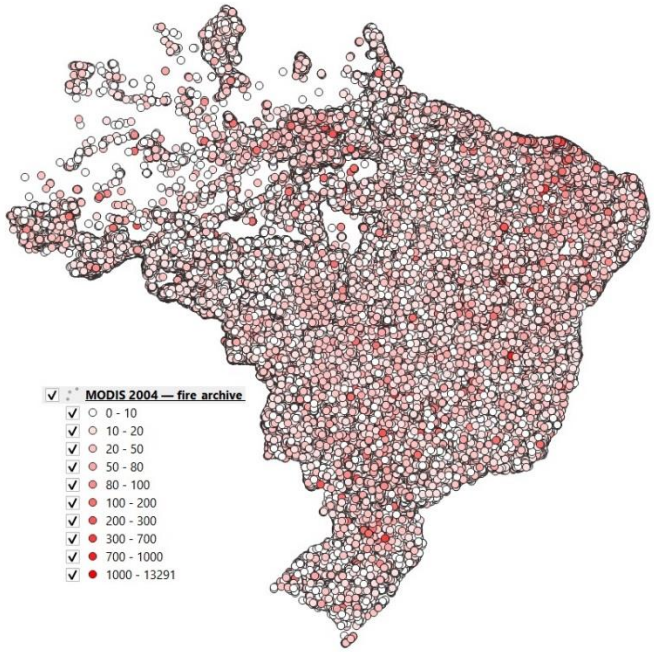

Figure 118 - Dispersion of MODIS FRPs values classified on the map for the year 2004

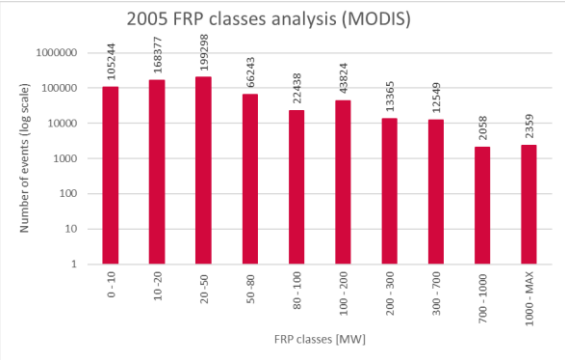

Figure 119 - Histogram describing the trend of the MODIS FRPs classes in the year 2005

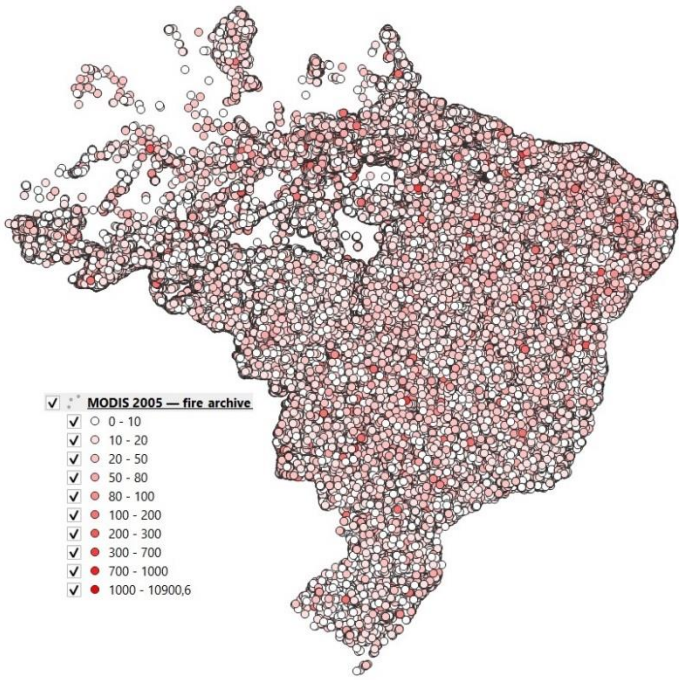

Figure 120 - Dispersion of MODIS FRPs values classified on the map for the year 2005

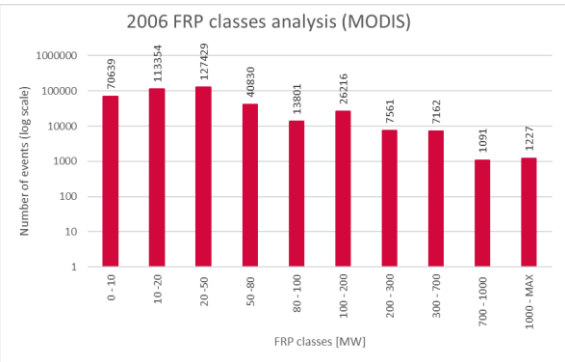

Figure 121 - Histogram describing the trend of the MODIS FRPs classes in the year 2006

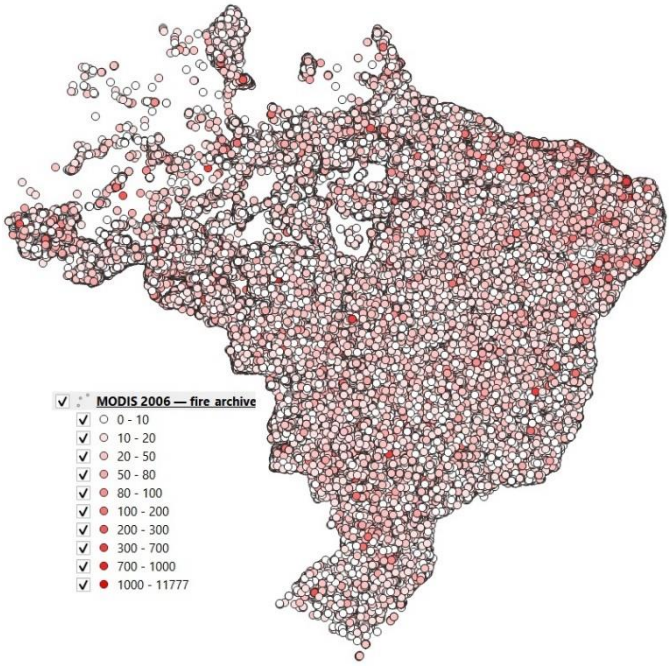

Figure 122 - Dispersion of MODIS FRPs values classified on the map for the year 2006

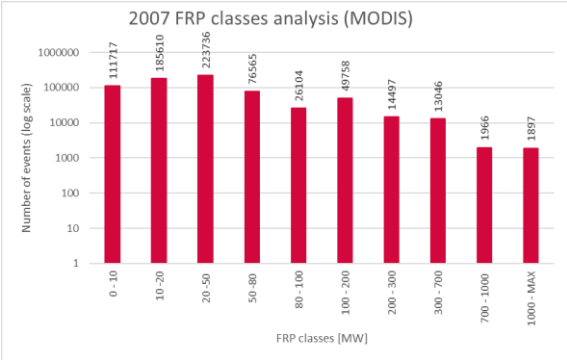

Figure 123 - - Histogram describing the trend of the MODIS FRPs classes in the year 2007

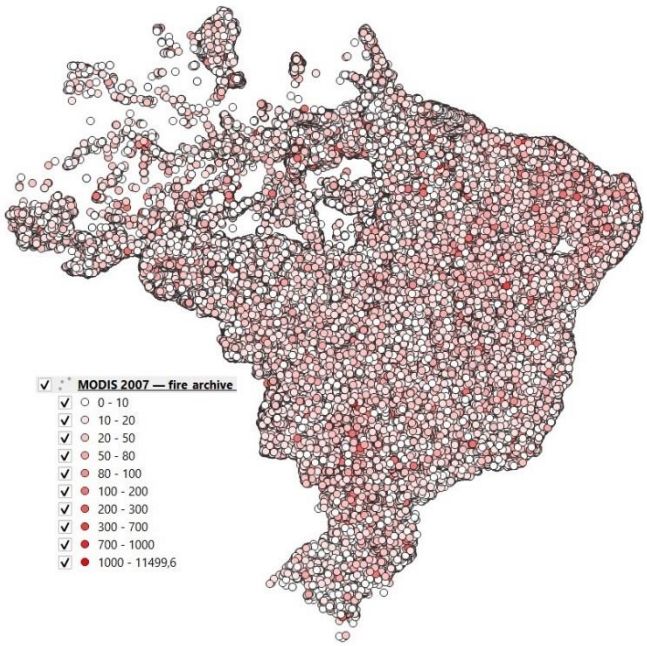

Figure 124 - Dispersion of MODIS FRPs values classified on the map for the year 2007

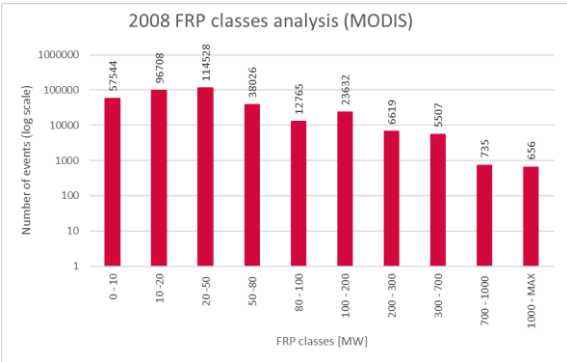

Figure 125 - Histogram describing the trend of the MODIS FRPs classes in the year 2008

Figure 126 - Dispersion of MODIS FRPs values classified on the map for the year 2008

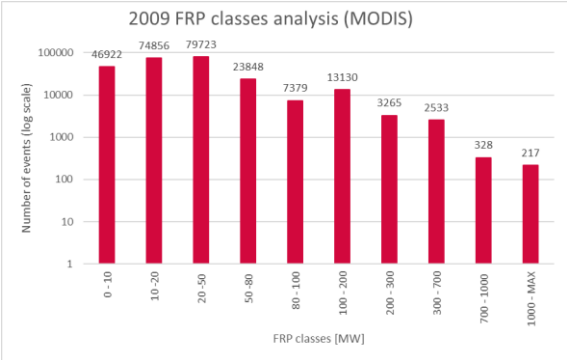

Figure 127- Histogram describing the trend of the MODIS FRPs classes in the year 2009

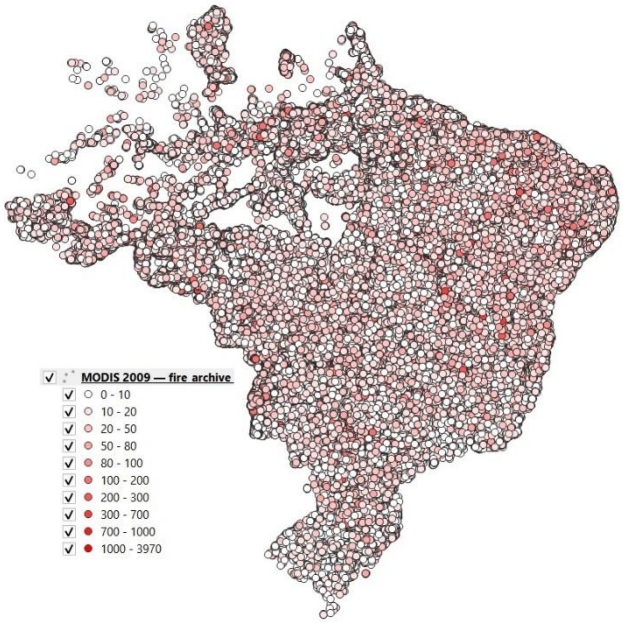

Figure 128 - Dispersion of MODIS FRPs values classified on the map for the year 2009

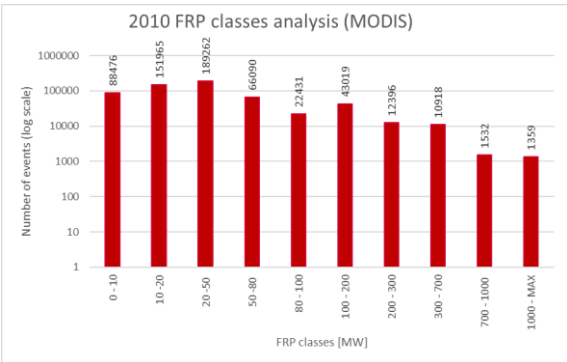

Figure 129 - Histogram describing the trend of the MODIS FRPs classes in the year 2010

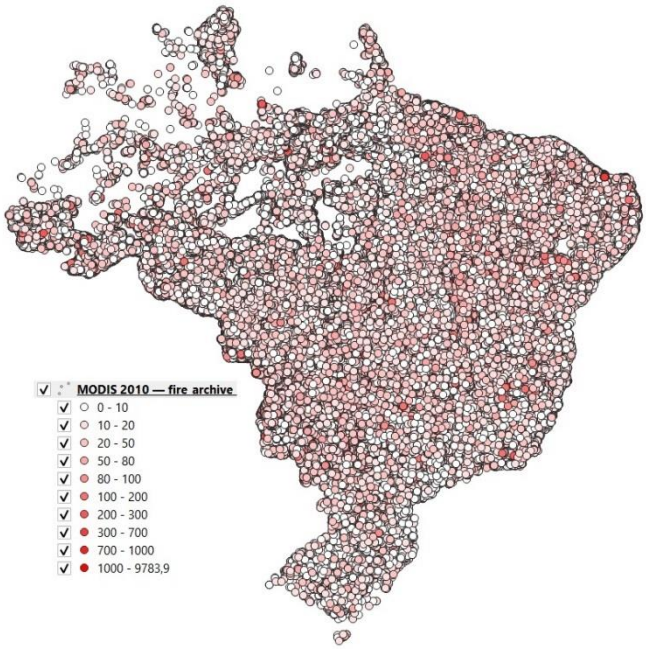

Figure 130 - Dispersion of MODIS FRPs values classified on the map for the year 2010

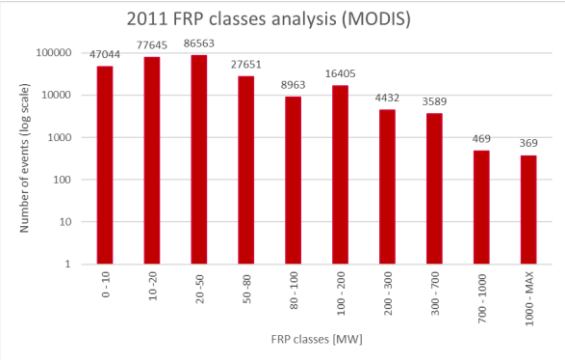

Figure 131 - Histogram describing the trend of the MODIS FRPs classes in the year 2011

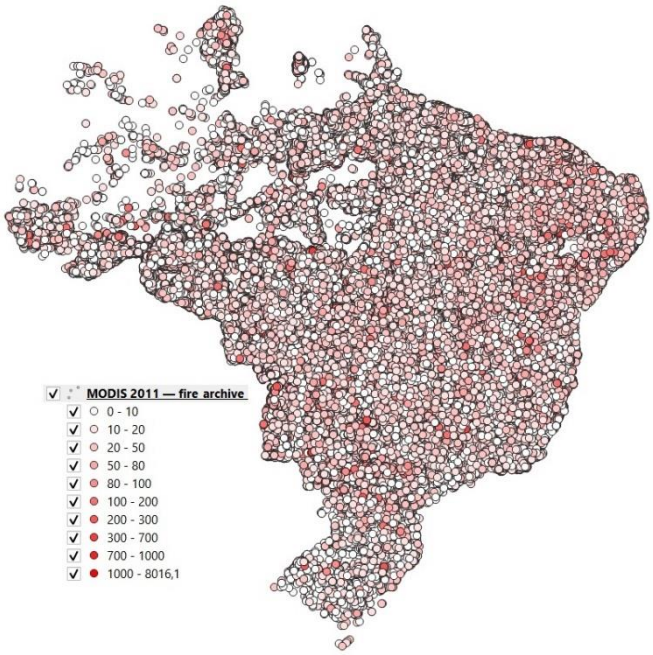

Figure 132 - Dispersion of MODIS FRPs values classified on the map for the year 2011

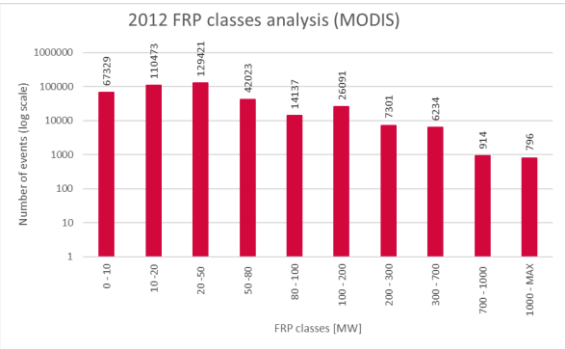

Figure 133 - Histogram describing the trend of the MODIS FRPs classes in the year 2012

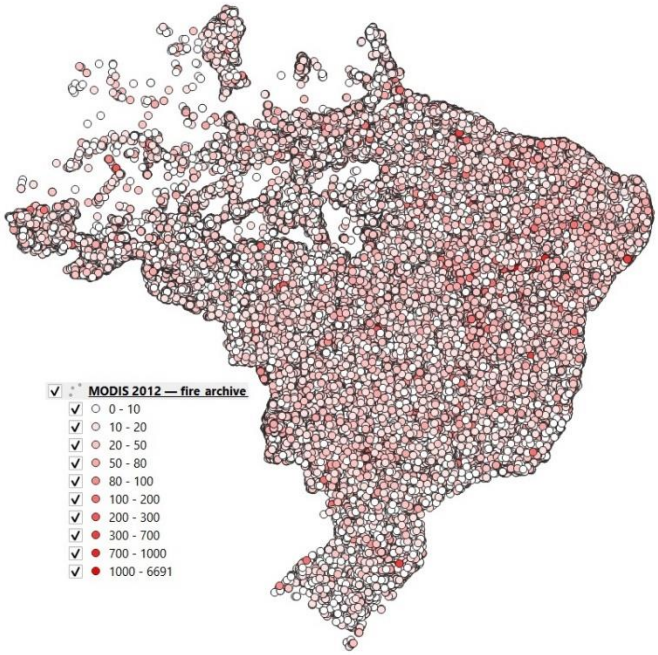

Figure 134 - Dispersion of MODIS FRPs values classified on the map for the year 2012

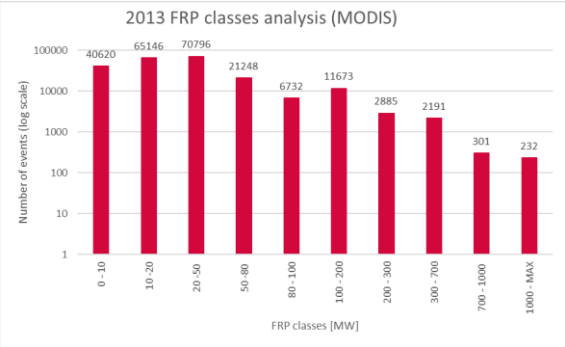

Figure 135 - Histogram describing the trend of the MODIS FRPs classes in the year 2013

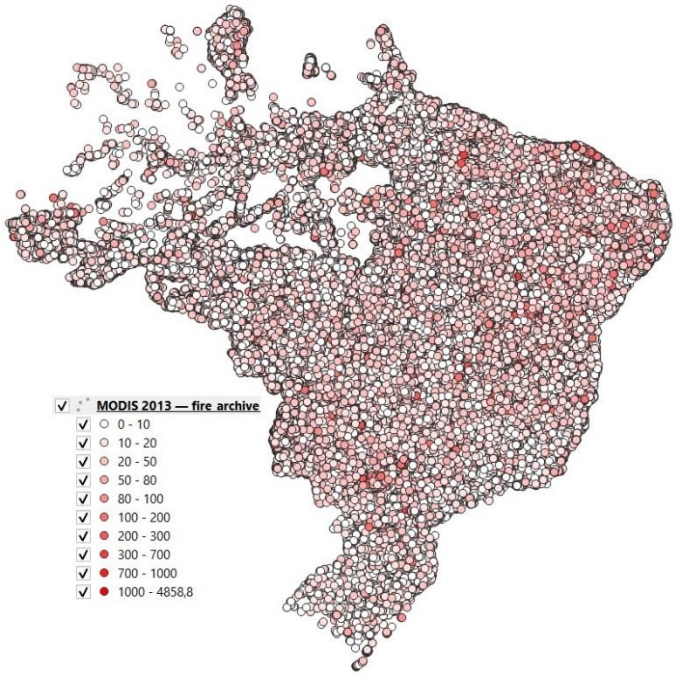

Figure 136 - Dispersion of MODIS FRPs values classified on the map for the year 2013

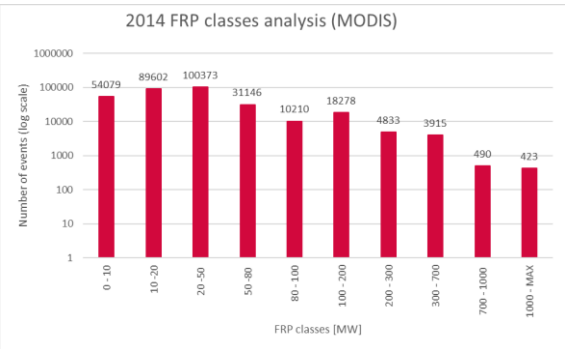

Figure 137 - Histogram describing the trend of the MODIS FRPs classes in the year 2014

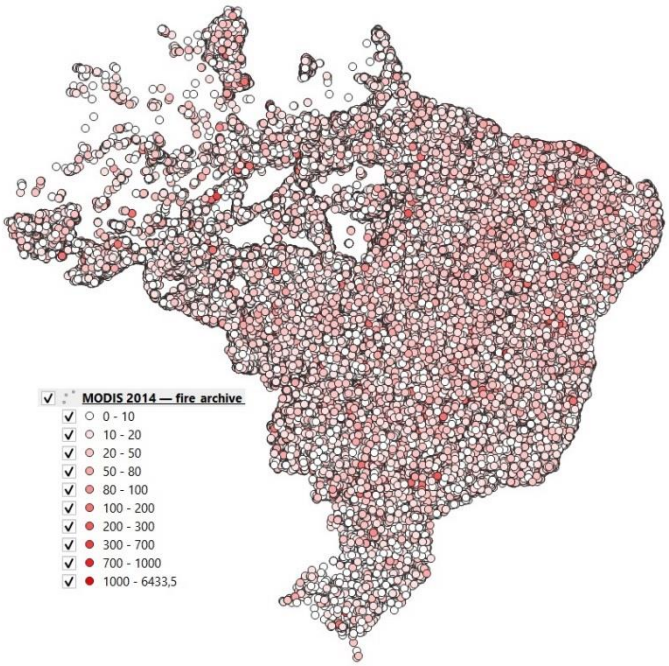

Figure 138 - Dispersion of MODIS FRPs values classified on the map for the year 2014

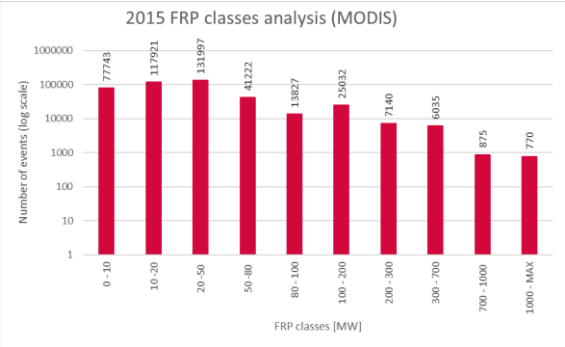

Figure 139 - Histogram describing the trend of the MODIS FRPs classes in the year 2015

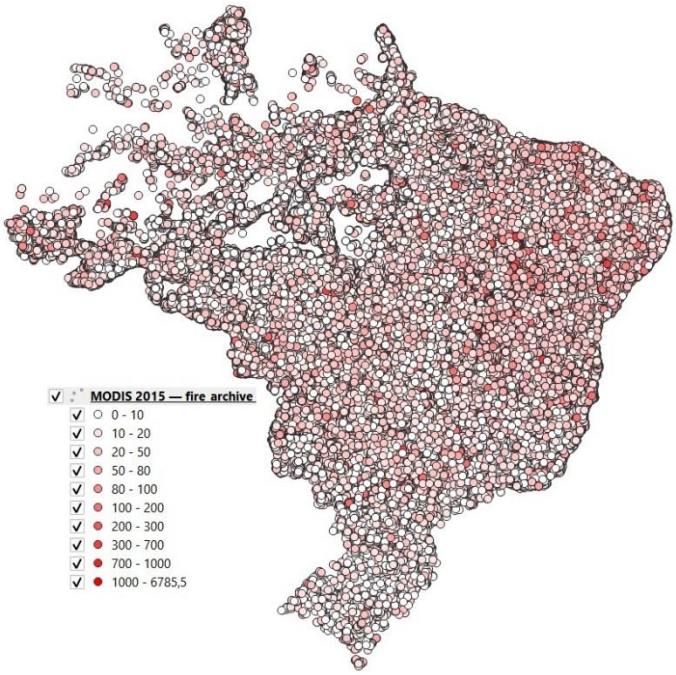

Figure 140 - Dispersion of MODIS FRPs values classified on the map for the year 2015

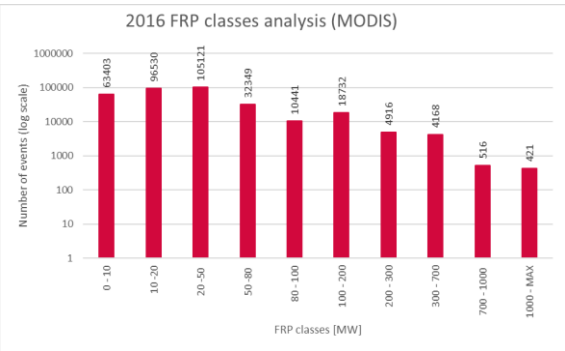

Figure 141 - Histogram describing the trend of the MODIS FRPs classes in the year 2016

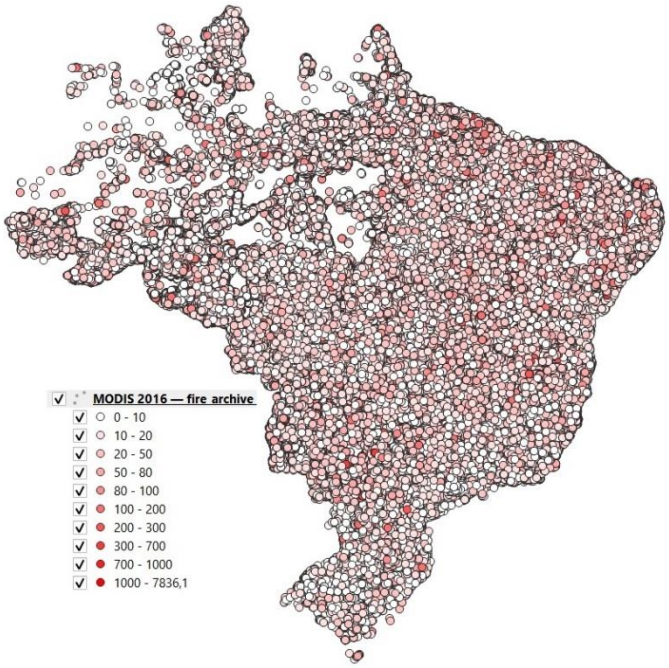

Figure 142 - Dispersion of MODIS FRPs values classified on the map for the year 2016

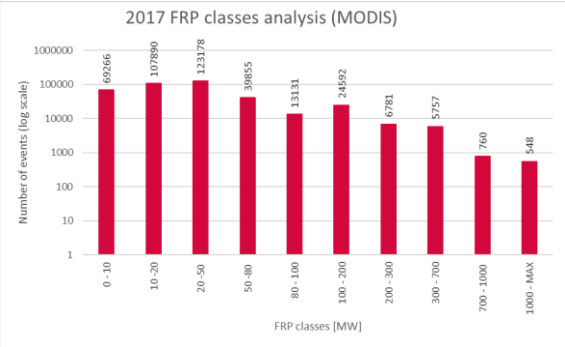

Figure 143 - Histogram describing the trend of the MODIS FRPs classes in the year 2017

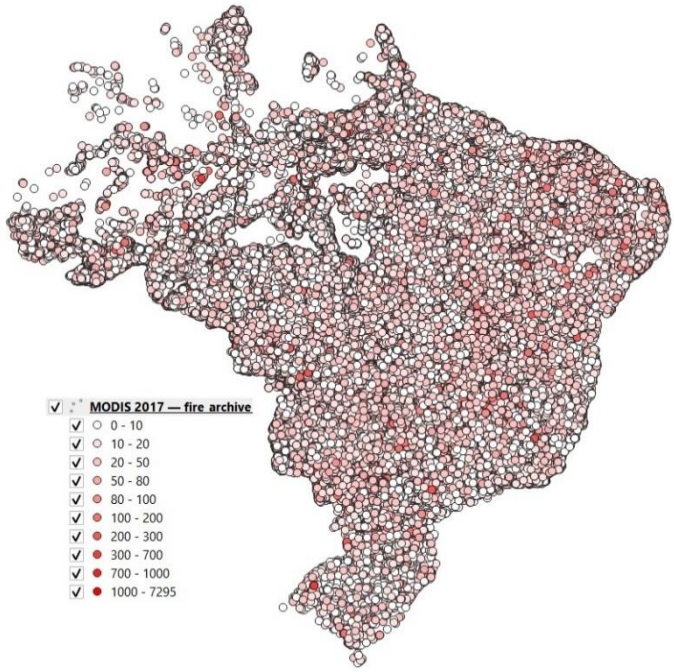

Figure 144 - Dispersion of MODIS FRPs values classified on the map for the year 2017

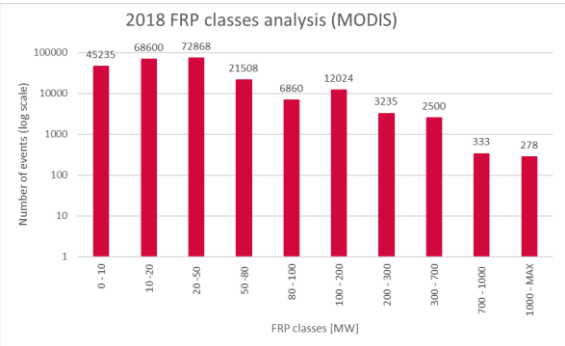

Figure 145 - Histogram describing the trend of the MODIS FRPs classes in the year 2018

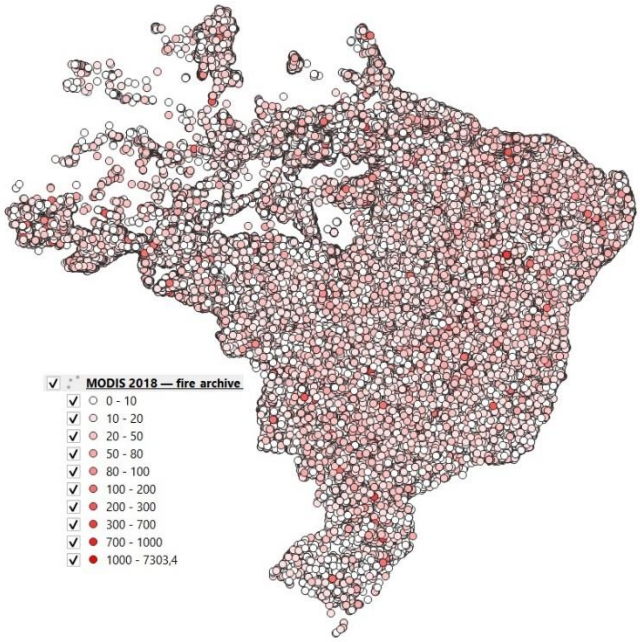

Figure 146 - Dispersion of MODIS FRPs values classified on the map for the year 2018

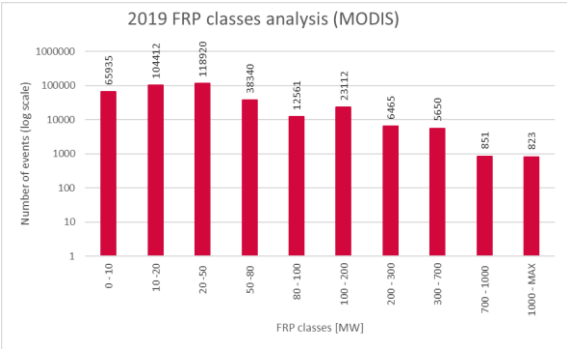

Figure 147 - Histogram describing the trend of the MODIS FRPs classes in the year 2019

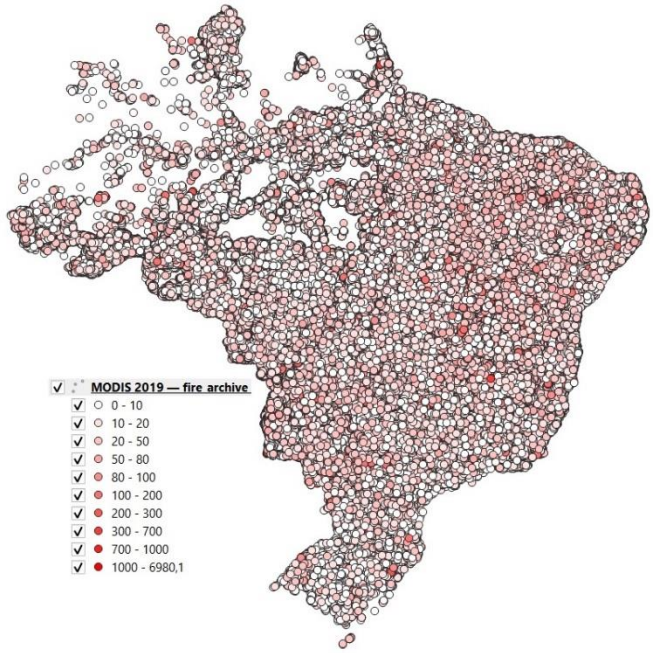

Figure 148 - Dispersion of MODIS FRPs values classified on the map for the year 2019

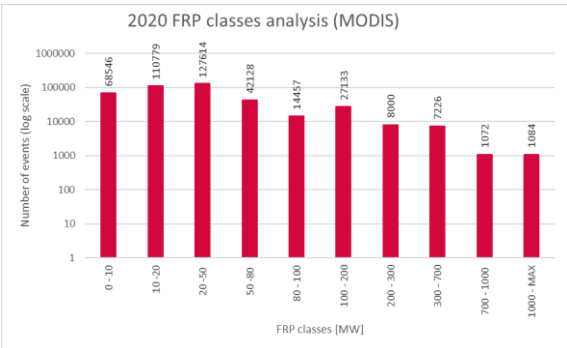

Figure 149 - Histogram describing the trend of the MODIS FRPs classes in the year 2020

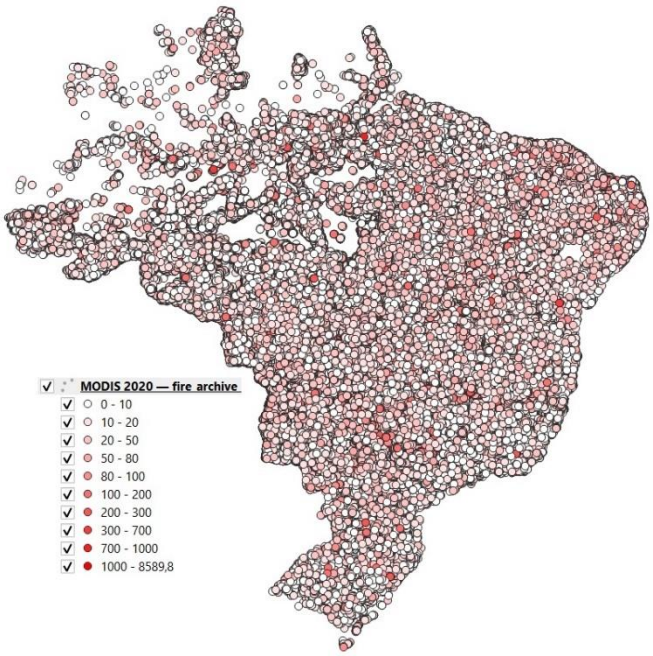

Figure 150 - Dispersion of MODIS FRPs values classified on the map for the year 2020

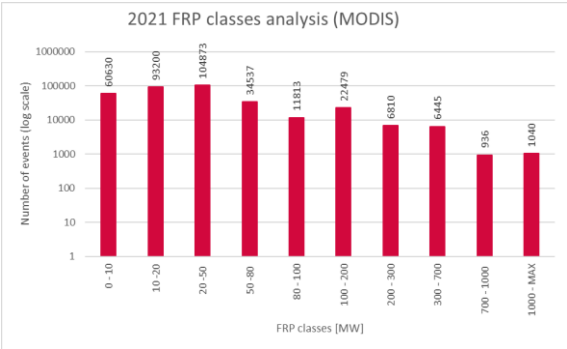

Figure 151 - Histogram describing the trend of the MODIS FRPs classes in the year 2021

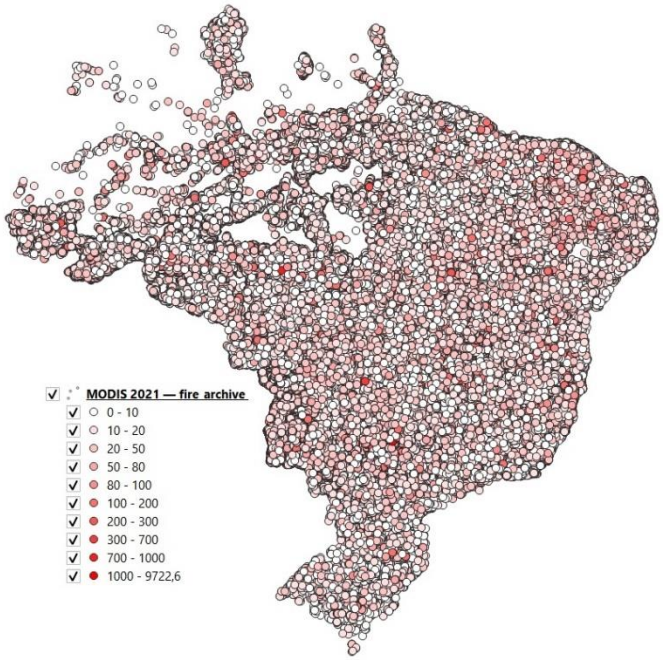

Figure 152 - Dispersion of MODIS FRPs values classified on the map for the year 2021

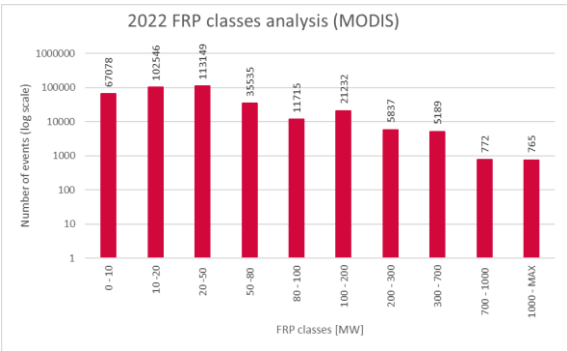

Figure 153 - Histogram describing the trend of the MODIS FRPs classes in the year 2022

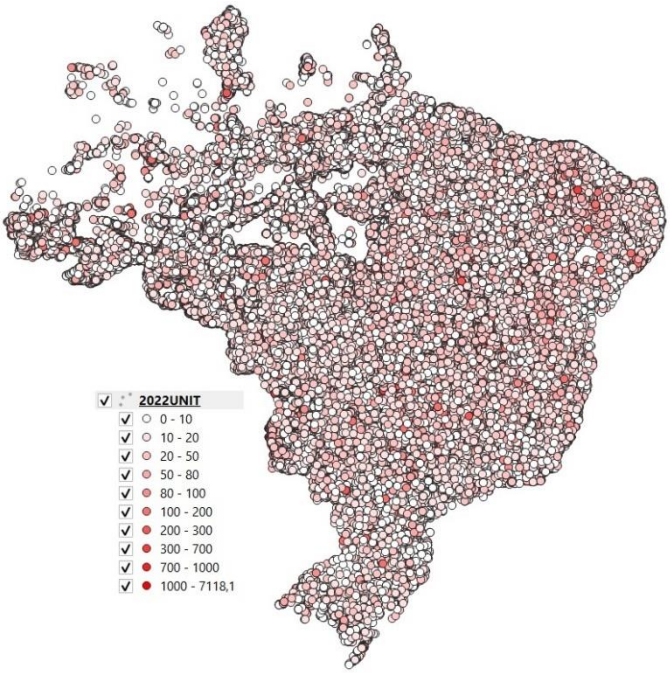

Figure 154 - Dispersion of MODIS FRPs values classified on the map for the year 2022

3.4.2 VIIRS SUOMI NPP FRP ANALYSIS: FRP classification

The following table shows for each year and for each class the corresponding number of events about the VIIRS SUOMI NPP data.

Years	Number of events	FRP classes										Max Value
	[10^3]	0 - 10	10 -20	20 -50	50 -80	80 - 100	100 - 200	200 - 300	300 - 700	700 - 1000	1000 - MAX	
2012	1'603	1'137'147	254'145	149'810	32'834	9'969	15'797	2'992	1'342	58	14	1'369.96
2013	858	607'093	142'610	79'374	16'377	4'634	6'874	1'147	479	17	8	1'900.97
2014	1'217	863'738	195'598	112'948	24'022	7'300	11'008	1'987	838	40	22	1'804.80
2015	1'713	1'228'119	264'819	154'777	34'431	10'184	16'259	3'184	1'309	65	17	1'634.04
2016	1'296	929'257	202'752	117'723	25'153	7'326	11'468	1'932	802	31	20	1'920.15
2017	1'535	1'082'739	246'581	145'723	32'435	9'267	14'670	2'799	1'231	76	20	1'725.14
2018	907	647'052	144'719	82'856	17'905	5'031	7'524	1'392	638	23	19	1'626.27
2019	1'453	1'018'197	236'231	140'198	30'609	9'197	14'684	2'808	1'409	70	9	1'282.11
2020	1'663	1'136'753	273'135	175'767	40'268	12'096	19'495	3'754	1'847	90	32	1'945.18
2021	1'323	909'878	212'401	135'907	32'701	10'094	16'891	3'666	1'982	119	27	1'319.69
2022	1'477	1'052'936	229'293	136'325	30'599	9'072	15'180	3'014	1'405	35	7	1'585.54

Table 16 - Number of events for each class in each year of the VIIRS SUOMI NPP FRPs

In the second column it is possible to see the total number of events, the other columns of the tab. 16 show how many events there were for each class in each year.

The division into classes (Tab.16) draws attention to the high presence of low FRP values, i.e. the predominance of FRP values between 0 and 30 MW or otherwise the predominance of FRP values in the range 0<FRP<100 [MW].

The predominant presence of low values (white color) is evident in the QGIS maps below (Fig. 156-158-160-162-164-166-168-170-172-174-176), so especially for VIIRS data, filtering using the confidence level will be useful in order to ensure data quality.

On the following pages, it is possible to see a histogram for each year describing the trend of the quantity of FRPs events detected, according to the division into classes concerning the VIIRS SUOMI NPP data, and the same events on the map given by QGIS divided by colours according to the FRPs classes.

FRP classification representation

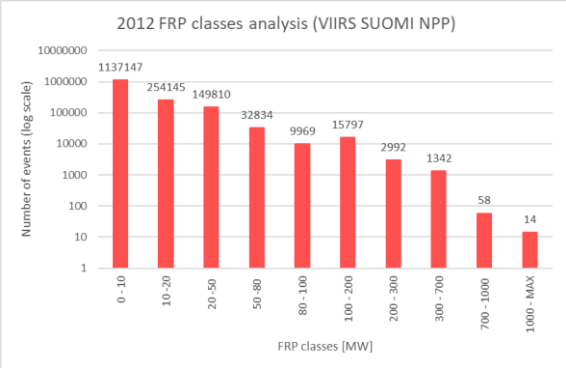

Figure 155 - Histogram describing the trend of the VIIRS SUOMI NPP FRPs classes in the year 2012

Figure 156 - Dispersion of VIIRS SUOMI NPP FRPs values classified on the map for the year 2012

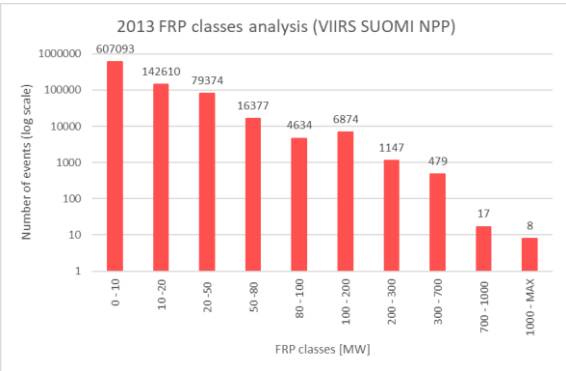

Figure 157 - Histogram describing the trend of the VIIRS SUOMI NPP FRPs classes in the year 2013

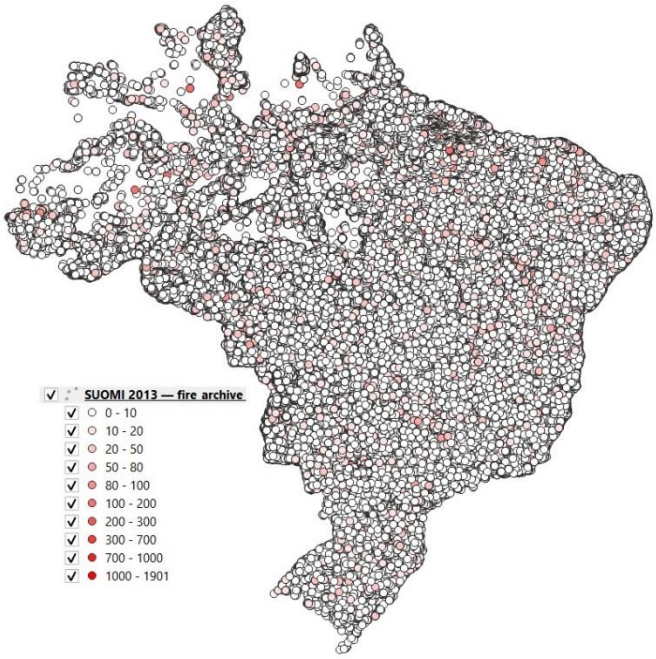

Figure 158 - Dispersion of VIIRS SUOMI NPP FRPs values classified on the map for the year 2013

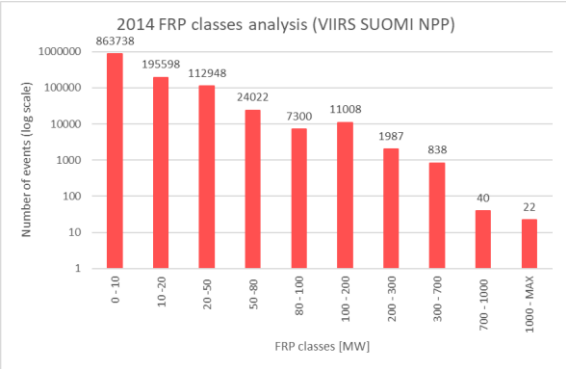

Figure 159 - Histogram describing the trend of the VIIRS SUOMI NPP FRPs classes in the year 2014

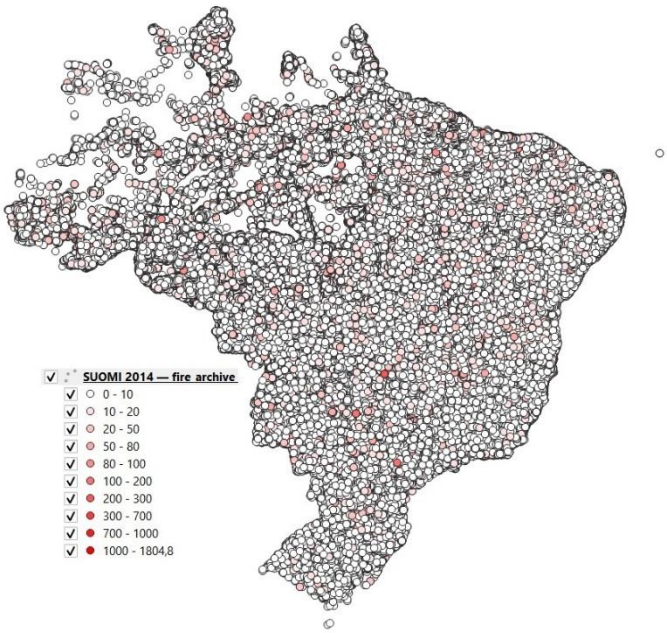

Figure 160 - Dispersion of VIIRS SUOMI NPP FRPs values classified on the map for the year 2014

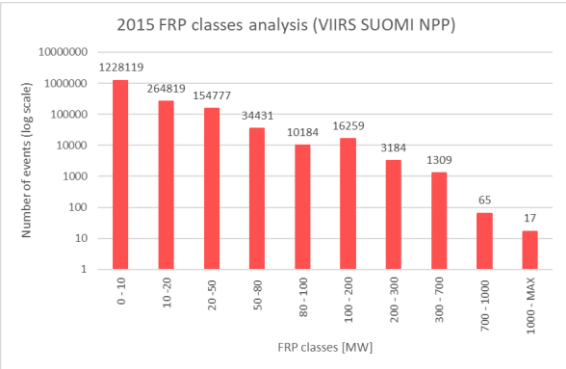

Figure 161 - Histogram describing the trend of the VIIRS SUOMI NPP FRPs classes in the year 2015

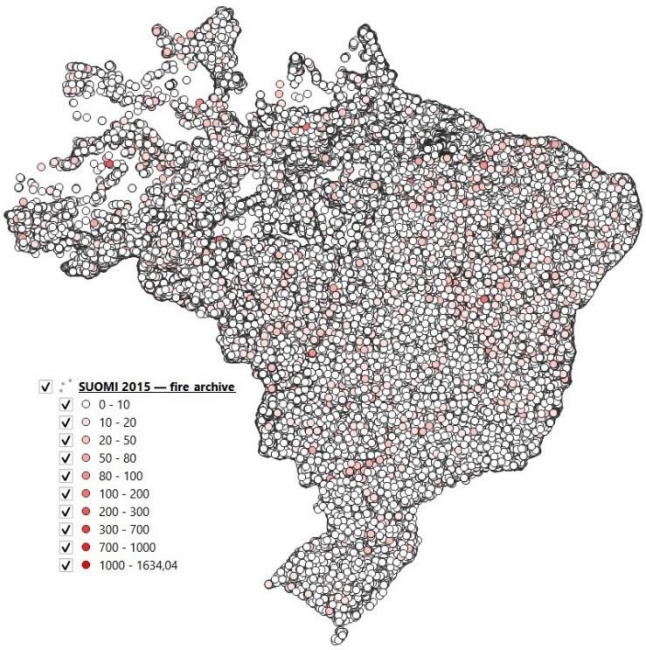

Figure 162 - Dispersion of VIIRS SUOMI NPP FRPs values classified on the map for the year 2015

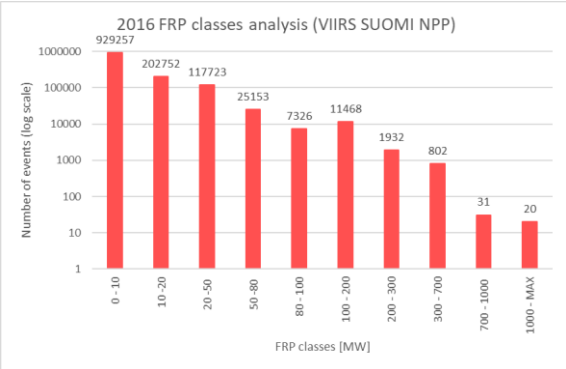

Figure 163 - Histogram describing the trend of the VIIRS SUOMI NPP FRPs classes in the year 2016

Figure 164 - Dispersion of VIIRS SUOMI NPP FRPs values classified on the map for the year 2016

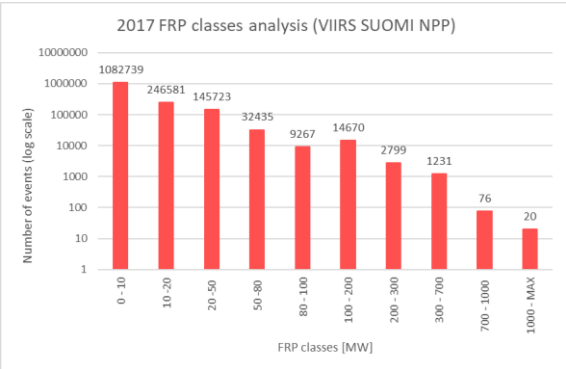

Figure 165 - Histogram describing the trend of the VIIRS SUOMI NPP FRPs classes in the year 2017

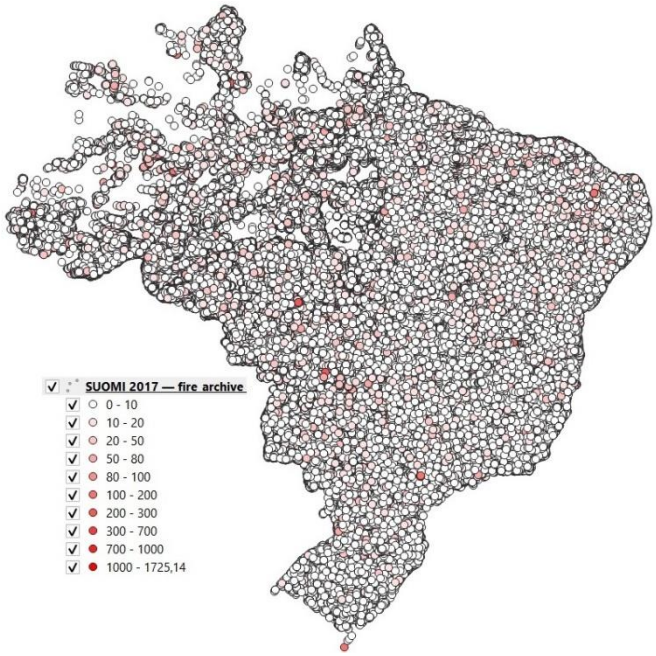

Figure 166 - Dispersion of VIIRS SUOMI NPP FRPs values classified on the map for the year 2017

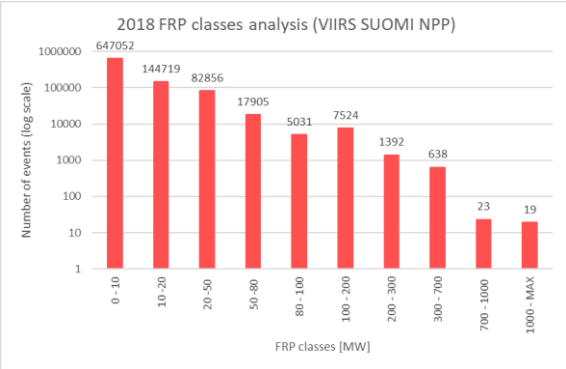

Figure 167 - Histogram describing the trend of the VIIRS SUOMI NPP FRPs classes in the year 2018

Figure 168 - Dispersion of VIIRS SUOMI NPP FRPs values classified on the map for the year 2018

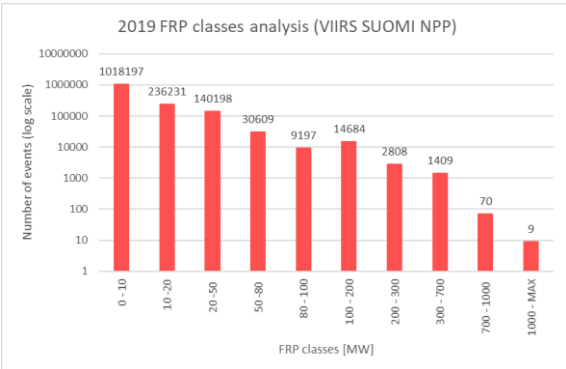

Figure 169 - Histogram describing the trend of the VIIRS SUOMI NPP FRPs classes in the year 2019

Figure 170 - Dispersion of VIIRS SUOMI NPP FRPs values classified on the map for the year 2019

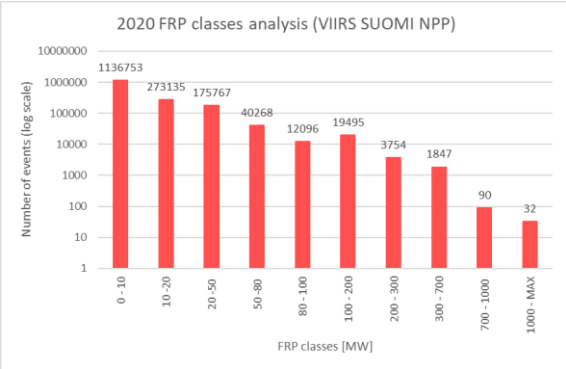

Figure 171 - Histogram describing the trend of the VIIRS SUOMI NPP FRPs classes in the year 2020

Figure 172 - Dispersion of VIIRS SUOMI NPP FRPs values classified on the map for the year 2020

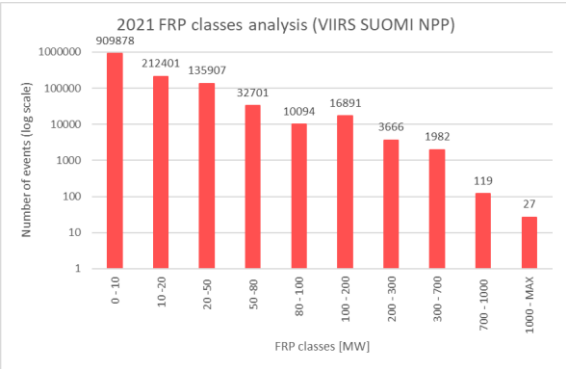

Figure 173 - Histogram describing the trend of the VIIRS SUOMI NPP FRPs classes in the year 2021

Figure 174 - Dispersion of VIIRS SUOMI NPP FRPs values classified on the map for the year 2021

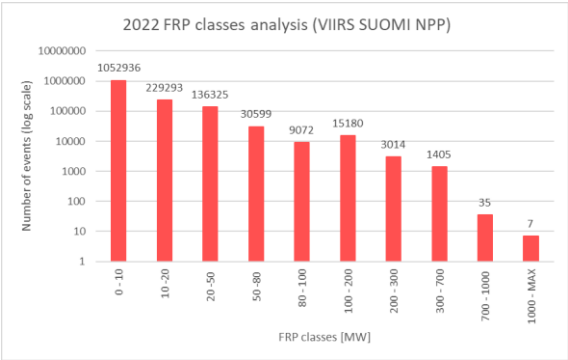

Figure 175 - Histogram describing the trend of the VIIRS SUOMI NPP FRPs classes in the year 2022

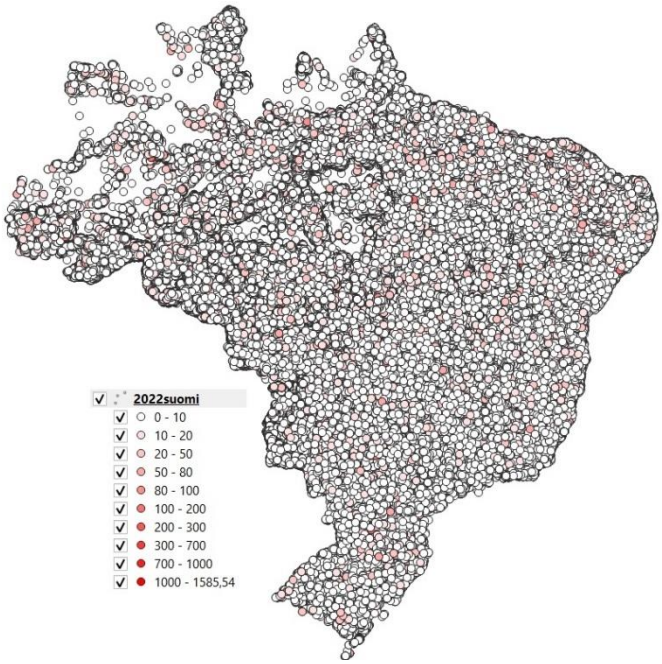

Figure 176 - Dispersion of VIIRS SUOMI NPP FRPs values classified on the map for the year 2022

3.4.3 MODIS DATA ANALYSIS: FRP classification with CONFIDENCE ≥ 80 %

The following table shows for each year and for each class the corresponding number of events about MODIS FRP data with confidence applied ≥ 80 %.

Years	Number of events	FRP classes										Max Value	MW Developed
		0 - 10	10 -20	20 -50	50 -80	80 - 100	100 - 200	200 - 300	300 - 700	700 - 1000	1000 - MAX		
2001	41'062	659	6'604	16'479	6'730	2'470	5'311	1'488	1'224	143	122	6'955.90	2'757'320
2002	181'656	1'313	15'887	65'627	33'040	13'215	29'819	10'127	9'808	1'590	1'871	8'005.50	24'898'401
2003	186'966	1'154	16'265	60'164	34'029	13'640	30'637	10'369	9'726	1'634	1'990	12'414.70	34'469'233
2004	222'935	1'348	18'870	79'037	40'313	16'347	37'470	12'830	12'632	2'166	2'701	13'290.90	48'039'941
2005	224'859	1'963	20'735	79'934	40'333	16'221	37'123	12'833	12'190	2'003	2'310	10'900.60	37'502'296
2006	137'997	970	11'664	51'592	25'162	10'194	22'452	7'233	6'950	1'062	1'194	11'777.00	21'567'678
2007	251'476	2'005	22'479	90'104	46'330	18'757	42'099	14'026	12'761	1'931	1'873	11'499.60	35'674'951
2008	122'735	927	10'340	46'119	23'083	9'307	20'242	6'389	5'343	726	647	7'958.70	11'895'249
2009	76'762	614	7'065	32'105	14'524	5'418	11'280	3'110	2'420	316	211	3'970.00	4'712'490
2010	216'295	1'769	19'101	77'804	40'343	16'091	36'408	12'024	10'732	1'511	1'355	9'783.90	25'566'415
2011	88'097	499	7'758	34'468	16'765	6'381	13'872	4'294	3'531	465	361	4'053.70	6'218'066
2012	136'253	1'280	12'509	50'696	25'442	9'956	21'986	7'067	6'086	897	780	6'691.00	12'668'930
2013	66'749	460	6'195	27'543	12'811	4'779	9'790	2'772	2'133	292	229	4'858.80	4'453'415
2014	99'431	783	9'297	39'124	18'592	7'294	15'348	4'628	3'805	479	418	6'433.50	7'912'663
2015	141'753	2'543	16'346	53'021	24'966	9'924	21'145	6'882	5'894	864	755	6'427.30	12'244'092
2016	105'708	1'359	11'183	41'269	19'256	7'416	15'939	4'708	4'049	504	415	7'836.10	8'761'972
2017	131'240	1'654	13'637	48'945	24'027	9'457	20'684	6'464	5'599	729	540	7'295.00	11'103'610
2018	69'022	709	7'222	27'692	12'580	4'802	10'158	3'115	2'418	330	274	7'303.40	5'504'142
2019	125'854	1'614	13'572	46'354	23'025	8'889	19'505	6'236	5'522	831	807	6'980.10	12'269'151
2020	143'037	1'627	14'819	51'368	25'997	10'446	22'650	7'595	7'003	1'042	1'059	8'589.80	16'870'228
2021	118'365	1'402	11'887	42'508	20'950	8'462	18'926	6'511	6'219	914	1'010	9'722.60	16'321'196
2022	120'335	1'249	12'927	45'473	21'992	8'627	18'173	5'665	5'074	756	756	7'118.07	11'603'711

Table 17 - Number of events for each class in each year of the MODIS FRPs with CONFIDENCE ≥ 80 %

In the second column you can see the total number of events, while the other columns of the tab. 17 show how many events there were for each class in each year.

The division into classes (Tab.17) using the confidence-filtered MODIS data shows that, for the most part, the data removed from the filtering are those of FRP<100 MW. The data with FRP>100 MW remained numerically almost unchanged compared to those in Tab. 15 (unfiltered). This is reflected in the qualitative view of the QGIS maps (for example Fig.179-181), this time represented with a predominance of red.

Considering the reliability of the data, the last column shows the amount of MW that have developed over the years; the calculation was carried out by multiplying the number of events in the given class by the corresponding value of [MW] in that class and finally summed up.

A histogram representing the trend can be seen in Fig.177

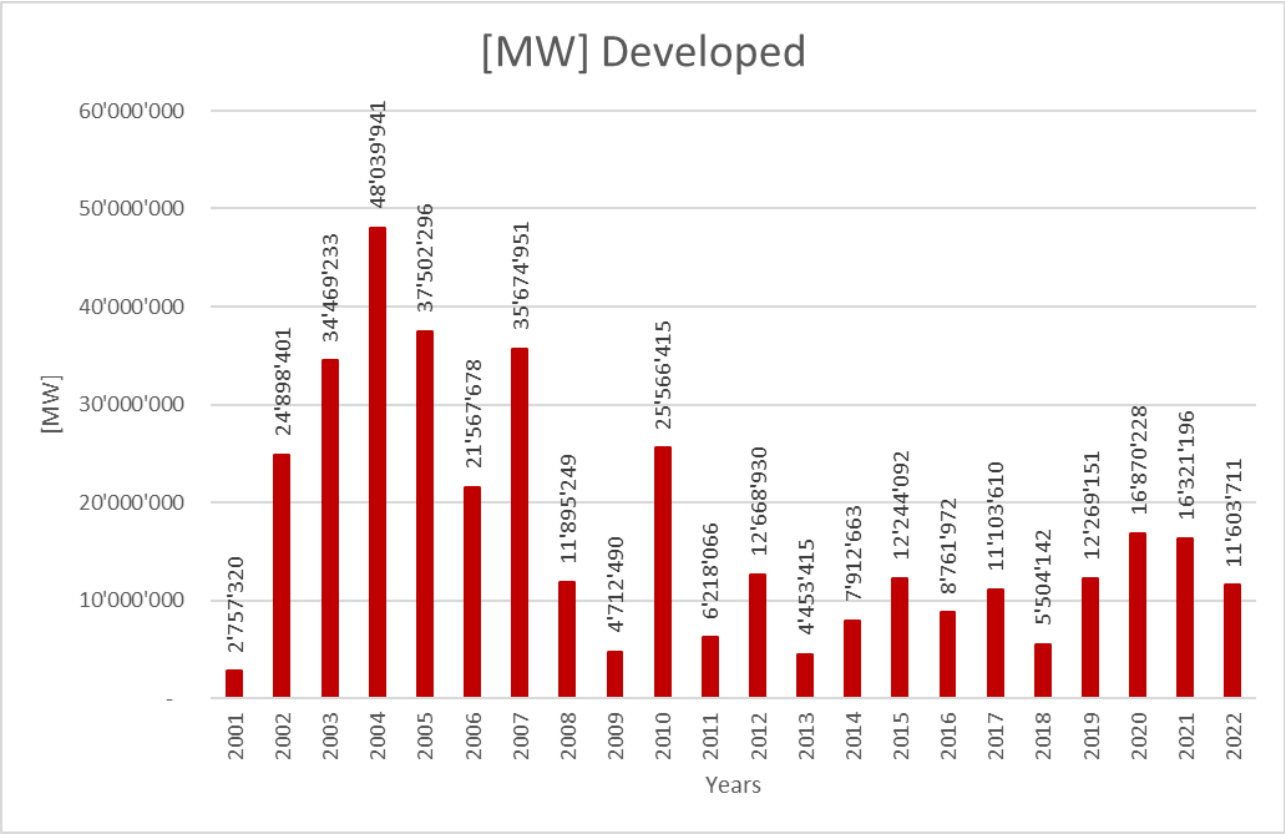

Figure 177 - Histogram describing the trend of the [MW] developed due to the FRP MODIS value with confidence applied

Also, in this case (Fig.177), the peaks correspond to the years 2004, 2007, 2010 with an almost constant subsequent trend increasing again in the years 2020, 2021.

On the following pages, it is possible to see a histogram for each year describing the trend of the quantity of FRPs events detected, according to the division into classes concerning the MODIS data, and the same events on the map given by QGIS divided by colours according to the FRPs classes.

FRP classification representation

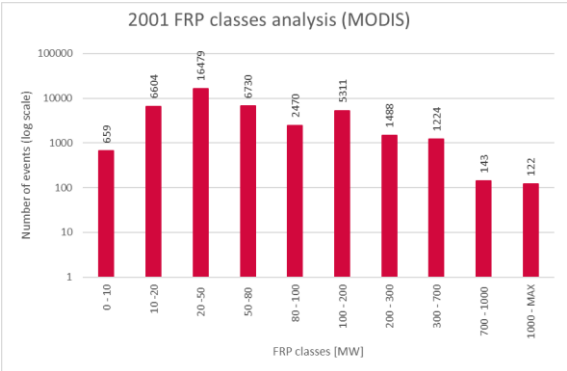

Figure 178 - - Histogram describing the trend of the MODIS FRPs classes with confidence ≥ 80 in the year 2001

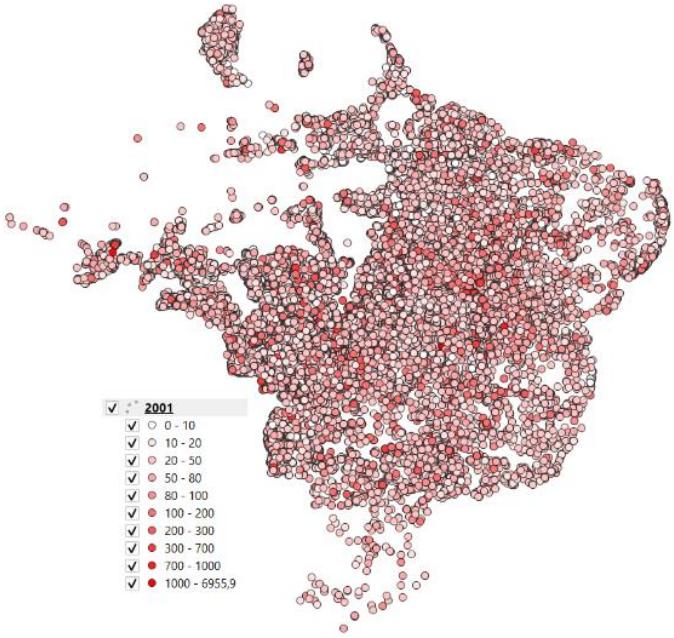

Figure 179 - Dispersion of MODIS FRPs values classified on the map with confidence ≥ 80 for the year 2001

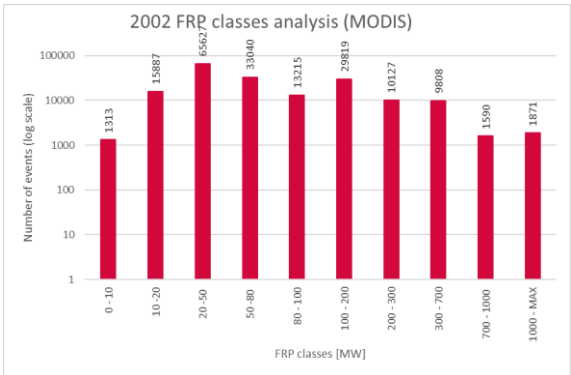

Figure 180 - - Histogram describing the trend of the MODIS FRPs classes with confidence ≥ 80 in the year 2002

Figure 181 - Dispersion of MODIS FRPs values classified on the map with confidence ≥ 80 for the year 2002

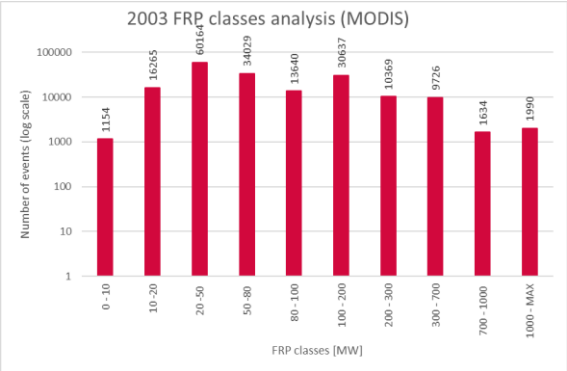

Figure 182 - Histogram describing the trend of the MODIS FRPs classes with confidence ≥ 80 in the year 2003

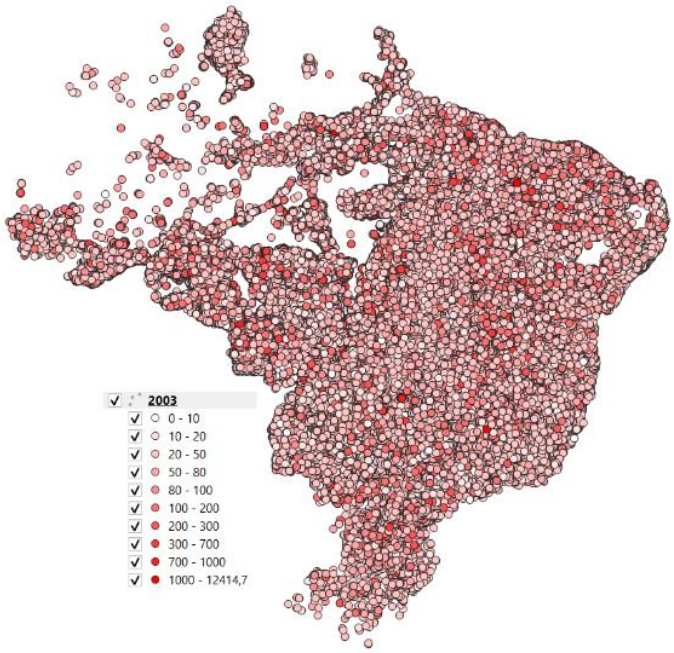

Figure 183 - Dispersion of MODIS FRPs values classified on the map with confidence ≥ 80 for the year 2003

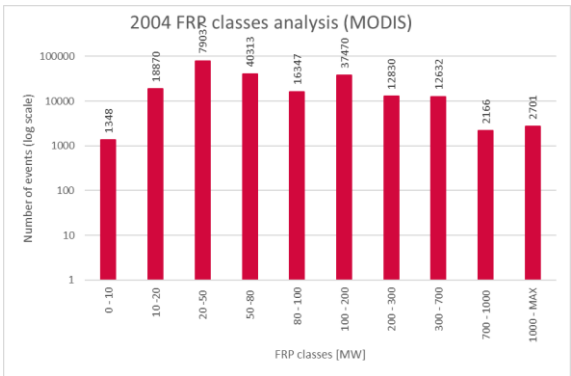

Figure 184 - Histogram describing the trend of the MODIS FRPs classes with confidence ≥ 80 in the year 2004

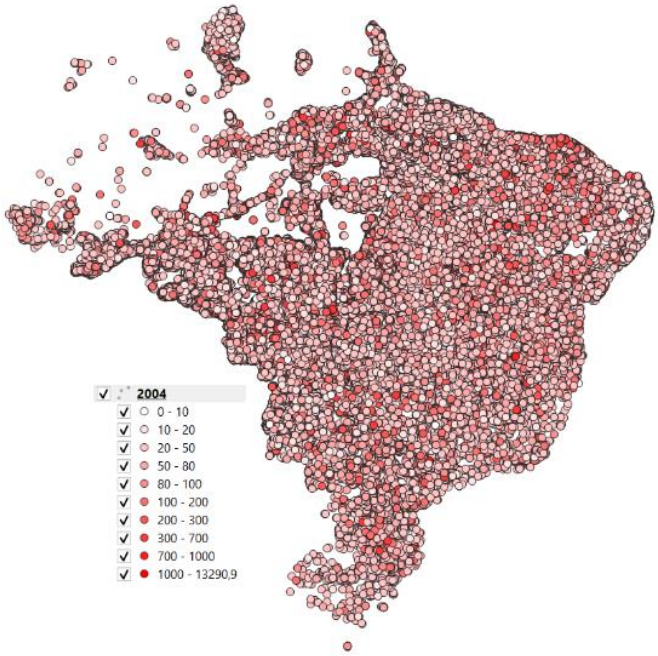

Figure 185 - Dispersion of MODIS FRPs values classified on the map with confidence ≥ 80 for the year 2004

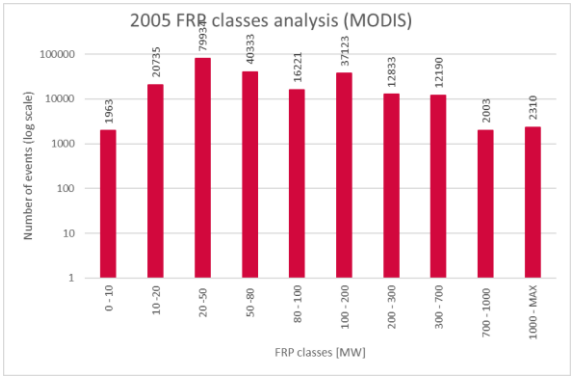

Figure 186 - Histogram describing the trend of the MODIS FRPs classes with confidence ≥ 80 in the year 2005

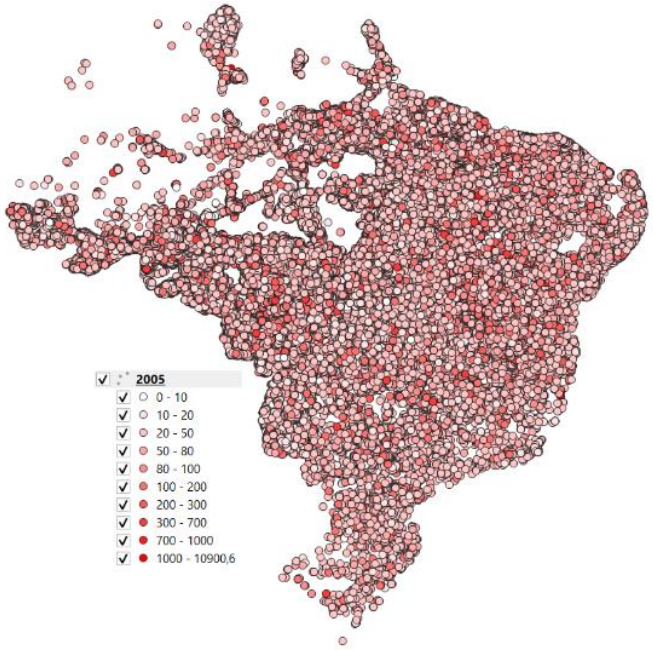

Figure 187 - Dispersion of MODIS FRPs values classified on the map with confidence ≥ 80 for the year 2005

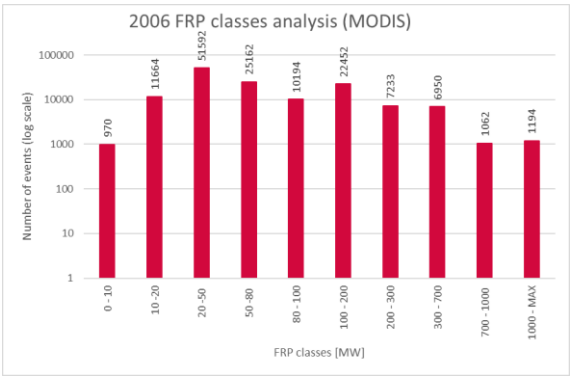

Figure 188 - Histogram describing the trend of the MODIS FRPs classes with confidence ≥ 80 in the year 2006

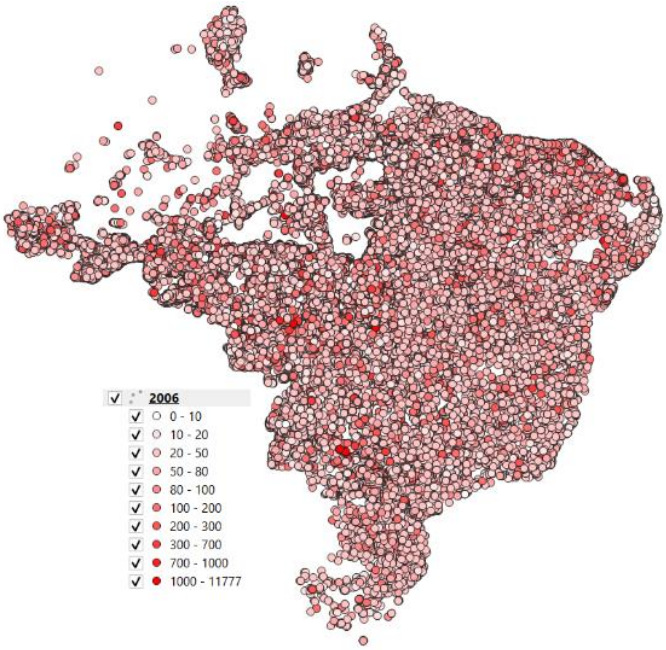

Figure 189 - Dispersion of MODIS FRPs values classified on the map with confidence ≥ 80 for the year 2006

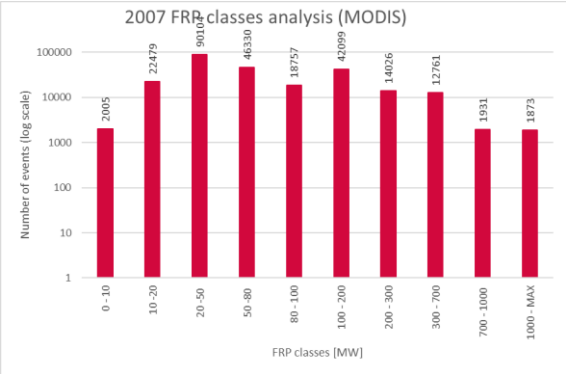

Figure 190 - Histogram describing the trend of the MODIS FRPs classes with confidence ≥ 80 in the year 2007

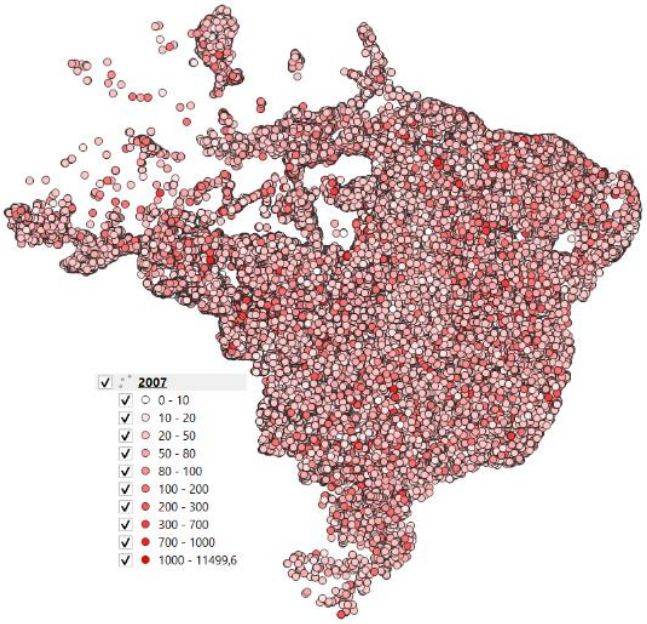

Figure 191 - Dispersion of MODIS FRPs values classified on the map with confidence ≥ 80 for the year 2007

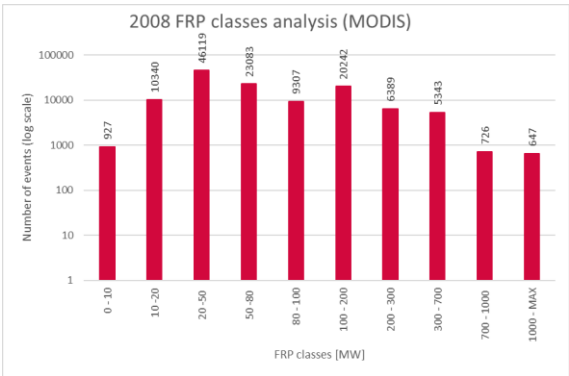

Figure 192 - Histogram describing the trend of the MODIS FRPs classes with confidence ≥ 80 in the year 2008

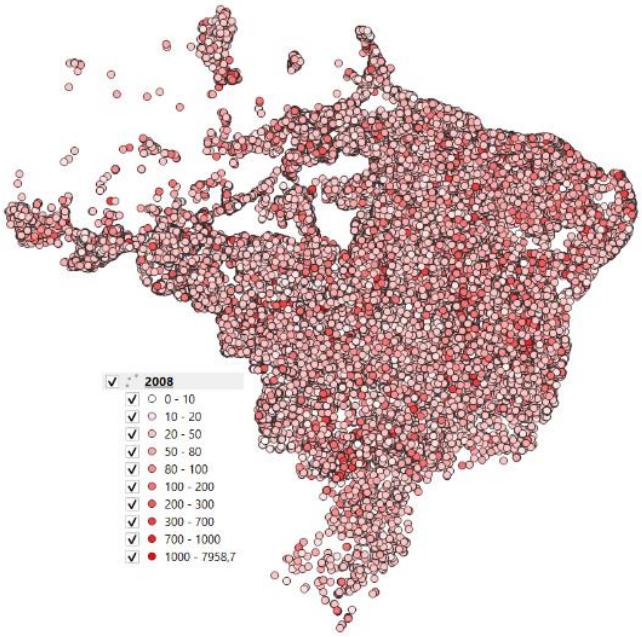

Figure 193 - Dispersion of MODIS FRPs values classified on the map with confidence ≥ 80 for the year 2008

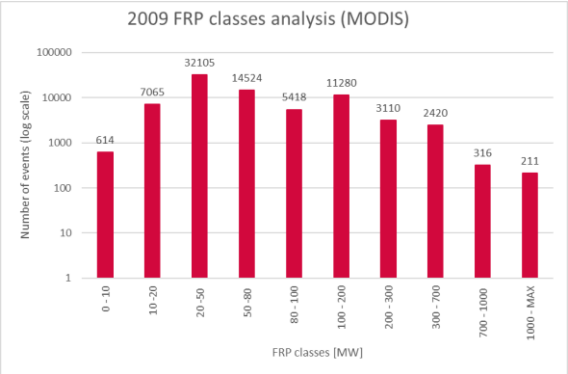

Figure 194 - Histogram describing the trend of the MODIS FRPs classes with confidence ≥ 80 in the year 2009

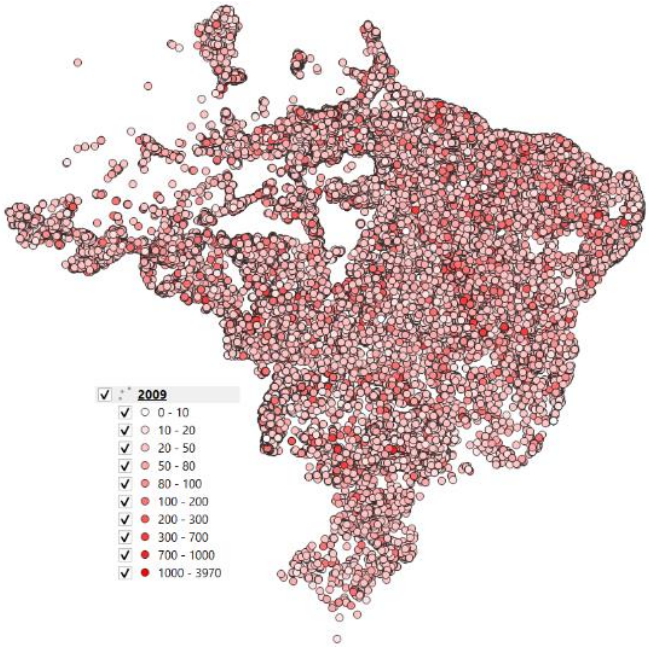

Figure 195 - Dispersion of MODIS FRPs values classified on the map with confidence ≥ 80 for the year 2009

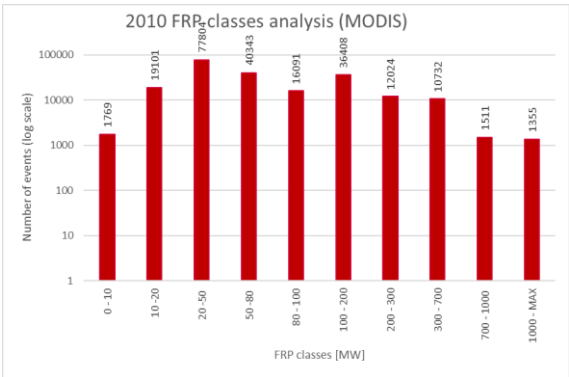

Figure 196 - Histogram describing the trend of the MODIS FRPs classes with confidence ≥ 80 in the year 2010

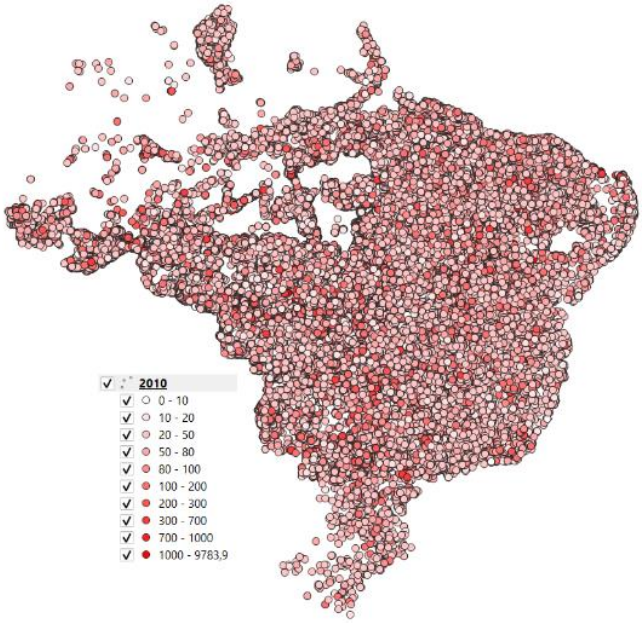

Figure 197 - Dispersion of MODIS FRPs values classified on the map with confidence ≥ 80 for the year 2010

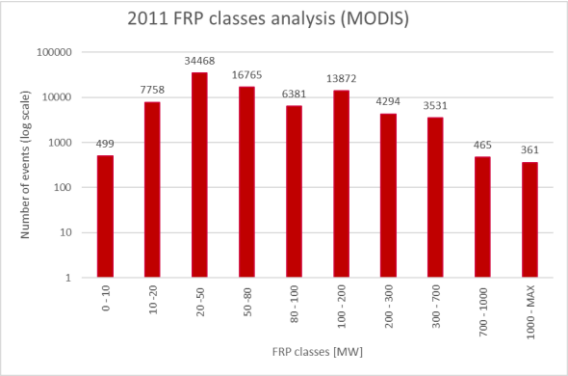

Figure 198 - Histogram describing the trend of the MODIS FRPs classes with confidence ≥ 80 in the year 2011

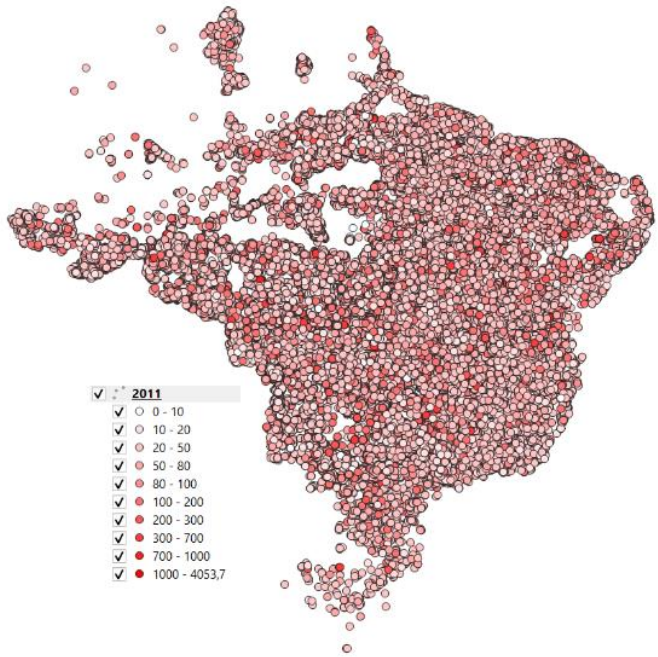

Figure 199 - Dispersion of MODIS FRPs values classified on the map with confidence ≥ 80 for the year 2011

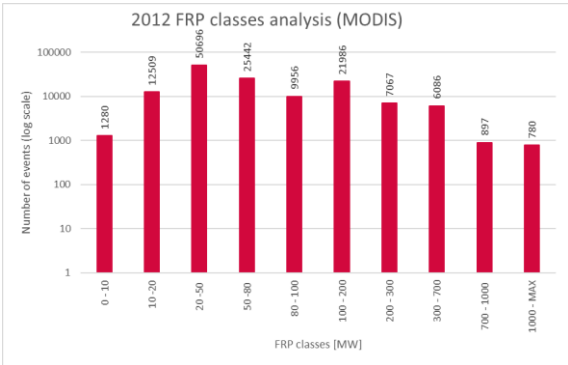

Figure 200 - Histogram describing the trend of the MODIS FRPs classes with confidence ≥ 80 in the year 2012

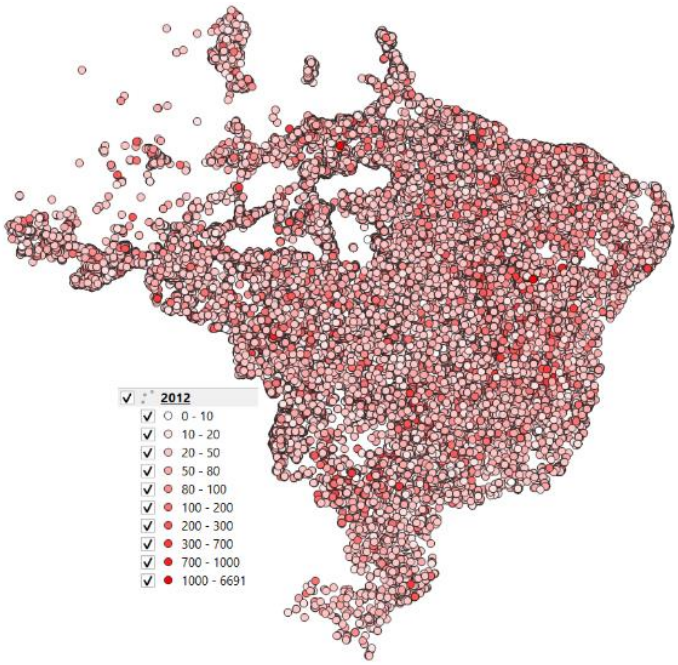

Figure 201 - Dispersion of MODIS FRPs values classified on the map with confidence ≥ 80 for the year 2012

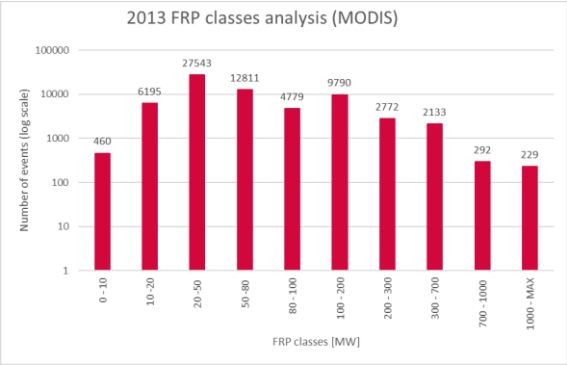

Figure 202 - - Histogram describing the trend of the MODIS FRPs classes with confidence ≥ 80 in the year 2013

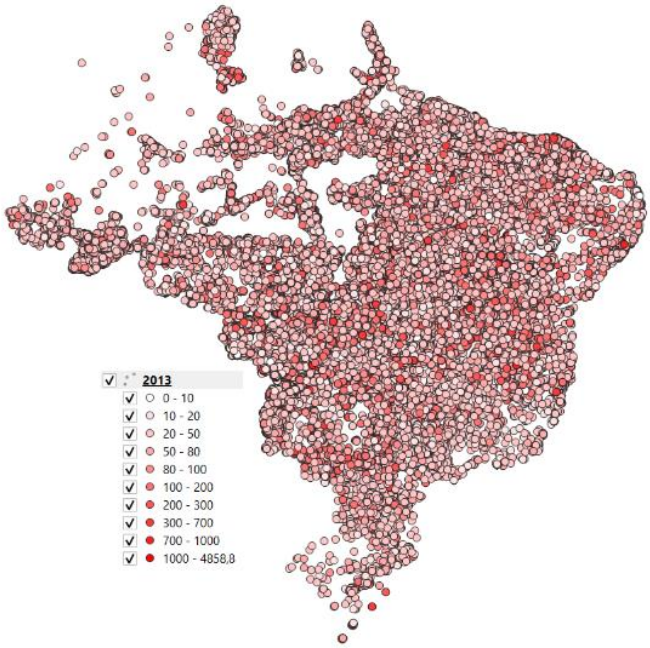

Figure 203 - Dispersion of MODIS FRPs values classified on the map with confidence ≥ 80 for the year 2013

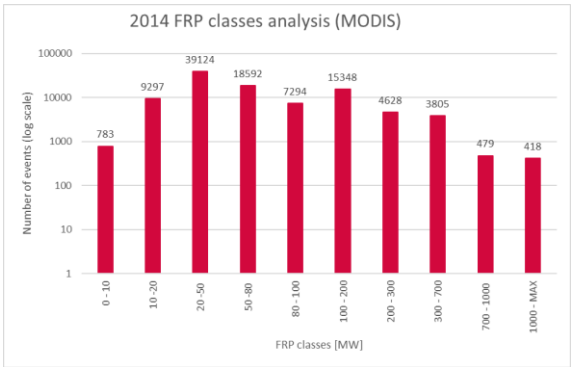

Figure 204 - Histogram describing the trend of the MODIS FRPs classes with confidence ≥ 80 in the year 2014

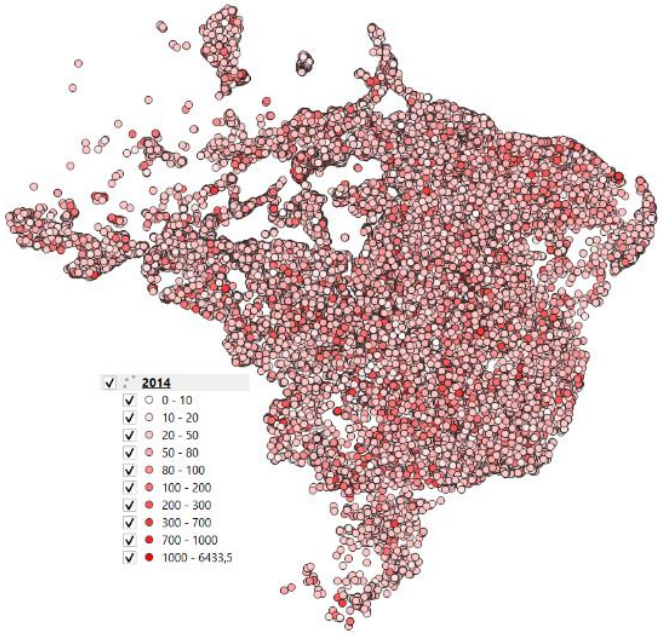

Figure 205 - Dispersion of MODIS FRPs values classified on the map with confidence ≥ 80 for the year 2014

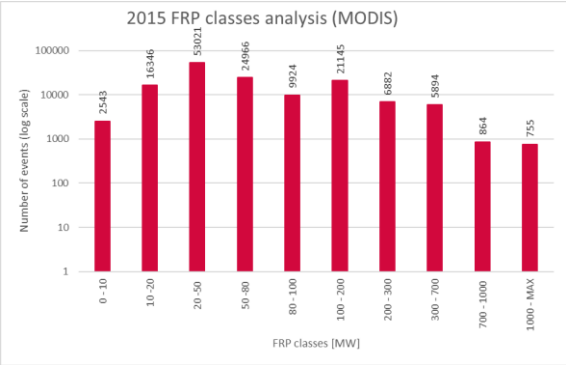

Figure 206 - Histogram describing the trend of the MODIS FRPs classes with confidence ≥ 80 in the year 2015

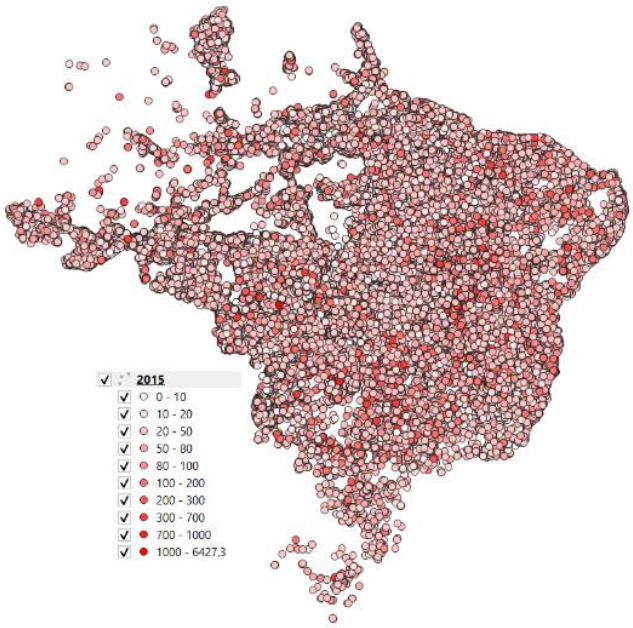

Figure 207 - Dispersion of MODIS FRPs values classified on the map with confidence ≥ 80 for the year 2015

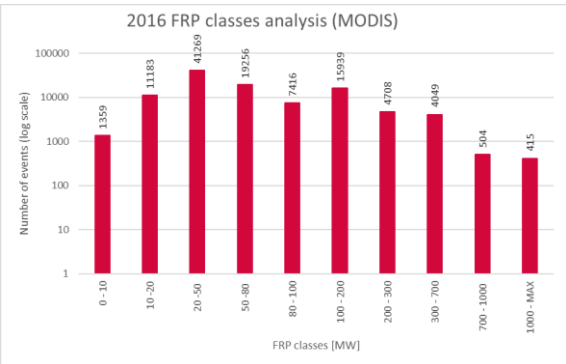

Figure 208 - Histogram describing the trend of the MODIS FRPs classes with confidence ≥ 80 in the year 2016

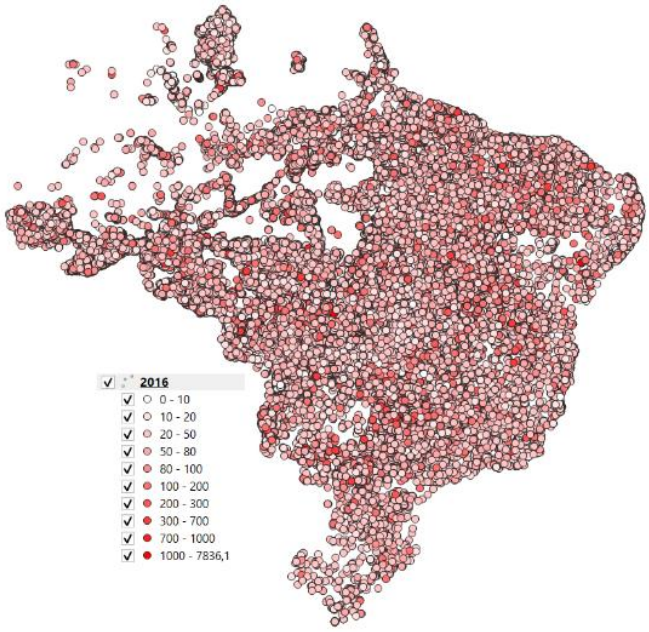

Figure 209 - Dispersion of MODIS FRPs values classified on the map with confidence ≥ 80 for the year 2016

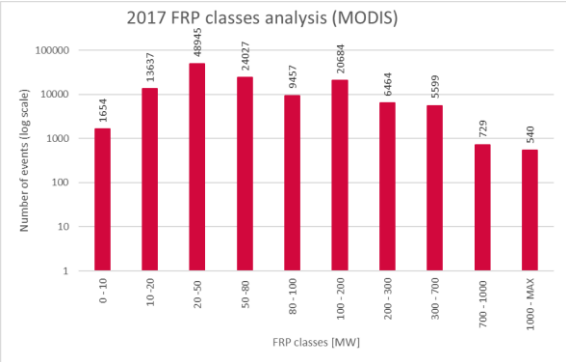

Figure 210 - Histogram describing the trend of the MODIS FRPs classes with confidence ≥ 80 in the year 2017

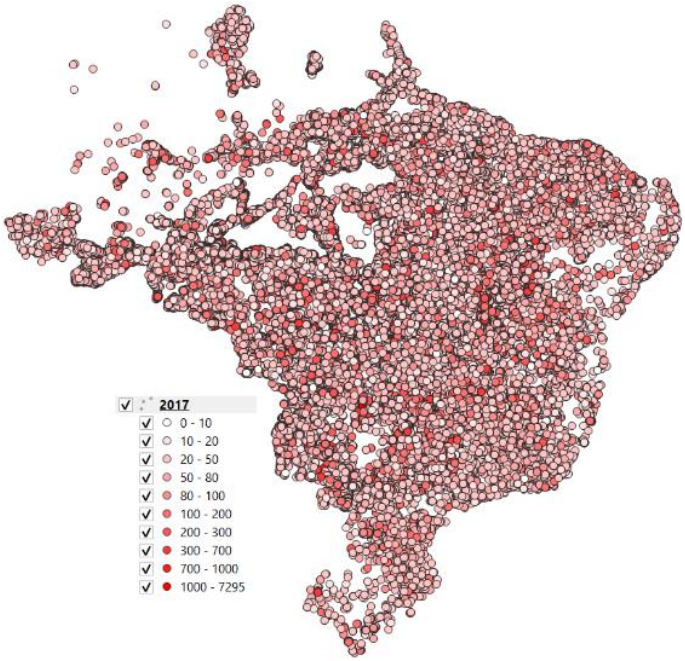

Figure 211 - Dispersion of MODIS FRPs values classified on the map with confidence ≥ 80 for the year 2017

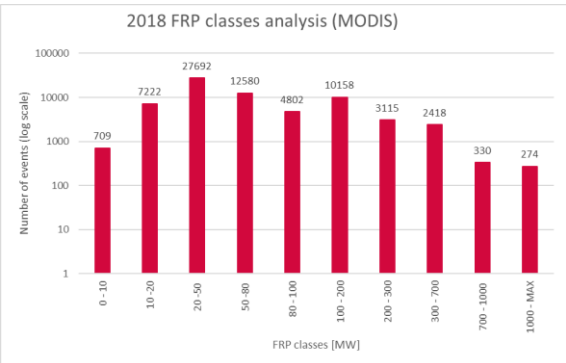

Figure 212 - Histogram describing the trend of the MODIS FRPs classes with confidence ≥ 80 in the year 2018

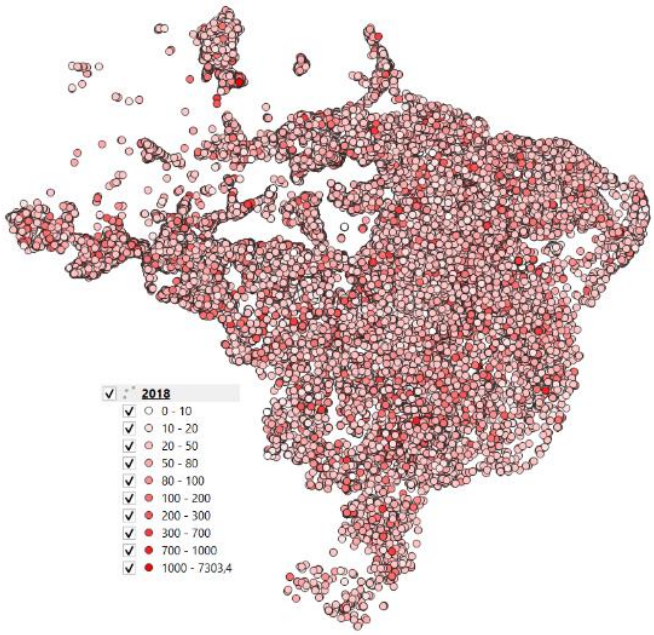

Figure 213 - Dispersion of MODIS FRPs values classified on the map with confidence ≥ 80 for the year 2018

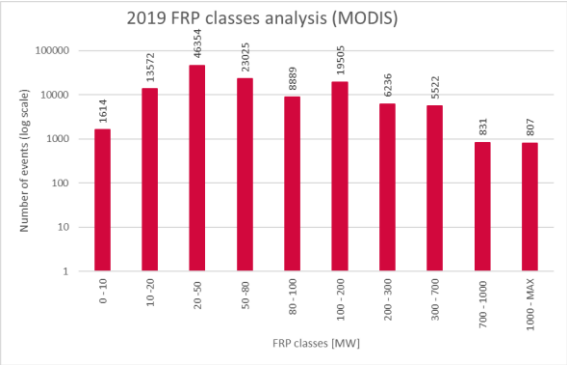

Figure 214 - Histogram describing the trend of the MODIS FRPs classes with confidence ≥ 80 in the year 2019

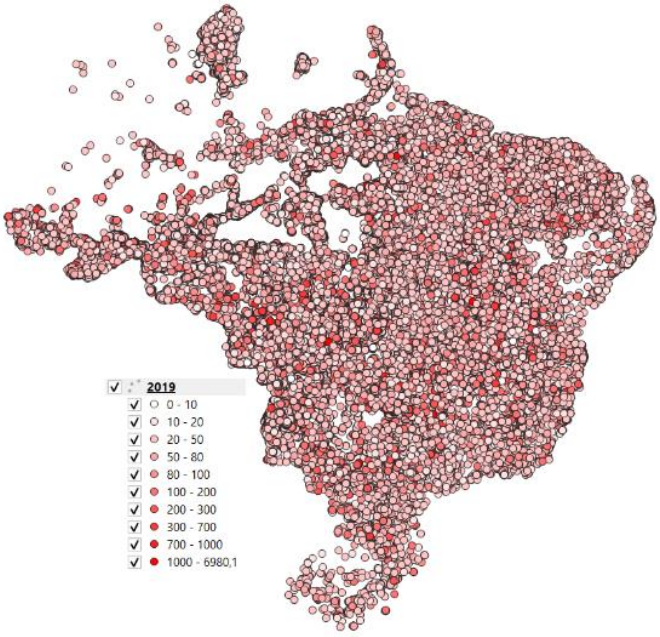

Figure 215 - Dispersion of MODIS FRPs values classified on the map with confidence ≥ 80 for the year 2019

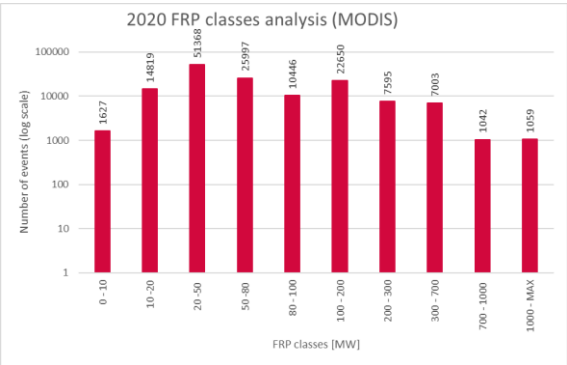

Figure 216 - Histogram describing the trend of the MODIS FRPs classes with confidence ≥ 80 in the year 2020

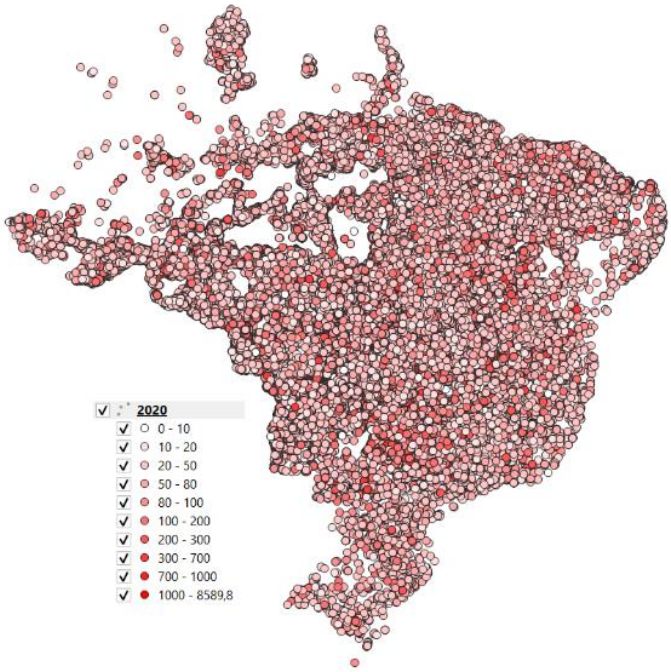

Figure 217 - Dispersion of MODIS FRPs values classified on the map with confidence ≥ 80 for the year 2020

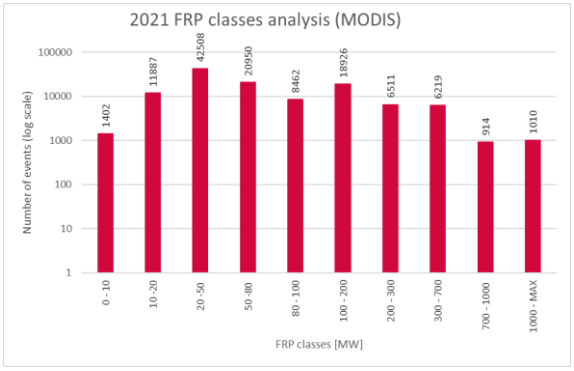

Figure 218 - Histogram describing the trend of the MODIS FRPs classes with confidence ≥ 80 in the year 2021

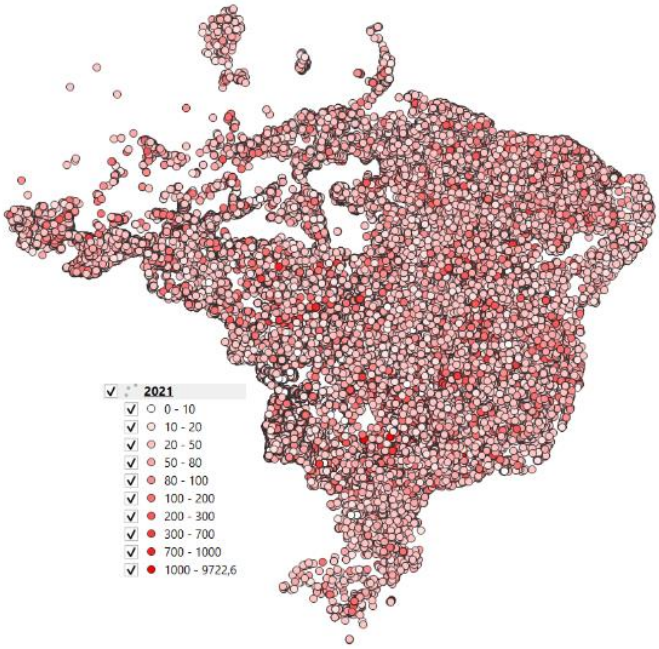

Figure 219 - Dispersion of MODIS FRPs values classified on the map with confidence ≥ 80 for the year 2021

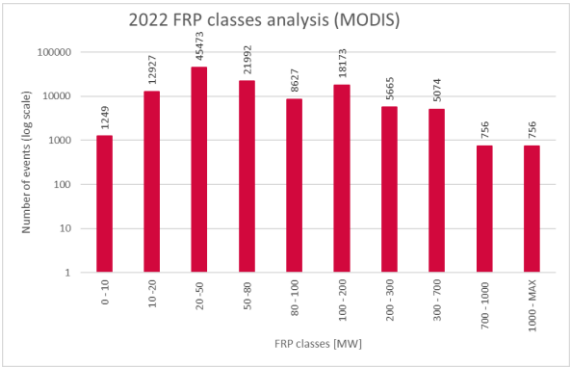

Figure 220 - Histogram describing the trend of the MODIS FRPs classes with confidence ≥ 80 in the year 2022

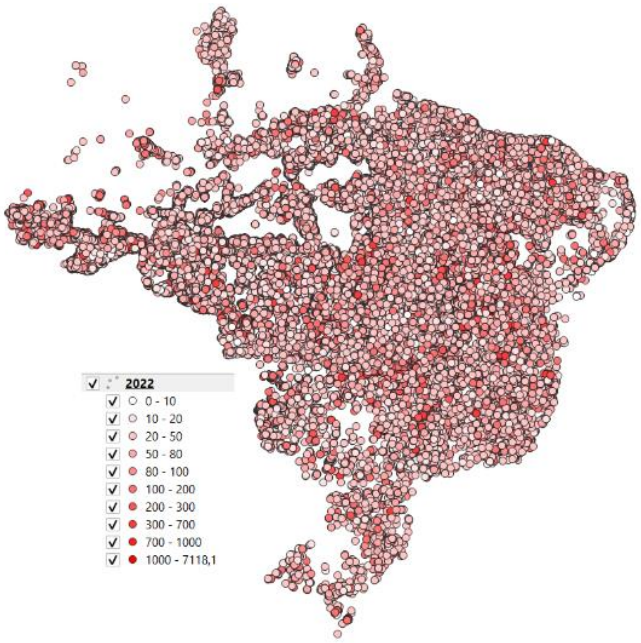

Figure 221 - Dispersion of MODIS FRPs values classified on the map with confidence ≥ 80 for the year 2022

3.4.4 VIIRS SUOMI NPP FRP ANALYSIS: FRP classification with CONFIDENCE = high

The following table shows for each year and for each class the corresponding number of events about the VIIRS SUOMI NPP data with confidence applied = high.

Years	Number of events	FRP classes										Max Value	MW Developed
		0 - 10	10 -20	20 -50	50 -80	80 - 100	100 - 200	200 - 300	300 - 700	700 - 1000	1000 - MAX		
2012	117'847	23'836	44'270	31'582	7'152	2'874	5'880	1'541	769	33	5	1'369.96	2'962'010
2013	54'678	11'775	21'874	14'398	2'756	1'052	2'101	501	260	9	5	1'900.97	1'243'555
2014	82'053	17'191	31'840	21'798	4'546	1'756	3'545	949	465	20	5	1'177.11	1'958'036
2015	118'305	22'929	45'044	32'187	7'479	2'777	5'672	1'536	722	33	5	1'086.66	2'945'183
2016	80'778	16'987	31'734	21'246	4'526	1'669	3'428	791	426	17	13	1'920.15	1'903'112
2017	108'370	21'254	41'429	29'561	6'667	2'430	4'997	1'374	684	44	9	1'725.14	2'692'696
2018	55'931	11'847	22'256	14'699	3'046	1'062	2'141	569	339	14	8	1'626.27	1'310'430
2019	102'466	20'236	38'319	28'191	6'261	2'380	4'991	1'342	787	44	7	1'282.11	2'629'985
2020	128'228	23'243	45'601	36'585	9'050	3'447	7'298	1'960	1'076	61	9	1'945.18	3'509'437
2021	97'286	17'412	34'228	27'036	7'005	2'743	6'026	1'753	1'084	54	15	1'298.76	2'824'671
2022	90'583	17'886	34'319	24'590	5'682	2'074	4'369	1'127	589	17	3	1'300.19	2'262'891

Table 18 - Number of events for each class in each year of the VIIRS SUOMI NPP FRPs with CONFIDENCE = high

In the second column you can see the total number of events, while the other columns of the tab. 18 show how many events there were for each class in each year.

The division into classes (Tab.18) using the confidence-filtered MODIS data shows that, for the most part, the data removed from the filtering are those of FRP<100 MW. The data with FRP>100 MW remained numerically almost unchanged compared to those in Tab. 16 (unfiltered). This is reflected in the qualitative view of the QGIS maps (for example Fig.224-226), this time represented with a predominance of red.

Considering the reliability of the data, the last column shows the amount of MW that have developed over the years; the calculation was carried out by multiplying the number of events in the given class by the corresponding value of [MW] in that class and finally summed up. A histogram representing the trend can be seen in Fig.222.

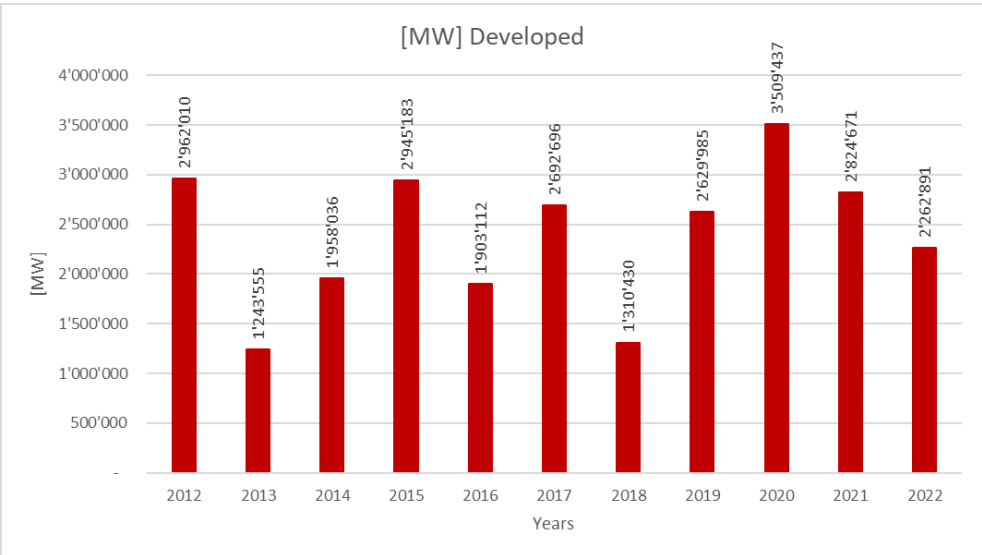

Figure 222 - Histogram describing the trend of the [MW] developed due to the FRP VIIRS S-NPP value with confidence applied

In the case of VIIRS data, the MW developed show a peak in the year 2012 and 2020.

On the following pages, it is possible to see a histogram for each year describing the trend of the quantity of FRPs events detected, according to the division into classes concerning the VIIRS SUOMI NPP data, and the same events on the map given by QGIS divided by colours according to the FRPs classes.

FRP classification representation

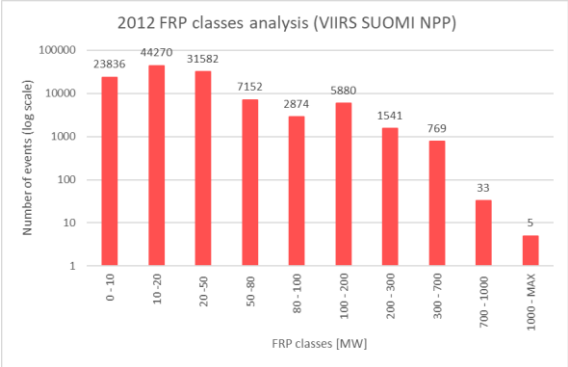

Figure 223 - Histogram describing the trend of the VIIRS SUOMI NPP FRPs classes with confidence= high for the year 2012

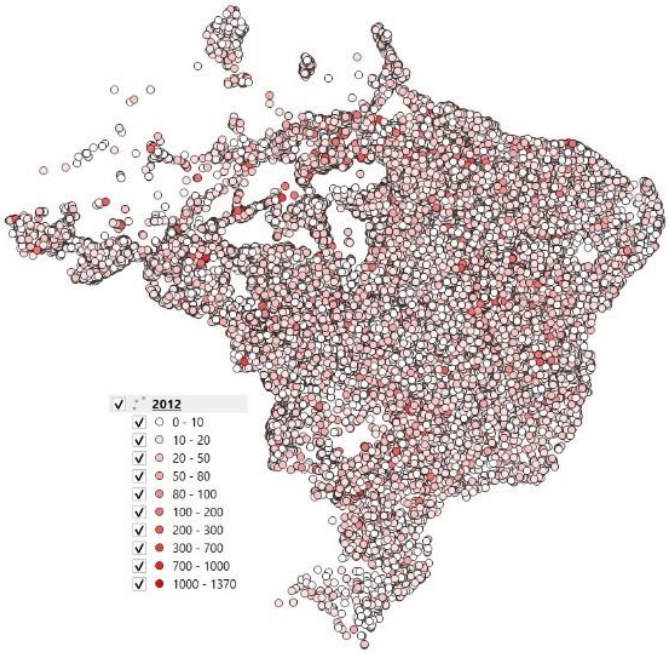

Figure 224 - - Dispersion of VIIRS SUOMI NPP FRPs values classified on the map with confidence = high for the year 2012

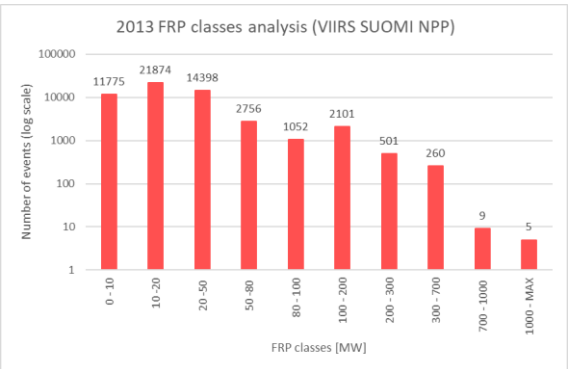

Figure 225 - Histogram describing the trend of the VIIRS SUOMI NPP FRPs classes with confidence =high for the year 2013

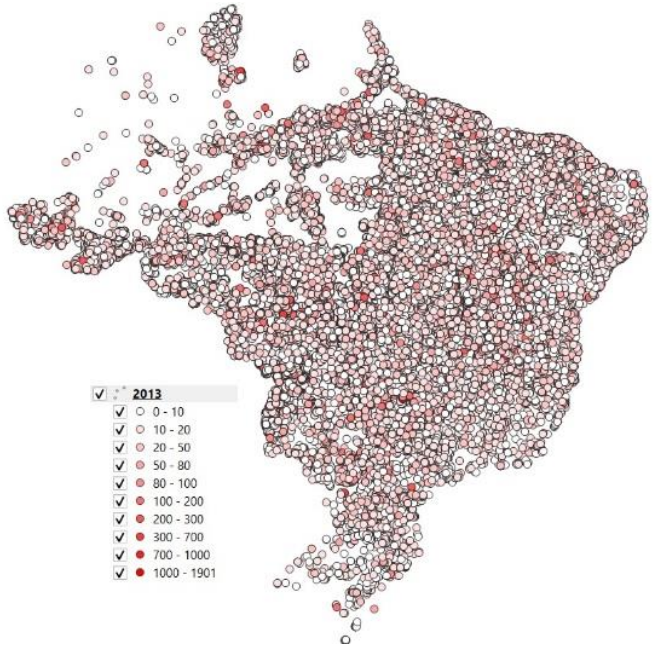

Figure 226 - Dispersion of VIIRS SUOMI NPP FRPs values classified on the map with confidence =high for the year 2013

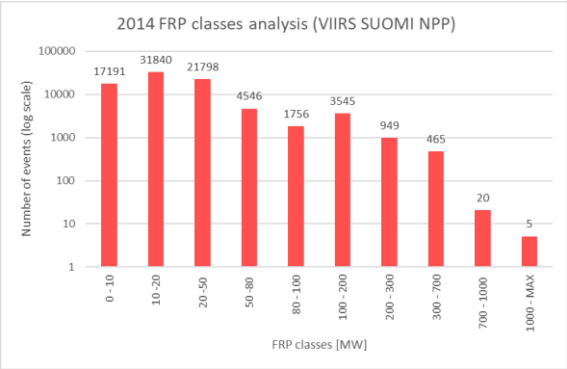

Figure 227 - Histogram describing the trend of the VIIRS SUOMI NPP FRPs classes with confidence =high for the year 2014

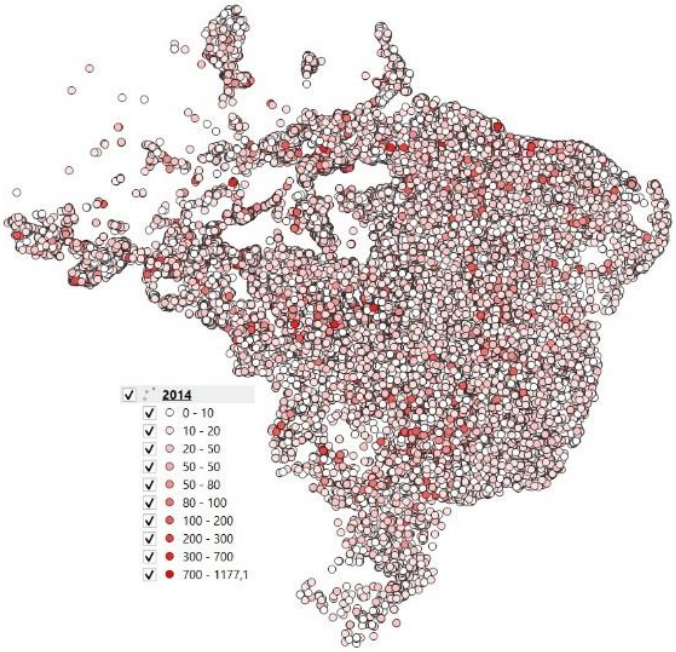

Figure 228 - Dispersion of VIIRS SUOMI NPP FRPs values classified on the map with confidence =high for the year 2014

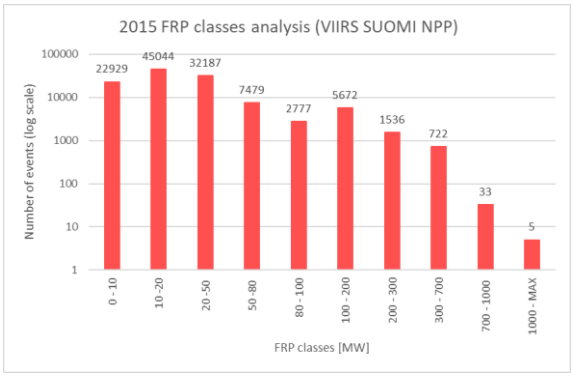

Figure 229 - Histogram describing the trend of the VIIRS SUOMI NPP FRPs classes with confidence =high for the year 2015

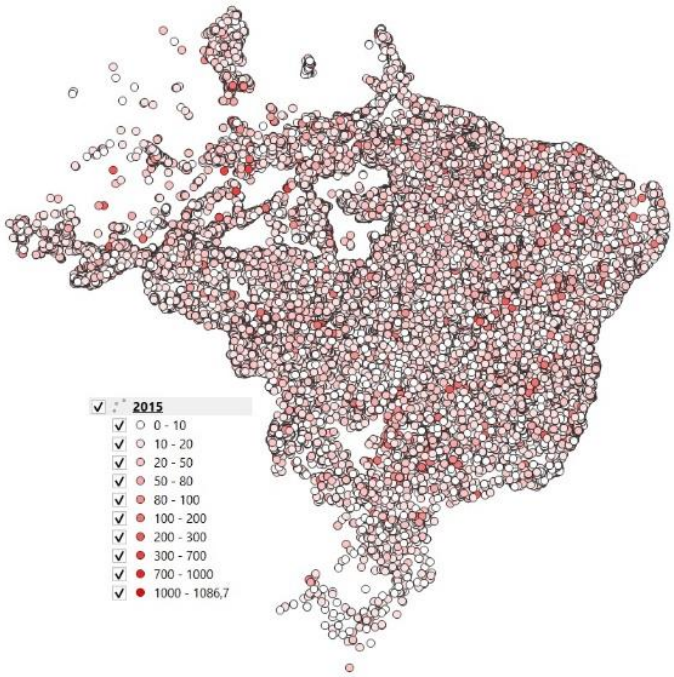

Figure 230 - Dispersion of VIIRS SUOMI NPP FRPs values classified on the map with confidence =high for the year 2015

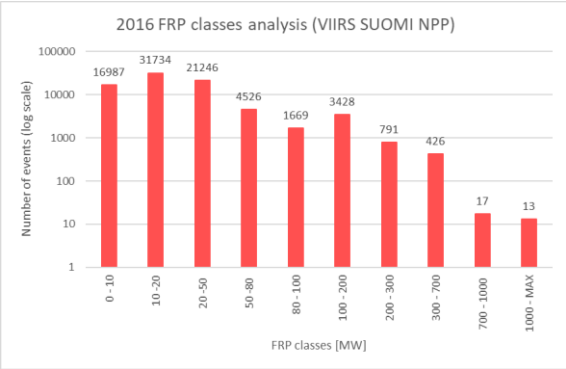

Figure 231 - - Histogram describing the trend of the VIIRS SUOMI NPP FRPs classes with confidence =high for the year 2016

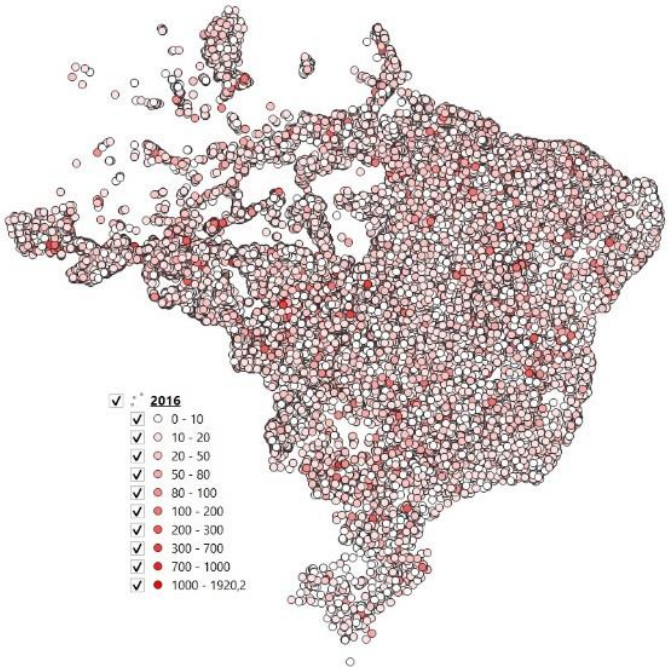

Figure 232 - Dispersion of VIIRS SUOMI NPP FRPs values classified on the map with confidence =high for the year 2016

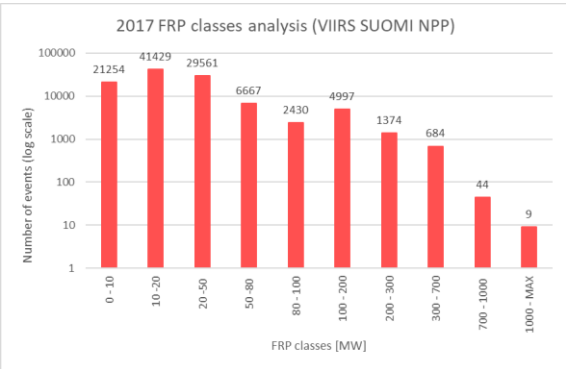

Figure 233 - Histogram describing the trend of the VIIRS SUOMI NPP FRPs classes with confidence =high for the year 2017

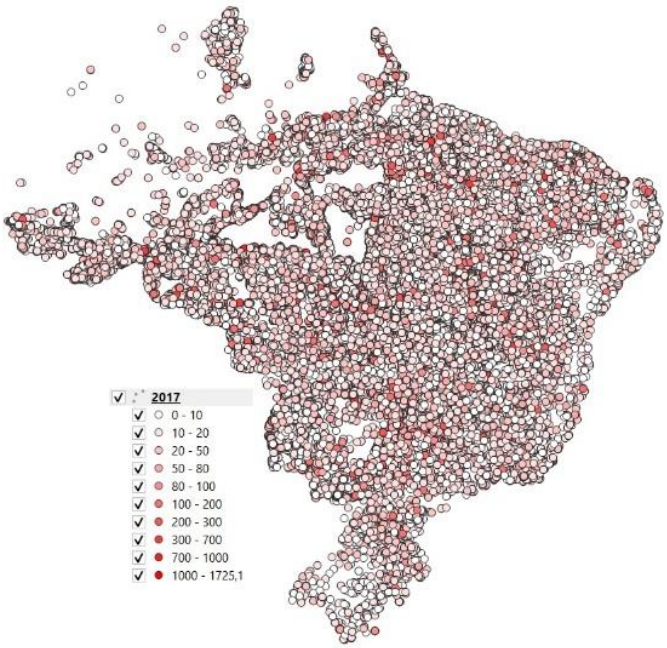

Figure 234 - Dispersion of VIIRS SUOMI NPP FRPs values classified on the map with confidence =high for the year 2017

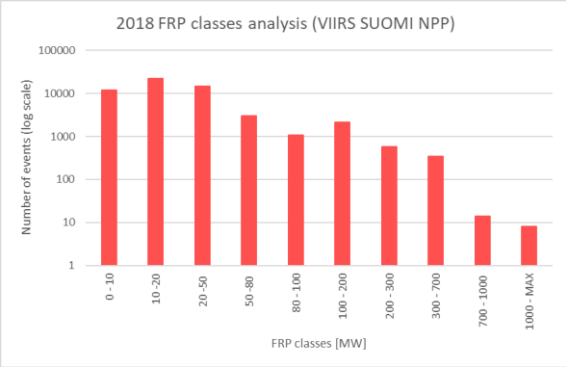

Figure 235 - Histogram describing the trend of the VIIRS SUOMI NPP FRPs classes with confidence =high for the year 2018

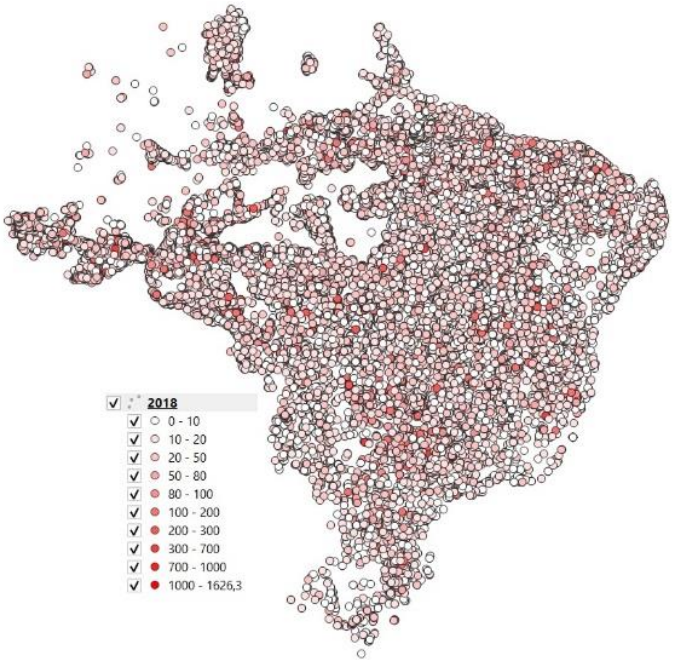

Figure 236 - Dispersion of VIIRS SUOMI NPP FRPs values classified on the map with confidence =high for the year 2018

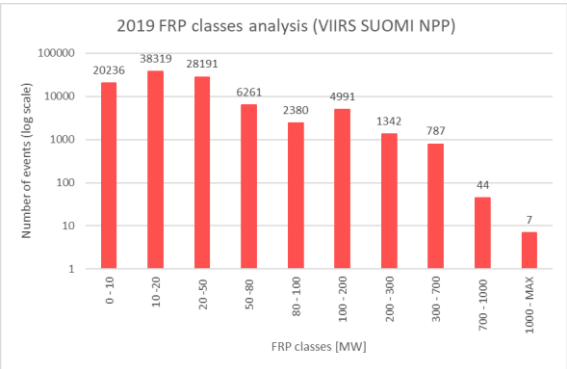

Figure 237 - Histogram describing the trend of the VIIRS SUOMI NPP FRPs classes with confidence =high for the year 2019

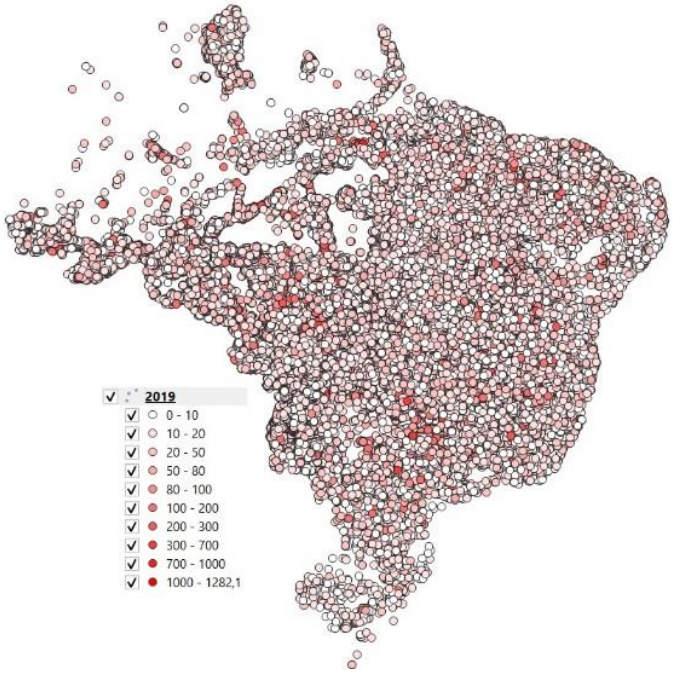

Figure 238 - Dispersion of VIIRS SUOMI NPP FRPs values classified on the map with confidence =high for the year 2019

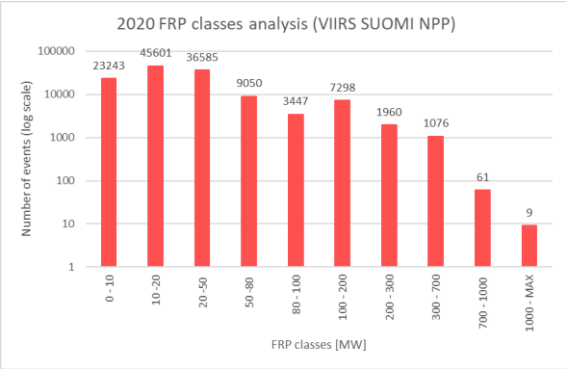

Figure 239 - Histogram describing the trend of the VIIRS SUOMI NPP FRPs classes with confidence =high for the year 2020

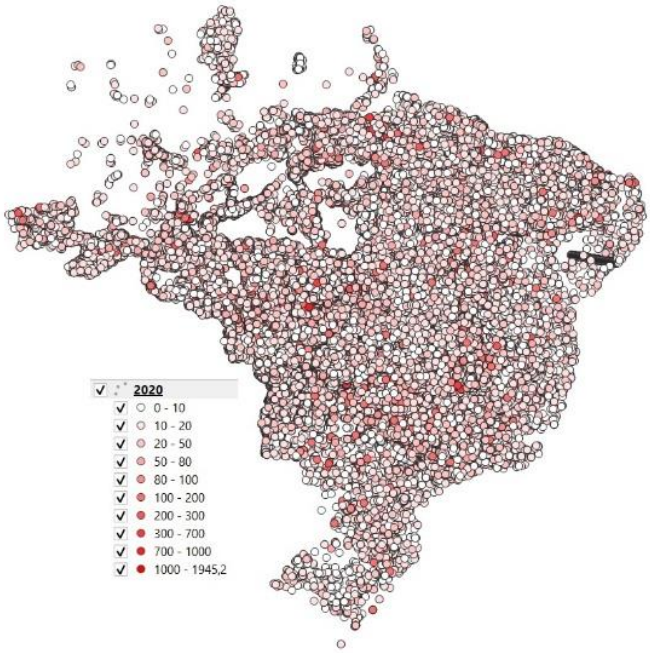

Figure 240 - Histogram describing the trend of the VIIRS SUOMI NPP FRPs classes with confidence =high for the year 2020

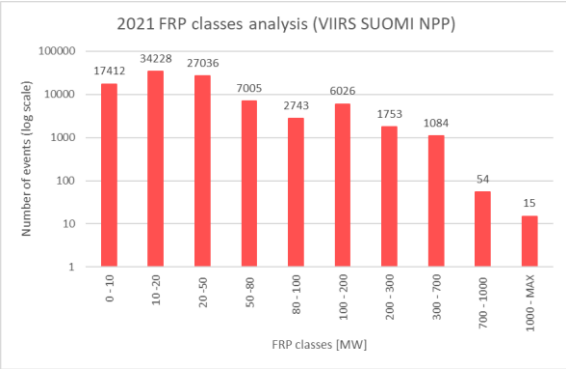

Figure 241 - Histogram describing the trend of the VIIRS SUOMI NPP FRPs classes with confidence =high for the year 2021

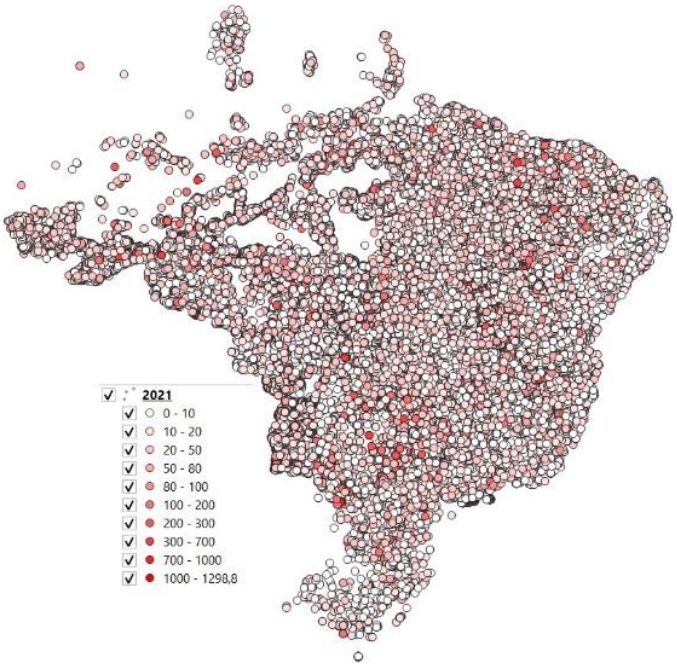

Figure 242 - Dispersion of VIIRS SUOMI NPP FRPs values classified on the map with confidence =high for the year 2021

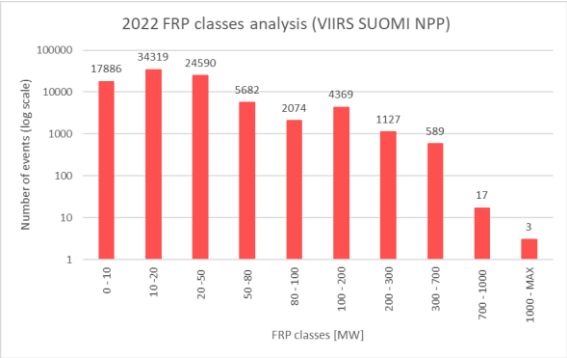

Figure 243 - Histogram describing the trend of the VIIRS SUOMI NPP FRPs classes with confidence =high for the year 2022

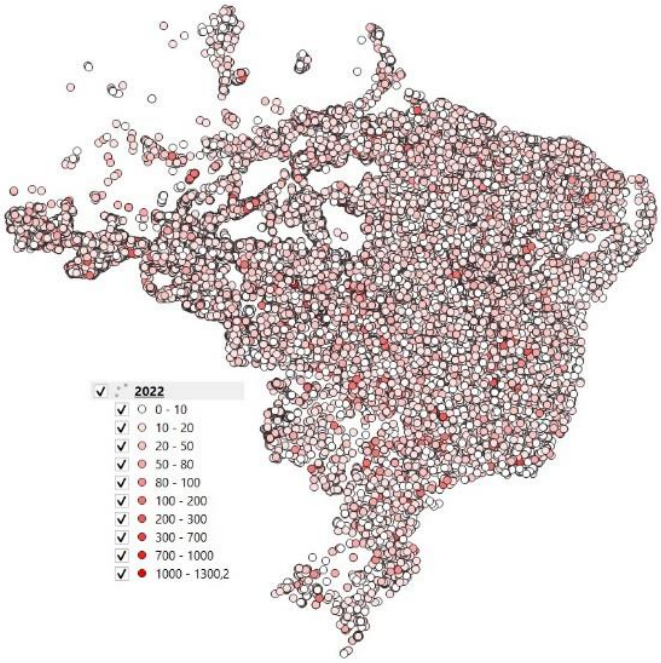

Figure 244 - Histogram describing the trend of the VIIRS SUOMI NPP FRPs classes with confidence =high for the year 2022

3.5 Statistical analysis: ANOMALIES

In data analysis, anomaly detection (also called outlier detection) is the identification of observations, items, rare events that differ significantly from the majority of the data.

An anomaly, in a set of observations, is an outlier, i.e. a value that is clearly distant from the other available observations. (Wikipedia 2022)

In this thesis, the mean value anomaly was calculated using this formula:

$$\text{Anomalies} = x_{i+1} - \frac{\sum_{i=1}^{n} x_i}{n}$$

Where x_i is the mean value, x_{i+1} is the mean value for the year concerned and n is the number of the observations considered.

As can be seen in the following tables, the anomalies have only been calculated for the last 5 years of data, which have a sufficient number of observations for the calculation.

Data filtered with the application of a confidence level proved to be more reliable, so the anomalies were calculated only in this case, for both sensors.

3.5.3 MODIS FRP Analysis: Anomalies of FRP Mean Values with CONFIDENCE ≥ 80 %

The FRP mean values from MODIS, with applied C ≥ 80 %, were used here for the calculation of the anomalies, the years considered being 2018 to 2022, so that there is enough previous data for the calculation. Both the calculation and the graph were made on Excel.

MODIS FRP	
Years	**Anomalies**
2018	-11,7104
2019	-0,0528
2020	5,1959
2021	10,3802
2022	-2,8421

Table 19 - Anomalies calculated for the last 5 years of annual mean values of MODIS FRP data with applied confidence ≥ 80%

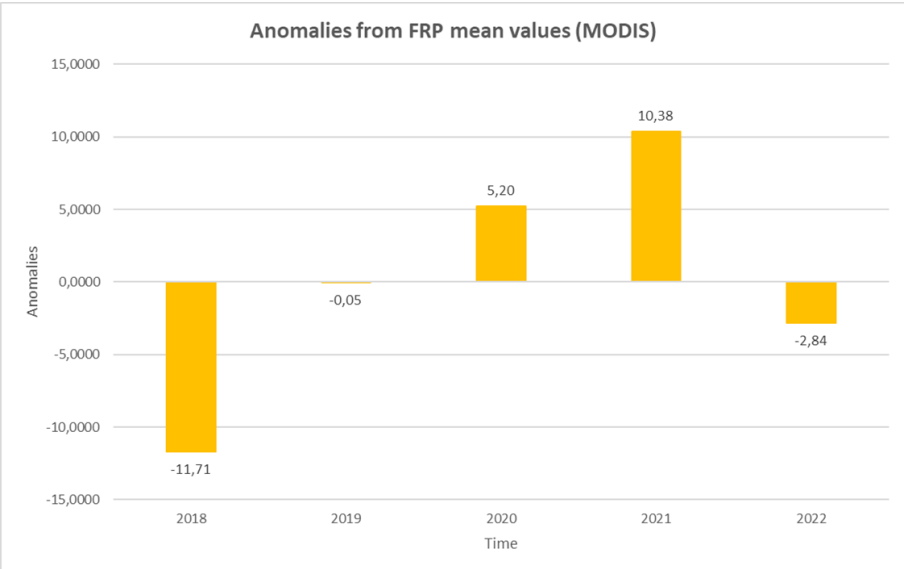

Figure 245 - Histogram describing the trend of the anomalies calculated for the last 5 years of annual mean values of MODIS FRP data with applied confidence ≥ 80%

The statistical anomalies in Fig 245. show an increasing trend, if we consider the standard deviation values to be high (Fig.105), the presence of these outliers is not of concern for the validity of our data.

3.5.4 VIIRS SUOMI NPP FRP ANALYSIS: Anomalies of FRP mean values with CONFIDENCE = high

The FRP mean values from VIIRS S-NPP, with C=high, were used here for the calculation of the anomalies, the years considered being 2018 to 2022, so that there is enough previous data for the calculation. Both the calculation and the graph were made on Excel

SUOMI FRP	
Years	**Anomalies**
2018	-1,4117
2019	2,4980
2020	4,9888
2021	7,1474
2022	-0,1683

Table 20 - Anomalies calculated for the last 5 years of annual mean values of VIIRS SUOMI NPP FRP data with applied confidence = high

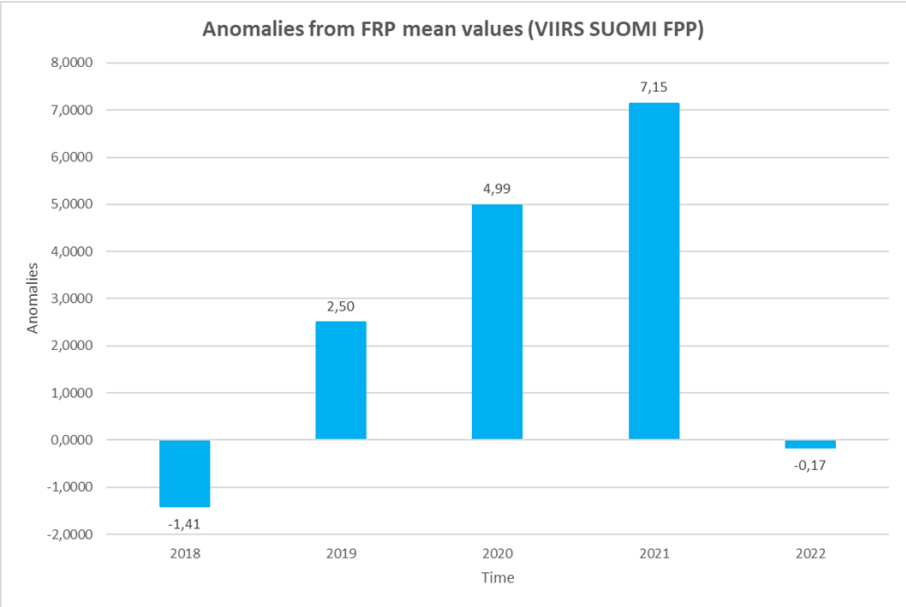

Figure 246 - Histogram describing the trend of the anomalies calculated for the last 5 years of annual mean values of VIIRS SUOMI NPP FRP data with applied confidence =high

The statistical anomalies in Fig 246. show an increasing trend, if we consider the standard deviation values to be high (Fig.109), the presence of these outliers is not of concern for the validity of our data.

3.6 Statistical analysis: TOTAL NUMBER OF EVENTS

In order to find out how many FAMF events occurred each year and compare them with each other, the annual data packages were used in QGIS to find out how many events there were each year and Excel to construct a histogram describing the trend.

This evaluation was carried out for both sensors, MODIS and VIIRS S-NPP, but only in the case with confidence-filtered data, as can be seen in the following chapters.

3.6.3 MODIS Data Analysis: Total Number of events with CONFIDENCE ≥ 80 %

MODIS	
Years	**Number of events**
2001	41062
2002	181656
2003	186966
2004	222935
2005	224859
2006	137997
2007	251476
2008	122735
2009	76762
2010	216295
2011	88097
2012	136253
2013	66749
2014	99431
2015	141753
2016	105708
2017	131240
2018	69022
2019	125854
2020	143037
2021	118365
2022	120335

Table 21 - Number of total events for each year about MODIS FRP data with applied confidence ≥ 80%

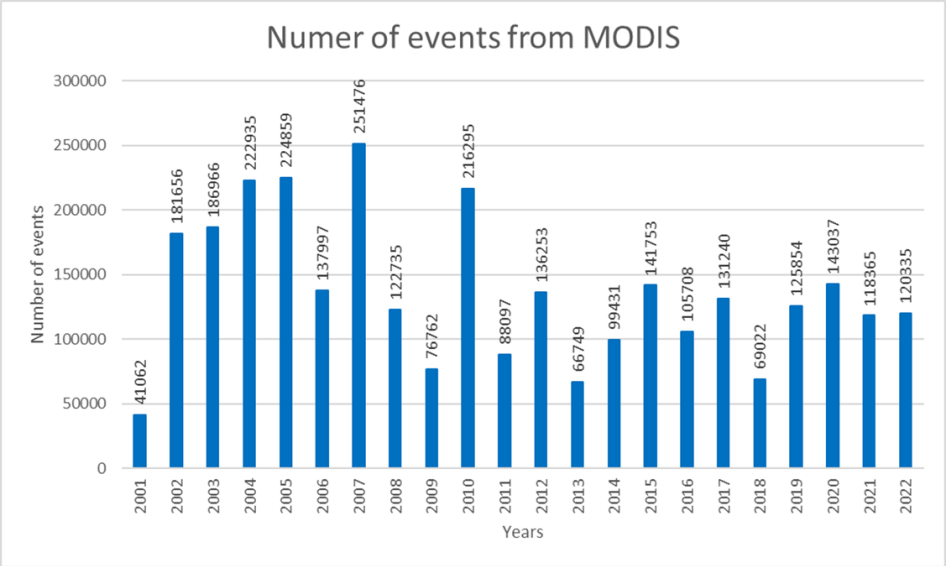

Figure 247 - Histogram describing the trend of the annual total number of events about MODIS FRP data with applied confidence ≥80%

The histogram in Fig. 247, with the total numbers of MODIS FRP events over the years, confirms a constant trend over the years with peaks in the years 2004,2005,2007,2010,2015,2019,2020.

3.6.4 VIIRS SUOMI NPP Data Analysis: Total Number of events with CONFIDENCE = high

VIIRS SUOMI FPP	
Years	**Number of events**
2012	117847
2013	54678
2014	82053
2015	118305
2016	80778
2017	108370
2018	55931
2019	102466
2020	128228
2021	97286
2022	90583

Table 22 - Number of total events for each year about VIIRS SUOMI NPP FRP data with applied confidence = high

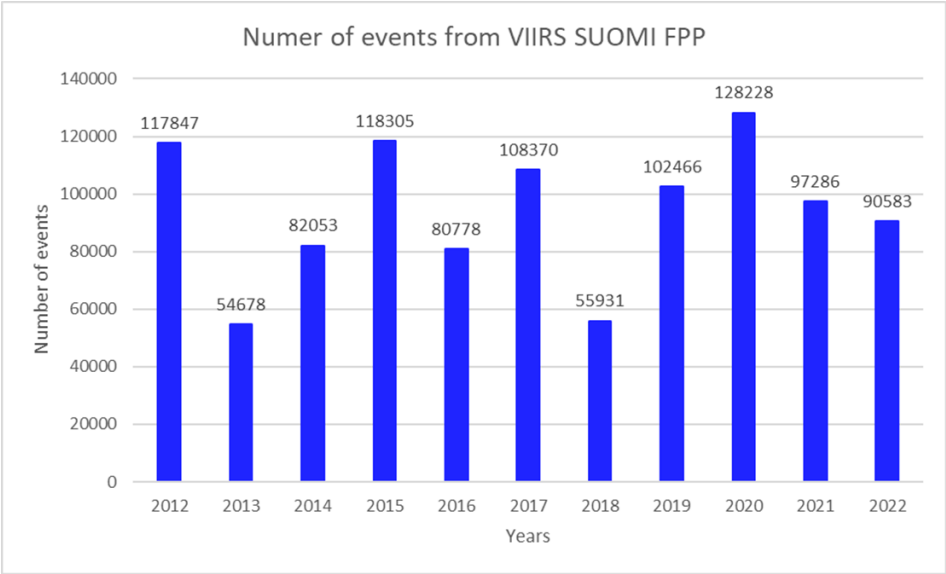

Figure 248 - Histogram describing the trend of the annual total number of events about VIIRS SUOMI NPP FRP data with confidence =high

The histogram in Fig. 248, with the total numbers of VIIRS S-NPP FRP events over the years, confirms a constant trend over the years with peaks in the years 2012,2015,2019,2020.

3.7 Statistical analysis: NUMBER OF EVENTS FOR FRP≥100MW

The purpose of this chapter is to find out how many FAMF events per year have a FRP ≥ 100 MW.

These results were taken after the division into classes discussed in Chapter 3.4, the division into FRP classes allowed us to see how many FAMF events there were for each class and those with FRP≥100 was added together.

These operations, carried out on Excel, were performed for both sensors treated and for data with the confidence filter.

3.7.3 MODIS Data Analysis: Number of FRP events ≥ 100 MW (with CONFIDENCE ≥ 80%)

MODIS	
Years	**FRP ≥ 100**
2001	8288
2002	53215
2003	54356
2004	67799
2005	66459
2006	38891
2007	72690
2008	33347
2009	17337
2010	62030
2011	22523
2012	36816
2013	15216
2014	24678
2015	35540
2016	25615
2017	34016
2018	16295
2019	32901
2020	39349
2021	33580
2022	30424

Table 23 - Number of MODIS FRP events (with applied confidence≥80%) with FRP ≥ 100 MW for each year

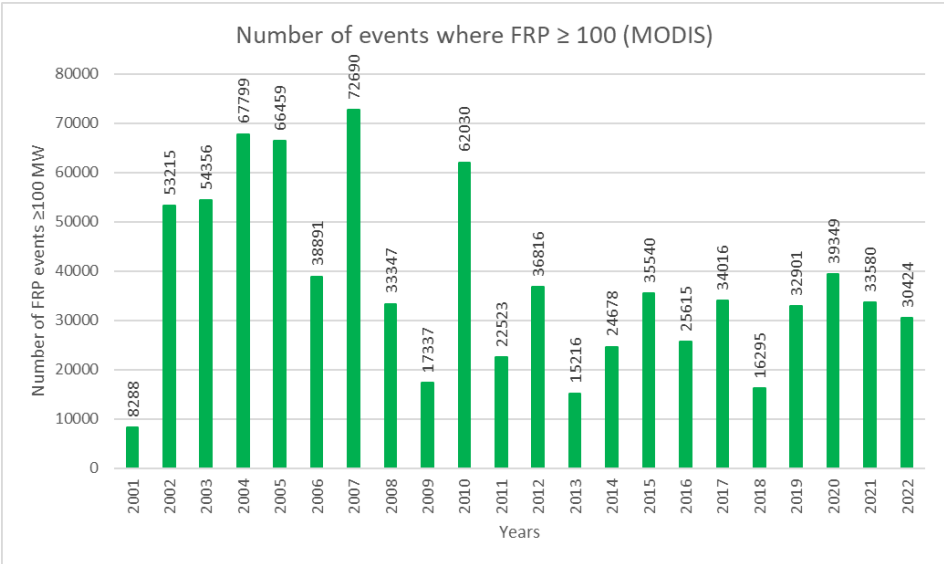

Figure 249 - Histogram describing the number of MODIS FRP events (with confidence ≥ 80%) with FRP ≥ 100 MW in the years

The histogram in Fig. 249, with the numbers of MODIS FRP≥100 MW events over the years, confirms a constant trend over the years with peaks in the years 2004,2005,2007,2010,2015,2020.

3.7.4 VIIRS S-NPP Data Analysis: Number of FRP events ≥ 100 MW (with CONFIDENCE = high)

VIIRS SUOMI FPP	
Years	**FRP ≥ 100**
2012	8228
2013	2876
2014	4984
2015	7968
2016	14253
2017	7108
2018	3071
2019	7171
2020	10404
2021	8932
2022	6105

Table 24 - Number of VIIRS SUOMI NPP FRP events (with applied confidence=high) with FRP ≥ 100 MW for each year

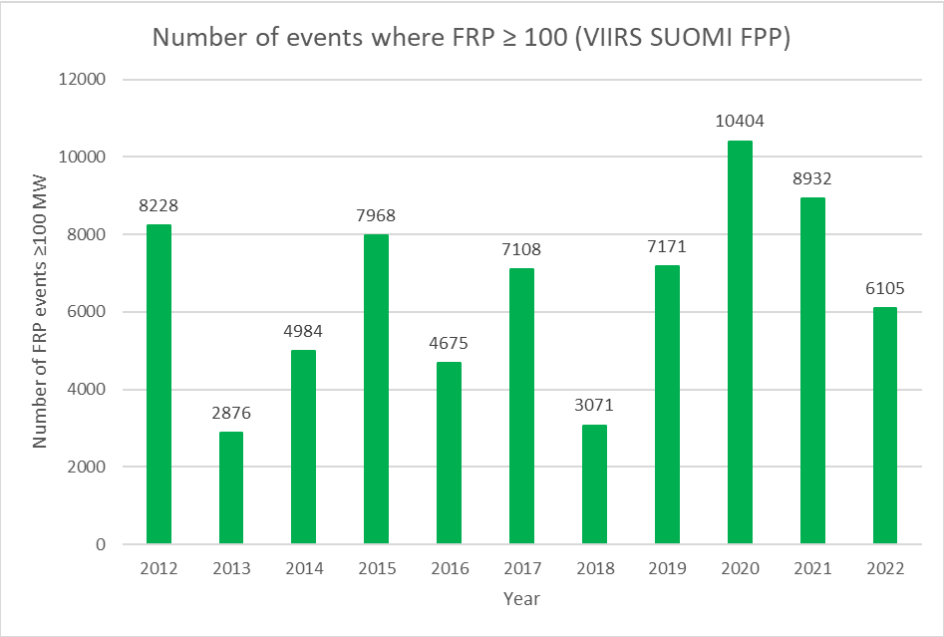

Figure 250 - Histogram describing the number of VIIRS SUOMI NPP FRP events (with confidence =high) with FRP ≥ 100 MW in the years

The histogram in Fig. 250, with the numbers of VIIRS SUOMI NPP FRP≥100 MW events over the years, confirms a constant trend over the years with peaks in the years 2012,2015,2020,2021.

3.8 Statistical analysis: NUMBER OF EVENTS FOR FRP≥300MW

The purpose of this chapter is to find out how many FAMF events per year have a FRP ≥ 300 MW.

These results were taken after the division into classes discussed in Chapter 3.4, the division into FRP classes allowed us to see how many FAMF events there were for each class and those with FRP≥300 was added together.

These operations, carried out on Excel, were performed for both sensors treated and for data with the confidence filter.

3.8.3 MODIS Data Analysis: Number of FRP events ≥ 300 MW (with CONFIDENCE ≥ 80%)

MODIS	
Years	**FRP ≥ 300**
2001	1489
2002	13269
2003	13350
2004	17499
2005	16503
2006	9206
2007	16565
2008	6716
2009	2947
2010	13598
2011	4357
2012	7763
2013	2654
2014	4702
2015	7513
2016	4968
2017	6868
2018	3022
2019	7160
2020	9104
2021	8143
2022	6586

Table 25 - Number of MODIS FRP events (with applied confidence≥80%) with FRP ≥ 300 MW for each year

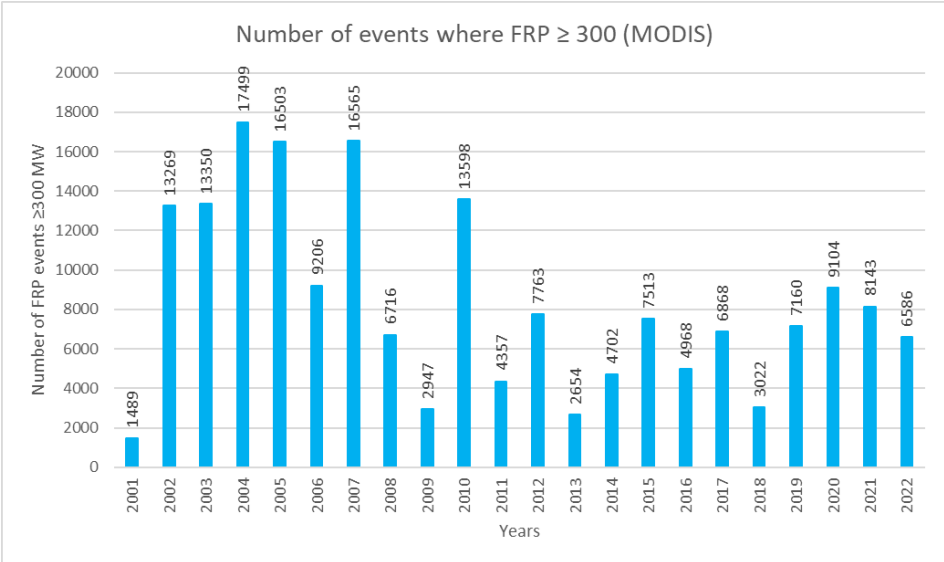

Figure 251 - Histogram describing the number of MODIS FRP events (with confidence ≥ 80%) with FRP ≥ 300 MW in the years

The histogram in Fig. 251, with the numbers of MODIS FRP≥300 MW events over the years, confirms, as Fig. 249, a constant trend over the years with peaks in the years 2004,2005,2007,2010,2015,2020.

3.8.4 VIIRS SUOMI NPP Data Analysis: Number of FRP events ≥ 300 MW (with CONFIDENCE = high)

VIIRS SUOMI FPP	
Years	**FRP ≥ 300**
2012	807
2013	274
2014	490
2015	760
2016	456
2017	737
2018	361
2019	838
2020	1146
2021	1153
2022	609

Table 26 - Number of VIIRS SUOMI NPP FRP events (with applied confidence=high) with FRP ≥ 300 MW for each year

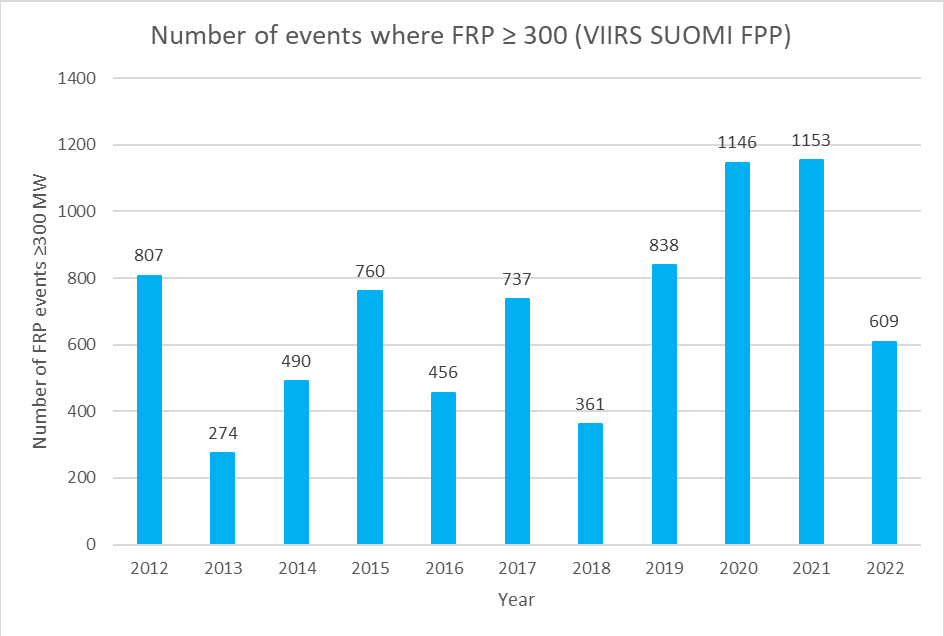

Figure 252 - Histogram describing the number of VIIRS SUOMI NPP FRP events (with confidence =high) with FRP ≥ 300 MW in the years

The histogram in Fig. 252, with the numbers of VIIRS SUOMI NPP FRP≥300 MW events over the years, confirms, as Fig.250, a constant trend over the years with peaks in the years 2012,2015,2020,2021.

3.9 GRAPHICAL ANALYSIS OF IMAGES: Fire and Thermal Anomalies provides from Worldview system

NASA provides insights into fires and thermal anomalies occurring daily around the world. Satellite-derived fire data and imagery available in Worldview are from the MODIS instrument aboard the Terra and Aqua satellites and the VIIRS instrument aboard the joint NASA/NOAA Suomi NPP and NOAA-20 satellites. Terra passes over the equator at approximately 10:30am (Day) and 10:30pm (Night) local time, NOAA-20 passes over the equator at approximately 12:40pm (Day) and 12:40am (Night) local time, and Aqua and Suomi NPP passes over the equator at approximately 1:30pm (Day) and 1:30am (Night) local time. The fire informations are available within Worldview approximately 3 hours after satellite overpass.

Data collected by the satellites utilize an algorithm that exploits the strong emission of mid-infrared radiation from fires and thermal anomalies - these fires and thermal anomalies are shown as orange (MODIS) or red (VIIRS) points. The points represent the center of a pixel within which one or multiple fires have occurred. For the MODIS instrument the point represents the center of a 1km pixel, for the VIIRS instrument the point represents the center of a 375m pixel.

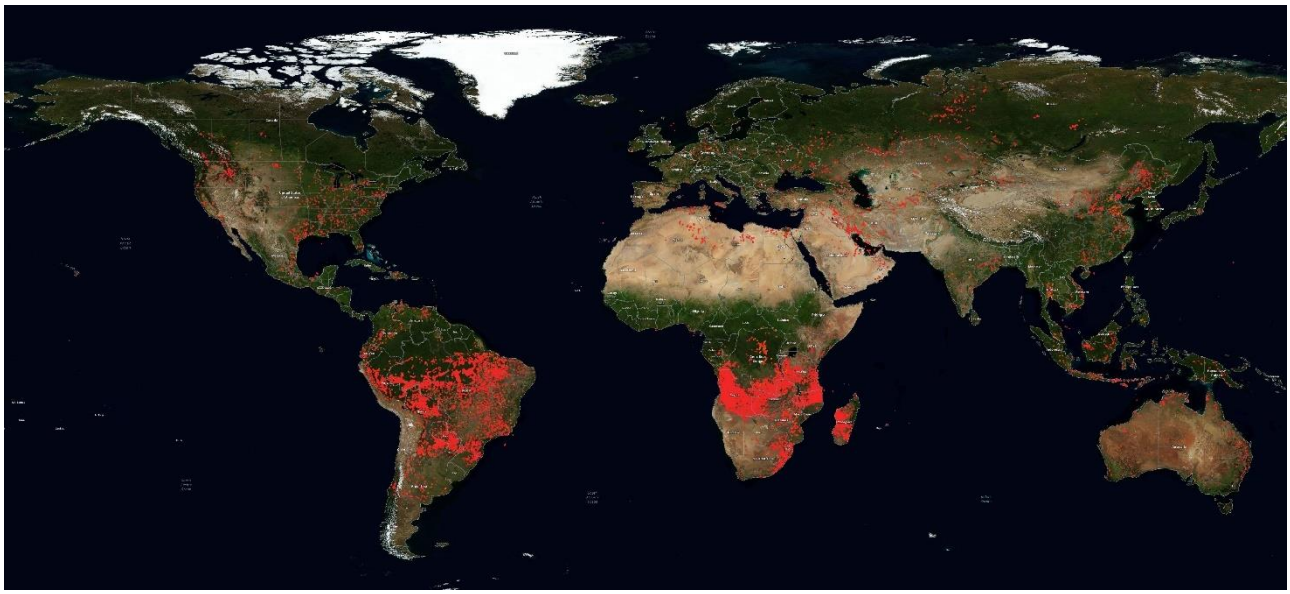

Figure 253 - Example of an image provided by the Worldview system of Fire and Thermal Anomalies in the world of 1st September 2022

In the next chapter there are pictures showing FAMF events (red dots) in the territory of Brazil.

The images from the Worldview portal were scanned using the 'Snapshot' function after setting the location and dates.

The dates chosen for this quick qualitative analysis concern daily data from January, February, March and April of 2022 and 2023 respectively.

The comparison should emphasise the difference in FAMF events that occurred and did not occur given the change in the country's political leadership.

3.9.1 Fire and Thermal Anomalies provides from Worldview system

Figure 254 - Amazon Forest with Fire and Thermal Anomalies January 2022

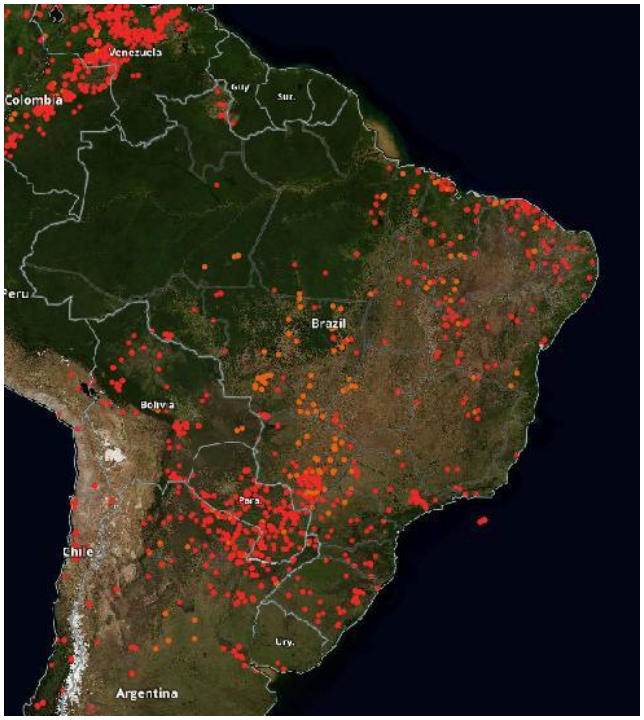

Figure 255 - Amazon Forest with Fire and Thermal Anomalies January 2023

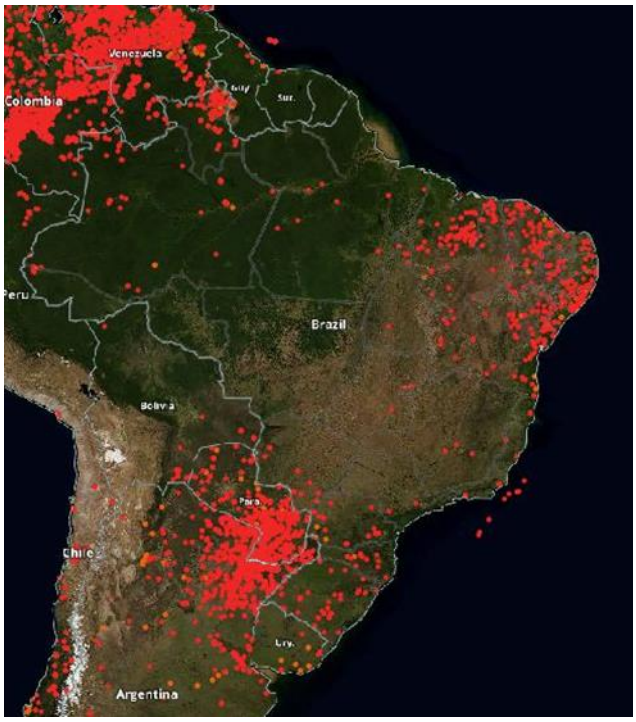

Figure 256 - Amazon Forest with Fire and Thermal Anomalies February 2022

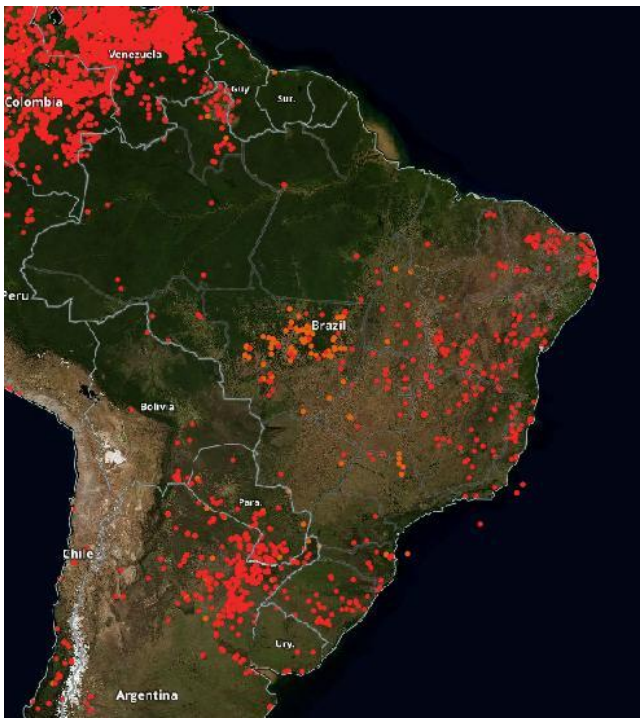

Figure 257 - Amazon Forest with Fire and Thermal Anomalies February 2023

Figure 258 - Amazon Forest with Fire and Thermal Anomalies March 2022

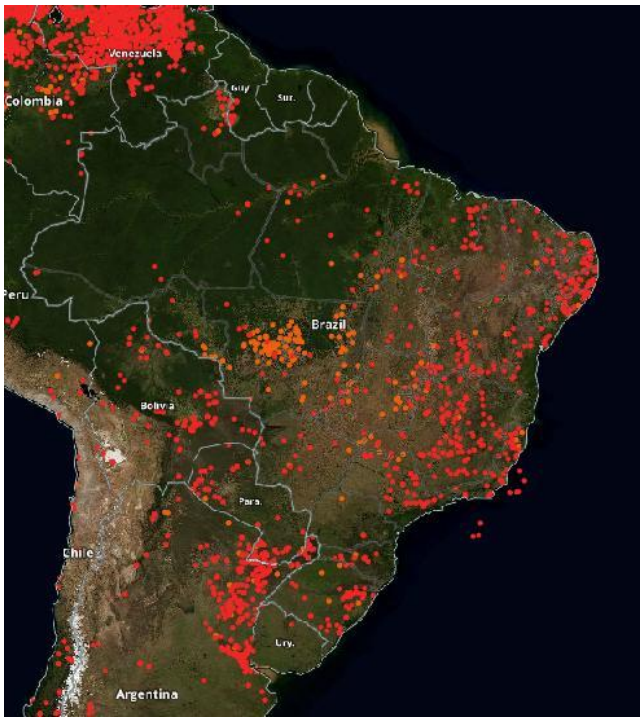

Figure 259 - Amazon Forest with Fire and Thermal Anomalies March 2023

Figure 260 - Amazon Forest with Fire and Thermal Anomalies April 2022

Figure 261 - Amazon Forest with Fire and Thermal Anomalies April 2023

The comparison, unfortunately, concerns little data because this thesis ends in May 2023, so the dry season has not yet begun. in any case, in the Brazilian Amazon Rainforest the FAMF events for January, March and April are similar, while it can be seen that in February the year 2022 had more events than the year 2023.

4. Conclusions

Fires are a critical part of the Earth System. In recent decades, they have altered the structure of ecosystems, biogeochemical cycles, and the composition of the atmosphere with unprecedented rapidity.

Satellite data on active fires have been widely used to study regional and global forest fire activity and their impact on air quality and environmental changes over the past decades.

This study is about fires in the Amazon Rainforest, studied through data collected by the MODIS and VIIRS sensors.

The most important variable for characterizing wildfires is fire radiative power (FRP) (i.e. the radiant energy released by fires), because it is a crucial variable to estimate socio-ecological impacts of fires as well as burned biomass and fire-induced emissions.

The first step in this work was, in fact, the qualitative analysis of the images that these satellites provide through the FIRMS web portal.

As mentioned above, the images show FAMFs for three months in each year since 2001. Comparing the various images, it can be seen that:

- for the month of August, the highest number of events is recorded in the years 2004, 2005, 2007 and then from 2017 to 2022;
- for the month of October, the highest number of events is recorded in the year 2004 and from 2017 to 2022;
- for December, the highest number of events is recorded in the year 2017 and from 2019 to 2022.

Note that for all three months used for the comparison the years 2019 to 2022 have a significant increase in fires, this could be due to an increase in the data collected because the VIIRS satellite has been in operation since 2012, but more probably it is due to Bolsonaro taking office as President of Brazil. Early in his term he decided, for example, to turn over indigenous reserves, which were previously managed by indigenous peoples, to the Ministry of Agriculture whose main interest is to make way for crops such as soybeans.

Bolsonaro then has an indirect responsibility: there is a law in Brazil that prohibits landowners from clearing more than one-fifth of their holdings. Bolsonaro has not changed this law, but since he became president, government operations to ensure the enforcement of this law have decreased, from January to April, by 70 percent, compared to the same period the previous year. This impunity would have led many landowners to stop complying with the measure and thus caused a large number of trees to be cut down and/or wildfires to develop.

The months of August, October, and December were chosen both because of the presence of the dry season but also because as can be seen in the quantitative analysis, in the first chapter that discusses the identification of the maximum FRP value, the maximum FRP values occur more or less during these periods.

In fact, in Tab.7 and Fig.92, which cover the maximum FRP values measured by MODIS, it can be seen that the maximum value is in the years 2004, 2005, 2007, and then the trend rises from 2016, peaking in 2021.

The data coming from VIIRS show that the trend of maximum values, observed in Fig.95, regarding the maximum FRP values of the VIIRS S-NPP shows an almost constant distribution, around the FRP value of 1500 MW. It is also possible to notice a peak in the values corresponding to the year 2020.

In each statistical analysis, a confidence was also chosen to be applied later. The confidence level is chosen to be applied to eliminate commissioning errors but also because extreme forest fires are chosen to be analysed, i.e., those whose intensity (FRP) was greater than or equal to 80 percent of the distribution of variables. Extreme fires contribute a large proportion of the total forest burned because the confidence level indicates that the data is less subject to error and because, it is possible that 70% of the extreme fires also fall within the largest 5% of fires (by area) identified.

After the confidence level is applied, the maximum FRP values from both MODIS and VIIRS do not change; the values remain the same in terms of both FRP and date and location of the event.

Comparison of the mean value with the standard deviation for both MODIS and VIIRS highlights a large standard deviation value compared with the mean, i.e., a significant deviation from the mean value of FRP.

A subsequent comparison made between the mean and median values of FRP, indicates that the standard deviation does not indicate an error in the data but, that these, are very different from each other.

In this regard, the division into classes (Chapter3.4) draws attention to the high presence of low FRP values, i.e., predominance of FRP values between 0 - 10 MW or otherwise the predominance of FRP values is in the range 0<FRP<100 [MW], especially in VIIRS data.

The application of confidence in both sensors does not result in significant changes in the behaviour of the mean value and the corresponding standard deviation, but the application of confidence is very useful when analysing total events.

Comparing, for example, the subdivision into classes of the FRP MODIS of chapter 3.4.1 (all data present) and that of chapter 3.4.3 (data filtered by confidence), it is evident how the application of the confidence level is very important in order to eliminate commission errors. In fact, the values that suffer a decrease are those of FRP<100 MW, on the contrary, the values of FRP >100 MW suffer a slight decrease, these considerations are valid for each year analysed.

This observation is also valid for the VIIRS data, where the difference between the data results with or without the confidence level applied is visually evident in the QGIS maps. Without the confidence level, the map is in fact predominantly white, and this colour coincides with the range 0<FRP<10 MW, whereas the values of FRP>100 MW, after filtering, decrease more than the same situation in the MODIS data.

The number of total MODIS and VIIRS events calculated before and after filtering are very different, undergoing a considerable decrease.

This diversity of data, resulted in a subsequent choice to show only data filtered through the confidence level, reflecting good data quality and configuration.

In the Chapter 3.6.3, the histogram in Fig. 247, with the total numbers of MODIS FRP events over the years, confirms a constant trend over the years with peaks in the years 2004,2005,2007,2010,2015,2019,2020. The histogram in Fig. 248, with the total numbers of VIIRS S-NPP FRP events over the years, confirms a constant trend over the years with peaks in the years 2012,2015,2019,2020.

Sections 3.7 and 3.8 show the number of events with FRP>100 MW and FRP>300 MW (from both sensors) and confirm the previous statements about the years with higher number of events, which in this case correspond to the years with higher FRP intensity.

In this regard in Chapters 3.4.3 and 3.4.4, in Tab.7 and Tab.8, the last column shows the amount of MW of fire that developed over the years. Histograms depicting the trend are in Fig.177 and Fig. 222.

In the case of MODIS data, the MW developed show peaks correspond to the years 2004, 2007, 2010 with an almost constant subsequent trend increasing again in the years 2020, 2021.

In the case of VIIRS data, the MW developed show a peak in the year 2012 and 2020.

In conclusion, it is evident from all the analyses that the greatest intensity and number of events occur in the years 2004, 2005, 2007,2010,2012 and 2019 to 2022.

Before 2000, there is no data regarding the number of fires in the Amazon Rainforest, but it is known that deforestation was very high in order to build roads through the forest and because of these roads that allowed easy access.

In many areas of the Amazon, deforestation caused a rapid depletion of the land that limited the profitability of agricultural plantations, leading settlers to quickly convert agricultural fields back to pastures for livestock. While government incentives and less labor required for ranching allowed greater gains for settlers than agriculture, environmentally this represented the beginning of intensive exploitation of the Amazon rainforest. In fact, the growing need for space for ranching often led to the settlers' application of the "slash and burn" method, which through the setting of fires (even uncontrolled fires) allowed large areas of forest to be obtained for grazing (Wikipedia, 2023).

In 2004 the number of fires and the intensity of fires is the highest since there have been surveys from satellites, this data has been relevant in planning fire containment methods.

To try to limit these phenomena, 3 steps have been carried out:

- From 2004 a law tried to require farmers and ranchers to consider 80% of their properties as reserve, but it was not respected.
- Between 2005 and 2009 there were several factors: more police controls; declining earnings from soybeans (grown in the Amazon); environmental campaigns and boycotts of companies responsible for deforestation.

- Since 2009, even as soybean earnings recovered, the government established a credit policy for the Amazon: farmers and ranchers in the most ruined areas were excluded from cheap credit until deforestation declined.

In 2015, illegal deforestation in the Amazon was again on the rise for the first time in decades, largely due to consumer demand for products such as palm oil.

As explained above, since 2019, under President Bolsonaro the number of fires and deforestation in general in Brazil has increased significantly.

5. References

- NASA VIIRS Land Science Investigator Processing System (SIPS), Product User's Guide Version 1.4
- Amazon carbon emissions double mainly by dismantled in law enforcement. (L.V.Gatti)
- Unraveling the Role of Temperature and Rainfall on Active Fires in the Brazilian AmazonUsing a Nonlinear Poisson Model (C. Lima)
- Quantification of MODIS fire radiative power (FRP) measurement uncertainty for use in satellite-based active fire characterization and biomass burning estimation (Patrick H. Freeborn, Martin J. Wooster, David P. Roy, and Mark A. Cochrane)
- https://eospso.nasa.gov/
- https://aqua.nasa.gov/content/formation-flying
- https://www.earthdata.nasa.gov/learn/backgrounders/remote-sensing
- https://it.wikipedia.org/wiki/Amazzonia
- https://files.worldwildlife.org/wwfcmsprod/files/Publication/file/1w8fz5mktn_lar__ingles_23_dic_2022.pdf
- Comparison of Fire Radiative Power Estimates from VIIRS and MODIS Observations. (Fangjun Li, Xiaoyang Zhang)
- Spatio-temporal patterns of extreme fires in Amazonian forests. (Ana Cano-Crespo)
- Living Amazon Report 2022 (https://files.worldwildlife.org/wwfcmsprod/files/Publication/file/1w8fz5mktn_lar__ingles_23_dic_2022.pdf)
- https://it.wikipedia.org/wiki/Deforestazione_della_foresta_Amazzonica
- https://it.wikipedia.org/wiki/Amazzonia